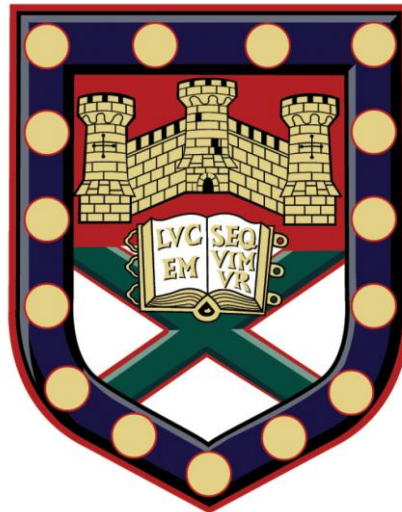


Shedding New Light on Cancer with Non-Linear Optical Microscopy



Submitted by Saleh Ahmad S. Alghamdi to the University of Exeter
as a thesis for the degree of Doctor of Philosophy in Physics,
25th June 2019

This thesis is available for Library use on the understanding that it is copyright material and that no quotation from the thesis may be published without proper acknowledgement.

I certify that all material in this thesis which is not my own work has been identified and that no material has previously been submitted and approved for the award of a degree by this or any other University.

..... Saleh Ahmad S. Alghamdi

Abstract

Oesophageal cancer, one of the most aggressive cancer types is considered the seventh most common cancer in terms of incidence and the sixth most common cause of cancer deaths worldwide due to late diagnosis. In the UK, the oesophageal cancer incidence rate has increased by approximately 10% since the 1990s. At present, histopathology is the gold standard method for the diagnosis of oesophageal cancer, which rely on biopsy collection using an endoscopy procedure followed by the histological sample's preparation. This method is invasive, time-consuming, and largely based on the pathologist's experience of diagnosis. Therefore, new diagnostic techniques are required to provide non-invasive methods for early and rapid diagnosis.

Raman scattering has the potential to replace histopathology as the gold standard for diagnosis for a wide range of diseases. Raman scattering provides stain-free imaging with chemical-specificity derived from the intrinsic vibrational signatures of biomolecules. However, the low scattering cross-section severely limits the image acquisition speeds and like conventional histopathology, requires tissue sectioning to provide morphological imaging below the surface of tissue biopsies.

Stimulated Raman scattering (SRS) has recently appeared as a powerful technique for (near)real-time Raman imaging in intact tissue samples. The

Abstract

work in this thesis aimed to develop the stimulated Raman scattering (SRS) for rapid wavelength tuning and chemical imaging of clinical samples, such as cancer biopsies. This was achieved by making modification to a laser cavity to reduce the time of the wavelength tuning by approximately 35 times compared to the original cavity design. Furthermore, the cavity modification led to the spectra being separated efficiently and the wavelength tuning controlled by cavity length changes only.

The improved design was applied to image frozen oesophageal tissues, which have four major pathology groups, normal, inflammation, columnar-lined (Barrett's) oesophagus (CLO) and low-grade dysplasia. A large area imaging was performed using the SRS technique at 2930 cm^{-1} for four different oesophageal tissues, which presented the morphological and structural information. However, histopathological diagnosis depends on the visualisation of the cell nucleus in the tissue. This component was not highlighted until the stimulated Raman histology approach was developed for small regions of interest in the CLO and the low-grade dysplasia sample, which required two different frequencies at 2840 cm^{-1} and 2930 cm^{-1} . All SRS images were compared to haematoxylin and eosin (H&E) stained sections.

Further comparisons were made between SRS and Raman imaging techniques, with SRS offering faster acquisition times and a higher spatial resolution. The spectral signature for the different pathological groups in the oesophageal tissues were explored in the high wavenumber ($2800 - 2930\text{ cm}^{-1}$) region using hyperspectral SRS and compared with the spectra from the Raman. K-means clustering analysis was used to explore the morphochemical information using the CLO and low-grade dysplasia sections. Both techniques were able to demonstrate unique information such as the epithelial cells that form the oesophagus glands and surrounding connective tissue.

Abstract

It is concluded that SRS has the power to be one of the ideal imaging modalities to gather the molecular information in biological samples. However, it still needs more development due to the complexity of the system.

Dedication

To my great mother,
my wife Asma,
my brothers and sisters,
my lovely children
Ahmad
Lauren
Azam

Acknowledgements

After all the hard work to finish this thesis, there are people who deserve my thanks for helping and supporting me.

First of all, my deepest and heartfelt thanks to my supervisor Professor Julian Moger for supporting and encouraging me throughout this work in every possible way. I feel extremely lucky to have had this opportunity to study in this wonderful research group. I would like to thank him for all the long hours he spent teaching me to think creatively and write logically. I would also like to thank him for the open-door policy which provided me with very effective advice when needed. Thanks also for the weekly group meeting which was really helpful for me to develop my discussion skills and kept us updated on new research. I would also like to express my sincere gratitude to my second supervisor Professor Nick Stone for his help, advice, and valuable suggestions whenever needed. Without Nick, all the pathological work in this thesis would not have been finished.

Second, I want to thank Professors Hugh Barr and Neil Shepherd from Gloucestershire hospital for providing all clinical samples and pathological information. Many thanks also to Sivaraman Subramanina who spent long days helping me to write hyperspectral scanning software and solve any technical issues I experienced. Special thanks to Nick Gaunt for all his efforts to help me, to Kelly Curtis and Chun-Chin Wang for helping me in the laser lab and to all biophysics group members.

Acknowledgements

Finally, a huge thank you to my great mother for her continuous support during the past four years on my PhD program and for her love of life; you are the source of my inspiration and my happiness. Also, I would like to thank my wife Asma. Without you, I cannot imagine how I could have done my research here; thank you from the depth of my heart. My brothers and sisters, thank you for always encouraging me to do my best. My children Ahmed, Lauren and Azam, you are the secret of my success and my determination in life, all my love for you.

Contents

List of Figures	12
List of Tables	17
List of Acronyms	18
1 Introduction	20
1.1 Research aims and objectives	20
1.2 Thesis outline	21
1.2.1 Chapter 2: Background	21
1.2.2 Chapter 3: Theory	21
1.2.3 Chapter 4: Method and instrumentation	22
1.2.4 Chapter 5: Development of the OPO cavity	22
1.2.5 Chapter 6: The development in coherent Raman imaging	22
1.2.6 Chapter 7: The oesophagus	23
1.2.7 Chapter 8: Conclusion and Future Work	23
1.3 Cancer	23
1.4 The oesophagus	25
1.5 Oesophageal cancer	27
1.5.1 Incidence and geographical distribution	27
1.5.2 Histological subtypes	30
1.5.3 Pathogenesis	31
1.5.4 Risk factors	32

Contents

1.5.5	Progression of Barrett's oesophagus toward OAC.....	33
1.6	Current diagnostic techniques	37
1.6.1	Endoscopy	37
1.6.2	Histopathology	39
1.7	Grading and Staging of oesophageal cancer	41
1.8	Novel optical diagnostic techniques	44
2	Background	50
2.1	Introduction	50
2.2	Raman spectroscopy	51
2.3	Coherent Raman scattering techniques	58
2.3.1	Coherent anti-Stokes Raman spectroscopy (CARS)	59
2.3.2	Stimulated Raman spectroscopy (SRS)	63
2.4	Summary	67
3	Theory	69
3.1	Introduction	69
3.2	Theory of Raman scattering	70
3.3	Coherent anti-Stokes Raman scattering	75
3.4	Stimulated Raman scattering	84
3.5	Summary	87
4	Method and Instrumentation	89
4.1	Introduction	89
4.2	Raman microspectroscopy	90
4.2.1	Instrumentation for Raman microspectroscopy	92
4.2.2	System calibration	97
4.3	Coherent Raman scattering set-up	101
4.3.1	Coherent anti-Stokes Raman scattering (CARS)	101
4.3.2	Stimulated Raman scattering (SRS)	105
4.4	Large area montage	106
4.5	Hyperspectral SRS	106
4.6	Multivariate analysis	107
4.7	Sample collection and preparation	107

Contents

5	Development of the OPO Cavity	109
5.1	Introduction	109
5.2	The Optical parametric oscillator (OPO)	110
5.2.1	Introduction	110
5.2.2	Theory of optical parametric conversion	111
5.2.3	Phase-matching	113
5.2.4	The optical parametric system	115
5.3	Development of the OPO cavity for rapid wavelength tuning	116
5.4	Performance of the OPO	118
5.5	Hyperspectral scanning software	122
5.6	Performance of the hyperspectral software	125
5.6.1	Hyperspectral Software with the Original OPO design	125
5.6.2	Hyperspectral software with the new OPO design....	130
5.7	Summary	135
6	The Development in Coherent Raman Imaging	137
6.1	Introduction	137
6.2	Coherent Raman imaging	138
6.2.1	Laser power estimation	139
6.2.2	Laser damage threshold.....	140
6.3	Large area montage	146
6.4	Stimulated Raman scattering hyperspectral stack	154
6.5	Performing the SRS hyperspectral	157
6.6	Laser power normalization	158
6.8	Summary	162
7	The Oesophagus	164
7.1	Introduction	164
7.2	Measurement protocol	165
7.3	SRS large area montage of oesophagus tissue	167
7.3.1	Normal squamous epithelium cells in oesophagus tissue	168
7.3.2	Columnar-lined (Barrett's) oesophagus (CLO)	171

Contents

7.3.3	Low-grade dysplasia	173
7.4	Stimulated Raman Histology (SRH)	175
7.5	Comparison between Raman and SRS techniques	180
7.5.1	The spectra of oesophagus tissue	180
7.5.2	Raman and SRS images	184
7.6	K-means clustering	187
7.7	Summary	194
8	Conclusion and future perspective	196
	References	202
	Appendices	223

List of Figures

1.1	The percentage of the 20 most cancer cases in the UK in 2015..	24
1.2	a) Oesophagus and surrounding organs, and (b) Cross section of the wall of a normal oesophagus	26
1.3	The incidence of oesophageal cancer in males and females in the 20 countries in Europe	27
1.4	The survival rate of oesophageal cancer up to 10 years for men and women adults aged (15-99) in England and Wales (2010-2011)	28
1.5	The survival rate of adult males and females with oesophageal cancer according to age in England (2009-2013)	29
1.6	The survival rate of oesophageal cancer in England (1971-2011) for women and men adults aged (15-99)	30
1.7	The two major histologic subtypes of oesophageal cancer	31
1.8	An endoscopy photograph of the oesophagus	35
1.9	H&E images of the four categories of BO dysplasia/ neoplasia ...	36
1.10	Harvest a sample of tissue (Biopsy) from the oesophagus using endoscope	38
1.11	Flow diagram to epitomise the multi-step process to prepare a histological sample	39
1.12	The TNM categories of oesophageal cancer	42
3.1	Light scattering by an induced electric dipole	71

List of Figures

3.2	Rayleigh scattering and Raman Stokes and anti-Stokes scattering denoted by a Jablonski energy diagram	74
3.3	(a) phase matching angle, (b) phase matching condition in the forward CARS and (c) the backward CARS	80
3.4	CARS signal generation energy diagram	82
3.5	Resonance and nonresonance CARS	83
3.6	Stimulated Raman scattering process	85
3.7	The detection mechanism of (a) Stimulated Raman loss (SRL) and (b) Stimulated Raman gain (SRG)	87
4.1	A typical experimental scheme for a Raman microscopy (InVia, Renishaw, UK). (a) Photograph of the Raman experimental set-up, (b) Sketch of the optical set-up of the Raman spectrometer shows the beam paths for the 785/830 nm laser resulting Raman signal	91
4.2	Simplified diagram of the Raman scattered light on the CCD detector	96
4.3	Raman spectrum in fingerprint and HWN region of the CaF ₂ substrate	97
4.4	Raman spectrum of the Si wafer for the x-axis calibration	99
4.5	Raman spectra for the Neon lamp (Ne) with (a) 785 nm streamline configuration and (b) 830 nm streamline configuration	100
4.6	Simplified schematic diagram of the experimental setup of the coherent Raman techniques	103
4.7	Photographs of the coherent Raman set-up	104
4.8	The protocol of the sample preparation	108
5.1	The OPO cavity. Image (a) shows a photograph of the OPO optical unit with an internal spectrometer; Image (b) shows the Construction of a ring cavity OPO with a conventional design	112
5.2	the control electronic console photograph	113
5.3	Construction of the ring cavity OPO and tuning principle with the new dispersion block	118
5.4	The OPO power as a function of the wavelength with a fixed	

List of Figures

LBO temperature for 10 different temperatures	120
5.5 Assessing the performance of the OPO	121
5.6 Assessing the piezo performance as a function of the wavelength	122
5.7 The hyperspectral software	124
5.8 Schematic of the piezo central calibration	125
5.9 Relative piezo position change as a function of the wavelength..	127
5.10 Typical tuning curve of the temperature when tuning the OPO-crystal pumped at 516 nm	127
5.11 Schematic of the hyperspectral software steps with the standard OPO cavity	129
5.12 The consuming time of each wavelength tuning step	131
5.13 The reading of the wavelength tuning on the OPO screen (red) and on the software control panel (blue)	131
5.14 SRS images and spectra of the PS and PMMA beads	132
5.15 Raman spectra of the PS (a) and PMMA (b)	133
5.16 Assessing the performance of the software with the two OPO designs	134
6.1 Time averaged power measurement	139
6.2 Transmission through the Olympus 60X water objective lens	140
6.3 Transmitted light images used to study the photodamage on a biological sample using different pump and Stokes powers	144
6.4 Dependence of photodamage percentage on the actual pump power from 120 mW up to 170 mW	145
6.5 The field of view as a function of zoom factor with two different objective lenses	147
6.6 The coverslip curvature effect on SRS mosaic images	148
6.7 An illustration of the process of acquiring a large area montage in the hyperspectral software	149
6.8 Large area montage of SRS images of an oesophagus tissue ...	152
6.9 Image normalisation of an SRS mosaic of oesophagus tissue ...	153
6.10 Initial fixing of the Raman shift of interest performs a single vibration frequency imaging	155

List of Figures

6.11	Acquired image of a multiple Raman shift using imaging techniques for wavelength tuning	155
6.12	Hyperspectral SRS imaging technique	156
6.13	Hyperspectral SRS images of a polystyrene bead	158
6.14	An illustration of the process for extracting the SRS spectrum of the ROI based on the piezo position	159
6.15	Comparison of the fluctuations in the laser power from the OPO during the tuning	160
6.16	Comparison between the SRS spectra normalised by the OPO power recorded from the OPO screen (b), and the actual power recorded from the diode (a); (c) is the Raman spectrum of the PS bead	161
7.1	Large area images of the oesophagus tissue at different grads ..	166
7.2	SRS large area montage for different pathological areas in the oesophagus tissue	169
7.3	SRS and H&E images of oesophagus tissue	170
7.4	Large area montage of Columnar-lined (Barrett's) oesophagus tissue using SRS at $2,930\text{ cm}^{-1}$	172
7.5	SRS images to illustrate the low-grade dysplasia in Barrett's oesophagus tissue	174
7.6	Stimulated Raman histology (SRH) for the small ROI of Columnar-lined (Barrett's) oesophagus (CLO) tissue	177
7.7	Stimulated Raman histology (SRH) for the small ROI of Low-grade dysplasia in Barrett's oesophagus tissue	179
7.8	The mean Raman spectra of four pathological groups of oesophagus tissue	181
7.9	The mean SRS spectra for four pathological groups at CH chemical bond in the HWN	183
7.10	Images of oesophagus tissue at CH_3 stretch vibration at $2,930\text{ cm}^{-1}$ using Raman and SRS	186
7.11	Scheme of the steps of the K-means clustering method	187
7.12	Analysis of a mixture of polystyrene and PMMA using K-means clustering method	190

List of Figures

7.13 Comparison of the result of k-means cluster analysis for contiguous sections of CLO in oesophagus tissue in the HWN region using Raman and SRS	192
---	-----

List of Tables

1.1	Summary of the cancer staging of oesophageal cancer	43
1.2	A brief comparison between the infrared and Raman techniques	47
5.1	Constant values of the polynomial equations	126
7.1	The most important measurement parameters used for comparison between Raman and SRS techniques	193

List of Acronyms

GI	Gastrointestinal
GE	Gastroesophageal junction
OSCC	Squamous cell carcinoma
OAC	Adenocarcinoma
BO	Barrett's oesophagus
GRED	Gastroesophageal reflux symptoms
CLO	Columnar-lined (Barrett's) oesophagus
TNM	Tumour grade, Node, Metastasis
H&E	Haematoxylin and Eosin
NIR	Near Infrared
UV	Ultraviolet
CRS	Coherent Raman scattering
CARS	Coherent anti-Stoke Raman scattering
SRS	Stimulated Raman scattering
SHG	Second-harmonic generation
HWN	high wavenumber region
OPO	Optical parametric oscillator
SRH	Stimulated Raman histology
SRL	Stimulated Raman loss
SRG	Stimulated Raman gain
FWM	Four-wave mixing
CCD	Charged-Coupled Device

List of Acronyms

NA	Numerical aperture
PMT	Photomultiplier tube
PD	Photodiode
AOM	Acousto optical modulator
LIA	Lock-in amplifier
FOV	Field of view
PMMA	Polymethyl methacrylate
PS	Polystyrene
ROI	Region of interest

Chapter 1

Introduction

1.1 Research aims and objectives

Histopathology is considered as the gold standard method for diagnosis of oesophageal cancer. This method depends on the collection of the biopsy based on the endoscopy procedure followed by several time-consuming chemical steps to prepare the sample for inspection under a microscope. Raman is a label-free technique, which has proven it has the capability to offer quantitative, sensitive, and chemically specific information about significant biological components in tissues and cells that contribute to discriminating between normal and diseased tissues in the oesophagus. However, standard Raman spectroscopy involves the spontaneous scattering of inelastic light and suffers from relatively weak signals leading to acquisition time that are not compatible with clinical imaging. Coherent Raman techniques including coherent anti-Stokes Raman scattering (CARS) and stimulated Raman scattering (SRS) are capable of overcoming these major limitations in Raman scattering and could be utilised for biomedical imaging.

Introduction

This thesis aims to:

1. Develop the coherent Raman scattering techniques, primarily SRS, to provide rapid wavelength tuning and to acquire hyperspectral images to extract the SRS spectra.
2. Demonstrate the potential of the SRS technique for acquiring a quick and high-quality large area montage by resolving the main limitations in the CRS imaging techniques.
3. Apply this approach to the clinical samples to identify the different morphological structures in the oesophagus tissues and compare these with the gold standard method Haematoxylin and Eosin.
4. Compare the SRS spectra to spectral information available from Raman using multivariate statistics. The spatial information available from Raman and SRS will be explored and compared with the histopathology approach.

1.2 Thesis outline

This section will present a brief outline of each chapter in this thesis.

1.2.1 Chapter 2: Background

This chapter will briefly review the development and applications of the Raman scattering and coherent Raman scattering techniques including CARS and SRS.

1.2.2 Chapter 3: Theory

This chapter will provide the main theoretical principles that have supported this thesis. The first topic covered is the theory of Raman scattering as the study undertaken is concerned with enhancing the application of Raman techniques in biology. This is followed by the principles of the coherent anti-

Introduction

Stokes Raman scattering. Finally, the chapter will provide the principles of the stimulated Raman scattering.

1.2.3 Chapter 4: Method and instrumentation

This chapter provides a detailed description of the experimental set-up and detection methods used to perform spontaneous and coherent Raman microscopy. This is followed by a brief description of the data analysis method and the samples preparation in this thesis.

1.2.4 Chapter 5: Development of the OPO cavity

This chapter will present a novel modification and automation of the OPO cavity. The chapter will begin with a brief background of the OPO followed by explaining the novel modification of the OPO cavity. Investigation of the performance of the OPO cavity will then described. This chapter will also provide a detailed description of the hyperspectral scanning software, which allows rapid automatic wavelength tuning.

1.2.5 Chapter 6: The development in coherent Raman imaging

This chapter will focus on the method used to acquire hyperspectral SRS data, which allows for the rapid extraction of the SRS spectra based on the modification of the OPO cavity and hyperspectral software described in Chapter 5. This chapter also features the development that was applied to the microscope to improve its performance in terms of providing high quality images using the SRS technique to create a large area montage. This approach will contribute to the ability to orientate the montage against the pathology images of the gold standard method (hematoxylin and eosin, H&E) for the comparison.

1.2.6 Chapter 7: The Oesophagus

This chapter will present the SRS and Raman measurements of oesophageal tissue. It will mainly focus on the SRS images of oesophagus tissue, with the aim to demonstrate the ability of the SRS technique for rapidly producing images of unstained tissues over a large area similar to the H&E to identify different oesophageal structural features. This study also investigated the comparison between SRS and Raman techniques concerning the spatial and spectral information available. Finally, different regions of the tissue were determined by identifying the chemical signatures using a K-means clustering approach.

1.2.7 Chapter 8: Conclusion and Future Work

This chapter provides a set of conclusions from the entirety of the thesis after having provided results in chapter 5-7, followed by a brief description of future work.

1.3 Cancer

According to cancer research in the UK, one in two people will be infected by cancer in their lifetime, with more than 350,000 new cases reported every year [1]. There are more than 100 different cancer types, the ten most common cancers worldwide being lung, breast, colon, prostate, stomach, liver, cervical, oesophagus, bladder cancer, and non-Hodgkin lymphoma. Oesophageal cancer is deemed one of the most aggressive kinds of cancer that the 7th most common type of cancer worldwide and the 6th most common cause of cancer deaths [2]. In the UK approximately 9000 new cases are discovered every year [3]. Figure 1.1 shows the percentage of cancer cases in the UK for the 20 most common cancers, with oesophageal cancer accounting for 2% of cases [4].

Introduction

Cancer is known as a group of diseases involving abnormal cell growth that can potentially spread and threaten other tissues [5]. This antisocial behavior of body cells typically happens when various genetic abnormalities accumulate in the cells' DNA. Cells contain a gene specifically meant to prevent cancer from occurring. This gene is known as a tumor suppressor gene, which works to stop a cell from growing out of control by restricting its activity.

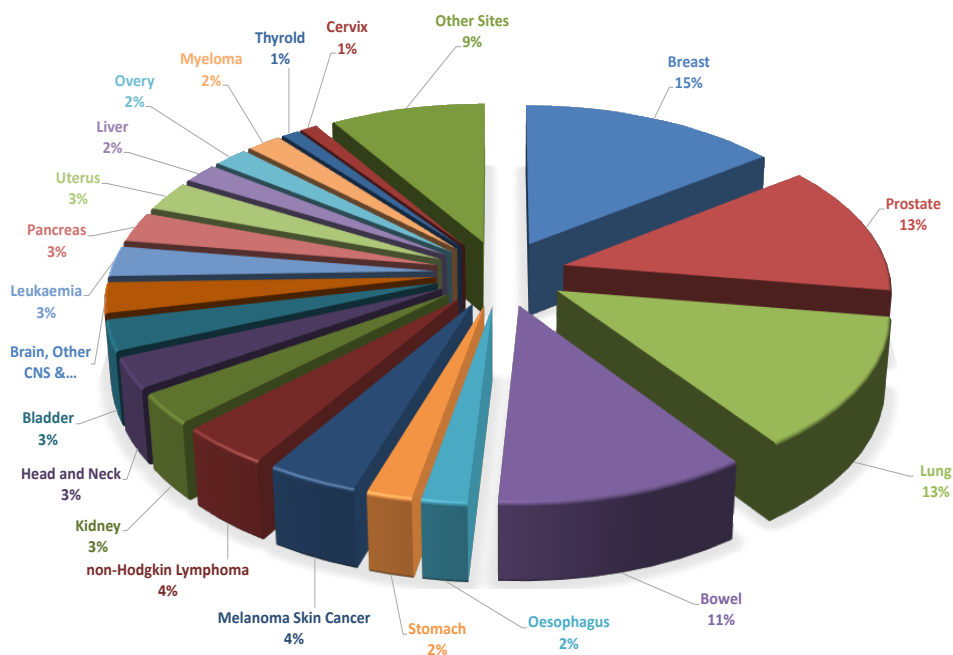


Figure 1.1:The percentage of the 20 most cancer cases in the UK in 2015 [4].

Cells also contain what are known as proto-oncogenes, which do the exact opposite when activated into oncogenes. There are also many other factors which are linked to this as cancer is incredibly complicated. DNA and genes are relatively fragile and they are therefore susceptible to mutation and damage. A tiny mutation can overlap with genes when the tumor suppressor gene is deactivated. Due to several regulatory genes and their promoters have been changed or damaged, which makes the tumor even more vulnerable to mutation. This may deactivate DNA repair genes leading to

Introduction

further susceptibility and problems. If the tumor turns malignant, it is likely to spread and can cause damage to surrounding tissues and move around the body. Therefore, DNA mutation is essentially the key that causes cancer.

The common risk factors include tobacco smoking, drinking alcohol and poor diet. These activities may introduce harmful cancer-causing chemicals into the body, which cause changes to the genes inside a cell. Another factor is the infection as viruses carry their own genetic information into cells thus altering them. A further factor is age. Cancer is more common among the aging population, where 67% of cancer deaths, with 60% of new cancer cases occurring in people more than 65 years old [1]. The combination of age, risk factors and genetics in most cancer cases result in uncontrollable cell growth.

A tumor usually begins as a benign growth for many cancers, however, there are precursor lesions which have the potential to become malignant. Therefore, early diagnosis is very important to identify abnormal growths and prevent them spreading, which helps to improve the prognosis of the patient and to increase their survival rate. This study will provide a theoretical background on the statistics, physiology and cancer pathology of oesophageal cancer and then a discussion on the current diagnostic methods and what improvements novel optical methods could offer.

1.4 The oesophagus

The oesophagus, an organ of the gastrointestinal (GI) system, is a muscular tube about 25 cm long in adults that allows food and liquid to pass through from the pharynx to the stomach. It is located behind the heart and trachea, passing through the diaphragm until it reaches the uppermost region of the stomach as shown in Figure 1.2 (a). The upper part of the oesophagus is opened by a special ring of muscle, called the upper oesophageal sphincter, when it senses liquid and food coming towards it. There is another special ring of muscle located in the lower part of the oesophagus near the

Introduction

gastroesophageal (GE) junction. This ring is called the lower oesophagus sphincter and it controls the movement of food from the oesophagus into the stomach and keeps the stomach's acid and digestive juices out of the oesophagus between meals [6]. The wall of the oesophagus consists of four different layers: mucosa, connective tissue (submucosa), layers of muscle fibers (muscularis) between layers of fibrous tissue, and an adventitia.

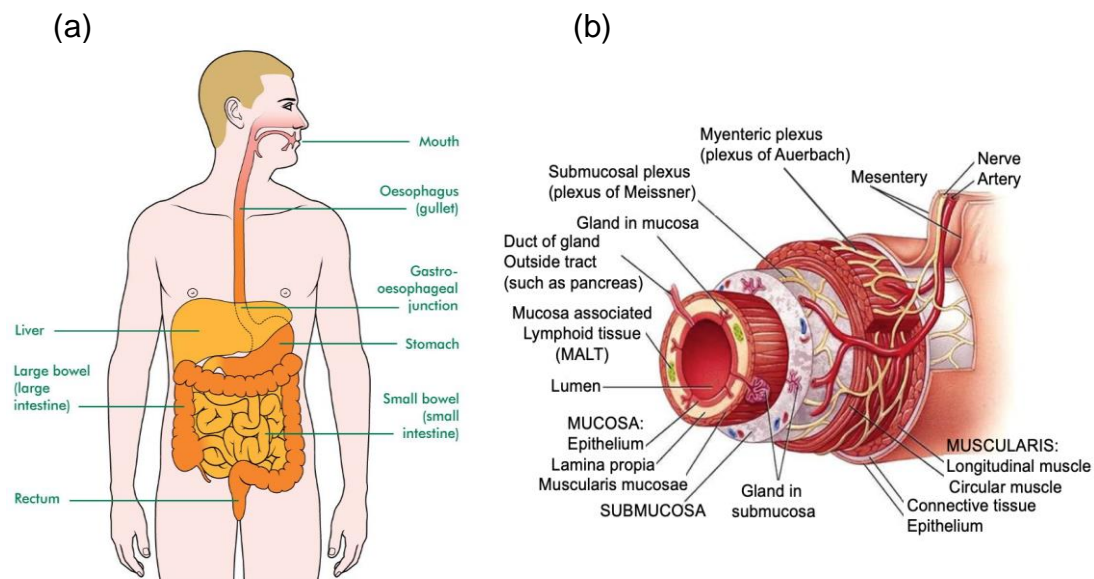


Figure 1.2: (a) Oesophagus and surrounding organs [7], and (b) Cross section of the wall of a normal oesophagus that demonstrates the four different layers [8].

Figure 1.2 (b) shows the four different layers of the wall of the oesophagus. The mucosa layer consists of a stratified squamous epithelium of approximately three layers of squamous cells, followed by two thin layers of connective tissue and smooth muscle, respectively. The second layer, made of connective tissue, comprises mucus glands, blood vessels, and lymphatic channels. The third layer, made up of muscle fibers, controls the function of motion. The last layer, the adventitia, is an external fibrous layer covering the outermost part of the oesophagus.

Introduction

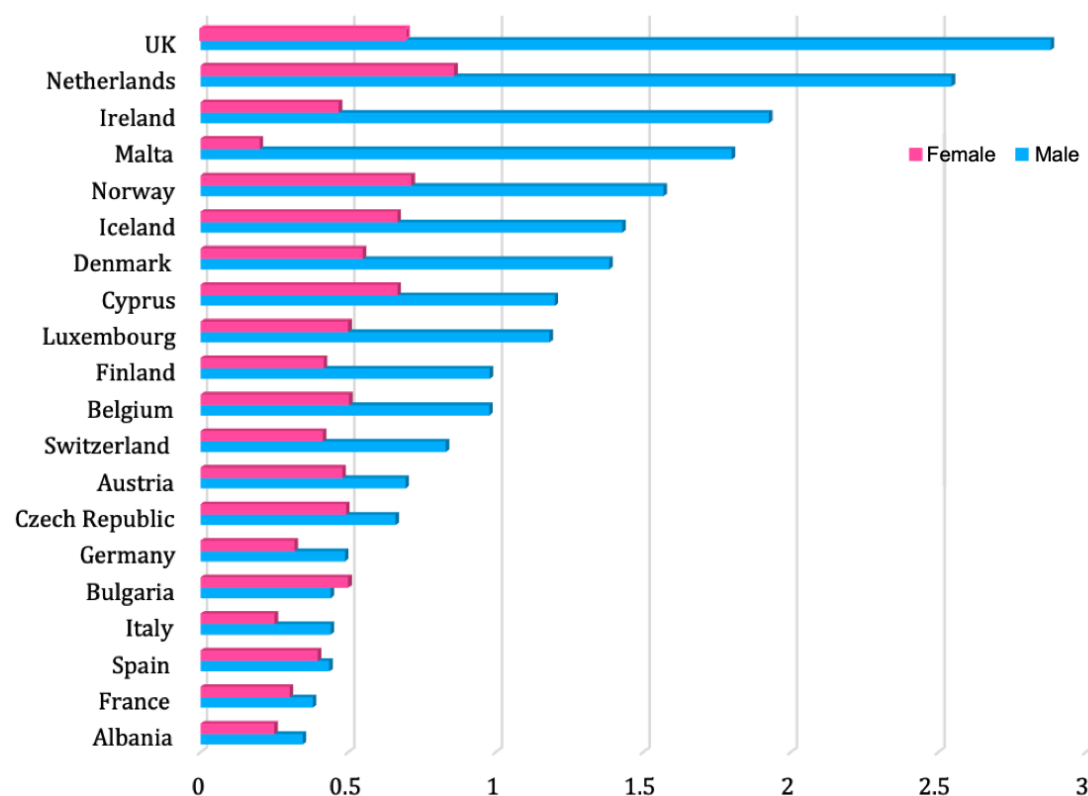


Figure 1.3: The incidence of oesophageal cancer in males and females in the 20 countries in Europe with the highest rate of oesophageal cancer incidence in the UK [9].

1.5 Oesophageal cancer

1.5.1 Incidence and geographical distribution

Oesophageal cancer is the 7th most common type of cancer in terms of incidence worldwide and the 6th most common cause of cancer deaths as mentioned above. In 2018, approximately 572,000 new cases were discovered and about 509,000 deaths worldwide, which signifies that oesophageal cancer is accountable for an estimated 1 in every 20 cancer deaths [2]. Figure 1.3 shows the highest rate of oesophageal cancer in the top 20 countries in Europe where data was available [9]. In the UK, oesophageal cancer incidence has increased about 10% in males but has decreased by

Introduction

9% in women since the early 1990s. Between 2013 and 2015 in the UK, around 9000 new cases of oesophageal cancer occurred every year (about 25 cases every day), with the highest incidence rate occurring in people aged 85 to 89 years old. Oesophageal cancer was the ninth most common cancer in males (about 6200 new cases) and the fifteenth most common cancer in women (about 3000 new cases) in the UK in 2015. Approximately 70% of oesophageal cancer cases were diagnosed at a late stage, where the most incident cases of oesophageal cancers occurring in the lower third part of the oesophagus [3].

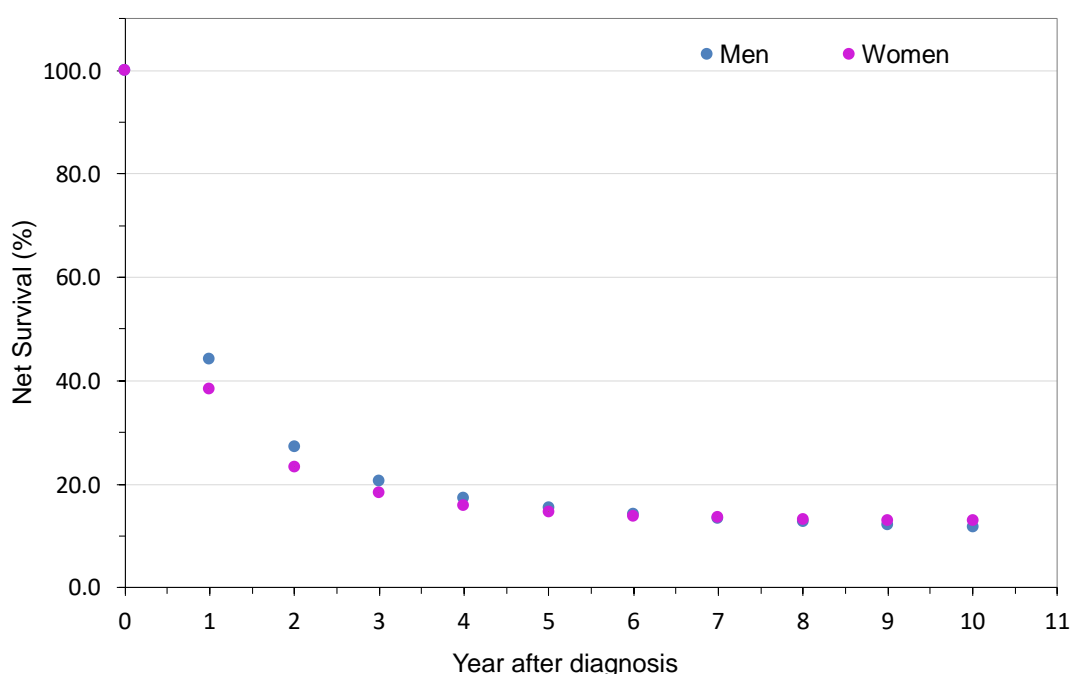


Figure 1.4: The survival rate of oesophageal cancer up to 10 years for men and women adults aged (15-99) in England and Wales (2010-2011) [10].

In general, in the UK the oesophageal cancer is the seventh most common cause of cancer deaths, with approximately 22 deaths every day (7900 every year). In 2016, there were more than 5500 oesophageal cancer deaths in males and around 2500 deaths in females, which accounted for 5% of all cancer deaths [3]. Oesophageal cancer deaths have increased in the UK since the 1970s by more than 57% in males and around 9% in females.

Introduction

However, this rate is planned to reduction by 16% between 2014 and 2035, which means that to 13 deaths per 100,000 cases by 2035. Between 2010 and 2011, more than 12% of cases diagnosed with oesophageal cancer survived for ten years or more in England and Wales, while about 15% survived for five years or more and about 42% survived for one year or more.

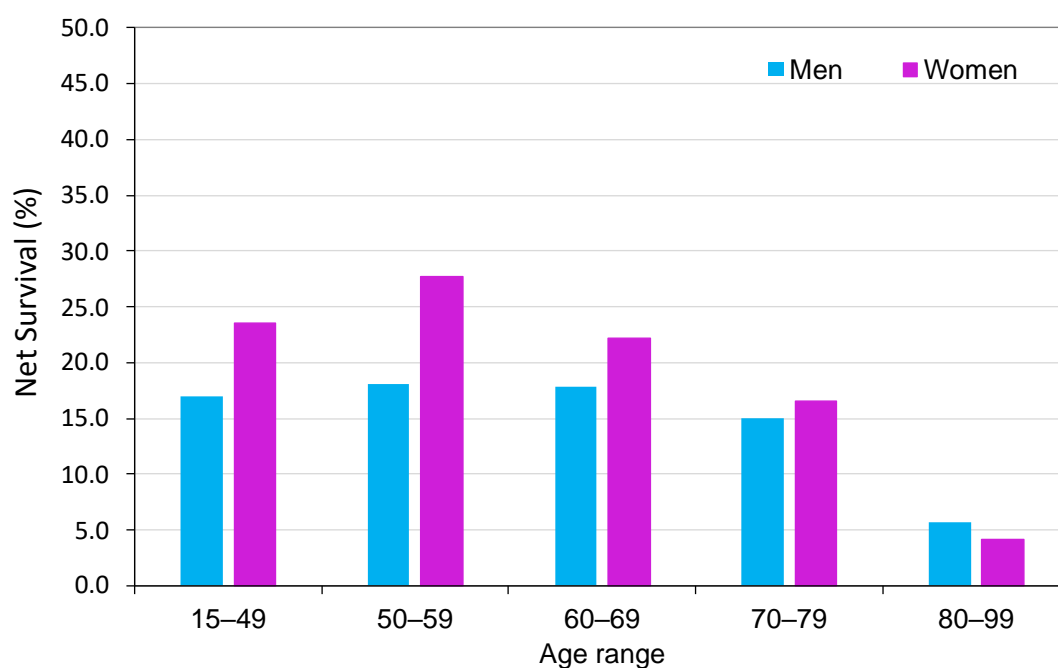


Figure 1.5: The survival rate of adult males and females with oesophageal cancer according to age in England (2009-2013) [10].

The survival rate of oesophageal cancer for one year is lower in females than in males, while it is equal at six and ten years. Figure 1.4 shows the survival rate up to 10 years after diagnosis of oesophageal cancer for female and male adults aged between 15 and 99 in England and Wales during 2010 and 2011 [3]. Oesophageal cancer can occur at any age, but the survival rate is higher for younger adults. As the figure shows, in England between 2009 and 2013, almost 25% of women and more than 20% of men diagnosed with oesophageal cancer aged 50-59 survived for 5 years or more, while only approximately 5 in 100 cases diagnosed aged 80 and over survived (see Figure 1.5). However, the survival rate has improved in the UK during the last four decades, increasing to 10 in 100 people diagnosed with oesophageal

Introduction

cancer surviving for 10 years or more compared to only 5 in 100 people in the 1970s as shown in Figure 1.6 [10].

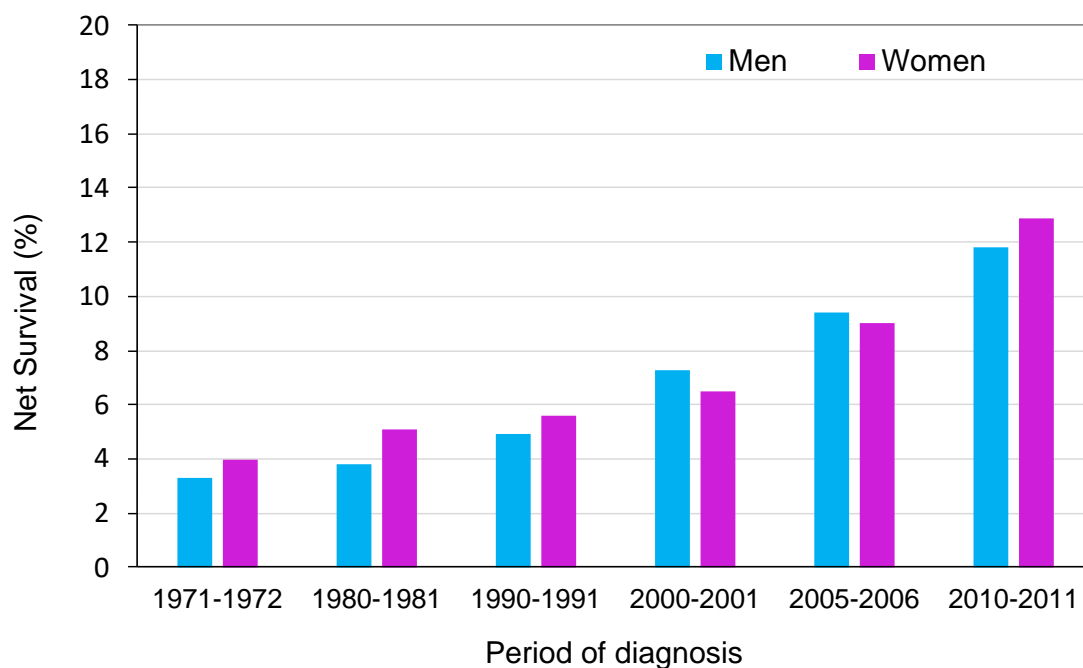


Figure 1.6: The survival rate of oesophageal cancer in England (1971-2011) for women and men adults aged (15-99) [10].

1.5.2 Histological subtypes

There are two main kinds of oesophageal cancer, oesophageal adenocarcinoma (OAC) and oesophageal squamous cell carcinoma (OSCC) (see Figure 1.7) [11]. Together, these account for more than 90% of all oesophageal cancers worldwide [2]. OSCC develops in the upper and middle portions of the oesophagus from mutations in the squamous epithelial cells, which form the lining of the oesophagus. OAC occurs mainly in the lower part of the oesophagus above the junction of the oesophagus and stomach (gastro-oesophageal junction) (GEJ) following a precursor condition called Barrett's oesophagus (BO), which is an important pre-malignant step [12]. Recently, extensive genomic analysis of OSCC and OAC patient biopsies have been done to confirm and implement this classification at a molecular level, which has clearly defined these two cancer subtypes as distinct

Introduction

molecular entities [11]. The risk incidence of cancer is higher with patients suffering from BO compared with the general population [13]. Noteworthy, the number of new cases of OAC has increased to 55% compared to 28% of OSCC cases in recent years in England [3]. Therefore, in this work we focus on the multi-step disease progression of OAC.

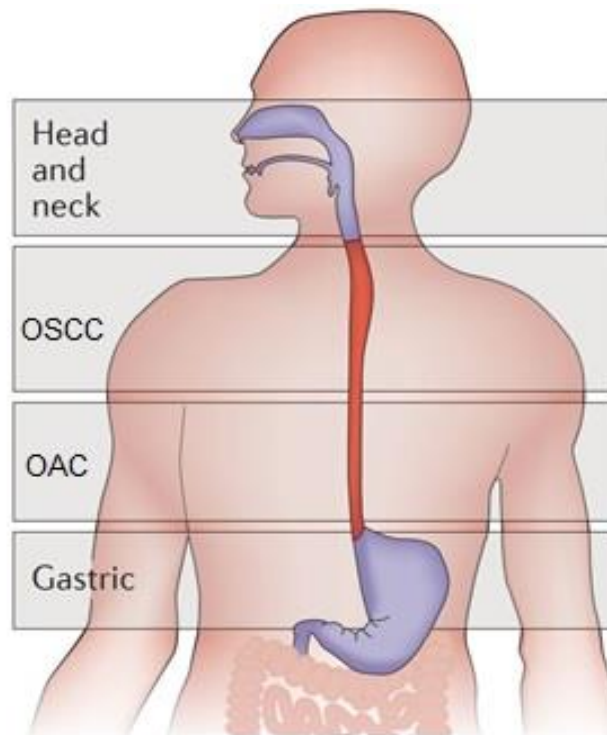


Figure 1.7: The two major histologic subtypes of oesophageal cancer, adapted from reference [11]

1.5.3 Pathogenesis

So far, scientists have not reached a full understanding the pathogenesis of oesophageal cancer. However, it has been proposed that a series of genetic changes correlating with chronic inflammation gives cells carcinogenic properties (autonomous cell proliferation, invasion, resistance to growth inhibitory signals and apoptosis, unlimited replication, and metastasis),

Introduction

leading to the dominance of mutated cells over normal cells [14]. Chronic inflammation is believed to be the causal factor of both OSCC and OAC of the oesophagus, although risk factors vary as it will be described below [15]. The tumor may develop due to different factors such as BO, submucosal glands or occasionally within the ectopic gastric epithelium located within the oesophagus for the OAC and from the normal non-keratinised squamous cell mucosa for the OSCC. However more than 80% of OAC cases develop from BO [16].

1.5.4 Risk factors

There are multiple factors causing oesophageal cancer, with various risk factors considered to be largely responsible for the striking differences in the incidence rate of oesophageal cancer that was observed over time between populations. Generally, old age is considered the most common factor causing a rise in the incidence of oesophageal cancer. Most diagnosed patients are between the ages of 55 and 85 [1,6], and the disease is characterised by a male predominance. There are other risk factors of oesophageal cancer such as obesity, gastroesophageal reflux, use of tobacco, drinking alcohol, low dietary intake of fruit and vegetables, and these are all risk factors for both OAC and OSCC.

Gastroesophageal reflux symptoms (GER), obesity and tobacco smoking

The two major risk factors for oesophageal adenocarcinoma are Gastroesophageal reflux symptoms and obesity. Gastroesophageal reflux symptoms increase the risk incidence of OAC by 2 to 8 [17,18]. Moreover, this risk is increased for patients suffering from more severe reflux symptoms, i.e. of a higher frequency, duration, and severity [17]. Obesity, especially of the abdominal type, raises the risk of OAC between 2 and 4 times, seemingly

Introduction

independently of GER symptoms [19]. Tobacco smoking is one of the common risk factors for OAC and increases the risk by about 50% [20,21]. The risk is increased more than expected when a high BMI and GER symptoms are combined, suggesting an amplifying association, whilst no such effect has been observed when GER symptoms or obesity are combined with tobacco smoking [20].

Other risk factors

Several risk factors have been reported that might increase the risk of OAC such as being of the male gender [21], having Caucasian ethnicity [22], drinking alcohol [23], and a low dietary intake of fruit and vegetables [24].

1.5.5 Progression of Barrett's oesophagus toward OAC

Barrett's oesophagus (BO) is a condition that affects the lower part of the oesophagus and results from chronic gastro-oesophageal acid reflux sustained over a prolonged period of time [25]. Therefore, in an attempt to adapt to the more acidic conditions, the normal squamous cells are replaced by columnar epithelium cells that are typically similar to the cells in the stomach or intestines. Although the exact origins of BO are unknown, it is thought that stem cells which are probably located at the basement membrane and progress towards the lumen of the oesophagus causes the formation of metaplastic cells that undergo an altered differentiation [26–29].

A long-standing Gastroesophageal reflux disease causes repeating mucosal injury and inflammation that leads to the development of BO [30,31], where about 10% of people with chronic symptoms of GER develop BO [32]. Due to the asymptomatic properties of the condition, the correct population spread of BO is difficult to establish. However, population-based studies point a spread of 1.6-6.8% [33]. BO raises the risk of incidence of OAC 30 to 60 times

Introduction

compared to the general population [34, 35]. However, only 0.12-0.63% of cases per 1000 patients suffering from BO develop into OAC with an annual risk of 0.1-0.6% [34,36]. The absolute risk of developing the disease is limited and the total death rate in BO patients is identical to that of the general population [37].

Diagnosis of Barrett's oesophagus requires both endoscopic and pathologic assessment. Endoscopy is the current gold standard method for firstly diagnosis of oesophageal cancer, but the final result must be proven by a histological inspection of an endoscopic biopsy sample [38]. The patients who are suspected of oesophageal cancer undergo a primary diagnostic procedure using a flexible upper endoscopy to evaluate tumour length and location relative to the GEJ. To confirm the diagnosis histologically and to determine the tumour type and grade, biopsies must be taken concurrently with the endoscopy procedure. This procedure is recommended typically in patients with several risk factors such as those aged over 50 years old, of male gender, of Caucasian ethnicity with chronic GER symptoms, patients with an elevated body mass index, and patients with evidence of a hiatal hernia and intra-abdominal distribution of body fat [39]. Once viewing the oesophagus in a region where BO is present (>1 cm above the GOJ) using an endoscope, the normal squamous epithelium is characterised by a light pink colour, while the columnar epithelium of BO appears a dark red in colour (see Figure 1.8) [40].

Histologically, Barrett's oesophagus is diagnosed if the normal squamous epithelium cells have changed to columnar epithelium cells. BO contains three types of mucosal metaplasia (intestinal, cardiac and fundic mucosa), relating to the region in the body where these cells are normally found. The intestinal metaplasia is the most likely of these three types to develop to oesophageal adenocarcinoma especially in adults. Also, goblet cells and mucous cells are the other features apparent in addition to epithelial metaplasia at a histological level [25]. At present, dysplasia is considered the best biomarker to indicate a patient with a high risk for development to oesophageal adenocarcinoma.

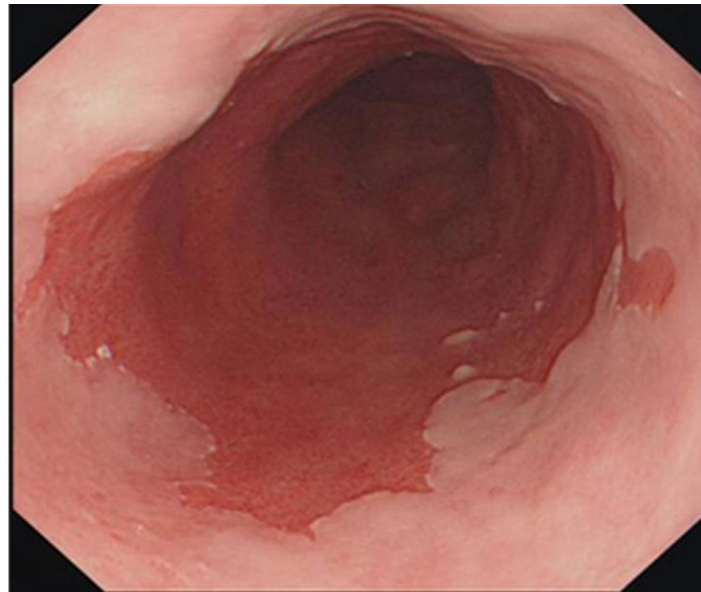


Figure 1.8: An endoscopy photograph of the oesophagus, where the columnar epithelial cells appear a dark red in colour and can be distinguished visually from normal squamous cells, which appear pink [40].

Dysplasia is defined as neoplastic epithelium or an abnormality of development and differentiation in the morphology of the Barrett's oesophagus cells. There are four categories that classify a dysplasia in BO, indefinite for dysplasia, negative for dysplasia, low-grade and high-grade dysplasia [41]. Figure 1.9 shows the four categories of BO dysplasia/neoplasia. The negative for dysplasia is presented in Figure 1.9 (A), where the BO mucosa shows that the maintenance of surface maturation is distinguished by darkly colour nuclei with stratification at the base of the glands, while in the surface the nuclei are bright, lack stratification, and preserve polarity. Architecturally, an abundant lamina propria surround the glands, where, if inflammation is present, reactive nuclear changes can appear.

The second category is indefinite for dysplasia, where the changes in deeper glands indicative of/consistent with dysplasia represent the BO mucosa in this category, but the surface maturation is maintained. The cytologic atypia in this

Introduction

category contains nuclear membrane irregularities, increased mitosis, and nuclear hyperchromasia. The third category is low-grade dysplasia, which is presented in Figure 1.9 (B). The BO mucosa often contains architectural distortion with glandular congestion appearing on the surface in the case of inflammation. Hyperchromasia, nuclear enlargement, stratification and mucin loss are shown in the nuclei in the surface mucosa, where there is an intense contrast among neoplastic and non-neoplastic mucosa.

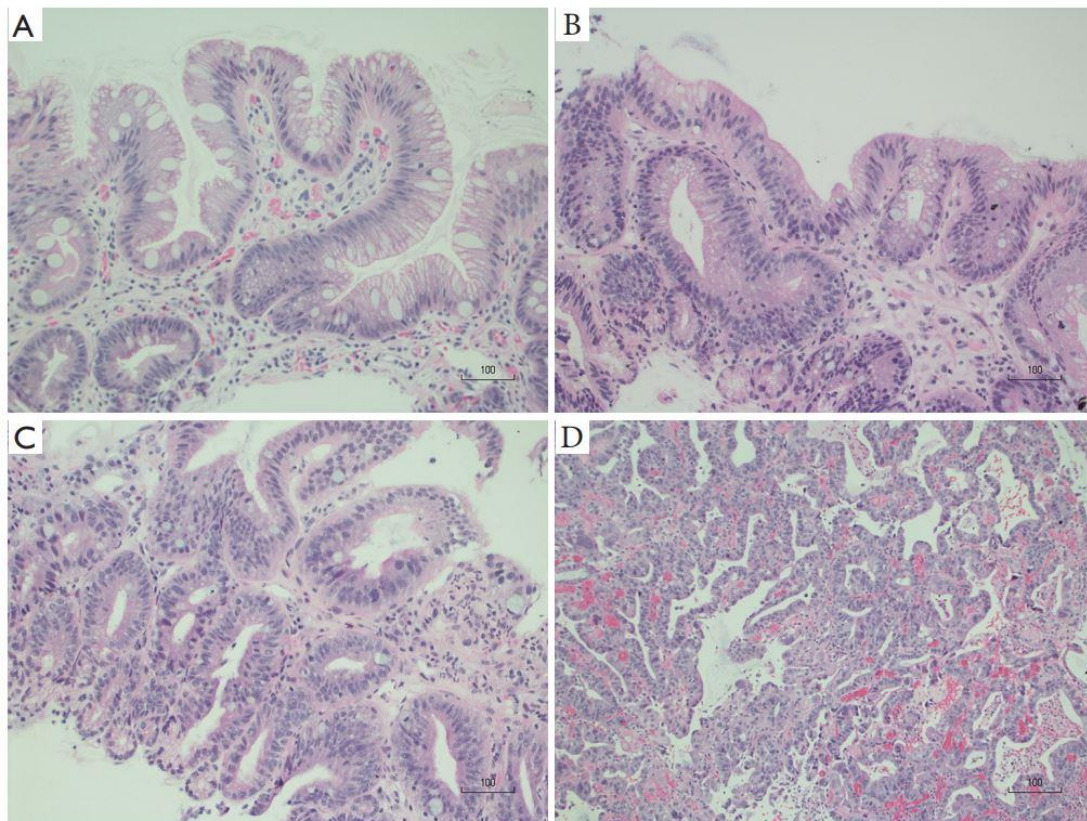


Figure 1.9: H&E images of the four categories of BO dysplasia/ neoplasia. BO with negative for dysplasia (A). BO with low-grade dysplasia (B). BO with high-grade dysplasia (C). BO with intramucosal adenocarcinoma (D) [42].

Figure 1.9 (C) shows the high-grade dysplasia, where the BO mucosa displays a loss of surface maturation as in glandular congestion and low-grade dysplasia. In this category loss of polarity occurs in the nucleus and they are rotated, magnified, hyperchromatic with another inconspicuous nucleoli. At the architectural level, the Inflammation is less comparing to the

Introduction

cytologic atypia. The characteristics of reactive/reparative changes can be highlighted based on the existence of ulceration, prominent nucleoli, and/or active inflammation features.. Figure 1.9 (D) shows the BO with intramucosal adenocarcinoma, where invasion of carcinoma into lamina propria defines intramucosal adenocarcinoma. The features of intramucosal adenocarcinoma can be distinguished through the presence of single cells and small clusters inside the lamina propria, and a syncytial growth pattern with back-to-back glands. According to the American Gastroenterology Association (AGA), the monitoring of BO is done every 6-12 months if the biopsy is low-grade dysplasia and every 3-5 years if the biopsy is negative for dysplasia. Whereas for the high-grade dysplasia, it is recommended to use endoscopic ablation therapy and a follow-up every three months. [42].

1.6 Current diagnostic techniques:

Major symptoms of oesophageal cancer (dysphagia and weight loss, followed by GER, odynophagia, and dyspnoea) usually do not appear before the disease reaches an advanced stage [12]. There are two main methods of diagnosis of oesophageal cancer, endoscopy and histopathology, as mentioned above.

1.6.1 Endoscopy

Endoscopy is an invasive procedure that allows the clinician to visualize organs from inside the body. Endoscopic probes can be inserted through a small hole in the body such as the mouth, nose and anus until it reaches the suspicious areas. It consists of a flexible tube with a light digital camera in the end and is connected with a computerised system that shows the work being done. It also uses forceps and scissors to collect a biopsy that could be cancerous. The endoscopy is considered safer and faster than a surgery procedure. However, it still has some low risks such as infection, chest pain, organ damage and bleeding [38,43,44].

Introduction

An upper endoscopy is a common way of diagnosing oesophageal cancer. A tube is inserted through the mouth to look for signs of illness in certain areas in the oesophagus (see Figure 1.10) [45]. The upper endoscopy can be utilised as a biopsy, also to define the extent of the tumor. The lining of the oesophagus and any abnormalities can be seen using the camera on the end of the endoscope. When collecting a biopsy, it can be used not only for a cancer diagnosis, but also can help to distinguish different types of cancer such as OAC or OSCC that require very different treatments. However, this procedure must be confirmed by a histological inspection of an endoscopic biopsy sample.

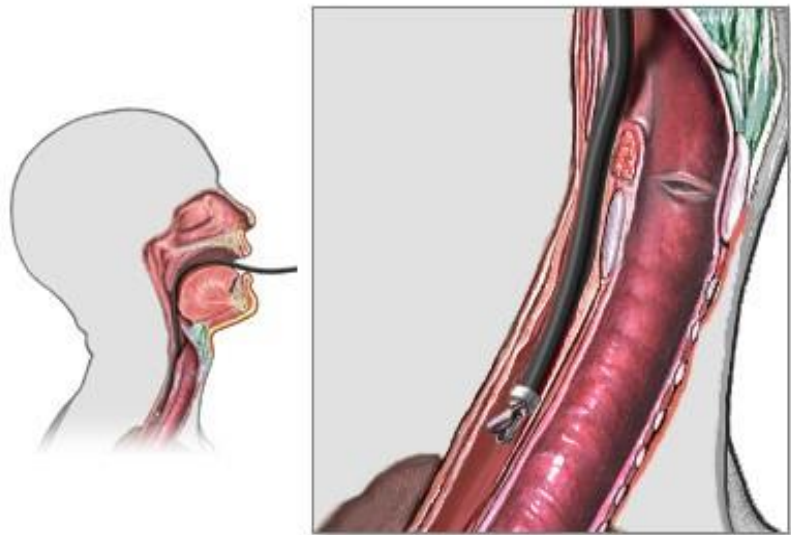


Figure 1.10: Harvest a sample of tissue (Biopsy) from the oesophagus using endoscope [45].

Biopsy

A biopsy is a small piece of tissue that is collected from a patient using surgery or an endoscopy. There are several types of biopsy techniques such as endoscopy biopsy, surgical biopsy and needle biopsy. Most types of

Introduction

cancers are discovered after taking a biopsy from a suspicious area, which is then sent to the pathology lab for examination by a pathologist [46].

1.6.2 Histopathology

Histopathology is the procedure that deals with the specimen after it is collected from the patient. In the pathology lab the specimen undergoes several steps to prepare the sample for an examination by a pathologist (see figure 1.11).



Figure 1.11: Flow diagram to epitomise the multi-step process to prepare a histological sample [47].

Introduction

Fixation is the first step after the specimen is harvested from the body. The main reason for fixation is to maintain the tissue in as life-like a state for as long as possible. Fixation should be implemented as soon as possible after removal of the tissue (in the case of surgical pathology) or not long after death (in an autopsy) to avoid autolysis. The next step is the tissue processing, which converts the tissue into a suitable form that can be made into thin microscopic sections. Paraffination is most commonly used, since it has the same density as tissue. There are two main steps in this processing: **dehydration** and **clearing**. Because the wet tissue cannot be infiltrated directly, dehydration is performed to remove the free water from the tissue and leave the bound water in place using an alcohol (e.g. ethanol, methanol or acetone). Clearing agents must be dissolvable with the dehydrants to be effective to eliminate them followed by the paraffin later to allow for complete infiltration. Currently, xylene is widely used as a clearing agent in the tissue processing [47]. Nevertheless, it has the unwanted characteristic of drying tissue samples due to it is insoluble in water and also it has the ability to remove the water from the tissue.

Embedding: most fresh tissue is very sensitive, and it can be crushed easily. Therefore, it is out of the question to prepare thin sections from it unless it is maintained chemically. Paraffin or plastic resin are the most two common embedding agents that are mixed with the tissue. Upon setting this embedding becomes rigid, enabling the specimen to be sectioned.

Frozen section: this is the second method that is used to make the tissue hard enough for sectioning. The tissue must be frozen to a very low temperature using liquid nitrogen or dry ice, for instance.

Tissue sectioning: the purpose of sectioning is to cut the tissue to slices of a few tens of microns thick using a device called a microtome.

Staining: the aim of staining is to provide contrast of cellular components in optical microscopy. Stains and dyes are usually used in biology and medicine

Introduction

to highlight cellular structures in biological tissue under a microscope. There are several dyes that can be used in the staining process that are chosen for their ability to stain different cellular components of tissue. Haematoxylin and Eosin (H&E) is a common combination used in the staining process, with other stains being used in specific situations according to diagnostic requirements. The cell nuclei are often stained in blue colour by the hematoxylin, while the extracellular and cytoplasm are stained in pink colour by the eosin. A general overview of a tissue's structure and the general distribution of cells are provided by the stain. Once the sample is ready, it is sent for examination under the microscope [47].

To conclude, histopathology is considered as the gold standard method for the confirmation of many cancers. However, this method causes a delayed diagnosis up to several days because it requires the tissue to undergo many complicated steps before examination. The pathologist's experience plays a significant role in correctly identifying the morphology of cancerous cells using a light microscope, and there is still a big disagreement concerning the grading of cancers between pathologists [47].

1.7 Grading and staging of oesophageal cancer

Grading: the scale used for grading oesophageal cancer cells is from Grade 1 (G1) to Grade 3 (G3) depending on the degree of abnormality. G1 is well differentiated, which means the majority of cancer cells look mostly like normal cells. G2 is moderately differentiated, with the degree of abnormality in cells being higher than G1 and lower than G3. G3 is poorly differentiated/undifferentiated, which means it no longer resembles normal cells.

Introduction

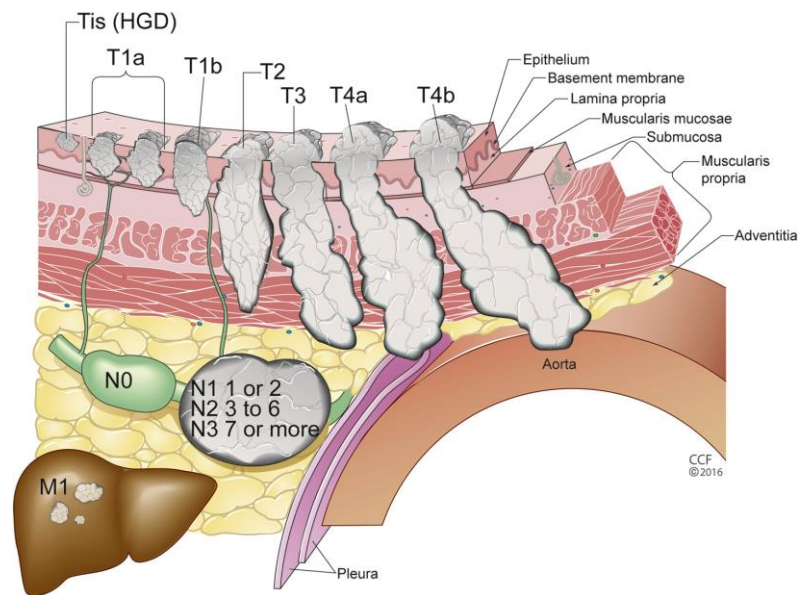


Figure 1.12: The TNM categories of oesophageal cancer [48]

Staging: the common way to stage oesophageal cancer is using the TNM system, which comprises the primary tumour (T), regional lymph nodes (N), and metastasis (M). There are five stages for oesophageal cancer, which are numerically categorised from 0 to 4 (see Figure 1.12). Stage 0 (high grade dysplasia) is the earliest stage of oesophageal cancer where several abnormal cells in the inner lining of the oesophagus, dysplastic cells, are localised in the mucosa. Oesophageal cancer is then staged from 1 to 4, according to the structure and position of the tissue affected in the body, as seen in Table 1.1.

Introduction

Stage	TNM	Oesophageal cancer growth and spread
Stage 1	1A	T1, N0, M0 Growth not exceeded the submucosa.
	1B	T2, N0, M0 Growth into the muscularis layer.
Stage 2	2A	T3, N0, M0 Growth into the covering of the external surface of the oesophagus.
	2B	T1 or 2, N1, M0 Growth no further than the muscle layer Spread into 1 or 2 nearby lymph nodes.
Stage 3	3A	T4a, N0, M0 Growth into the tissue covering the outside of the lungs. Growth into the covering of the outside of the heart. Growth into the muscle located at the bottom the rib cage.
		T3, N1, M0 Growth into the membrane covering of the outside of the oesophagus. It is in one or two nearby lymph nodes.
		T1 or 2, N2, M0 Growth not exceed than the layer of muscle Spread to three to six nearby lymph nodes.
	3B	T3, N2, M0. Growth into the membrane covering the outside of the oesophagus. Spread to three to six lymph nodes.
	3C	T4a, N1 or 2, M0 Growth into the tissue covering the outside of the lungs, the covering of the outside of the heart and the muscle at the bottom of the rib cage. It is in up to six lymph nodes.
		T4b, Any N, M0 Growth into nearby structures (a spinal bone, windpipe, or a blood vessel). Spread to any number of local lymph nodes.
	Any T, N3, M0 The cancer appears at any size. Spread to more than seven nearby lymph nodes.	
Stage 4	Any T, Any N, M1 Cancer is considered as an advanced stage. Spread to other parts of the body (e.g. liver or lungs).	

Table 1.1: Summary of the cancer staging of oesophageal cancer [48].

1.8 Novel optical diagnostic techniques

Conventional histopathology is the current gold standard method based on the endoscopy and biopsy procedures for the pathological diagnosis of oesophageal cancer. However, a large amount of tissue should be harvested, and it undergoes several complicated chemical steps for preparation, such as dehydration, fixation, slicing, staining and mounting [47]. These steps are necessary for a pathologist to provide a full tissue cellular morphology view, from which a diagnosis is done. However, this is invasive and time-consuming, typically taking hours for up to several days. Therefore, new diagnostic techniques are required to provide fast and accurate images that look like the histological images to help in surgical procedures and decision making.

Vibrational spectroscopy techniques based on both Raman scattering and infrared (IR) absorption, offers many potential advantages, which are intensively used for biochemical applications, shows great promise to become a valuable tool. It can deliver quantitative, sensitive, and chemically-specific information about important biological components in a group of cells and tissues [49]–[51].

Raman spectroscopy rely on the inelastic light scattering of photons through they interaction with molecular vibration. To excite a specific vibration of a molecule requires the energy difference between the incident photon and the inelastic scattered photon; this difference is termed the ‘Raman shift’. A molecule has a unique combination of Raman shifts that can be considered as a “finger-print”. This makes it readily possible to identify the distinct chemical and molecular features of biological molecules such as lipids, proteins and DNA without exogenous labels. Thus, the unique pathological information can be extracted from the changes in these molecular fingerprints. Raman has been proven to be an ideal technique for real-time measurements, in turn making it very useful for biomedical applications [52].

Introduction

Raman scattering suffers from relatively weak signals, with typically only 1 in 10^6 photons undergoing inelastic scattering, which is the main limitation of Raman spectroscopy. The elastic Rayleigh scattering signals, as well as tissue auto-fluorescence, often overwhelm Raman [52, 53]. Due to using Raman techniques in strongly optical scattered tissue environments, and the low signal efficiency, Raman often has limited speed. This makes Raman spectroscopy usually demand high-powered lasers, which may cause damage to the tissue specimen, which means that a balance needs to be achieved to avoid damage.

For imaging tissue using Raman, there are several challenges, such as the highly scattered and inhomogeneous nature of tissue. Due to the high absorption of tissue, background fluorescence from endogenous fluorophores can be an issue. These fluorophores can absorb laser photons and emit photons of longer wavelength, which leads to a broad background signal. Therefore, an NIR laser source (785 nm) is often used to overcome the inherent fluorescence and also to reduce the sample damage in comparison to shorter visible wavelengths. In addition, using near-infrared wavelengths, the energy is not enough to excite the molecules to an electronic state, which prevents fluorescence from occurring, and offers a significant reduction in the fluorescent background [55].

Infrared (IR) spectroscopy is based on measuring the absorbed light as it interacts with a sample [49]. IR is able to detect the stretching and vibrational modes of covalent bonds, where during the vibration the molecule must undergo a dipole moment change to make the transition to IR active. Organic molecules are the most commonly used with IR spectroscopy, although some inorganic molecules can also be analysed. In general, IR cannot be used to determine the whole structure of a molecule, due to the IR peaks for the different C-C and C-H bonds limited with the amount of noise. The most common ways in which a covalent molecule can stretch are symmetric and asymmetric stretching, where molecules can move through space and can decrease or increase in the bond length. Based on the strength of the bonds

Introduction

in the molecule and various functional groups that have a known specific absorption range, the frequency at which the vibration occurs can be accurately determined, which make it easy to deduce some functional groups from a spectrum [49-51].

In IR spectroscopy, many sample preparation methods are used before inspection in a spectrometer. These depend on the type of the material being analysed. For instance, two salt plates, which are transparent to infrared light, are used for liquid samples, as the liquid can be encased between them. While with solid samples, there are many ways used for preparation such as applying the sample as a thin layer on salt plates after being dissolved in an appropriate solvent. The time-consuming sample preparation is considered one of the most major limitations in IR spectroscopy. For measuring the sample, there are two main measurements are performed after the sample is ready. The first is used as a reference (air or solvent that a compound is dissolved in) to remove any background noise that may affect the results, then followed by the sample itself. An IR light source is directed towards the sample after it is passed through a monochromator. When the sample absorbs or reflects the light, the remaining wavelengths of light are detected at the IR detector. The functional groups in the molecule can be then determined by measuring how much energy was absorbed at each frequency [49-51]. Table 1.2 shows a comparison between the IR and Raman techniques.

Fine temporal and spatial resolutions are required for biomedical studies, as the specimens are usually live, and the environment is complex. Raman is considered far from being an ideal imaging technique due to the previous limitations. Thus, coherent Raman techniques are an alternative approach explored in this thesis.

Introduction

IR	Raman
Absorption	Scattering
Based on a change in dipole moment (No symmetric stretches observed)	Based on a change in polarisability with vibrational motion
Only occurs in NIR and IR spectral regions	Observed at all wavelengths
It has strong signal	Suffers from a weak signal
Water is highly absorbed	Water is very weak scattered, which is not a problem
Provides broad spectral features	Provides sharp spectral features for molecular fingerprinting
Sample preparation in most cases is required	Sample preparation is not required

Table 1.2: A brief comparison between the infrared and Raman techniques.

Coherent Raman scattering is a nonlinear optical technique that includes CARS and SRS, which require ultra-fast pulsed laser excitation [55]. This technique can provide an increase in signals that have a non-linear dependence on the total incident power, which causes the Raman signal to be enhanced, and provides faster acquisition times. CARS is suitable for biological imaging at video rates [56]. The CARS signal can be readily separated from the fluorescent background, as they are located on the blue side of the excitation lasers. However, CARS suffers from a non-resonant background, which distorts the spectral shape and reduces the imaging contrast [56]. This makes CARS spectroscopy much more complicated than Raman spectroscopy. Several retrieval algorithms are required to extract the Raman information from a CARS spectrum to make it more useful [55–57]. For these reasons, CARS was excluded from this thesis.

SRS can overcome the main limitations of both CARS and Raman techniques. It is free from the non-resonant background, and the extracted SRS spectrum matches the Raman spectrum. SRS has been applied in a range of studies in materials science, chemistry, the biosciences, biomedical

Introduction

and pharmaceutical areas [59–62]. For instance, the high speed imaging capability of SRS thus reveals features that cannot be seen with other techniques and has been used to visualise living cells and tissues and seed coatings providing both mechanistic information and kinetic insight into living processes [63]. SRS can provide biological imaging at video time frame rates similar to CARS [64]. The CH stretching vibrations in the high wavenumber (HWN) region between 2800 cm^{-1} and 3100 cm^{-1} is the region of interest in this thesis. The SRS technique discussed in this work is an imaging technique, which produces great chemical contrasts in the region of interest. The hyperspectral stack approach has been applied to extract the SRS spectrum via sequential tuning of one of the laser wavelengths. The optical parametric oscillator (OPO) is responsible for the wavelength tuning in this setup, which works based on three main mechanisms: crystal temperature, Lyot filter, and cavity length but these steps cause a delay in wavelength tuning. In biomedical imaging, fast procedures are required, thus, developments in the OPO for rapid wavelength tuning were applied by adding a dispersive block into the OPO cavity and reducing the mechanical steps from three to two. This approach offers a fast tuning of 35 times the standard design.

For tissue imaging, the SRS technique has undergone many stages of development since its discovery. Recently, A new approach called stimulated Raman histology (SRH) has been proposed to identify the cell nuclei and cell bodies in a tissue section, using SRS at two different frequencies at 2850 cm^{-1} (lipids) and 2930 cm^{-1} (lipids/protein) to recreate the staining effect that is used in the H&E method. The visualisation of the cell nuclei and cell bodies are the two main elements which histopathology diagnostics requires. There are a various large number of proteins inside the nucleolus membrane [65, 66]. Therefore, by subtracting the two SRS images at 2930 cm^{-1} and 2850 cm^{-1} , the proteins will be highlighted, which causes an increase in the contrast of the nuclei cell [67]. SRS is a unique technique that has the ability to image cell bodies at CH_2 and cell nuclei at CH_3 chemical bonds. This approach was applied to healthy and cancerous colon , pancreas and brain

Introduction

sections to provide rapid free microscope images in a good agreement with standard histology [66, 67]. SRS opens up a new area to develop real-time and label-free cancer diagnoses and treatments. In this work, different oesophageal tissues were used, which is discussed in greater detail throughout the thesis.

Chapter 2

Background

2.1 Introduction

Raman scattering provides an intrinsic and unique chemical fingerprint derived from molecular vibration. Raman spectroscopy has been utilised for many years to observe and study biological materials and systems [68]. Raman imaging (spectral intensity values are collected simultaneously from the whole region of interest) is limited in terms of its applications because despite being a valuable information source, it has relatively weaker signal intensity as compared to other modalities like fluorescence microscopy. Over the past fifteen years, however, coherent Raman imaging techniques have evolved that are now able to capture rich chemical information with near real-time acquisition [64]. This method is now emerging as a powerful tool for obtaining functional information of biological systems without exogenous staining. In this chapter, a brief review of the development and application of these techniques will be presented.

2.2 Raman spectroscopy

Raman scattering is a non-parametric optical phenomenon resulted from the interaction between the incident light with a molecule and its related vibrational states. This was discovered in 1928 by Sir C V Raman and K S Krishnan [69]. He studied the illumination of a specimen using a monochromatic light of frequency ω_p and studied the scattering of a whole spectrum of light. Rayleigh scattering, an elastic interaction, was responsible for the most critical feature of the spectrum happening at the incident monochromatic light of frequency ω_p . This was as he had expected. The inelastic interactions between the molecular vibrations from a specimen and incident photons resulted in the observation of weak spectral lines. The spectral lines had shifted frequencies due to the transfer of energy during this process, which is known as Raman effect. These frequencies, $\omega_p \pm \omega_R$, correspond to Stokes ($\omega_p - \omega_R$) and anti-Stokes shifts ($\omega_p + \omega_R$). As discovered by Raman and Krishnan, the material is highly identified through these shifts and their resulting spectra. This discovery (Raman effect) resulted in Raman being awarded the 1930 Nobel Prize in Physics. The incident field at ω_p of the electromagnetic spectrum in most cases is within the infrared or visible range. Whereas the molecule vibrations can be directly investigated at ω_R .

There are several advantages of Raman-based technologies in cancer diagnostics, particularly to provide unique information about significant biological components groups of cells and tissues [51,52]. The energy difference between the incident photon and the inelastic scattered photon is the energy obligatory to excite a specific vibration of a molecule. This makes the biological molecules like lipids, proteins and DNA that have distinct chemical and molecular features to be easily identified and quantified without using labels. Pathogenic information can be taken from the changes in these “molecular fingerprints” [52]. Furthermore, Raman scattering is well-matched with excitation sources of Near Infrared (NIR) along with molecular specificity, which the maximum depth of penetration in tissue is lie at this range of the

Background

wavelength [79]. Spectra readings also can be readily harvested from the body surface due to NIR being minimally absorbed by water and haemoglobin. This makes the technique ideal for real-time measurements and in turn makes it very useful for biomedical imaging [79].

In order to be translated into a diagnostic technique, further development is required to use Raman scattering technique in the diagnosis of cancer. Even with numerous well-understood limitations that should be resolved, there is a great potential for improvement [64]. As mentioned previously standard Raman spectroscopy involves the spontaneous scattering of inelastic light and suffers from weak signals, where Raman cross-section is about 10^{-30} cm² per molecule. In addition, it frequently has overwhelmed by the elastic Rayleigh scattering signals in addition to tissue auto-fluorescence [53,54]. It often has limited speed because of the low signal efficiency and therefore, the utilisation of Raman techniques in robustly optically scattering tissue environments faces hurdles due to this long acquisition time (1-10 second per pixel prohibit high-resolution imaging). This is also the reason for Raman spectroscopy often requiring high-powered lasers. However, these lasers can cause damage to biological samples under conditions that are not conducive [80]. Several Raman enhancement techniques, including coherent Raman scattering imaging modalities depend on Raman scattering, multimodal integration, and selective sampling Raman microscopy, were developed to address this issue. Several approaches were offered to improve the Raman signal such as using the nanomaterials, photonic structures, hand-held diagnostic devices and endoscopes. By developing these techniques, significant steps have been taken towards increasing the diagnostic speed and precision. They also depend on cost effective that could be accepted by healthcare services [80].

To include all the applications of Raman spectroscopy for the identification of disease in the literature review will make it too vast. This chapter focuses on its application as a tool to discover the biochemical changes that take place during the process of carcinogenesis, moving towards cancer diagnosis and

Background

screening. Differentiation between normal and diseased tissues in many different areas, such as the brain [72–77], the lungs [78, 79], oesophageal and gastric [80–89] can be done through the Raman technique and this has already been demonstrated. Measurements with the fingerprint region, which is typically defined as (400 – 1800 cm^{-1}) are the focus of the majority of publications in the literature using Raman spectroscopy. The fingerprint region has a lot of biochemical information that is useful for diagnosis. The less commonly used region is the high wavenumber (HWN), defined as (2400 – 3800 cm^{-1}), but this may offer several benefits, especially for in-vivo applications. The HWN region has a reduction in fluorescence in its measurements. For in-vivo probe measurements, the use of the HWN region may seem more appealing. However, as the peaks are broadband and overlapping, the interpretation in the HWN region can be tricky even though it can provide complementary information to that of the fingerprint region. It also provides information on proteins and lipids within a sample as it contains information about the C-H stretching vibrations.

The fact that the fibre-optic Raman probes rely on the HWN region between 2400 cm^{-1} and 3800 cm^{-1} could be utilised to describe brain tissue ex-vivo was presented by Koljenovic et. al [74]. The high-wavenumber spectral region was used to avoid the background Raman scattering resulting from silica fibres in its measurement, where it is still able to provide a diagnostic power and high biochemical specificity [72,90]. A multivariate classification method was enhanced by the authors that permitted distinguish the structure of the brain based on the biochemical contrast. The Raman spectra of white matter consisted features similar to sphingomyelin and cholesterol.

In 2010, Kirsch et al. studied the possibility of utilising a fibre-optic Raman probe for diagnosis brain tumours [84]. An accuracy of $\sim 250 \mu\text{m}$ was achieved by a diagnosis without exogenous labels of induced brain tumours in mice utilising Raman spectral maps through an area of $3.6 \times 3.2 \text{ mm}^2$. Two years later, primary brain cell density was studied by Krafft et al. utilising Raman spectroscopy in the fingerprint region between 600 cm^{-1} and 1800 cm^{-1} [86].

Background

The Raman spectra provided a better contribution from nucleic acid in comparison to healthy tissue for high-grade gliomas. The capability to produce Raman spectral images utilising raster-scanning approach in a good agreement with the images acquired by H&E was also demonstrated by the authors [86].

In addition, NIR Raman spectroscopy was used by Hamaguchi et al. in 2001 to demonstrate the potential of distinguish between malignant and healthy lung tissues ex-vivo using a 1064 nm laser excitation source [79]. Sharp peaks situated at 1449 cm^{-1} and 1667 cm^{-1} were found in the cancerous tissues corresponding to collagen. In another similar study, Huang et al. utilised NIR Raman spectroscopy to discriminate between healthy and diseased bronchial tissues [88]. In this study, probing was conducted between 700 cm^{-1} and 1800 cm^{-1} utilising a near-infrared (785 nm) laser excitation source. Important spectral differences of bands related to collagen, lipids and amino acids were revealed by the measurements.

Pure compounds are found to have a molecular fingerprint with distinct peaks at particular wavenumbers. This was revealed by the Raman spectra conducted in these compounds. However, this spectral information becomes complex when measuring a mixture of compounds, such as in tissues, as it involves several overlapping peaks. Multivariate techniques such as principal components analysis (PCA) [80,81], k-means cluster analysis [100], and linear discriminant analysis (LDA) [101], are combined with Raman to separate these peaks. Principal component fed linear discriminant analysis is utilised as a common approach to make discriminant models [82–84]. The Raman classifier models are frequently described as having specificity and sensitivity in their performance. The overfitting of data was avoided, where the models are cross validated [94]. Raman techniques have the capability to distinguish between the healthy and diseased groups in the oesophagus and gastric area with high sensitivity and specificity.

Another concentrate of diagnostic research utilising the Raman spectroscopy

Background

technique has been for oesophageal and gastric cancers. A Raman spectroscopy technique was utilised to develop a fibre-optic for *in vivo* diagnosis of OSCC during clinical endoscopy [95]. The clinical value of this fibre-optic was evaluated by Wang et al., who were able to acquire both fingerprint between 800 cm^{-1} and 1800 cm^{-1} and HWN region from 2800 cm^{-1} to 3600 cm^{-1} Raman spectra from oesophageal tissue *in vivo* at the same time. This was done using a rapid fibre-optic Raman endoscope. For this, 48 oesophageal patients undergoing endoscopic examination were considered and 1172 *in vivo* fingerprints and high wavenumber Raman spectra were taken from them. 80% of this total Raman dataset was used for training and 20% for testing. The training dataset was used to improve diagnostic algorithms for tissue classification utilising the partial least squares-discriminant analysis (PLS-DA) and leave-one patient-out cross-validation (LOPCV). The fingerprint and HWN Raman spectroscopy in the training measurements simultaneously delivered a diagnostic specificity of 97.4% and sensitivity of 97.0% for OSCC classification as shown by PLS-DA-LOPCV. Based on the simultaneous fingerprint and HWN Raman technique, a relating diagnostic specificity of 93.6% and sensitivity of 92.7% for OSCC classification was awarded on the application of a diagnostic algorithm to the independent testing measurement. This proved to be outstanding to both the fingerprint and HWN Raman technique utilised separately.

A numeral of studies to investigate the possibility of Raman spectroscopy in the diagnosis of stomach and oesophageal cancer were performed by the Huang and Yeoh groups. In one of the studies, approximately 18 spectra have been extracted from the dysplastic gastric specimens and about 54 spectra from healthy tissues from the 30 patients participating. The technique used was narrow-band Raman spectroscopy. It provided a result of 96.3% specificity and 94.4% sensitivity [96]. In another related study, this group focused on 67 gastric patients. Gastric cancer was diagnosed with an accuracy of 93.7%, with 94.0% sensitivity and 93.4% specificity [102]. Moreover, Raman spectroscopy was used to test if they could distinguish between benign and malignant stomach ulcers. This test provided sensitivities

Background

and specificities of 82.1% and 93.8% for classification of healthy tissue, 84.7% and 94.5% for benign ulcers, 90.8% and 93.8% for malignant ulcers, respectively [102]. Subsequently, they improved the overall accuracy and obtained an accuracy of 94.6% for an *in vivo* gastric cancer diagnostic [104].

Another group that has meaningfully worked to the explanation of Raman techniques from the laboratory to the clinic is the Stone group. A Raman probe was prepared and assessed for oesophageal diagnostics on excised biopsy specimens in 2011 by Kendall et al. A total of 123 samples were used to derive 1304 Raman spectra to study normal, low and high-risk samples. Barrett's oesophagus was classified as normal to low risk and dysplasia and cancer were classified as high risk. Test and training sets were used in this methodology, which provided 66–84% sensitivity and 81–96% specificity [105]. To try and reveal surface lesions that might have been treated through endoscopic therapy, the work was done by Almond et al. in 2014. They developed a unique custom Raman probe by employing a confocal design to examine superficial tissues. This endoscopic Raman spectroscopy technique was able to detect Barrett's oesophagus that related to high-grade dysplasia and OAC with a sensitivity of 86% and specificity of 88% [106]. This was while their research was restricted to effectiveness of *ex vivo* resected specimens. In the meantime, this group is concentrating on maximising the performance in a clinical trial by creating various probes, adjusting tolerance levels and assessing their application of endoscopic Raman spectroscopy with Barrett's oesophagus.

Bergholt et al. used the stomach tissues, oesophagus and gastrointestinal tract (*in vivo* and *ex vivo*) to study Raman spectra. The results showed that the variability was significant between the spectra from the oesophagus and the stomach. The cancerous tissues from both areas were distinguishable with an accuracy of 94.7% for the oesophagus and 89.3% for the stomach [107]. It also showed, however, that the Raman spectra from various anatomical places inside a tissue were almost similar. Another study combined auto-fluorescence with Raman spectroscopy measurements to

Background

investigate the relevance. The test provided a 92.2% diagnostic accuracy for gastric cancer. This was better than the independent assessment of the two approaches by themselves, i.e. 89.7% for Raman spectroscopy and 86.3% for auto-fluorescence [108].

Another subsequent study was conducted by Bergholt et al. that provided an accuracy of 96.0% in the diagnosis of oesophageal cancer. The study used wide-field imaging modalities (e.g. narrow-band imaging and white light reflectance) to guide the Raman spectroscopic assessment [109]. In another study, 305 patients were examined by developing a completely automated online Raman spectroscopy platform for gastric cancer diagnosis with a multimodal image-guided sampling. This study provided a diagnostic accuracy of 85.6% [110]. Subsequent work was done to demonstrate that it was possible to make use of technology to target specific biopsy sites and to provide a way to distinguish more consistently between dysplastic and neoplastic lesions [100].

2.3 Coherent Raman scattering techniques

Coherent Raman scattering (CRS) is a non-linear optical process, which plays a significant role among novel label free nonlinear microscopy techniques [64]. CRS techniques provide a nonlinear dependence on the incident light fields unlike linear Raman, generate coherent radiation and are sensitive to the similar molecular vibrations probed in Raman. The sample is excited in CRS techniques by the pump beam (ω_p) and the Stokes beam (ω_s), which are two collinear and superimposed laser beams at different frequencies. If the difference between the Stokes beam and the pump beam ($\omega_p - \omega_s$) matches a molecular vibration, the CRS signal is significantly increased, and a stimulated and coherent excitation of molecular vibration modes is achieved. The signal is stronger than Raman scattering by five orders of magnitude [93]. The strong signal leads to much faster imaging speed based on vibrational contrast than the one acquired by Raman microscopes reach to a video rate [109]. Currently, the CARS technique and SRS technique are the most common CRS methods for bioimaging. Due to the presence of a non-resonant background in CARS, the spectral shape is distorted and reduces the imaging contrast, which makes CARS spectroscopy much more complicated than Raman spectroscopy. Thus, to extract the Raman information from a CARS spectrum, several retrieval algorithms are required to make it as useful as a Raman spectrum [55–57]. SRS is a technique testing the similar vibrational modes of molecules that are observed in Raman scattering. In addition, SRS offers other advantages: firstly, SRS is background free, which means there is a clear signal on a resonance that vanishes off resonance, allowing a detection limit close to the shot noise and providing an improvement in sensitivity surpassing the detection limit for CARS [103,105]. Secondly, SRS produces spectra similar to those of Raman [105]. Finally, the SRS signal has a linear response to the concentration of Raman oscillators in the focal volume, allowing straightforward quantification [105, 106].

2.3.1 Coherent anti-Stokes Raman spectroscopy (CARS)

In 1965, Terhune et al. documented the first CARS observation at the Ford Motor Company [107]. The use of the first CARS microscope was stated in 1982 by Duncan and coworkers [108]. The CARS imaging of living cells with a collinear beam geometry and femtosecond (fs) pulses was demonstrated by Zumbusch et al. in 1999. This was the trigger for the development of modern CARS microscopy [109]. Cheng et al. demonstrated that polarisation of CARS can distinguish the nonresonant background. This was done by utilising picosecond (ps) lasers to excite a single Raman band [110] and subsequently, to be able to image living cells, they developed high speed laser-scanning CARS [111]. Simultaneously, it was shown that epi-detected CARS microscopy minimised the detection of nonresonant signals [112]. Later on, it was utilised to provide video-rate imaging [113]. In theory, to understand the radiation pattern of CARS, a Green's function model was improved [114]. An important development in 2002 was multiplex CARS microscopy as it allowed the simultaneous detection of various Raman bands, where both an femtosecond-pulsed laser and a picosecond-pulsed laser were used to explain this [115,116]. Algorithms were used to enable the quantitative multiplex CARS imaging to obtained spectra from the CARS signal similar to the Raman spectra [117,118].

CH-stretch vibration in the HWN: The range of the CH-stretch spectral has a combination of main and minor peaks. There are four main peaks usually located at 2845 cm^{-1} , 2880 cm^{-1} , 2930 cm^{-1} , and 2960 cm^{-1} , which correspond to CH_2 and CH_3 (symmetric and asymmetric stretching), respectively, and can have a significant overlap. Two minor peaks located at 3008 cm^{-1} and 3060 cm^{-1} , due to $\omega_{=\text{CH}}$ and aromatic ω_{CH} and due to water ω_{OH} they have a broad resonance between the wavenumbers at 3000 cm^{-1} and 3600 cm^{-1} .

The influence of Fermi resonances and the direct coupling make CH stretch vibrations more sensitive as they able to present important shifts and broaden

Background

the CH stretch vibrations peaks [119]. The best-placed approaches to leverage the information consisted in the position and shape of the peaks changes are the spectroscopic and spectral focusing of CARS [119]. The vibrational contrast in narrowband methods return as dissenting to a narrow spectral band [109]. While the excitation is adjusted to present mainly on a single resonance in the CH stretch region. In general, the signal contains smaller contributions from multiple resonances because of spectral overlap. The signals from CH₂ and CH₃ are often utilised to identify the relative abundance of lipids and protein where the ratio of their moieties differs significantly in these chemical families [109]. For this purpose, one peak is typically utilised from each pair as the information limited in the symmetric and asymmetric peak is greatly redundant.

The advantage of CARS in the HWN, in generating a contrast equivalent to a haemotoxylin and eosin (H&E) stain has been evaluated by several studies [120]. the CARS images in comparison to H&E images, Evans et al. concluded that CARS can offer the same image information on utilising CH₂ and CH₃ [120]. Inspection of tum to H&E stained images our environments and margins was enabled by “pseudo-H&E” got through CARS imaging without staining. There was also no clear evidence of photodamage although 300 frames were acquired [121].

Raman and CARS were compared in the brain by Meyer et al. Like the H&E-contrast images, from CARS-contrast, it can be acquired quantitative tissue morphology metrics, which demonstrated the ability to extract the ratio of nucleus-to-cytoplasm, nucleus size, shape, and cell density [122]. However, a shape metrics and nuclear density might not be dependable like H&E due to nuclei lack CH₂ contrast. The Wong et al. on the other hand, utilised fundamentally CH₂ CARS contrast and image separation to identify the size and volume of cell, distance between cells and other metrics. This was achieved to categorise cancer kinds in breast and lung, which provided hopeful results for the variance diagnosis of cancer in these samples [123,124]. Further comparison of metrics from H&E and CARS was presented

Background

by Uckermann et al. They found that additional relevant information was provided by CARS via the signal amplitude [120].

In addition, CARS CH_2 and CH_3 contrast were utilised to investigate lipid metabolism in cancer. This is also to transmission morphological information during mimic H&E stain, and to discriminate cell subtype based on lipid content [125]. A contrast in CH_2 to evidence alternative of healthy white matter with lipid lacking astrocytic glioma was found by Evans et al. [126]. They also found excess lipids as a possible indicator for circulating tumour cells [127]. Spectral differences were found when studied the ratio of protein and lipid in a mouse breast cancer model developed by Chowdary et al [128]. In a similar manner, a CH_2 contrast is gradually shown in the infiltrative region about glioblastoma was also found by Uckermann et al. This was with a quite distinct contrast level in the healthy zone [120]. Some of the other studies used CH_2 contrast levels to distinguish between glioblastoma and metastasized in the brain. Meyer et al. found that in a finding propped by Raman and IR imaging, the metastases maintained a chemical profile that was identical to the originating tissue [129].

From CH_2 and CH_3 , the narrowband CARS contrast could in addition be combined with contrast from other approaches even though it alone is useful in many cases. Yue et al. provided guidance for the acquisition of Raman spectra to visualise mammary acini by using CARS signal from CH_3 . They conducted later spectral analysis and noticed vicissitudes in locative distribution of lipids with a lack of polarity in mammary acinus [130]. There have been similar tests conducted by the Popp et al. [129,131]. A very small number of CARS scans in the region from 1000 cm^{-1} to 3000 cm^{-1} were conducted by Krafft et al. for a comparison between CARS and Raman imaging of colon sections. They found enough information to determine two cell kinds and able to determine regions of healthy or diseased tissue. The CARS images were similar to those derived from Raman scattering in the exact spatial specimen regions and were acquired 10^6 times faster than Raman [98]. In subsequent studies to characterise tissues, additional CARS

Background

peaks were used in combination with other contrast techniques. The collagen fibrils and excited fluorescence were generated from the same pulse by second harmonic generation (SHG) and two-photon excited fluorescence (TPEF), respectively, which increased the CARS signal from intrinsic fluorophores (e.g. collagen, flavins, NADPH and elastin). To study the white matter in the brain, elastin, granule layer, cellular cytoplasm, collagen, elastic fibres, NAD(P)H, myelin, triglycerides, and lipid droplets in perivascular tissue, CARS contrast at various Raman shifts simultaneous with intrinsic contrast from SHG and TPEF were used by Meyer et al. [129,131].

Fingerprint vibration region: As mentioned earlier, the quantification and morphology of some types can be obtained using CH-stretch contrast. Fingerprint spectra can be used to identify cell phenotype [132] and they are also useful for information for many more types of diagnostic value.

To recover the Raman fingerprint signals during phase retrieval, spectral gating of CARS signal is required, which uses singular value decomposition to also facilitate the removal of system noise [133]. Spectroscopic images receptive to phase retrieval can be generated by the delay-scan of spectrally focused CARS [134,135]. In addition to this, numerous approaches to inherently spectroscopic CARS microscopy were developed. Nevertheless, the majority of these are not efficient enough for creating biological images [136]. Broadband CARS spectra at a spectral acquisition rate of ≈ 20 Hz were generated using this approach. This approach had a strong CH stretch however the fingerprint spectra were quite weak [137]. In a few cases, the quality of fingerprint spectra significantly enhanced by utilising a temporally compressed Stokes source and by implementing a narrowband sub-nanosecond probe. For the temporally compressed Stokes source, a transform-limited broadband pulse excites the vibrational coherence much further efficiently than separate pulses and acts both as a pump and Stokes. By using this, CARS spectra was possible with a 280 Hz spectral acquisition rate, and uniformly high SNR through the spectrum. This corresponded to 170 kHz single spectral element acquisition, supposing a resolution of 5 cm^{-1} [65].

Background

Much less studies on histological samples utilising fingerprint CARS is available as the great-quality fingerprint spectra in an imaging method has only been possible fairly recently. The use of principal component analysis to distinguish between white matter and grey, and the ID of Purkinje cells and granule layers in rat brain tissue, with a relatively weak fingerprint signal, was studied by Pohling [138]. He found that the assignments on structure corresponded with those acquired from H&E. In addition, Camp et al. in another study identified numerous diagnostically significant types and features directly from spectral peaks in murine brain tissue. Impulsive coherence generation was responsible for the importantly better signal noise ratio in the fingerprint [65,139].

CARS, SHG and TPEF signals were gained concurrently in a fingerprint region in the rat glioblastoma study by Camp et al [65]. SHG is usually utilised to identify collagen but it was noted that if the triple-helical structure is normal and on the aligning of the optical polarisation and fibril axes, the protein only in this case generates an SHG response [129].

2.3.2 Stimulated Raman spectroscopy (SRS)

Woodbury and Ng first observed the stimulated Raman scattering (SRS) in 1962 [140]. It was not till 2008 when the first biological applications were reported that it was finally considered a promising tool for use on biological tissues [103,105]. This technique has steadily grown in popularity and the number of publications applying this to biological samples has also increased [141].

CH-Stretch vibration in the HWN: Similar to CARS, numerous approaches were used for SRS imaging in this region such as spectral focusing method [142], fast spectral scanning [143,144] and real-time multi-band imaging [145].

Background

In the CH-stretch region, both give similar chemical information, where with SRS the histology studies are quite matching to CARS.

A comparison between the H&E images and those produced with SRS at CH_2 and CH_3 were done by Lu et al. [146]. Ji et al. studied the cell density from both H&E and SRS images and found them not distinguishable. The protein and lipid ratio from the SRS technique was utilised. It can be observed that the SRS bands offered a better uniqueness between the two regions in the brain (grey and white matter) than was potential with H&E. The vessels and red blood cells were identified by extracting the morphological features of SRS images. TPA of heme may have given the contrast. In addition, the necrotic regions were categorised by lower protein signal and lack of nuclei, and it appeared as if the regions of higher protein signal indicated collagen. Several fresh brain tissues were collected to obtain a classifier based on axonal density, cellularity, and ratios of lipid and protein using SRS contrast CH_2 and CH_3 . The tumour infiltration detection was done with sensitivity of 97.5% and specificity of 98.5% [147]. SRS images were found to be better than H&E images for detecting glioma. It was also found that the study of invasive tumour cells in peri-tumour brain tissue that seems healthy could be done through SRS microscopy. Unprocessed tissue was used to acquire SRS images at CH_2 and CH_3 to recapitulate image contrast from H&E, with taking into account the improvement of intrasurgical tissue sampling, presented by Orringer et al. [66]. H&E tissue specimens were harvested from thirty patients and the pathologist diagnosis conducted based on a comparison with proximally located SRS was found to agree 92% of the time. Based on SRS contrast, 90% accuracy was reached to distinguish between diagnostic classes of a tumour using algorithms. The relation between the Gleason scores of prostate tissues and the cholesterol ester was studied using SRS spectra in the region between 2800 cm^{-1} and 3000 cm^{-1} and multivariate curve resolution analysis method, this was done by Cui et. Al. [148]. The relation between the ratio of the cholesterol and the fraction of total lipids was studied in the CH stretch region at 2870 cm^{-1} and was found proportional because of cholesterol ester. This was conducted by calibrated surrogate mixture for

Background

cellular lipid content. Sufficient discrimination often provided by a small number of peaks is useful even though the complete spectral information in the CH region is occasionally beneficial. Tissues from a model of the tumour-graft mouse using spectrally scanned SRS through the range from 2800 cm^{-1} to 3100 cm^{-1} were examined by Otsuka et al. [149]. It was found that even though the spectral data set could be reduced by $> 95\%$ through independent component analysis, it was still possible to obtain images to visualise lipid droplets, nucleus, red blood cells, and zymogen granules and detect the alignments of the irregular glandular cell. In a similar study, SRS spectroscopy was used over the range from 2800 cm^{-1} and 3100 cm^{-1} to spatially separate between the specified keratinocyte differentiation and characterise them from Langerhans cells [150]. The important contrast at CH_2 and CH_3 is considered the key variations primarily morphological where the nuclear prominence and cell shape vary among the cell types. The other nonlinear contrast mechanisms were merged with the vibrational signal from SRS in yet another study. SRS images were acquired at CH_2 and CH_3 bands for haemoglobin TPA and merged to provide a contrast similar to the H&E that to extract the main histologic features from various brain regions, was done by Freudiger et al. [151]. Another study observed important variances in the nuclear region of healthy and cancerous areas utilising both human and animal tumour models, Galli et al. [152]. For imaging the morphological in prostate and liver tissue samples, and for the directing to classify lipid droplets (LDs) Yue et al. used SRS CH_2 contrast [153]. Sarri et al. presented for the first-time a combining SRS and SHG to visualise tissue sections from the normal and cancerous GI tract. This approach allows performing stimulated Raman histology (SRH) to produce histology images of frozen and fresh colon and pancreas tissue sections at the two different frequencies corresponding to CH_2 and CH_3 chemical bonds with the near perfect agreement with conventional histopathological images. In this study, SRH microscopy has proven that it can be used to investigate the change in the morphological and the common architecture changes of the tissue at the subcellular level on millimeter size GI tract tissues [67].

Background

Fingerprint vibration region: Similar to CARS, there are fewer examples of SRS performed with contrast in the fingerprint region. The difficulty in acquiring image contrast using fingerprint Raman peaks for typical modulation schemes was shown by Ozeki [144]. A highly efficient signal generation technique was used to overcome the issue of weak fingerprint signal in CARS [65]. Modulation schemes that discriminate against problematic background signals enough for the observation of the fingerprint peaks was developed. This is despite the fact that a comparable improved efficiency signal generation method has not yet been found for SRS. A scheme to utilise the equal modification symmetry of different background signals, which offers enough classification to extract the fingerprint spectra from rat skin, was proposed by Berto et al. [154]. At pixel (the smallest unit of a digital image or graphic that can be shown and performed on a digital display device) acquisition rates (each 10 kHz), cell nuclei were imaged by Zhang et al. using SRS at 785 cm^{-1} [155]. An SRS modification approach that seems to be 3 - 4 times more effective in refusal of background signals that change slowly pattern with an excitation wavelength compared with amplitude modification was demonstrated by Fu et al. [156]. A delay-modulated spectral focusing was used to achieve $\approx 10\text{mmole/L}$ sensitivity from 720 cm^{-1} peaks in neuronal tissue at an acquisition rate of 250 kHz pixel.

SRS in combination with SHG, TPEF and THG techniques was used to image Colon tissues collected from 9 patients. It was observed that the ratio of the protein and water increased, which were imaged at CH_3 stretch vibrations and 3250 cm^{-1} , respectively while the ratio of lipids reduced, which was imaged at CH_2 stretch vibrations at 1445 cm^{-1} and 1745 cm^{-1} [157].

2.4 Summary

Raman scattering is far from being an ideal imaging technique due to slow acquisition speed. This is despite its rapid development as a spectroscopy technique capable of acquiring a Raman spectrum to reveal molecular information at one data point within a matter of seconds. Biomedical studies require fine temporal and spatial resolutions as the samples are usually live and the environment is complex, while Raman yield a great deal of spectral information, a long pixel dwell time (10 seconds) and produce high resolution imaging applications. The weak Raman signals are also overwhelmed by the problematic auto-fluorescence from biologic samples. These are the reasons that hinder its further development and there are fewer applications in biomedical studies.

Stimulated Raman scattering (SRS) is capable of overcoming these disadvantages in Raman scattering and could be utilised for biomedical imaging. The dramatic increase in the efficiency of the weak Raman transition is affected by the coherent two-photon Raman process by adopting the stimulated emission amplification principle. The maturation of ultrafast lasers makes it more popular. To study the vibrational excited-state dynamics of molecules, stimulated Raman scattering was developed as an ultra-fast spectroscopic technique [65]. This technique has been widely utilised. Even though SRS has been proposed as a contrast mechanism for microscopy it was not entirely suitable as a biocompatible imaging technique. Another coherent Raman scattering process called CARS has been developed and applied as a biomedical imaging technique for almost 20 years. However, it has its own disadvantages such as severe spectral distortion, unwanted non-resonant background, non-straightforward concentration dependence and coherent image artefacts.

These shortcomings of CARS were overcome by the development of SRS microscopy for high-speed biomedical imaging with shot noise limited sensitivity. This technique provided much improved performance immediately,

Background

overcoming all the above-mentioned shortcomings of CARS. This is combined with the fact that SRS microscopy is immune to the auto-fluorescence background in biological specimens. This is due to a unique detection system different from both Raman scattering and CARS. It can be deduced that the fast image acquisition and linear signal dependence of SRS microscopy would be an ideal imaging modality to gather the molecular information in biological samples. Label-free detection of biomolecules, video-rate SRS imaging on live animals and tumour imaging are some of the areas of biomedical applications where SRS microscopy has proven its worth and unique value.

The work in this thesis will show a novel development for the first time on a custom-built imaging platform based on a laser scanning microscope and a picosecond pulse laser system by installing a new dispersive block in the OPO cavity. This development contributes to rapid wavelength tuning and fast extraction of the SRS spectra at the CH stretch vibration in the HWN region. The development will also extend to enhance the microscope performance for acquiring a quick and high-quality large area montage by writing new hyperspectral software, which makes the system easier and more effective to use. Stimulated Raman histology is a new approach that will be applied for the first time on the oesophagus tissue and which works based on two different frequencies at the CH₂ and CH₃ chemical bond to highlight the different morphological structures in the tissue similar to H&E images. Finally, the K-mean clustering method will be used for comparison of the spatial and spectral resolution and to determine the structural features of oesophagus tissue in the HWN region using Raman and SRS techniques.

Chapter 3

Theory

3.1 Introduction

The application of Raman and SRS imaging techniques to characterise or image biological tissues is described in this thesis. As stated in the introduction, the aim of this thesis is to develop the stimulated Raman scattering technique (SRS) for the rapid wavelength tuning and performance of hyperspectral SRS images to extract spectra rapidly. An outline of the main theoretical principles that have supported this thesis is included in this chapter. The first topic covered in section 3.2 is the theory of Raman scattering as the study undertaken is concerned with enhancing the application of Raman techniques in biology. This is followed by the principles of the coherent anti-Stokes Raman scattering in section 3.3. Finally, section 3.4 provides the principles of the stimulated Raman scattering.

3.2 Theory of Raman scattering

The deflection of light when electromagnetic waves (EW) come in contact with obstacles is regarded as light scattering. An induced electric dipole moment is achieved when the incident electric field at frequency (ν_0) disturb the electrons within the sample molecules periodically. This is a result of the interaction between the incident electromagnetic waves and molecules, which cause to scatter the light when this disturbance of the electronic cloud is increased. The scattering processes can be classified in two categories: Rayleigh or Mie-Tyndall scattering, which is the elastic scattering (Rayleigh) at the similar frequency (ν_0) as the incident electromagnetic wave; and Raman and Brillouin scattering, which is the inelastic scattering (Raman) of photon emitted radiation at different frequency (ν) than that of the incident photon.

Smekal (1923) made the first theoretical predictions of inelastic scattering light. Raman and Krishnan followed this with the first experimental observation in 1928, which known as the Raman shift where the frequency shift in the spectrum of scattered photon associated with incident photon [69]. The Raman shift can be calculated by the following equation:

$$\Omega(cm^{-1}) = 10^{-7} \left(\frac{1}{\lambda_{excitation}} - \frac{1}{\lambda_{Raman}} \right) \quad (3.1)$$

where the Raman shift is denoted by Ω , the λ_{Raman} indicates the Raman wavelength and the $\lambda_{excitation}$ indicates the wavelength of the excitation laser source.

Theory

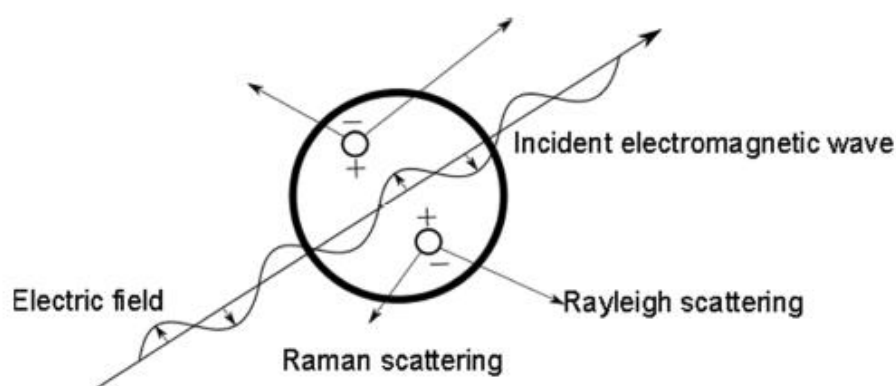


Figure 3.1: Light scattering by an induced electric dipole moment because of an incident electromagnetic wave.

The explanation of the Raman effect, when interpreted in a classical way, is the interaction between the incident radiation of electric field E and a molecule. An electric dipole moment P is induced by the incident electromagnetic field (see Figure 3.1).

$$P = \alpha E \quad (3.2)$$

where electric polarisability of the molecule is denoted by α and E indicates the amplitude of the electrical field.

An intrinsic property of the molecule is its polarisability, which relies on the the chemical bonds and the electronic structure. Depending on the symmetry of non isotropic molecules, it could differ with interatomic distances and location.

Classical electromagnetic theory can be used to obtain a simple qualitative description of Raman scattering. An electromagnetic wave can be defined by the equation:

$$E = E_0 \cos(2\pi\nu_0 t) \quad (3.3)$$

where the frequency is denoted by ν_0 . From Equations (3.2) and (3.3) you can

Theory

assess that the induced electric dipole moment is time dependent.

$$P = \alpha E_0 \cos(2\pi\nu_0 t) \quad (3.4)$$

It can be assumed that one molecule cannot rotate, but free to vibrate. In the equilibrium position, the electron is fixed in space while the nuclei has the capability to vibrate about this positions. Variations will be induced in the molecule polarisability by any disturbance in the electronic cloud. This variation during the molecular vibrations can be defined by extending the polarisability α in a Taylor series:

$$\alpha = \alpha_0 + \frac{\partial\alpha}{\partial x_i} x_i \quad (3.5)$$

Where x_i is the coordinate of vibration, which can be presented as a sinusoidal function with regards to vibration frequency, ν_i indicates the characteristic frequency of natural vibrational mode and t indicates the time.

$$x_i = x_i^0 \cos(2\pi\nu_i t) \quad (3.6)$$

Equation (3.5) when combined with Equation (3.6) gives:

$$\alpha = \alpha_0 + \alpha_1 x_i^0 \cos(2\pi\nu_i t) \quad (3.7)$$

where $\alpha_1 = \frac{\partial\alpha}{\partial x_i}$ and α_0 denotes the initial polarisability.

The expression of the induced electric dipole moment is [140]:

$$P = \alpha_0 E_0 \cos(2\pi\nu_0 t) + \alpha_1 E_0 \cos(2\pi\nu_0 t) \cos(2\pi\nu_i t) \quad (3.8)$$

Trigonometric identity used for rearranging Equation 3.8 is shown by:

$$\cos a \cos b = \frac{\cos(a+b) + \cos(a-b)}{2} \quad (3.9)$$

and:

Theory

$$P = \alpha_0 E_0 \cos(2\pi\nu_0 t) + \alpha_1 E_0 \frac{\cos 2\pi(\nu_0 + \nu_1)t + \cos 2\pi(\nu_0 - \nu_1)t}{2} \quad (3.10)$$

Classical electromagnetic theory was used to obtain Equation (3.10), but it also helps to get numerous significant properties of Raman scattering procedures. The first property is that there is linear dependence on the laser intensity by the polarisation and scattering intensity. Raman active only occurs with the vibrations that change the polarisability of the molecule $\frac{\partial\alpha}{\partial x_i} \neq 0$. The Raman shift, which is the variation in frequency, may be negative or positive based on the laser frequency. Rayleigh scattering is much stronger than Raman scattering as $\alpha_1 \ll \alpha_0$.

In addition, from Equation (3.10) it can be observed that light will be scattered by the molecule at three different frequencies. The first term is the Rayleigh scattering, in which the emitted photon has the same frequency as the incident photon, ν_0 . The anti-Stokes Raman scattering [158] is the second term that contains waves with frequencies $\nu_0 + \nu_i$ that relate the outgoing scattered photons with an increase in frequency by an amount ν_i . Finally, Stokes Raman scattering, which is the third term $\nu_0 - \nu_i$, is related to a reduction in the frequency of the consequencing scattered light [159].

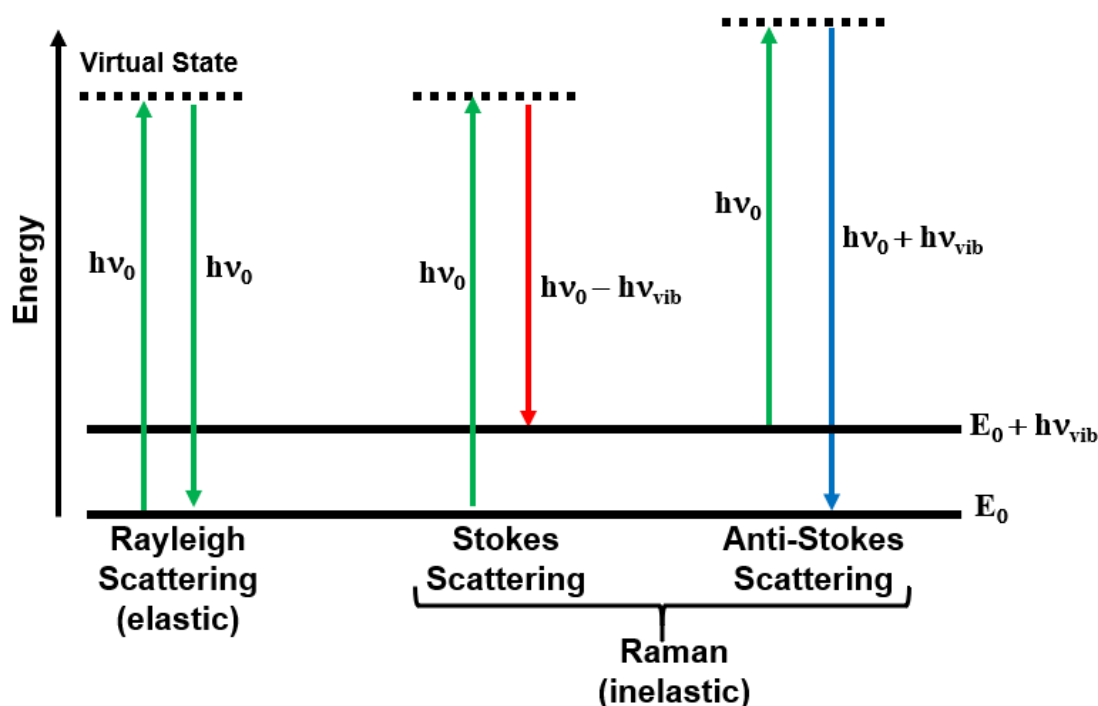


Figure 3.2: Rayleigh scattering and Raman Stokes and anti-Stokes scattering denoted by a Jablonski energy diagram [160].

The Jablonski diagram (Figure 3.2) can also be used to visualise the Stokes and anti-Stokes Raman scattering. The relationship between the change in energy, ΔE , and frequency is given by the following equation:

$$\Delta E = h\nu_0 \quad (3.11)$$

Stokes scattering is the process in which energy difference is lost when the molecules are excited from the ground state to a virtual state followed by relaxation and back to a vibrational state. On the other hand, in the case of anti-Stokes scattering, the excitation occurs from a vibrational level where the molecule is already there to a higher virtual state followed by relaxation and back to the ground state, which the molecule will obtain energy. Expectations at room temperature is that the majority of the molecules will be in the ground state, which means that the most of Raman scattering will be conquered by Stokes Raman scattering. Boltzmann's equation can be utilised to calculate

Theory

the population of the excited and vibrational ground states [158], which affects the ratio among intensities of the Stokes and anti-Stokes scattering:

$$\frac{I_{Stoke}}{I_{anti-Stoke}} = \left(\frac{\nu_0 - \nu_i}{\nu_0 + \nu_i} \right)^4 e^{\frac{h\nu_i}{k_B T}} \quad (3.12)$$

where the absolute temperature is denoted by T and the Boltzmann constant by K_B .

The proportional nature of the Raman intensity with 4th power of the frequency is provided in Equation 3.12. While, the intensity of the Raman scattering is presented as [159]:

$$I = KI_0\alpha^2(\nu_0 \pm \nu_i)^4 \quad (3.13)$$

where the series of constants is represented by K and the intensity of the incident radiation by I_0 .

The difference in frequencies between the scattered and incident photons, termed the Raman shift, is conventionally measured by Raman spectroscopy in wavenumber, units of cm^{-1} . The plots of scattering intensity are the Raman spectrum that is a function of the Raman shift. The characteristic peaks corresponding to the vibrational modes of the bonds present vary among molecules, which gives them each a unique Raman fingerprint. Weak signals, which require long acquisition times limit Raman. This is a small cross section, typically 10^6 times weaker in biological tissue when compared to fluorescence.

3.3 Coherent anti-Stokes Raman scattering

The Raman signal is significantly enhanced by Coherent Raman techniques. Coherent anti-Stokes Raman scattering (CARS) is a nonlinear process, which

Theory

is able to produce signal intensities of typically more than five orders of magnitude greater than Raman [93]. By using a Taylor expansion, the relationship can be extended between the polarisation and the electric field to consider nonlinear terms and is expressed as:

$$P = \epsilon_0 [x^{(1)} E + x^{(2)} E^2 + x^{(3)} E^3 + \dots] \quad (3.14)$$

where the linear susceptibility is responsible for linear interactions with materials such as absorption, which is denoted by $x^{(1)}$. The nonlinear susceptibilities including the second order (e.g. second harmonic generation (SHG) and two-photon fluorescence (TPF)) and the third order (e.g. Raman scattering and coherent Raman scattering techniques) interactions are denoted by $x^{(2)}$, $x^{(3)}$, respectively. It should be noted that Raman is a linear process, although it is as a result of a third order interaction with the material, where there is a linear relationship between the incident intensity and the resulting signal intensity. On the other hand, CARS and SRS are nonlinear processes.

CARS is a four-wave mixing (FWM) process related to the third order susceptibility tensor of the medium. The process includes three coincident fields: a pump with a frequency of ω_p , Stokes with a frequency ω_s , and a probe field with ω_{pr} frequency. A third order nonlinear polarisation $P^{(3)}$ is induced in the specimen and an anti-Stokes Raman signal of the frequency [161] is generated:

$$\omega_{as} = \omega_p + \omega_{pr} - \omega_s \quad (3.15)$$

Where ω_{as} is the frequency of the anti-Stokes field. The pump and the probe photons can be from the same laser ($\omega_{pr} = \omega_p$) to reduce the complexity, known as degenerate CARS. The optical mixing of electromagnetic waves can describe the CARS signal. Maxwell's equations govern the behaviour of electromagnetic waves [155], where the nonlinear

Theory

wave equation can be written [151]:

$$\nabla \times \nabla \times E(\mathbf{r}, t) + \frac{n^2}{c^2} \frac{\partial^2 E}{\partial t^2} = - \frac{1}{\epsilon_0 c^2} \frac{\partial^2 P^{(3)}}{\partial t^2} \quad (3.16)$$

The relation between the electric field and the third order polarisation of the molecule is observed from equation 3.16. The wave equation can be solved by considering the electric field as a plane wave, expressed by:

$$E(z, t) = E_{as} e^{i(\omega_{as}t - k_{as}z)} \quad (3.17)$$

From equation 3.17 into equation 3.16,

$$E_{as}(L) = -i \frac{\omega_{as}}{n_{as} \epsilon_0 c} P_{as}^{(3)} \cdot L \frac{\sin \left[\frac{\Delta k L}{2} \right]}{\frac{\Delta k L}{2}} e^{-\frac{i \Delta k L}{2}} \quad (3.18)$$

where L indicates the interaction length with the medium, Δk is the wave vector mismatch between the incident and CARS field. and n_{as} is the refractive index. The field strength of the excitation electric fields E, and the nonlinear optical susceptibility of the medium, $\chi^{(3)}$ determine the magnitude of the third order nonlinear polarisation $P^{(3)}$:

$$P^{(3)}(\omega_{as}) = \chi^{(3)} E_p^2 E_s \quad (3.19)$$

where the electric field of the pump beam is denoted by E_p and the electric field of the Stokes beam by E_s . From equation 3.19 into equation 3.18, the electric field can be written as:

$$E_{as}(L) = -i \frac{\omega_{as}}{n_{as} c} \chi^{(3)} E_p^2(\omega_p) E_s(\omega_s) \cdot L \frac{\sin \left[\frac{\Delta k L}{2} \right]}{\frac{\Delta k L}{2}} e^{-\frac{i \Delta k L}{2}} \quad (3.20)$$

Theory

The optical response of the material to an applied laser is described by the resonant third order nonlinear susceptibility ($\chi_r^{(3)}$), which is given as:

$$\chi_r^{(3)}(\omega_{as}) = \frac{\left(\frac{N}{3m}\right) \left[\frac{\partial \alpha}{\partial Q}\right]^2}{\omega_{vib}^2 - (\omega_p - \omega_s)^2 - 2i(\omega_p - \omega_s)\gamma} \quad (3.21)$$

where N is the number of oscillators in the excitation volume. The intensity of the anti-Stokes is found by taking the square of the modulus of the electric field, and it can be shown as [162]:

$$I_{as}(L) = \frac{n_{as}c}{8\pi} |E_{as}(L)|^2 \propto \frac{\omega_{as}^2}{n_{as}c^2} |\chi^{(3)}(\omega_{as})|^2 I_p^2 I_s L^2 \left[\frac{\sin\left(\frac{\Delta k L}{2}\right)}{\left(\frac{\Delta k L}{2}\right)} \right]^2 \quad (3.22)$$

where the intensities of the pump beam and Stokes beam are denoted as I_p and I_s , respectively, L indicates to the interaction length of the pump and Stokes with the medium, $\chi^{(3)}$ is the third order electric susceptibility, and Δk is the phase mismatch.

It is evident that the anti-Stokes signal is directly proportional to the square modulus of the third order susceptibility, indicating the proportional nature of CARS signal to N^2 , since $\chi^{(3)} \propto N$. Higher sensitivity is provided to CARS when compared to Raman scattering [162,163] by the signal generated from the oscillators that constructively interfere. It is further enhanced by the pulsed excitation provided by the non-linear dependence on excitation. In Equation (3.22) Δk is given by

$$\Delta k = k_{as} - (2k_p - k_s) \quad (3.23)$$

where the wave vectors of the pump, Stokes and anti-Stokes field are k_p , k_s and k_{as} , respectively.

Theory

Quadratic variation in CARS intensity from the interaction length is present when a well-phased matching $\Delta k = 0$ is achieved, which typically takes place only in the gas medium. Δk will not equal zero in solid and liquid media due to media dispersion. In this case the phase matching is achieved if the pump and the Stokes beams are crossed (the non-collinear geometry) at angle θ . If the beams are not crossed, in the case of $\Delta k \neq 0$, the CARS signal intensity shows sinusoidal variations with the path length, as shown in Equation (3.22). Maximum CARS conversion efficiency is provided by the path length, which is the coherence length L_c . This occurs when

$$\frac{\Delta k L_c}{2} = \frac{\pi}{2} \quad (3.24)$$

So, L_c is defined as:

$$L_c = \frac{\pi}{\Delta k} \quad (3.25)$$

A phase matching condition is achieved when Δk is close to zero and generates a maximum anti-Stokes signal from the excited volume. the phase matching angle is shown in Figure 3.3 (a) and the different practical phase matching systems in CARS microscopy procedures are presented in (b) and (c). The phase matching condition for CARS spectroscopy is achieved by controlling the angle between the two incident beams in a 2D configuration. The obstacle that proved challenging in employing CARS in imaging was this phase matching condition. In 1999, CARS was performed for the first time in microscopy, which was achieved by using an objective lens with a high numerical aperture to focus the collinear-aligned beams tightly and satisfy the phase matching condition [162].

Theory

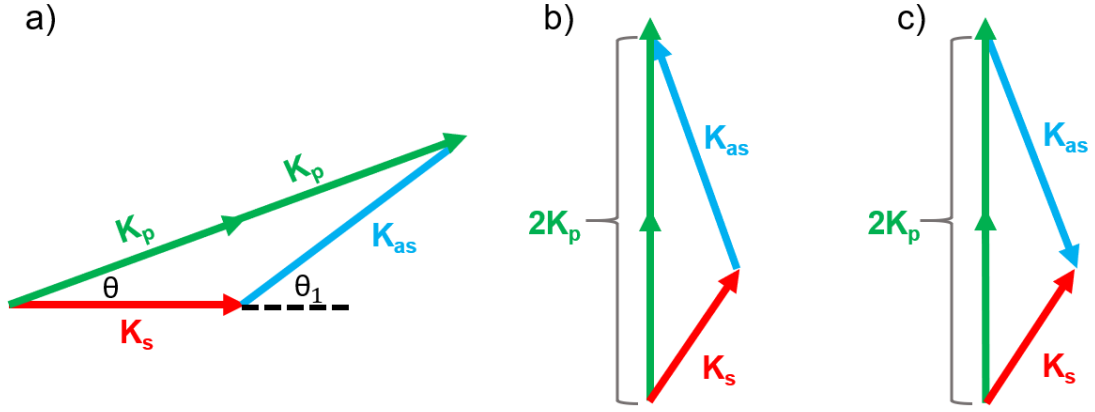


Figure 3.3: (a) phase matching angle, (b) phase matching condition in the forward CARS and (c) the backward CARS [162].

A non-resonant background has proven to be the main limitation of CARS. Dependent on the electronic and molecular structure of the medium, it arises from the third order susceptibility characterising the nonlinear optical response of a medium and governs the wave propagation [164]. Resonant and non-resonant parts are present in the total nonlinear susceptibility:

$$x^{(3)} = x_r^{(3)} + x_{nr}^{(3)} \quad (3.26)$$

The electronic oscillations that still occur in the absence of resonant Raman modes result in a non-resonant part that is frequency independent. There may also be two-photon absorption when it is close to a real electronic state. The nonlinear optical susceptibility can be written as [161]:

$$x^{(3)} = \frac{A_R}{\Delta - i\Gamma_R} + \left(x_{nr}^{(3)} + \frac{A_t}{\omega_t - 2\omega_p - i\Gamma_t} \right) \quad (3.27)$$

where the detuning term is denoted by $(\Delta = \Omega - (\omega_p - \omega_s))$, the vibrational

Theory

frequency of the medium denoted by Ω , the half-width at half maximum of the Raman line(s) of the medium by Γ_R , and the half-width at half maximum of the two-photon electronic transition of the medium by Γ_t . The Raman scattering is denoted by A_R and the two-photon absorption cross section constant by A_t [161].

In Equation (3.27), the first term is the vibrational resonant contribution denoted by $x^{(3)}$ (Figure 3.4A). The non-resonant term of $x^{(3)}$ that is in parentheses is the second term. It involves an enhanced non-resonant term that is a result of the two-photon electronic resonance (Figure 3.4C), and a Raman shift non-resonant term that is independent (Figure 3.4B).

Real ($Re(x)$) and imaginary ($Im(x)$) elements are contained in the resonant susceptibility. A dispersive line shape related to the nonlinear refractive index of the medium is a part of the real element. The CARS signal intensity has a quadratic proportion to $x^{(3)}$. The proportionality, considering the resonance and non-resonance component Equation (3.27), can be expressed as

$$I_{CARS}(\Delta) \propto |P^{(3)}|^2 \propto |x_{nr}^{(3)}|^2 + |x_r^{(3)}(\Delta)|^2 + 2x_{nr}^{(3)}Re x_r^{(3)}(\Delta) \quad (3.28)$$

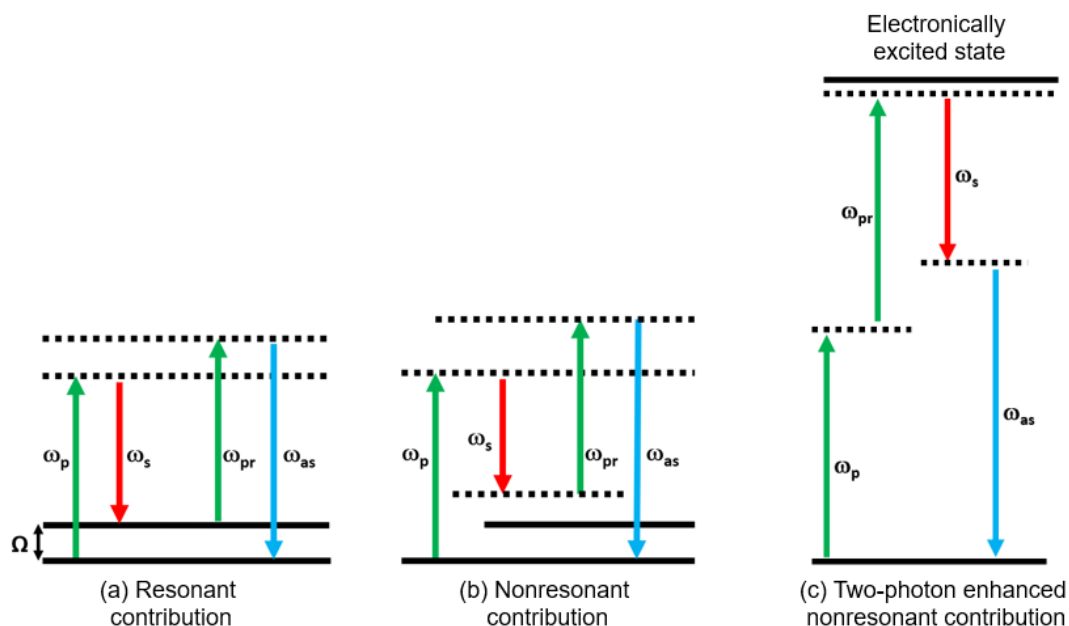


Figure 3.4: CARS signal generation energy diagram. (A) Resonant CARS ($\Omega = \omega_{\text{vib}}$); (B) Non-resonant CARS that is generated by an electronic contribution; (C) Non-resonant CARS that is a result of two-photon resonance of the pump beam associated with excited electronic states (Virtual states are indicated by dotted lines).

Figure 3.5 illustrates the physical concept of Equation (3.28). Figure 3.5 (a) includes each term of the equation plotted as a function of the detuning (Δ). There is no change in the first term, $|x_{nr}^{(3)}|^2$ on altering the detuning over a Raman vibrational mode. On the other hand, the second term behaves like a Raman peak. The addition of the three terms is influenced by $\Delta = 0$, around which the third term (mixing term) is dispersive (Figure 3.5 b). When compared to Raman, the detected CARS signal peak is red shifted. The negative contrast of the active Raman medium is created by the dip at the blue end of the peak (the black holes in Figure 3.5 e).

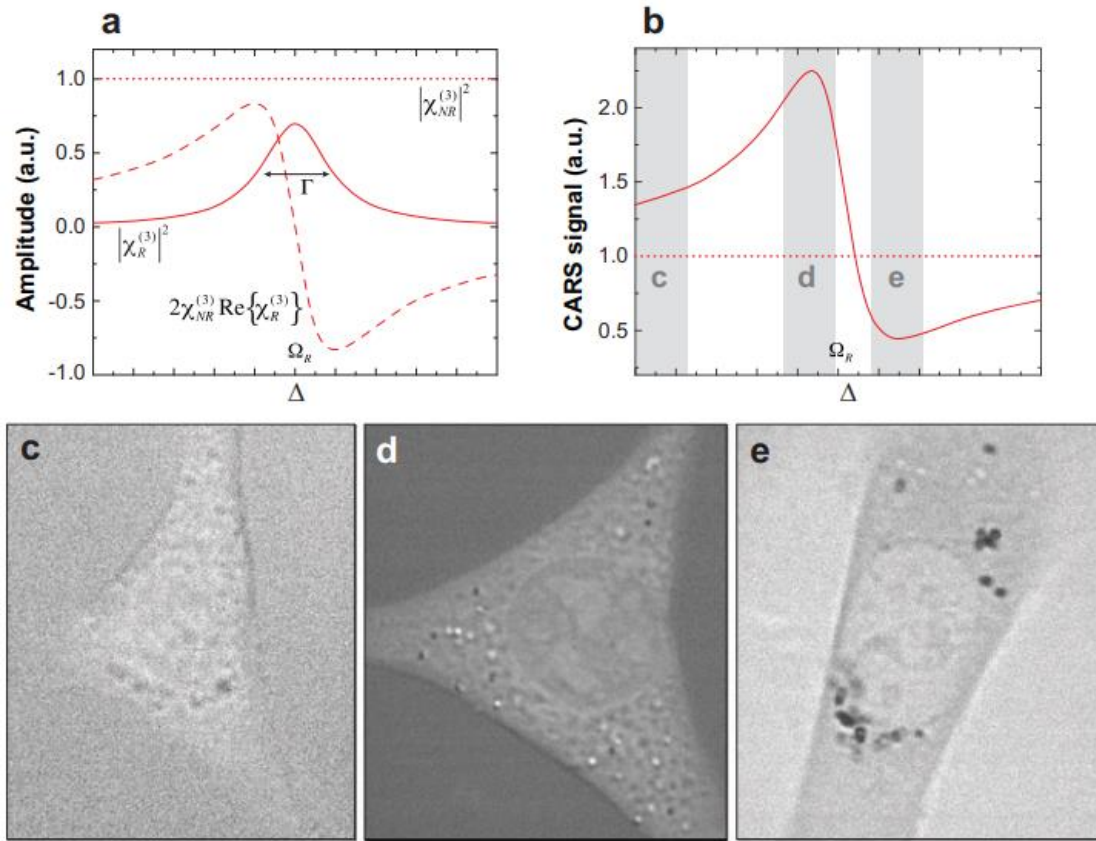


Figure 3.5: Resonance and nonresonance CARS (the image was taken from [162]). The straight horizontal line, in image (a), denotes the nonresonance term of Equation (3.28). The solid line peak-like curve coincides with the second term of the equation. The third term of the same equation is represented by the dashed curve. Image (b) plots the summation of the three terms of the equation. The images (c), (d) and (e) are CARS images of a biological cell with image (b) highlighting the corresponding detuning.

The difference in frequency between the pump and Stokes beams to achieve the maximum third order resonant susceptibility (Equation 3.21) should be equal to the vibrational frequency or frequencies of the medium of interest.

$$\omega_{vib} = \Omega = \omega_p - \omega_s \quad (3.29)$$

In order for the confinement of the wave vector mismatch to be fulfilled

(Equation 3.23), the pump and Stokes beams need to overlap. As the high peak, power-pulsed laser sources are used, the two laser sources must be synchronised to obtain the spatial overlap requirement of the pump and the Stokes beams or the pulses. The paths of the pump and the Stokes beams are required to be the same.

The CARS microscopy signal is directional in the sense that it can be detected in both forward and backward (epi) directions. This is in contrast to the linear techniques such as Raman and fluorescence and is due to the coherent nature of signal generation. Different parameters affect the signal strength in the forward and backward directions. It is equally generated in both directions for a very thin object. For larger objects, the forward signal gains more intensity and there is a decrease in the backward signal, which has special practical implications for epi CARS microscopy [164]. First, a backward signal is generated for objects in the size range of $\lambda/3$ as their size is not enough for the generated signal to interfere destructively [165]. Second, a higher backward signal is permitted by the sharp discontinuity in the third order susceptibility $\chi^{(3)}$ in the focal volume. Third, there is the highly scattered medium with continuous change in the refractive index, where the forward signal is redirected toward the backward direction.

3.4 Stimulated Raman scattering

Apart from Raman and CARS, another coherent Raman scattering process to achieve and address the same vibrational signature is stimulated Raman scattering (SRS), whose excitation process is similar to that of resonant CARS [166]. Pump (ω_p) and Stokes (ω_s) are the excitation frequencies required. When the frequency difference between the pump and Stokes beams ($\omega_p - \omega_s$) matches the molecular vibrational resonance Ω_R , they coincide at the target molecule. The stimulated excitation enhances the molecular transition rate and the population is transferred from the ground state to the vibrational state through a virtual state (Figure. 3.6). Stokes

Theory

Raman scattering also involves a similar energy transfer process. The difference in the SRS process is a much stronger scattering instead of spontaneous transfer, in which the molecule is stimulated to the vibrational state [167]. Another difference is that the SRS process only occurs when $\omega_p - \omega_s$ matches a Raman mode. Therefore, there is no non-resonant background.

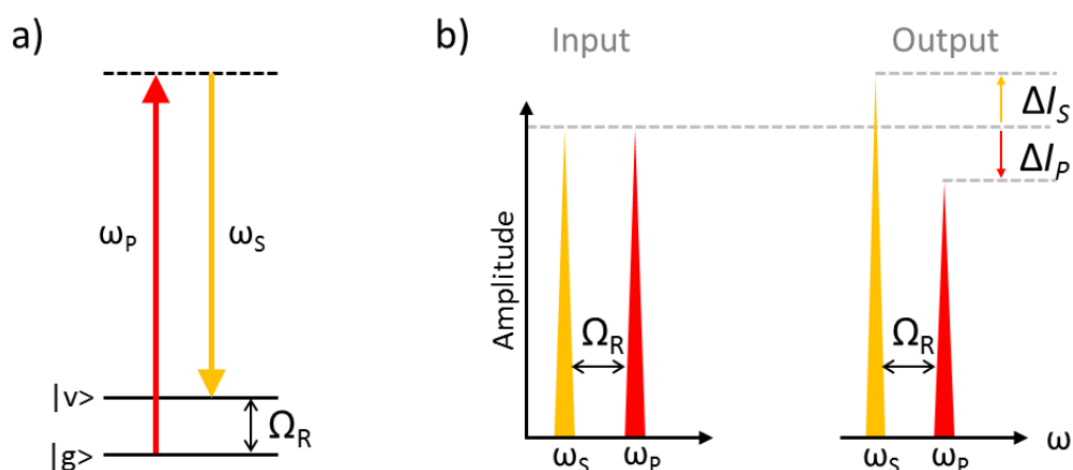


Figure 3.6: Stimulated Raman scattering process. The difference in frequency between the pump, denoted by ω_p , and Stokes, denoted by ω_s , is equal to the vibrational resonance of the target molecule that is denoted by Ω_R . (a) Molecular energy transfer. (b) The amplitude of the pump beam is reduced while that of the Stokes beam is increased [168].

The pump photons are absorbed by the molecule and the Stokes photons are generated, which is a result of the coherent excitation of molecular vibration. This, in turn, results in stimulated Raman loss (SRL, ΔI_p) or stimulated Raman gain (SRG, ΔI_s) of the intensity of the transmitted pump (I_p) or Stokes (I_s) beams, respectively (Fig. 3.6b). The Stokes beam is modulated at a known frequency when detecting the pump beam and the loss in the pump beam occurs at this same known frequency, known as modulation transferred decline. SRS can only occur when both beams are present so the effect is to turn the SRS signal 'on' and 'off'. The molecular transfer process for SRL and

Theory

SRG detection when the Stokes beam and pump beam are modulated, respectively is illustrated in Figure (3.7). The SRS signal is depicted by the change in intensity of the pump beam, ΔI_p . A filter blocks the Stokes beam after the sample. Highly sensitive lock-in detection is used to detect such small signals, which extract the SRS signal from the much larger pump laser background signal. Due to the same wavelength of the excitation and detection, the phase matching conditions for SRS are automatically fulfilled. It is at the resulting Stokes laser that the pump laser is modulated and the SRG is observed.

The intensity shift (ΔI_p or ΔI_s) change is determined by [166]:

$$\Delta I_p \propto -N \cdot \sigma_{Raman} \cdot I_p \cdot I_s \quad (3.30)$$

$$\Delta I_s \propto N \cdot \sigma_{Raman} \cdot I_p \cdot I_s \quad (3.31)$$

with N being the number of molecules in the probe volume, and σ_{Raman} the cross-section of the molecular Raman scattering.

The absence of the non-resonant background is the unique advantage of SRS in comparison to CARS. SRS is also linearly proportional to the oscillator concentrations that permit utilising it in quantitative analysis.



Figure 3.7: The detection mechanism of (a) Stimulated Raman loss (SRL) and (b) Stimulated Raman gain (SRG), adapted from [169].

3.5 Summary

This chapter covered the basic theory of Raman and coherent Raman techniques of CARS and SRS. CARS, a nonlinear process, has cubic and quadratic dependence on the incident laser intensity and the number of Raman scatters, respectively. This process produces a signal that is coherent, in phase and is emitted with a defined direction. The signal is only produced in the plane of focus due to phase matching conditions. This enables three-dimensional optical sectioning capabilities, which eliminates the need for tissue sectioning. The SRS process generated from actively driven vibrations is stimulated rather than spontaneous and unlike CARS does not suffer from a

Theory

non-resonant background that can distort spectral line shapes. This is so that the spectral information that matches Raman can be extracted. Quantitative measurements are possible as the signal is linearly proportional to the number of Raman scatters. There is quadratic dependence on the incident intensity in the SRS signal.

In this work, SRS was developed for high-speed biomedical imaging, which provided much improved performance immediately, overcoming the aforementioned shortcomings of CARS. Furthermore, SRS is immune to the auto-fluorescence background in biological samples due to a unique detection scheme different from both Raman scattering and CARS. It can be deduced that SRS is an ideal imaging modality to gather the molecular information in biological samples due to the fast image acquisition and linear signal of SRS microscopy. SRS microscopy has proven its worth and unique value on some of the areas of biomedical applications such as label-free detection of biomolecules, and video-rate imaging on tissue samples.

Chapter 4

Method and Instrumentation

4.1 Introduction

Raman scattering and coherent Raman scattering techniques were used to achieve the goals of this thesis. The background theory of these two techniques has been discussed in the third chapter. This chapter provides a detailed description of the experimental set-up and detection methods used to perform spontaneous and coherent Raman microscopy. This is followed by a brief description of the data analysis method and the sample preparation in this thesis.

The author's contribution in this chapter:

1. For the Raman system calibration, all samples were prepared by another member in the department, while all figures were measured and analysed by the author.
2. The protocol of the clinical samples preparation was written by the author.
3. The clinical samples were collected and prepared by a pathologist, except for the SRS slices, which were covered by another coverslip from the top

side and installed using a single layer of double-sided sticky tape by the author.

4.2 Raman microspectroscopy

The Raman microspectroscopy measurements in this thesis were performed using a commercially confocal Raman microscope (InVia, Renishaw, UK), with near infrared diode excitation lasers at 785 nm and 830 nm with a maximum excitation power of approximately 130 mW (in the sample). In this system, the ability to switch between these two lasers is very flexible and rapid controlled with Renishaw v.4.1 WiRE software, where each laser has a separate beam path. WiRE software (Version 4.1, Renishaw, UK) was provided by the manufacturer. Many parameters in addition to the type of excitation wavelength can be controlled through this software e.g. diffraction grating, microscope objective, exposure time, spectrum range, number of a scan, and laser power. Figure 4.1 shows a photograph and schematic description of the Raman spectrometer design used in this equipment. The laser light passes through a series of lenses and mirrors after entering the instrument. After the laser light is projected into the microscope, it is focused through the microscope lens (50X objective lens) onto the specimen on a motorised XYZ stage. The Raman back-scattered light is collected following interaction with the sample through the same objective lens that directs the light onto the specimen and is focused onto the diffraction grating. The Rayleigh light is blocked through a notch filter in order for the weak Raman light to be isolated from the more intense elastically scattered light. The diffraction grating then separates the Raman signal into its constituent wavelengths and directs it onto a Peltier cooled deep depletion Charged-Coupled Devices (CCD) detector, which then generates the measured Raman spectrum. Finally, the white light image is displayed by the camera that is located at the top of the microscope, which allows the software to provide a large area montage and then select the area of interest.

(a)



(b)

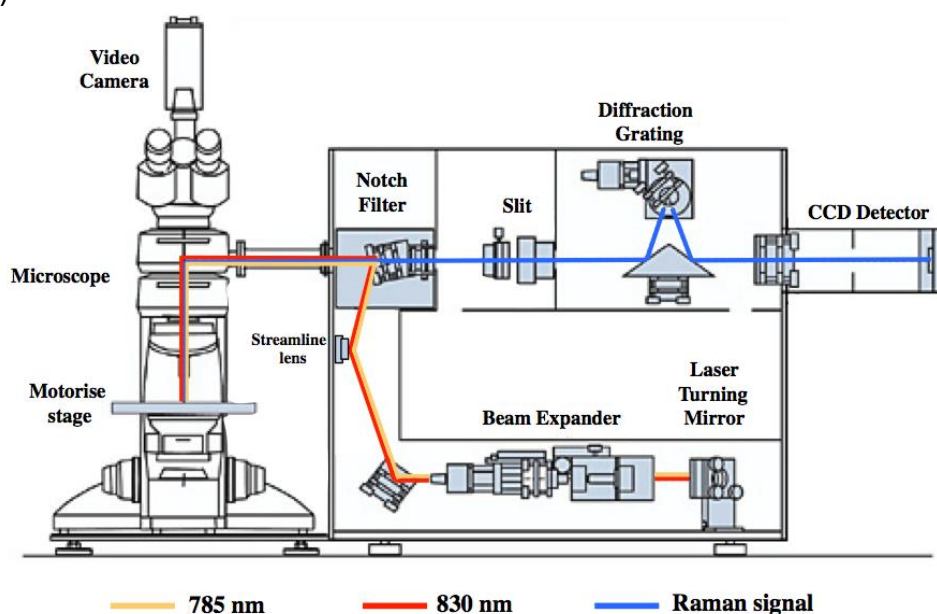


Figure 4.1: A typical experimental scheme for a Raman microscopy (InVia, Renishaw, UK). (a) Photograph of the Raman experimental set-up, (b) Sketch of the optical set-up of the Raman spectrometer shows the beam paths for the 785/830 nm laser resulting Raman signal.

4.2.1 Instrumentation for Raman microspectroscopy

Excitation source

A near-infrared (NIR) laser is the most common laser source used for biological samples due to its ability to improve one-photon fluorescence suppression, which can lead to a broad background in the spectra. In addition, because of the low energy of the laser when using the NIR wavelength, the sample damage is minimised to the lowest level, in comparison to those in the visible wavelength range. Thus, in the InVia Raman microscope, two laser sources were used in the NIR wavelength region (785 nm and 830 nm). In general, a shorter wavelength (785 nm) in NIR region is more efficient due to Raman intensity being inversely proportional to the λ^{-4} and also the CCD is more sensitive to the 785 nm wavelength when compared to 830 nm, especially in the HWN. The longer wavelength of the 830 nm laser is a factor 1.2 less efficient than 785 nm and a signal to noise ratio was predicted to be lower [170]. Thus, 785 nm was chosen to be used for the whole Raman measurements in the HWN in this study.

Sample illumination and signal collection

Light is efficiently collected in Raman microscopy using an optical microscope objective lens when an investigation of microscopic samples is needed. The objective lenses are considered one of the main configuration parts in the Raman spectrometer. It provides the potential to focus the laser beam on a tiny spot on the sample and maximises signal collection. Choosing the ideal objective lens and focusing the laser on a small spot contributes to rising the spatial resolution and maximising the gathering efficiency of the Raman scattered light, respectively.

Method and Instrumentation

A numerical aperture (NA) is a defining parameter of an objective, which characterise the ability of an optical system for light gathering and is shown as:

$$N.A. = n \sin\alpha \quad (4.1)$$

where the reflective index of the medium between the specimen is denoted by n and the objective, and the half angle of the cone of light is denoted by α . There are several objective lenses available in the InVia set-up 5X, 10X, 20X, and 50X. In this study, 50X (N plan, Leica) with an NA of 0.5 and a long working distance was used for Raman mapping and single spectra applications. While 5X (N plan, Leica) with an NA of 0.12 was used to obtain a large area montage and select the area of interest using the reflected white light to the camera installed on the top of the microscope.

Raman mapping

A Raman spectrum from each position on the sample (Spectral hypercube) was collected in a single file (Raman mapping), rather than a simple intensity image. Thus, to produce the Raman images it was necessary for the hypercube to be analysed. There are two Raman mapping methods available (point-by-point and streamline) in the Raman setup for fast Raman mapping to obtain spectral and spatial information.

Point-by-point mapping: in this method, the laser is focused on a spot in the sample. The sample is moved under the laser by a motorised stage in separate steps in the x-y direction or the z-direction. Raman spectra are sequentially obtained from an array of sample points (recorded at each point) covering the selected region of interest. This method takes a long time because of the stage movement and CCD record-out.

Streamline mapping: This method is similar to the point-by-point method; however, the laser illuminates a line on the sample rather than a spot. This approach saves time, due to the ability to collect Raman spectra

Method and Instrumentation

simultaneously from multiple positions on the sample, which is made of an accumulation of 6 points spectra. Also, with this method, the exposure time is reduced, which allows for the use of a higher laser power without damaging the sample. The Streamline mode generates high definition images of large sample areas quicker than the point mode. Due to the heterogeneity of most of the biological samples, the size and distribution of their components are required for a full understanding of them. This information can be collected very quickly and without sample damage by using streamline. Slalom mode is always used whenever using the Streamline mode to ensure the data is gathered from the whole area that is identified for analysis. The main limitation of this method is the long period of time needed when collecting Raman mapping with a high resolution over the large area. In this thesis, the Streamline mode was used for all Raman measurements.

Diffraction grating

The InVia Raman spectrometer is equipped with diffraction gratings as a spectral analyser. The Raman scattering light is spatially separated into the light with different wavelengths by the dispersive spectrometer, which is detected simultaneously by a CCD detector that exists in the focal plane of the focusing mirror. Three different gratings (300, 600, and 1200 lines/mm) are available in InVia Raman spectrometer. The 300 l/mm grating is the suitable one for covering the fingerprint and HWN regions ($>3500\text{ cm}^{-1}$) in a single scan, but with a low spectral resolution (7 cm^{-1}) and a long time for Raman mapping. The 600 l/mm and 1200 l/mm grating offer a higher spectral resolution than the 300 l/mm grating but with a low spectral range ($>2300\text{ cm}^{-1}$), which leads to measuring the fingerprint and HWN region separately. In this thesis, the region of interest is the CH stretching ($2800 - 3100\text{ cm}^{-1}$) in the HWN, which means 600l/mm and 1200 l/mm grating are both suitable to use. However, because the 1200 l/mm requires longer acquisition times, which cause an increase in Raman mapping times, we used 600 l/mm grating centred at 2500 cm^{-1} with 785 nm for the whole measurements recorded.

Detector

A Charged-Coupled Device (CCD) can be defined as a silicon-based multichannel array detector of UV, visible and near-infrared light. These kind of detectors are usually utilised for Raman spectroscopy due to their high sensitivity to light and allow multichannel operation [171]. Thus, CCD detectors are appropriate for an analysis of the inherently weak Raman signal and detect the entire Raman spectrum in a single acquisition. Pairs of the electron hole are created when the detector is exposed to the light. The photo-electron (charge) is registered due to the light interaction with each pixel, where, each pixel acts as an individual detector. The relation between the number of the acquired photo-electrons and the number of photons falling on each element is directly proportional. At the end of the measurements, the charge at each pixel is stored and converted from an analog to a digital value by the detector. The diffraction grating is used in the Raman spectrometer for dispersing the Raman scattered light as mentioned in the previous section and this light is then directed onto the long axis of the CCD array. The dispersed wavelength is detected by each pixel or closely spaced group of pixels. CCD detectors have the ability to cover a large wavelength response region ranging from 400 nm up to 1000 nm. The charge will be detected from the low cm^{-1} edge of the spectrum at the first pixel to the high cm^{-1} edge of the spectrum at the last pixel (see Figure 4.2). Therefore, while the line is scanned across the sample, the detector reads the data continuously [172].

The CCD detectors were chosen based on the laser wavelength that is used for excitation of the Raman scattering and the features of the spectrometer kind, which known as the spectral sensitivity, coverage and the speed of the acquisition. The generated noise (pixel and fixed pattern noise) able to characterise the performance of the CCD detector. The pixel noise is considered the difference in the values of charge read on a pixel, which has three main constituents: readout noise, dark noise, and photo shot noise from the light signal itself. The readout noise occurs due to the amplifier and electronics, which is existent on every readout. The dark noise relies on the

Method and Instrumentation

temperature of the detector and the exposure time of the measurement. Therefore, the CCD sensor must be cooled to a low temperature (e.g. to -75°C). The second type of noise is the fixed noise, which is a constant noise. This noise is due to the difference in the dark signal produced by each individual pixel and also sometimes due to irregularities during the fabrication of the CCD.

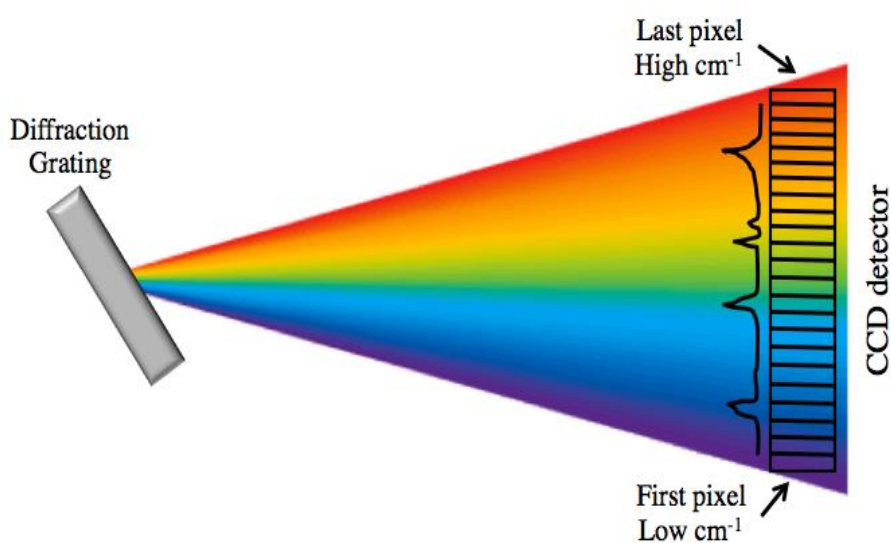


Figure 4.2: Simplified diagram of the Raman scattered light on the CCD detector.

The quantum efficiency is considered another significant characteristic of the CCD detectors, which is related to the spectral response of the CCD. It demonstrates the probability of a photon of a confirmed frequency to excite a photo electron in the silicon. The quantum efficiency is dependent on the absorption coefficient of the silicon and on the wavelength of the photons.

There are three types of CCD detectors widely used: front-illuminated, back-illuminated and back-illuminated deep depletion. The deep depletion detector is made from a thick silicon substrate of high sensitivity, which provides a maximum efficiency to NIR scattered radiation and is commonly an ideal approach for NIR dispersive Raman systems.

Raman spectroscopy substrates

Calcium fluoride (CaF_2) (Crystran, UK) was used in the Raman measurements. All tissues were mounted on the CaF_2 substrate. It was evident that it was an appropriate substrate for Raman measurements due to the significant lack of background where it only offers a peak at 321 cm^{-1} , which is outside of the region of interest. Figure 4.3 shows the Raman spectra of calcium fluoride at the fingerprint and HWN regions using a 785 nm laser line, grating of 600 l/mm, and an exposure time of 1 second.

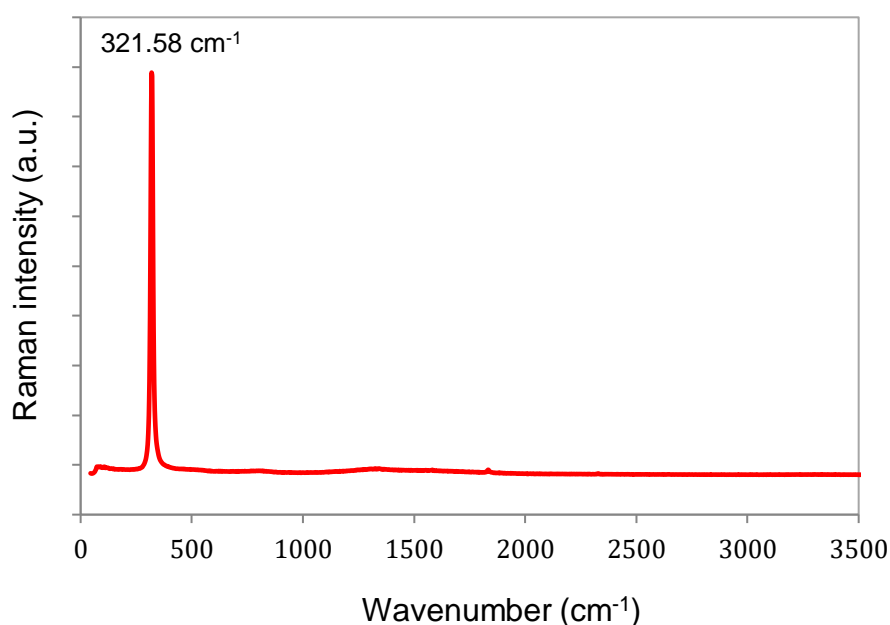


Figure 4.3: The Raman spectrum in the fingerprint and HWN region of the CaF_2 substrate using a 785 nm line and 600 l/mm grating, showing the CaF_2 peak at 321.58 cm^{-1} .

4.2.2 System calibration

Raman spectroscopy provides a unique information on molecules such as their geometry, physical or chemical environment and the ratio of each compound. Several information are expected to extract such as a number of

Method and Instrumentation

peaks and their positions and Raman intensity. Factors that need to be known such as the wavenumber, the resolution of spectral and intensity response of the device utilised. All of these rely on optics, the spectrometer, the laser source, temperature and exposure time. These factors must be performed at least once before each experiment but more often depending on the stability of the device and the needed accuracy. Thus, there are two main calibrations: Raman shift wavenumber and Raman intensity. The Raman shift wavenumber calibration depends on the laser wavelength and detector. The Raman intensity calibration depends on the spectrometer response and cross section.

Three different external standard samples were used for the system calibration: a silicon wafer (Si), green glass (gg), and neon lamp (Ne). This calibration was used to identify the accuracy, to identify the range of the Raman shift, to choose the standard specimen, to record the spectrum and to adjust the correlation curve parameters to fit the exact peak position. The Si wafer is used for x-axis calibration, which has a strong peak at $(520.7 \pm 0.5 \text{ cm}^{-1})$. Figure 4.4 shows the system x-axis calibration curve using the Si wafer, where the Raman spectrum was acquired with 5% power, one-second acquisition times, and 1 accumulation. The position of the Si peak can be found by using the peak fitting in the Wire software. Often, a slight shift occurs at the peak position, which is corrected by applying the offset. Using silicon for the x-axis calibration is an effective method but it is not enough to cover the whole Raman spectral region due to the strong Si peak being located at the beginning of the fingerprint region. Therefore, the external in-built neon lamp was used as the second standard sample for a more accurate calibration.

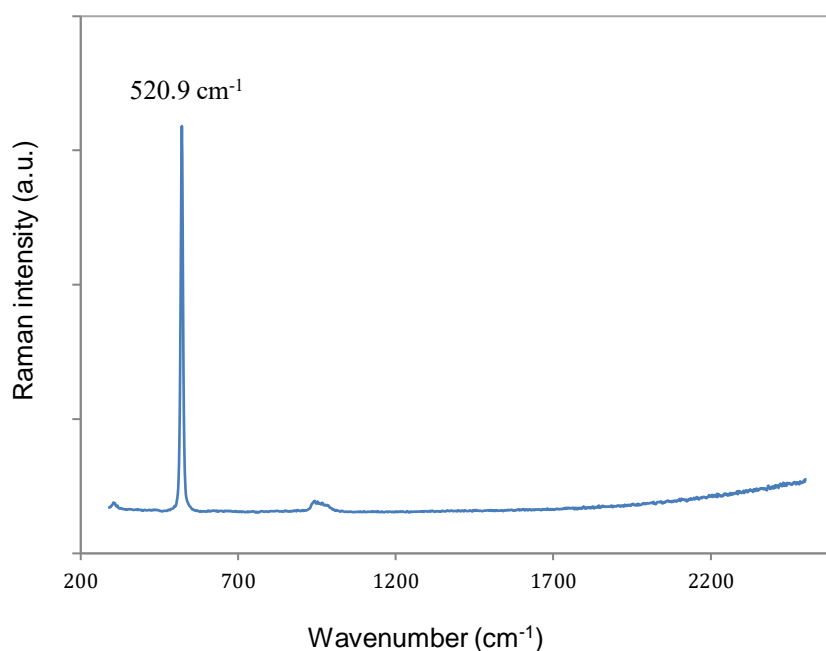


Figure 4.4: Raman spectrum of the Si wafer for the x-axis calibration, where the Si peak appears at 520.9 cm^{-1} .

The neon lamp provided a string of strong peaks of different known positions along the Raman wavenumber regions. Figure 4.5 shows the emission spectra of the neon lamp, which was produced for the 785 nm and 830 nm configurations. The Raman spectrum of the neon lamp sample was acquired with 100% power, 0.01sec acquisition times, and 1 accumulation. At fixed wavelengths, neon lamp peaks occurred and the laser was shuttered for those measurements. For the sample being measured, the same instrument set-up had to be used for the neon lamp measurements, where the corrections were performed after the measurement. The x-axis was recalibrated by fitting a polynomial function to the data after selecting known neon peaks positions.

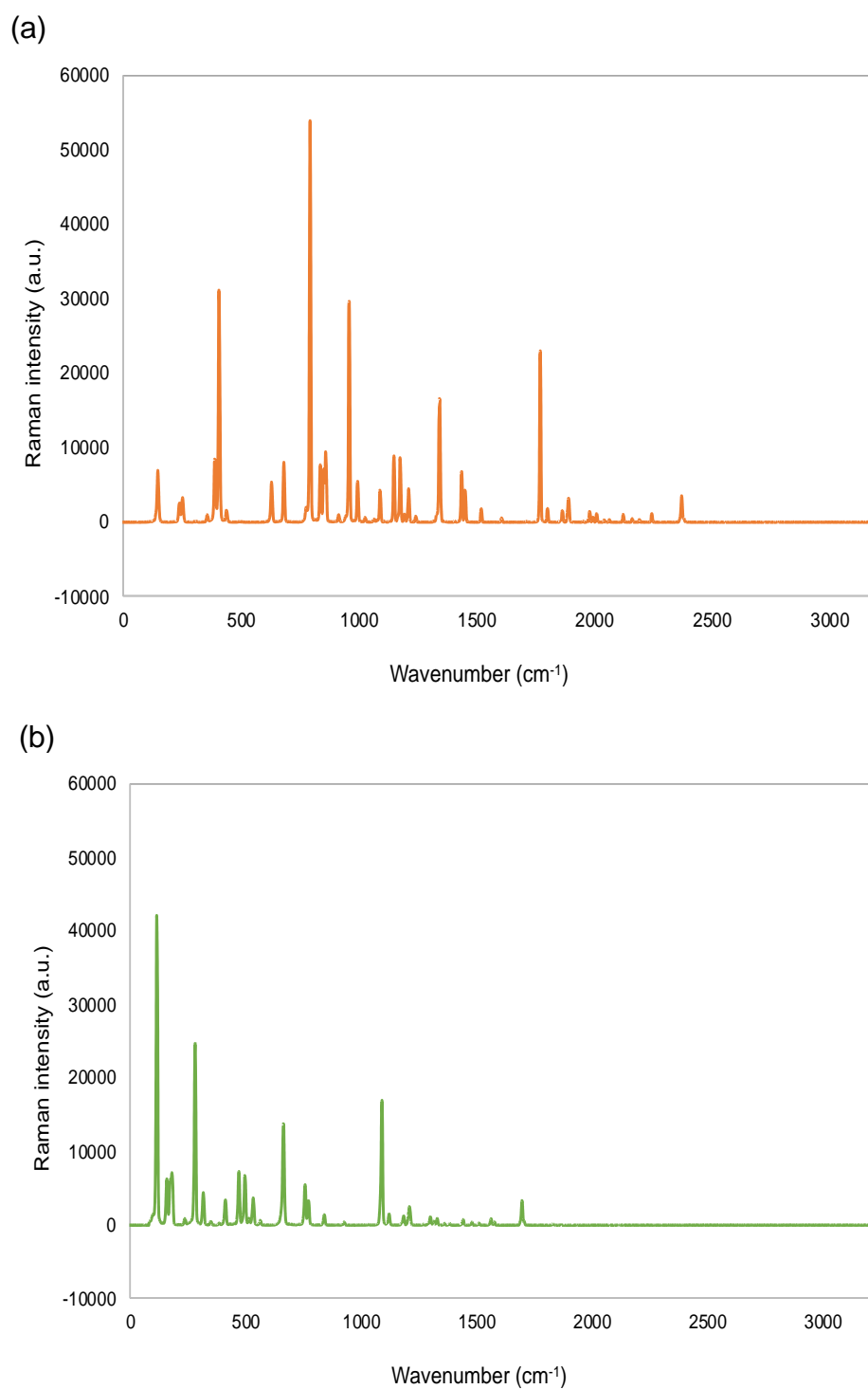


Figure 4.5: Raman spectra for the Neon lamp (Ne) with (a) 785 nm streamline configuration and (b) 830 nm streamline configuration.

The optics and detector that construct the spectrometer have changeable efficiencies as a function of wavelength. This difference is called the instrument response. Consequently, all recorded spectra are a mixture of the instrument response and sample spectra. The changing in the quantum efficiency of the CCD across the spectral range is considered as the main contribution. Thus, the standardised piece of green glass (gg) was used to correct this effect. The parameters that were used for the sample had to be the same as the gg spectrum recorded. To produce a correction function, the measured spectrum of the gg was split by an absolute gg spectrum. After producing the correction function, it was multiplied by the sample spectra. This effect is to increase the peaks toward the high Raman wavenumber. This correction is essential particularly in the HWN region, especially when any quantitative analysis is acquired.

4.3 Coherent Raman scattering set-up

This section will present the description of the measurement for the coherent Raman scattering technique (CRS) including coherent anti-Stokes Raman scattering and stimulated Raman scattering.

4.3.1 Coherent anti-Stokes Raman scattering (CARS)

CARS is a nonlinear optical technique that requires an ultra-fast pulsed laser. In this study, the CARS setup was performed using a Yb-fibre laser (Emerald engine, APE GmbH, Berlin, Germany) generating a 2 picosecond pulse duration with a bandwidth of 10 cm^{-1} and a repetition rate of 76 MHz at 1032 nm, which was frequency-doubled to pump an optical parametric oscillator (OPO, Levante Emerald, APE) to generate a signal beam tuneable from 690 to 990 nm, which known as the pump beam. The Stokes beam (ω_s) was generated directly from the laser source at 1032 nm, while the pump beam (ω_p) was split it into two parts to produce two different photons at near-infrared wavelengths. These two beams are conventionally known as a signal (at the

Method and Instrumentation

lower wavelength) ranging from 690nm to 990nm and idler (at the higher wavelength) ranging from 1150 nm to 2300 nm.

The pump and Stokes beams were spatially and temporally overlapped by changing the length of the optical path on the Stokes beam using a delay stage to obtain the same path difference created within the OPO. This made both Stokes and pump beams reach the microscopy simultaneously as shown in Figure 4.6. Photographs of the coherent Raman set-up are presented in Figure 4.7. The overlapped laser beams were then steered into a modified confocal laser scan unit (Fluoview 300, Olympus, Essex, UK) and an inverted microscope (IX71, Olympus, Essex, UK). The microscope had a MgF₂ lens and silver galvanometric mirrors to improve optical transmission in the NIR.

CARS was set up to image the biological structure in the CH Raman vibrational region at HWN from 2800 cm⁻¹ to 3100 cm⁻¹. The idler and signal beams were used as the pump at (780 - 800 nm) and Stokes at 1032 nm respectively. The sample was located on the stage between two objective lenses (forward and backward direction) inside an inverted microscope. The epi-CARS signal was collected from the backward direction by passing the signal through the sample and then back through the objective lens. Two objective lenses were used to tightly focus the light onto the sample. The first objective is typically a 60X water objective lens (UPLSAPO, Olympus) with a numerical aperture (NA) of 1.2 and a working distance of 0.28 mm, which was used to acquire a high-resolution image. The second one was a 20X air objective lens (UPLSAPO, Olympus) with a 0.75 NA and working distance of 1.2 mm, which provided a larger FOV. The 20X objective was used to identify the coordinates of the whole sample by scanning the large area using the motorised stage (Prior, Proscan) controlled by the Scanimage software (Vidrio Technologies). A long pass dichroic mirror (750dcxr, Chroma technologies) and two filters centred at 660 nm (660.0 IF 40D, Ealing) were located before the objective lens to split the signal from the laser and then detected by a photomultiplier tube (PMT, R3896, Hamamatsu Photonic UK).

Method and Instrumentation

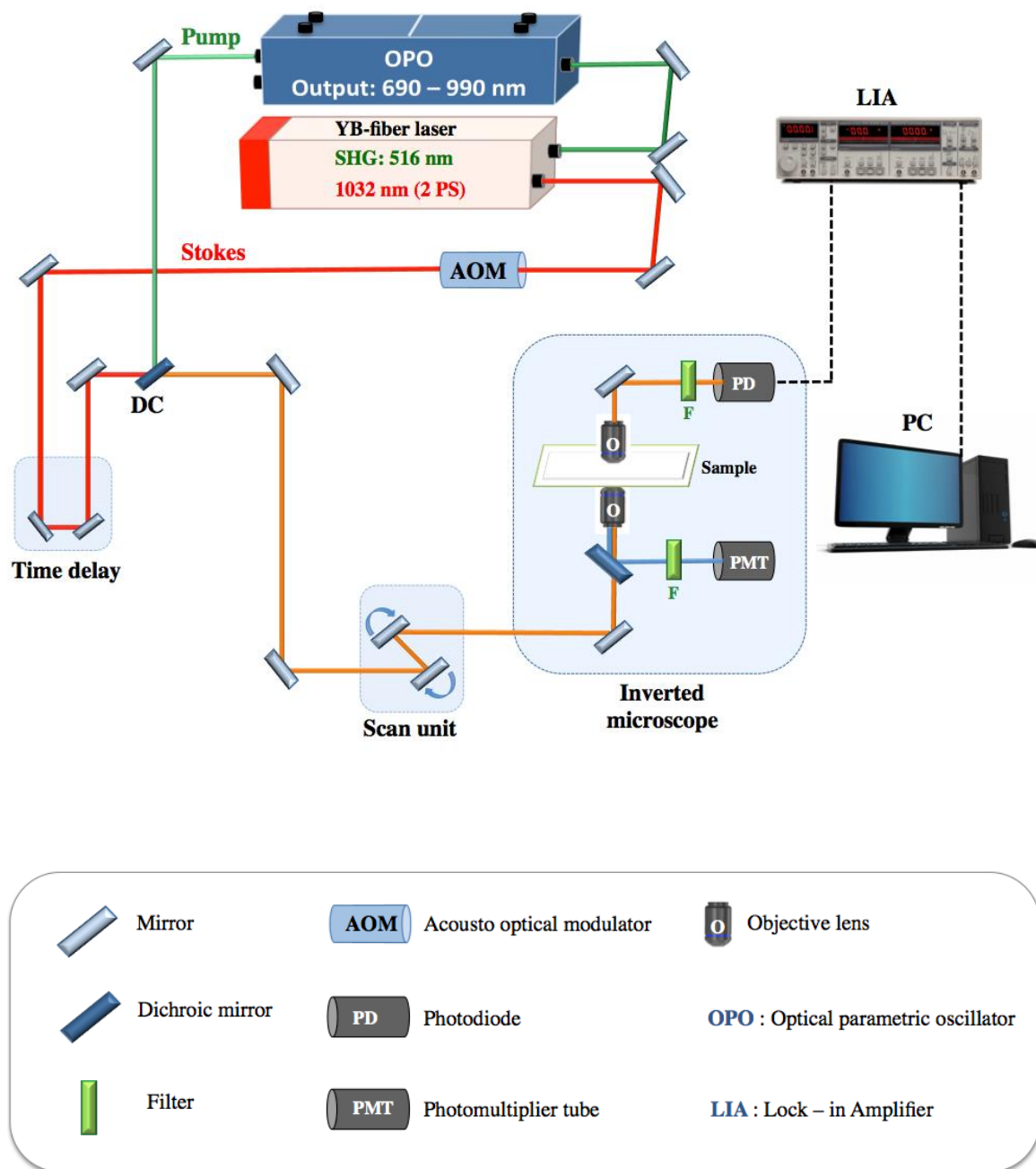
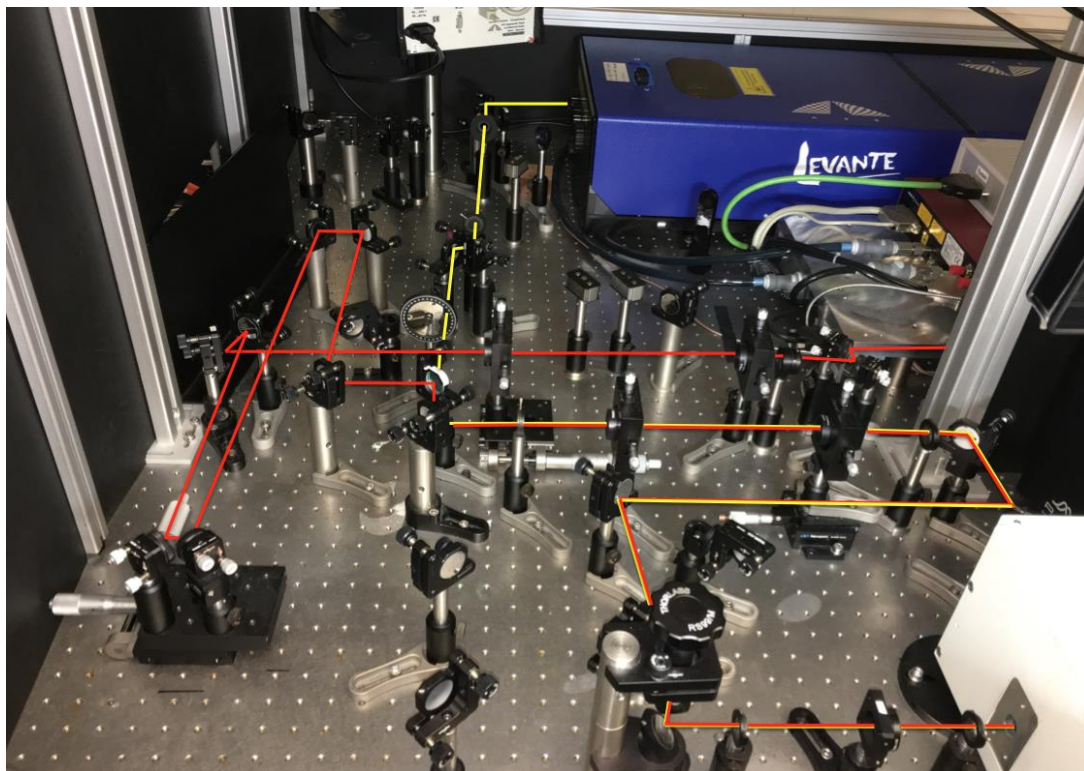
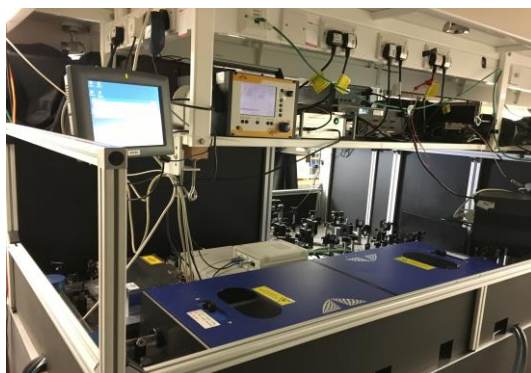


Figure 4.6: Simplified schematic diagram of the experimental set-up of the coherent Raman techniques.

(a)



(b)



(c)

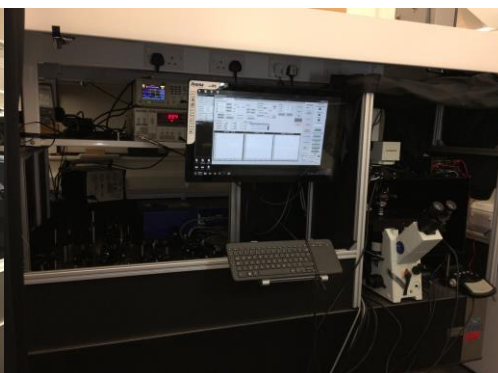


Figure 4.7: Photographs of the coherent Raman set-up. (a) Optical table shows mirrors, a dichroic mirror, and telescopes that guide the beams to the scan unit. (b) The set-up from the back shows the laser, OPO unit, and OPO controller. (c) The set-up from the front shows the lock-in amplifier, inverted microscope, and the PC touchscreen.

4.3.2 Stimulated Raman scattering (SRS)

A similar optical configuration to the CARS setup explained in the previous section was used to detect the SRS signal. An acoustic-optical modulator (MT200-A0.5-1064, AA Opto-Electronic) was located in the optical path of the Stokes beam (1032 nm) to modulate its amplitude at 8.4 MHz. The forward direction is mainly used to detect the signal of the SRS by focusing the light onto a silicon photodiode (FDS 1010, Thorlabs, Exeter, UK) with a 64 V reverse bias. A radio frequency Lock-in amplifier ((SR844, Stanford Research Systems, Sunnyvale, USA) was connected with the photodiode to extract the modulated signal referenced to the AOM driver. The silicon diode is more sensitive to the stimulated Raman loss (SRL) than a stimulated Raman gain (SRG) on the pump beam [173]. For the SRL imaging, the Stokes beam was blocked with a range of 890 ± 220 nm by two bandpass filters (CARS 890/220m, Chroma technologies, Vermont, USA), which were placed after the objective lens and the pump beam was detected. Because of the strong signal produced by the laser pulsing at 76 MHz, it was repressed by pre-amplifying the output voltage, filtered by a low pass filter (BLP-21.4 , Mini-Circuits) and then ended by a 50 Ω resistor.

There were three objective lenses available for the SRS forward detection. The first one was the air condenser lens (IX2-LWUCD, Olympus) with the numerical aperture (NA) of 0.55 and long working distance. The second one was the 100X Oil immersion lens (UPLSAPO, Olympus) with a numerical aperture of 1.4 NA and a working distance of 0.13 mm. The last one was the 60X water immersion lens (LUMPLFLN, Olympus) with 1 NA and a working distance of 2 mm. In this study, a 60X water immersion lens was used to obtain an efficient collection from the forward direction. All samples were mounted between two glass coverslips (deltalab, 24x50 mm, Nr.1) to overcome the short working distance limitation of the 60X water immersion lens in this work. Some of the transmitted light reflected the references photodiode (DET100A/M, ThorLabs). A glass coverslip was located after the

objective lens at a 45° angle that directed the light to the diode to collect the transmitted light.

4.4 Large area montage

To study the suspicious area in the biological tissue, acquiring a large field of view (FOV) image is required. This contributes to illustrating the whole tissue to determine the small area of interest and also to find the right orientation against the pathology images of the gold standard method (haematoxylin and eosin, H&E) for comparison. The FOV depends on three main parameters in the microscope, a magnification of the objective lens, number of the field, and the zoom factor that is controlled by Scanimage software. In this thesis, a 20X air objective lens from the backward direction and 60X water immersion from the forward direction were used with 2X zoom factor and 640 μm X 640 μm field of view to acquire a large area montage. For the small area of interest 60X water immersion (low working distance) from backward direction and 60X water immersion (high working distance) from forward direction were used with a 2.5X zoom factor and 200 μm X 200 μm field of view.

4.5 Hyperspectral SRS

In this research, we managed to modify the OPO for rapid wavelength tuning and then applied this approach to obtain hyperspectral SRS stacks and extract the SRS spectra rapidly. To achieve this, new hyperspectral software was written using MATLAB (2018a) to control the OPO and then integrate it with the Scanimage software for automatically tuning the wavelength and recording all parameters required for the experiment. To acquire hyperspectral SRS stacks with a high image quality, a 60X water immersion lens was used from the forward direction and the 60X water objective lens from the backward direction with a 2.5X zoom factor and 25 second frame rate of 512 X 512-pixels images. For extracting the SRS spectra rapidly, the

same objective lenses, that were used in the acquisition of hyperspectral SRS stacks were used, however, a 10X zoom factor and 4.5 second frame rate of 512 X 512 pixels images were used.

4.6 Multivariate analysis

Multivariate analysis is a powerful and popular branch of statistics which deals with several variables [174]. Most of the univariate analysis results translate themselves into multivariate analysis, but there are certain results which are very specific to multivariate studies. This is primarily because multivariate studies take account of the interrelationships between the variables, which cannot be done in univariate studies. Therefore, instead of looking at several variables separately, multivariate studies will assess them simultaneously and hence will be able to study interrelationships between the variables. Thus, multivariate analysis is very commonly used in spectroscopy for data reduction and quality improvements such as signal-to-noise ratio and resolution. It can also be used in a classification of information of the data and an appropriate display of information. In this study, K-means clustering was performed over the pre-processed spontaneous and stimulated Raman spectra.

4.7 Sample collection and preparation

All of the human oesophagus tissues that were used in this study were harvested from patients at the Gloucestershire Royal Hospital. The Gloucestershire local research ethics committee approved this procedure (see appendix for ethical approval). The usual routine for the GI surgical procedure was followed in this research. After collection, all of the biopsies were snap frozen in liquid nitrogen and stored in the freezer at -82° C. Dry ice was used when transporting the tissue from the hospital to Exeter, where immediately upon arrival they were stored in the freezer at -82° C.

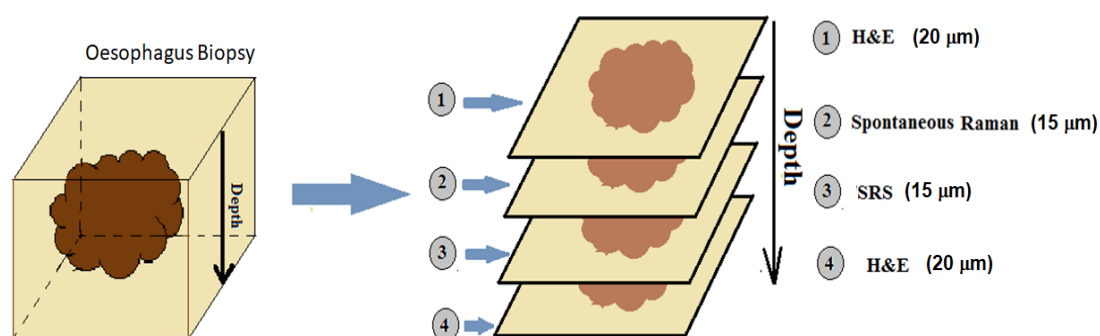


Figure 4.8: The protocol of the sample preparation, where each frozen oesophagus biopsy was cut into four contiguous sections for the H&E, Raman and SRS measurements

Each biopsy was cut by a pathologist into four contiguous cross sections using a microtome (see Figure 4.8). The first and the last sections were cut to a thickness of 20 μm and mounted onto microscope glass. H&E were used to stain these two sections for pathological analysis. For all H&E samples, a second coverslip was applied from the topside and installed from the edges using a single layer of double-sided sticky tape for protection. The second and the third sections were cut to a thickness of 15 μm . The second section was mounted onto CaF_2 , while the third section was mounted onto a coverslip for Raman and SRS measurement, respectively. This procedure was repeated five times with each biopsy to select the ideal section and avoid any imperfections of preparation. Before measuring any of the SRS samples, a second coverslip was applied and installed from the edges using a single layer of double-sided sticky tape to enable the use of the water lens. Before each measurement, the samples for Raman and SRS were removed from the freezer and kept at room temperature for 30 minutes, in order to melt the ice and bring it back to room temperature.

Chapter 5

Development of the OPO Cavity

5.1 Introduction

The aim of this chapter is to develop the performance of the OPO cavity in CRS for rapid wavelength tuning. To achieve this, modification and automation of the OPO cavity is required. A dispersive block was installed in the OPO cavity to improve and speed up the performance of the OPO. The dispersive block provides different wavelengths that have different reflective indices in the material. This leads to the spectra being separated very efficiently, and the tuning becomes easier with the cavity length changes [175]. Hyperspectral software has been developed for automatically controlling the OPO. In this chapter, the novel contribution to field is the modification of the OPO cavity controlled by the hyperspectral scanning software, which causes to speed up the wavelength tuning significantly.

The author's contribution in this chapter:

1. The hyperspectral scanning software was developed by the author with support from Sivaraman Subramanian.

2. The dispersion block was provided by Angewandte Physik und Elektronik GmbH (APE) for ultrashort laser pulse diagnostic and tuneable wavelength conversion.
3. All measurements relating to the characterisation of the OPO performance were performed by the author.
4. All figures in this chapter were measured, analysed, and plotted by the author.

5.2 The Optical parametric oscillator (OPO)

5.2.1 Introduction

The optical parametric oscillator (OPO, Levante Emerald, APE GmbH, Berlin, Germany) is a device that provides a nonlinear process [176]. It processes the pump beam synchronously generated by a mode-locked frequency doubled Yb fibre laser and is dependent upon collinear non-critical phase matched interaction in the lithium triborate (LBO). The OPO aims to transfer the Yb fibre wavelength of second harmonic at 516 nm very efficiently to the tunable wavelength of between 690 nm and 990 nm (signal) and between 1150 nm and 2300 nm (idler). The OPO tunable wavelengths can be defined by changing the temperature of a non-linear OPO crystal (coarse tuning), the angle of the Lyot filter (fine tuning), and the piezo position (i.e. the cavity length).

The OPO consists of the optical unit controlled by the control electronics console. A photograph and schematic of the OPO optical unit are shown in Figure 5.1 (a) and (b), respectively. The optical unit contains windows for the input pump and OPO radiation output, focusing the optics of the pump beam, the eight-mirror cavity, and sensor modules. There was a lens behind the output coupler for recollimation, a beam block for 516 nm radiation, and a beam splitter for the diagnostics. One of the mirrors was located on a

Development of the OPO Cavity

translation stage to synchronise the cavity round trip time to the pump laser repetition rate, combined with a piezo fine alignment element (PZT) for active cavity length stabilisation. The control electronics console (OPO controller) was used for controlling the optics unit. Figure 5.2 shows a photograph of the control electronic console. It contains the sensor amplifier, the piezo driver, the Lyot filter driver, the diagnostics control boards, and the temperature control unit for the nonlinear SHG crystal.

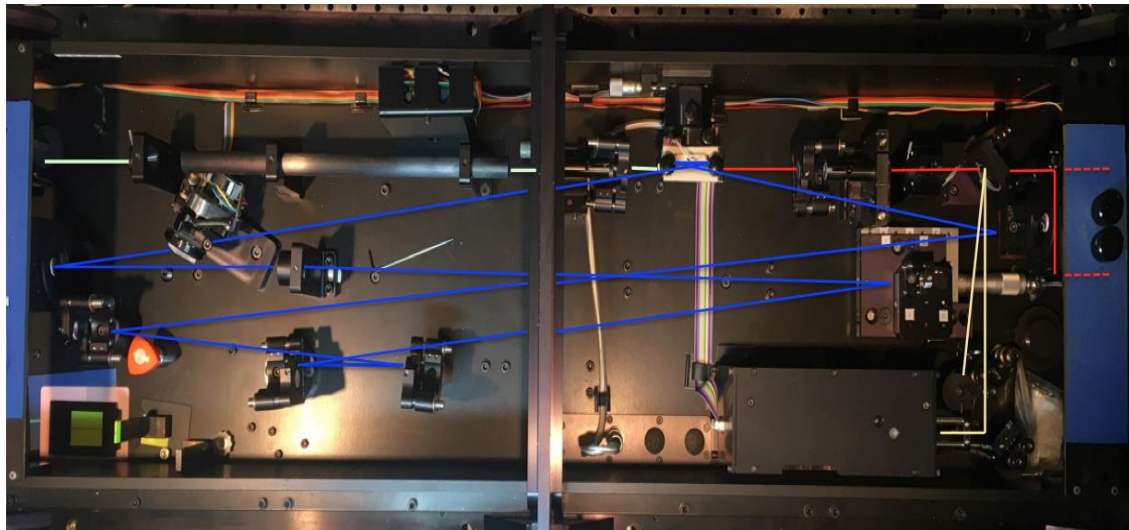
5.2.2 Theory of optical parametric conversion

In the OPO, a pump photon is converted into two photons of lower energy by using a nonlinear gain medium with large second susceptibility, $\chi^{(2)}$. Based on the peak power, the parametric process can be achieved with CW, pulsed or ultrafast pump sources. With the coming of reliable OPOs, high-powered mode-locked oscillators and high-quality non-linear crystals are viable sources of applicable tunable pulsed light. The physics behind an optical parametric process will be described in the next paragraphs.

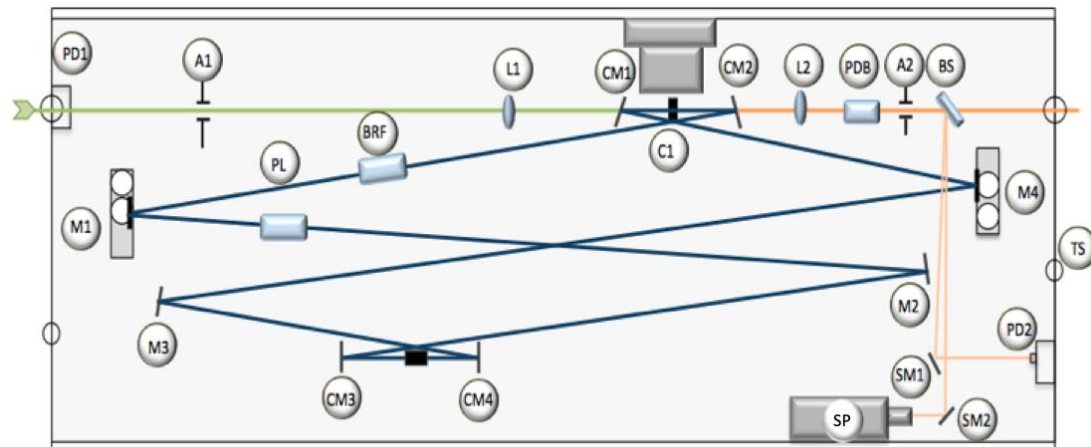
The optical parametric process generates two output waves, a signal and an idler, by converting an input pump wave. These three waves must be transferred through the nonlinear crystal at the same velocity in order to be in the same phase and to obtain an efficient energy transformation. This procedure indicates that the indices of refraction of the three waves are the same. Unfortunately, the dispersion of a crystal is mostly such that the indices are different for the pump, signal and idler beams. However, fortunately, the natural birefringence of uniaxial or biaxial crystals can be used to offset this dispersion. The direction of propagation can be achieved by corresponding with the two allowed orthogonally polarised modes through the two reflective indices in these crystals. The proper selection of polarisation and direction of propagation often leads to minimising the phase mismatch, with theoretically a mismatch of approximately zero (this is called phase-matching).

Development of the OPO Cavity

(a)



(b)



(A1,2) Apertures	(PL) Polarizer	(PD1) Pump power photo detector
(L1) Pump focus, Lens	(PDB) Pump beam dump	(PD2) Signal power photo detector
(L2) Collimation lens	(CM 1-4) Concave mirrors	(TS) Screw of translation stage
(M1-4) Plane mirrors	(BRF) Lyot filter	
(C1) OPO crystal	(BS) Beam splitter	
(SP) Spectrometer	(SM 1,2) Beam steering mirrors	

Figure 5.1: The OPO cavity. Image (a) shows a photograph of the OPO optical unit with an internal spectrometer; Image (b) shows the construction of a ring cavity OPO with a conventional design.

5.2.3 Phase-matching

There are two special techniques of phase matching (parallel and orthogonal phase-matching) that can be used to achieve the momentum conservation requirements. The type of phase matching that is used relies upon the crystalline structure and the orientation of the crystal regarding the pump beam. In orthogonal phase matching, the polarisation vector of the pump is parallel to the polarisation vectors of the signal and the idler, and the signal and idler polarisation vectors are perpendicular to each other. In the parallel phase matching, however, the pump polarisation vector is orthogonal and the polarisation vectors are parallel to that of the signal and the idler. Furthermore, noncritical phase matching occurs when the propagation direction is along one of the principal axes of a crystal, while it is critical for any other propagation direction. In general, small changes in the temperature and the alignment deviations affect the sensitivity of the phase matching process. Therefore, a wide acceptance angle in noncritical phase matching makes the process insensitive to these small changes, which permits the use of longer crystals that lead to higher conversion efficiency.



Figure 5.2: The control electronic console.

Development of the OPO Cavity

The conversion is restricted by:

1. The bandwidth of the pump beam.
2. The pump beam divergence.
3. The reverse conversion of the signal and idler to the pump beam.
4. Saturation and various nonlinear procedures.
5. Thermal and angular deviations from the typical phase matching conditions.

According to the two generated outputs, the signal can be defined by the shorter wavelength (higher frequency), and the idler by the higher wavelength (shorter frequency). The signal and idler are separated by the degeneracy point (the frequency separating), which occurs at twice the pump wavelength. These frequencies should obey the next frequency and the momentum conservation relations:

$$\omega_p = \omega_s + \omega_i \quad (5.1)$$

$$n_p \omega_p = n_s \omega_s + n_i \omega_i \quad (5.2)$$

where ω_p refers to pump frequency, n refers to a refractive index, ω_s and ω_i refer to the signal and idler frequency, respectively. It is often easier to present Equation 5.1 in an expression of the wavelength (λ) of the three beams, rather than the frequency, as shown in Equation 5.3.

$$1/\lambda_p = 1/\lambda_s + 1/\lambda_i \quad (5.3)$$

For the tuning of crystal OPOs, the phase-match (or momentum conservation, see Equation 5.2) condition mentioned above is the mechanism that is utilised for tuning the OPO's wavelength. This tuning can be achieved by changing the indices of refraction of the medium along the propagation direction through crystal rotation (angle-tuning), altering its temperature (temperature-tuning), or by applying an electrical field to the material (electro-optic tuning).

5.2.4 The optical parametric system

There are two fundamental setups which can be used to configure the optical parametric system. The optical parametric system is called an Optical Parametric Amplifier (OPA) when there is only one pulse in the crystal at any given time (i.e. the optical cavity is designed as a single pass). The system is called an Optical Parametric Oscillator (OPO) when the nonlinear crystal is located in a resonator, which sharply reduces the threshold of the nonlinear process. The system is called a synchronously pumped OPO if the optical cavity is created to be synchronised with the pump source. OPO synchronisation occurs if the round-trip time of the pulses in the cavity of the OPO is the same as the pump laser repetition rate. Optical gain is obtained, resulting in this resonance.

To avoid a high threshold synchronously pumped OPO, the build-up of the parametric waves or synchronisation are required. The OPO is called signal resonant or idler resonant if the cavity is designed to support the signal beam or idler beam, respectively. According to the above categories, there are sometimes references to a laser even though the system is technically not a laser. An OPA or OPO does not have the unique characteristic of energy storage that a laser does. Due to this energy storage, and as a result of a population inversion, conventional laser sources have optical gain. Optical gain in a parametric process is supplied through the simultaneous presence and the interaction of the optical fields in a crystal with a non-zero second-order susceptibility, $\chi^{(2)}$.

The OPO used in this thesis is synchronously pumped by the SHG of a mode-locked picosecond Yb fibre laser at a wavelength of 516 nm. It depends on noncritical phase-matching parametric interaction in the LBO. In order to make the system a signal resonant OPO, the cavity mirrors are created for the high reflectivity of the signal beam. The wavelength tuning can be defined by changing the temperature phase matching in the non-linear OPO crystal (LBO, rough tuning), the angle of the Lyot filter (fine tuning), and the piezo

position (cavity length). This procedure requires a feedback loop to optimise the temperature, Lyot filter, and Piezo position. The Lyot filter was the most problematic in this setup as it required readjusting the angle several times more than the others before getting an accurate tuning, which made the procedure very slow and in need of modification.

5.3 Development of the OPO cavity for rapid wavelength tuning

The aim of the work described in this chapter was to modify the way the OPO tuned to increase spectral acquisition speed. To achieve this, the OPO was developed by replacing the Lyot filter in the cavity with a new dispersion block.

A Lyot filter can be defined as an optical filter device depending on birefringence that offers a wavelength-dependent power transmission [177]. It is one of such optical filters to produce a narrow bandpass of transmitted wavelengths, which depends on the polarisation and propagation direction of light. The Lyot filter used in this work is comprised of two plates of stacked crystalline quartz and polarisers. In the simplest configuration, the beam is perpendicular to the plates, and the axis direction of the polarisers is oriented at 45° to the birefringent axis of each crystal. In a crystal, the light propagating contains two different linear polarisation components, which causes a different phase delay. For the two polarisation components, the relative phase delay depends on the wavelength. Thus, the loss of optical power depends on the wavelength at the subsequent polariser.

The dispersion in optics can be defined as the phenomenon that the phase velocity of a wave depends on its frequency [178]. The angle of refraction of different colours of light is one of the important results of dispersion. Therefore, a dispersive block is a medium that waves at various frequencies and travel at various velocities. Dispersion describes dependence on the wavelength for the speed of light in a given medium. Where in the material,

Development of the OPO Cavity

the blue wavelength parts propagate with lower speed of light than the red wavelength parts, which leads to a time delay between the different wavelength parts. The time delay remains constant when the pulse leaves the medium, which is called a positive chirp. Whereas, a negative group velocity dispersion (GVD) is generated by the optical gratings or the angular dispersion of prisms. A dispersive block used in this work consists of heavy flint glass, AR coated for signal, 50mm long, and single pass.

According to the above description, the OPO has three tuning mechanisms: crystal temperature, cavity length and Lyot filter. The crystal temperature is the phase matching temperature for the desired wavelength. If changing the wavelength to a lower value, then the pulse traveling time is slowed down due to dispersion in the transmission elements of the crystal and the Lyot filter. As there had to be precisely the same cavity length for the OPO as for the laser, it was necessary to compensate for the delay caused by the dispersion by adjusting the OPO cavity length. The Lyot filter was used for a final fine-tuning. However, the dispersion was not very high, and the phase matching of the bandwidth of the crystal was about 10 nm. Thus, the wavelength could be selected with the cavity length within this 10 nm range. On the other hand, the Lyot filter also has a transmission bandwidth and a second order transmission, which further complicated tuning, especially for longer wavelengths above 950 nm.

This modification involved removing the Lyot filter and inserting a dispersion block (provided by the APE) between the concave mirror (CM4) and plane mirror (M3) in the OPO cavity (see Figure 5.3). By balancing the overall Group Velocity Dispersion in the OPO cavity, the additional dispersion block, increased the separation of the frequencies inside the cavity allowing fine tuning of the performance by cavity length changes alone [175]. In general, the dispersion block provides different wavelengths that have different reflective indices in the material. In other words, only a short part of the phase-matched bandwidth is available in the crystal, then the next laser pulse appears, and the needed spectral part can be selected with the cavity length

Development of the OPO Cavity

only. With this, the tuning becomes much more stable and allows for the rapid tuning of output wavelengths based on the cavity length (piezo position), and without the need to use the Lyot filter, especially under 950 nm.

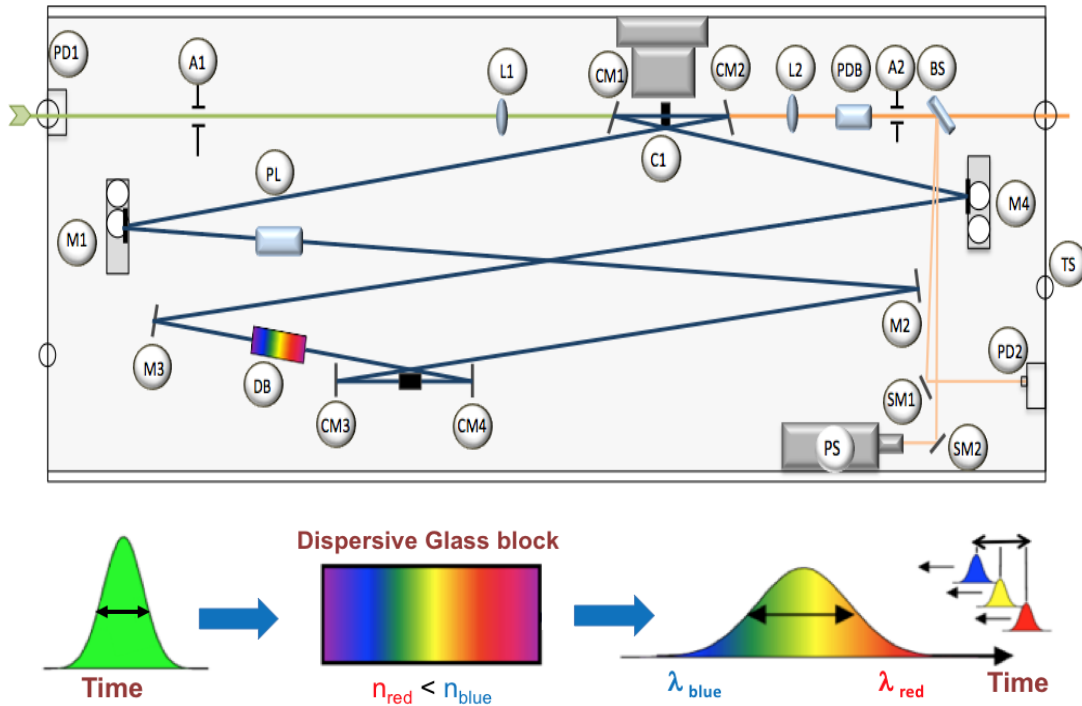


Figure 5.3: Construction of the ring cavity OPO and tuning principle with the new dispersion block, and without the Lyot filter to tune the output wavelength via cavity length tuning, where DB refers to the dispersion block.

5.4 Performance of the OPO

A comparison between the performances of the original OPO design and the new OPO design is presented in this section. Figure 5.4 shows the OPO power as a function of the wavelength at different temperatures to demonstrate the OPO performance for wavelength tuning for both the original cavity and the modified cavity. It can be seen that the wavelength tuning of the OPO was more stable with the new design compared to that of the conventional design. Additionally, the phase matching bandwidth of the crystal

Development of the OPO Cavity

increased up to 20 nm. However, it became broader after 950 nm (not presented here), which means that the Lyot filter was still necessary for the fine-tuning of the wavelength above 950 nm in order to obtain accuracy from 0.1 nm. The region of interest in this study is the CH vibration region in the high wavenumber region between 780 nm and 800 nm, and from 2,800 cm^{-1} to 3,100 cm^{-1} , which means there is no need to use the Lyot filter.

After the modification, the wavelength tuning routine became dependent on only two mechanisms: the crystal temperature and the cavity length. Figure 5.5 shows the OPO wavelength tuning as a function of the scan number and the fluctuation of the OPO power. The scan number indicates the number of frequencies or wavelengths required to cover the region of interest in the wavenumber region, which depends on the frequency step size. The dashed red line indicates the ideal tuning in the OPO. A slight instability was observed in the wavelength tuning of the OPO in both designs, where the OPO produced an increase and a decrease in the pump wavelength with an equal tuning step size. This issue should not significantly affect the measurement times or accuracy. In addition to wavelength instability, the SRS signal was directly affected by the fluctuation of the OPO power, where the relationship is linear between the SRS signal and the intensity of the pump beam. The power is presented in arbitrary units, and it is obvious there was a fluctuation of the OPO power with both designs, which affected the SRS spectral information that could be covered. However, the modified cavity produces a more stable output power when it gradually increases or decreases, which makes it possible for the SRS signal to recover from the system noise. A power normalisation technique must be applied correctly, as will be presented in greater detail in Chapter 6.

Development of the OPO Cavity

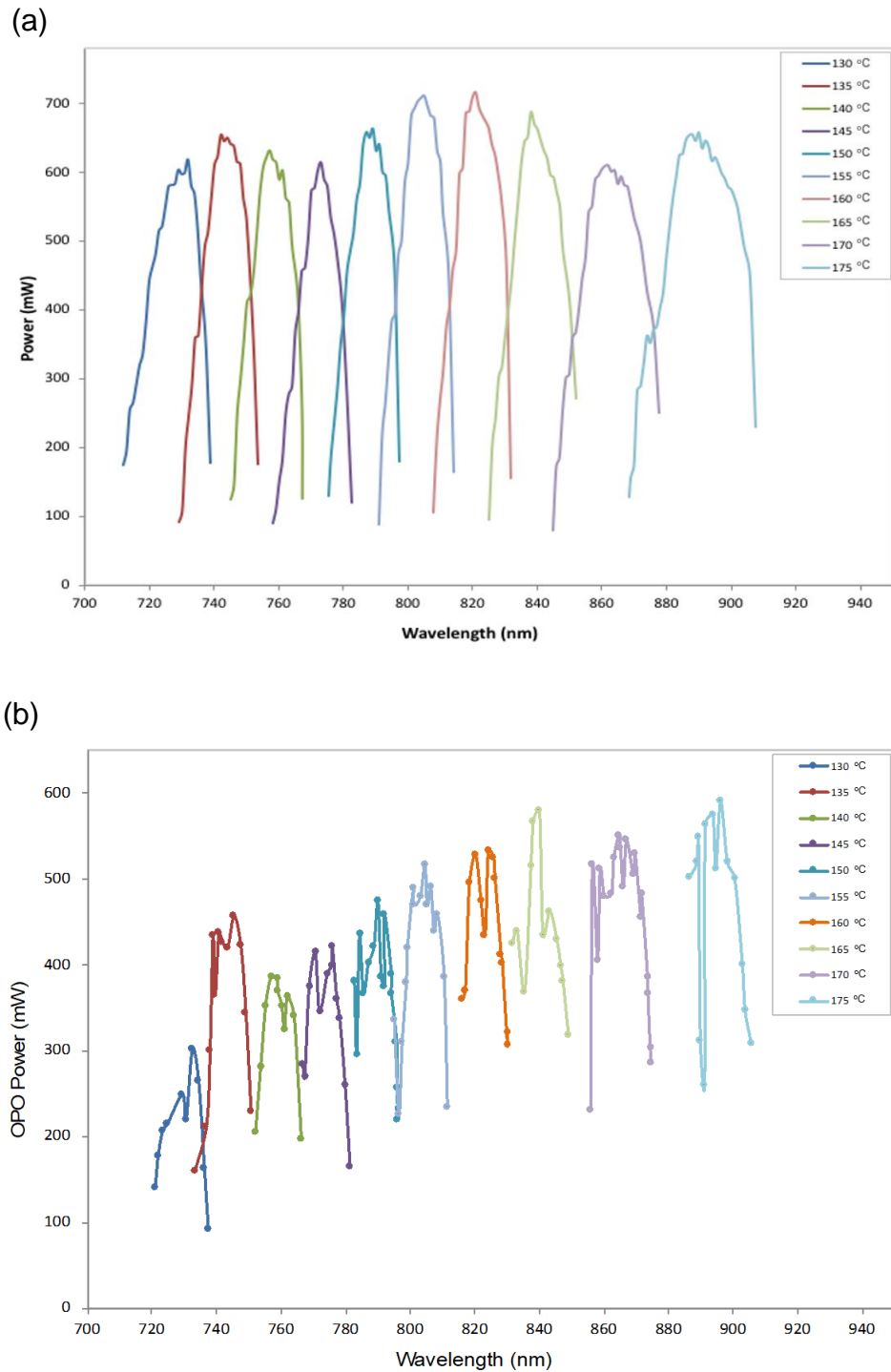


Figure 5.4: The OPO power as a function of the wavelength with fixed LBO temperature at 10 different temperatures: (a) with a modified cavity, and (b) with the original cavity.

Development of the OPO Cavity

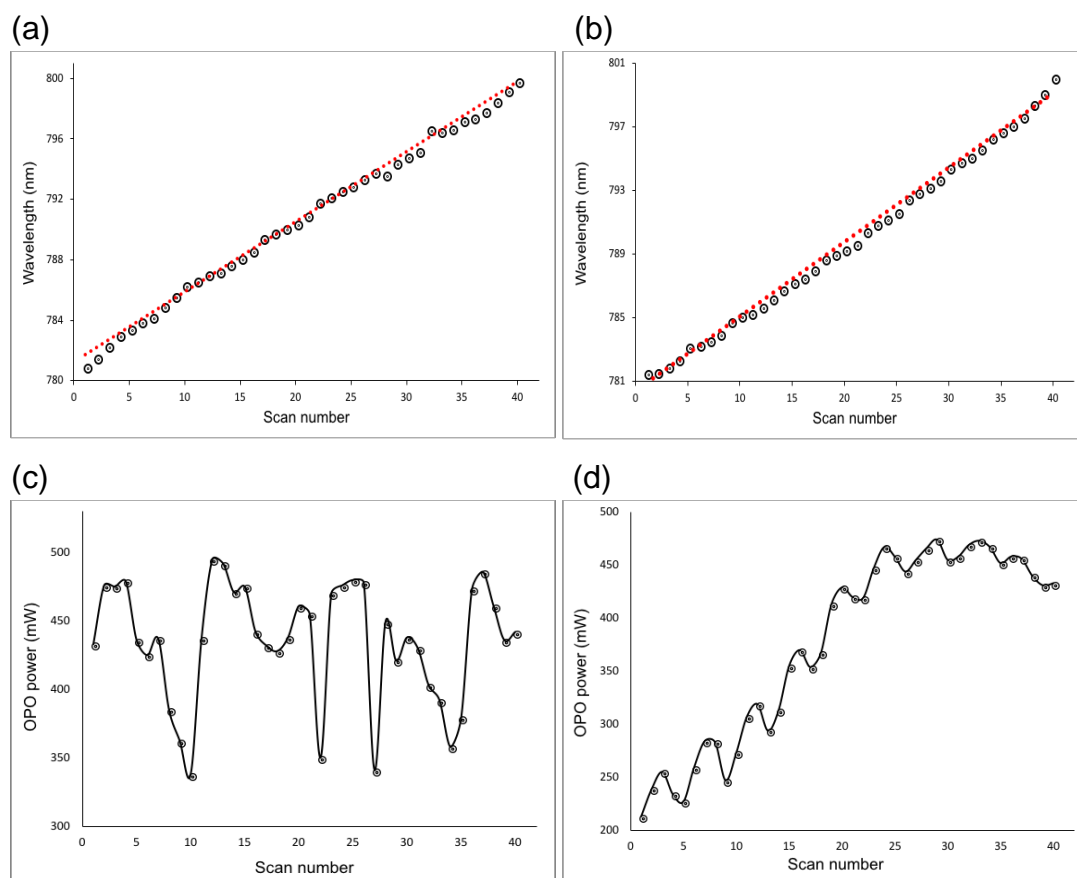


Figure 5.5: Assessing the performance of the OPO. (a) and (b) show the OPO wavelength tuning as a function of the scan number for the standard and new OPO design, respectively, where the dashed red line indicates the ideal tuning. (c) and (d) show the OPO power as a function of the scan number for the hyperspectral SRS stack with the conventional design at different temperatures, and with the new design at a fixed temperature of 152°C, respectively.

Finally, the performance of the piezo is investigated in this section. Figure 5.6 shows the piezo performance with both OPO designs. The new OPO design enhanced the piezo performance, which provided a separate wavelength with each piezo step and the relation between them is linear. The original design sometimes provided several wavelengths with the same piezo position.

Development of the OPO Cavity

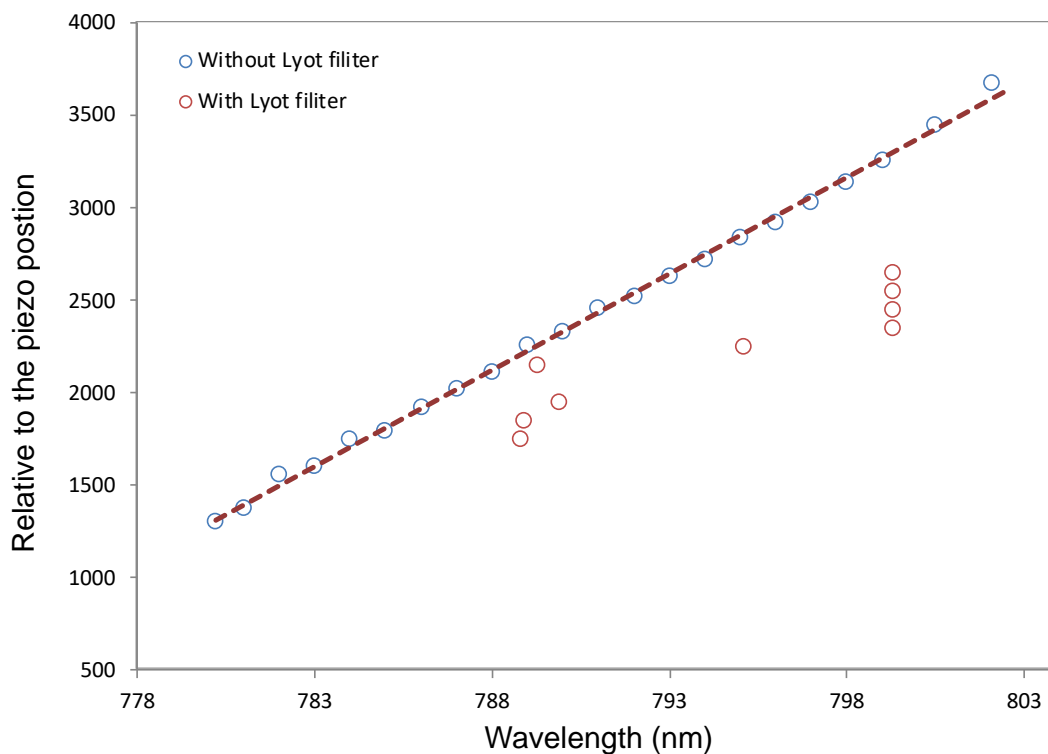


Figure 5.6: Assessing the piezo performance as a function of the wavelength with the Lyot filter at different temperature (red), and without the Lyot filter (blue) at a fixed temperature at 152°C.

5.5 Hyperspectral scanning software

During the course of this work, the new hyperspectral software was developed to allow rapid automatic wavelength tuning. This software has been written using Matlab (2018a) for controlling the OPO cavity (automatic tuning), and then integrating it with the Scanimage software. The Scanimage software is a free version, which is used to control a laser-scanning microscope. When running the programme, the user must determine the direction of the folder in the PC by browsing for where the images and the parameters text files are saved. The programme does not start scanning and recording data until the user sets up the required experimental parameters and clicks on the 'Start Scanning' button. This programme was constructed from multiple sections such as the COM port settings (serial port), the programme running controls,

Development of the OPO Cavity

indicators, main settings, the integrated Scanimage selected parts, the results section, and a large area montage. Figure 5.7 shows the hyperspectral software control panel for controlling the OPO cavity and is integrated with the Scanimage software for controlling the mechanical stage and the experiment parameters.

Wavenumber change setting: the user should input the required wavenumber (more comfortable to use) instead of the wavelength each time manually before starting scanning, and then click on Add Wavenumber. The wavenumber is then converted by the programme automatically to the correct wavelength in the OPO controller based on Equation 5.4.

$$\nu_{\text{vib}} = 1/\lambda_{\text{pump}} - 1/\lambda_{\text{Stokes}} \quad (5.4)$$

where ν_{vib} refers to the wavenumber, λ_{pump} refers to the tunable pump wavelength, and λ_{Stokes} refers to the Stokes wavelength fixed at 1,032 nm. For large numbers of wavenumbers, there is no need to input them separately. The user can save the whole wavenumber values in an Excel file and then import it by clicking on the Import Wavenumber button. To input new values, the user must clear the previous table by clicking on the Clear Table button or modify the values by double clicking on each value separately.

Piezo position: to obtain SRS hyperspectral stacks, the user should input the start piezo position and the last position to identify the initial frequency and the end frequency of the region of interest. The step size of the piezo position should also be selected to determine the amount of change in frequency and the number of images required. The piezo position ranges from 0 up to 4,095, and the piezo step size ranges from 0 to 100. Whenever the value of the piezo step is smaller, the SRS spectra become more accurate, but this is time-consuming.

Development of the OPO Cavity

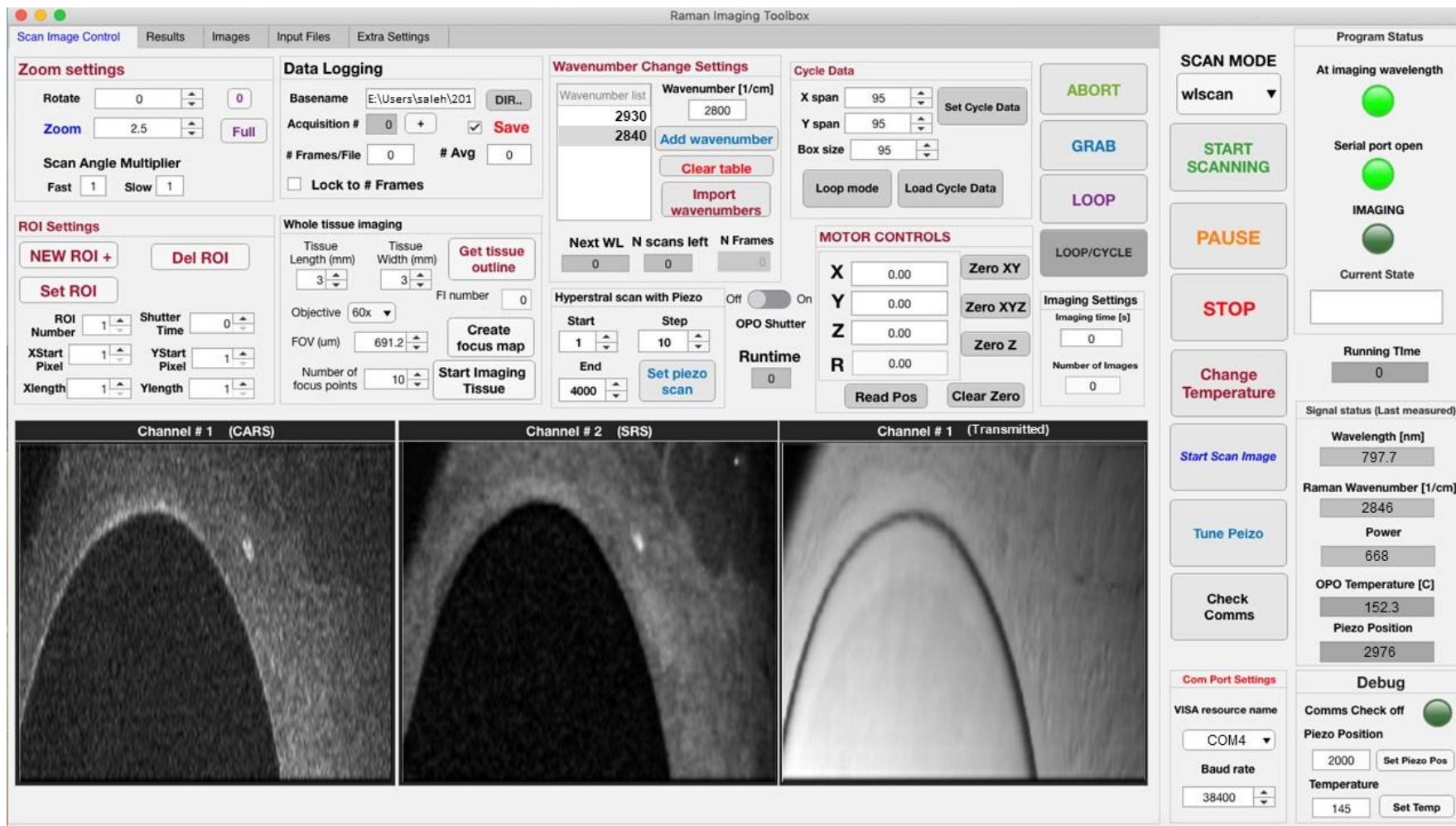


Figure 5.7: The control panel of the hyperspectral scanning software integrated with the Scimage software.

5.6 Performance of the hyperspectral software

5.6.1 Hyperspectral software with the original OPO design

This section features an investigation of the OPO performance with the original OPO design using the hyperspectral software. For the wavelength tuning, each OPO system has individual parameters provided by the APE Company. However, these parameters are variable over time. Therefore, all polynomial parameters of the LBO crystal temperature and the cavity length were extracted during this research. The user should choose the specific parameter files of the cavity length and LBO temperature after the programme has started running. The piezo position should be well centred to obtain the correct polynomial parameters for cavity length and temperature by tuning the system manually to 820 nm of the wavelength. Then, the piezo value should be set in the centre (about 2,000) compensated by the length micrometer screw to reach the maximum power. This procedure leads to the system being run with 820 nm of the wavelength again (see Figure 5.8).

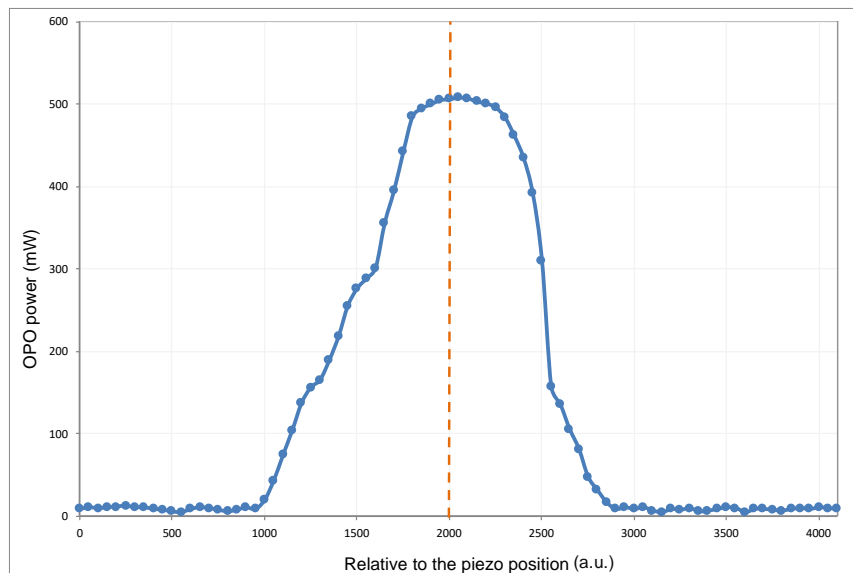


Figure 5.8: Schematic of the piezo central calibration, where the piezo central position is 2,000 with an 820 nm wavelength, which gives a maximum power of 508 mW. The dashed line indicates the piezo's central position.

Development of the OPO cavity

The polynomial parameters for the cavity length can be generated by tuning the system from 690 nm to 990 nm manually, e.g. in 10 nm steps, and writing down the piezo value for each wavelength (see Figure 5.9). The polynomial parameters for the temperature can be generated in the same way as for the cavity length. This can be created by tuning the temperature starting from 125°C to 180°C, e.g. in 5°C steps, and writing down the temperature value for each wavelength (see Figure 5.10). The polynomial coefficients are used for calculating the necessary phase matching temperature and relative cavity length for the input wavelength. Further, the parameters need to be constantly updated and listed in ascending order in the parameter file. After extracting the polynomial parameters, the following equations (Eq. 5.5 and Eq. 5.6) were applied in the programme to find the right position of the cavity length and crystal temperature. All of the figures were plotted using Excel 2017.

$$\text{Phase matching temp} = A\lambda^5 + B\lambda^4 - C\lambda^3 + D\lambda^2 - E\lambda + F \quad (5.5)$$

$$\text{Cavity Position (relative piezo Value)} = A\lambda^4 + B\lambda^3 - C\lambda^2 + D\lambda + E \quad (5.6)$$

Constant value	Phase matching temp	Cavity Position
A	$-3.335824 \times 10^{-10}$	-3.880585×10^{-8}
B	1.384736×10^{-6}	1.413513×10^{-4}
C	2.97379×10^{-3}	2.060849×10^{-1}
D	1.903513	1.455859×10^2
E	7.871061×10^2	-3.911923×10^3
F	1.296354×10^4	

Table 5.1: Constant values of the polynomial equations

Development of the OPO cavity

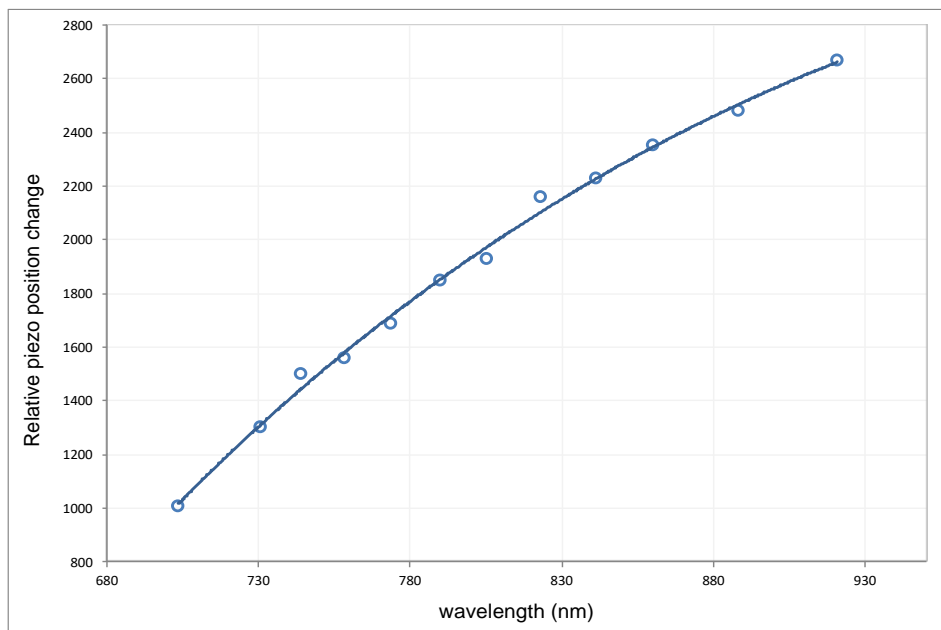


Figure 5.9: Relative piezo position change as a function of the wavelength for extracting the polynomial parameters of the cavity length.

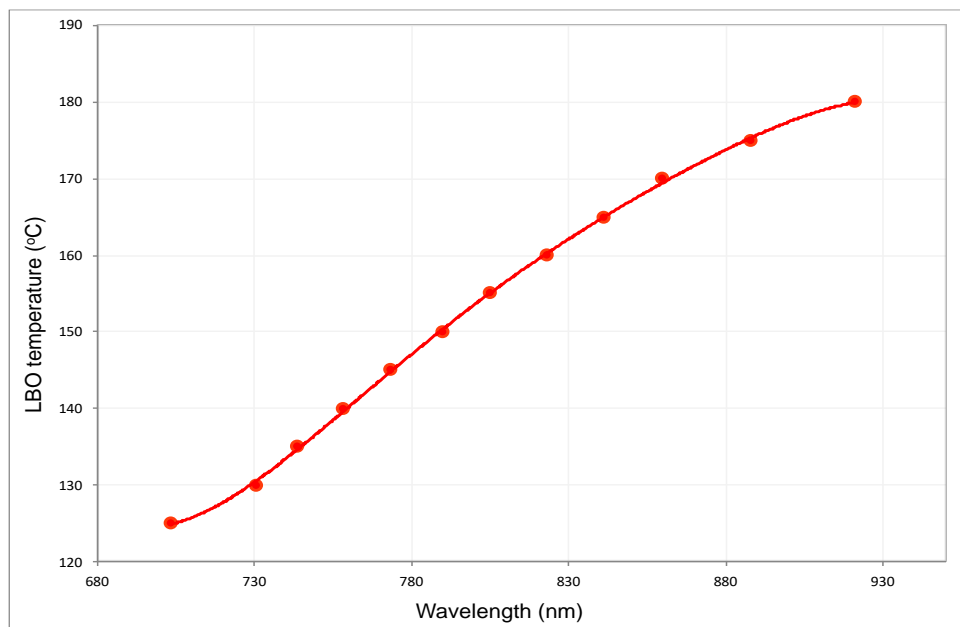


Figure 5.10: Typical tuning curve of the temperature when tuning the OPO-crystal pumped at 516 nm for extracting the polynomial parameters of the OPO crystal temperature.

Development of the OPO cavity

The hyperspectral software was designed to convert the three main steps of the wavelength tuning automatically in the original OPO design, as shown in Figure 5.11. In the first step, and without consideration of the wavelength, the programme optimised the OPO output power (maximising the power) by tuning the piezo voltage (i.e. changing the cavity length). To obtain the appropriate piezo position, the programme changed the cavity length for the requested wavelength based on the polynomial parameter file. The programme took the actual piezo position and the actual wavelength as a starting point. The actual piezo position is given as a value between 0 and 4,096 on the display, and the actual wavelength can be read from the OPO screen or from the control panel in the programme. However, at this stage, and because the cavity length and the temperature were not consistent for the same wavelength, it was possible to stop the OPO generation. Therefore, the programme moved to the second step to change the OPO crystal temperature (temperature lambda) depending on the polynomial parameter file. To reach the required temperature might take several minutes based on the amount of change in the temperature. Thus the temperature and the cavity length are re-established and the OPO generation is restarted. At every single temperature, there is a specific wavelength range spanning from 6 nm up to 10 nm. This can be achieved by changing the angle of the Lyot filter between -127° and $+127^\circ$, and the cavity length. However, some of the wavelengths are undetectable within this wavelength range, which means that accuracy of the temperature is necessary, as a variance of 0.1°C can make a difference. Also, there are several orders for the Lyot filter to access the same wavelength, with some giving more power than others, as shown in Figure 5.6.

If the requested wavelength is within the reachable range (i.e. about ± 5 nm), the Lyot filter is automatically turned by the programme to reach the requested wavelength (a narrow range of wavelength) without changing the crystal temperature. The Lyot filter changes the polarisation by only letting a narrow range of wavelength pass through it to the correct polarisation by going through the cavity in the right way. Then it takes the very narrow slice out, and the rest of that bandwidth does not make it around the cavity in the

Development of the OPO cavity

right way. Thus, the correct polarisation is significant in terms of making the photons arrive in the crystal at the exact same moment that the next new photons are coming into the crystal, by tuning the Lyot filter.

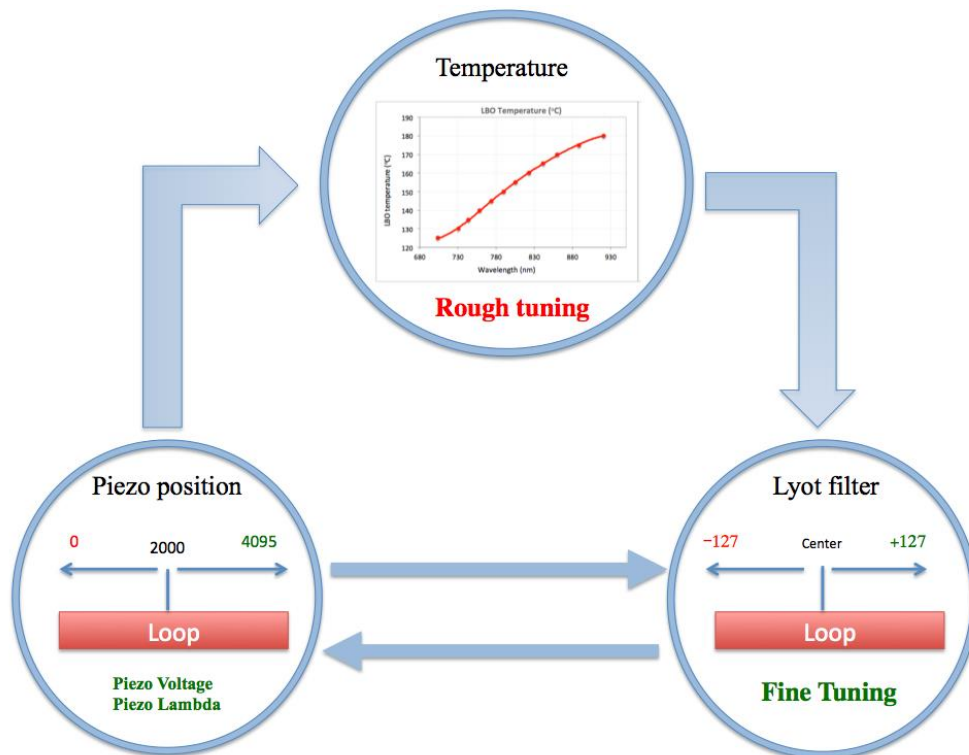


Figure 5.11: Schematic of the hyperspectral software steps with the original cavity for automatic wavelength tuning.

Based on the previous description, it can obviously be said that the programme depends on three steps to tune the wavelength automatically, in the following order: maximising the OPO power (piezo voltage, lambda), temperature lambda, and Lyot filter, which is a prolonged process.

5.6.2 Hyperspectral software with the new OPO design

Due to the slow process of the wavelength tuning in the standard OPO design, the hyperspectral software was successfully modified by reducing the wavelength tuning steps from three to two steps based on the modification in the OPO cavity. According to the description in section 5.4, the bandwidth of the LBO crystal was stretched to 20 nm wavelengths and a wavenumber of approximately 300 cm^{-1} , which was enough to cover the whole CH stretching vibration in the HWN region. This meant there was no need to change the temperature after adjusting it, which covered the region of interest. The wavelength was tuned by changing the piezo position only, which speeded up the tuning process. Moreover, the polynomial parameters of the cavity length and the LBO crystal temperature were not necessary with this version. After the user inputs the specific wavelength, the programme reads the actual wavelength and the piezo position and considers them the starting wavelength and position, respectively. Depending on the required wavelength, the piezo position will move in a positive or negative direction. The piezo position change in a positive direction leads to an increase in the wavelength, and it is reduced if the piezo position moves in a negative direction. The step size of the piezo position ranges between 0 and 100, where the maximum piezo value can tune the wavelength between 0.6 nm and 0.7 nm. Reducing the tuning steps from three steps to two, and modifying the software to fit with this development contributed to reducing the tuning consumption time from 58.8 seconds, with the conventional design, to only 1.67 seconds with the new design for each tuning step. The consumption time is the time required to tune the wavelength one step to the next wavelength (e.g. from 780nm to 781nm). This meant that the new OPO design offered a wavelength tuning which was 35 times faster than the standard design. Figure 5.12 shows the consumption time of the wavelength tuning step with both OPO designs at a fixed temperature at 152°C .

Development of the OPO cavity

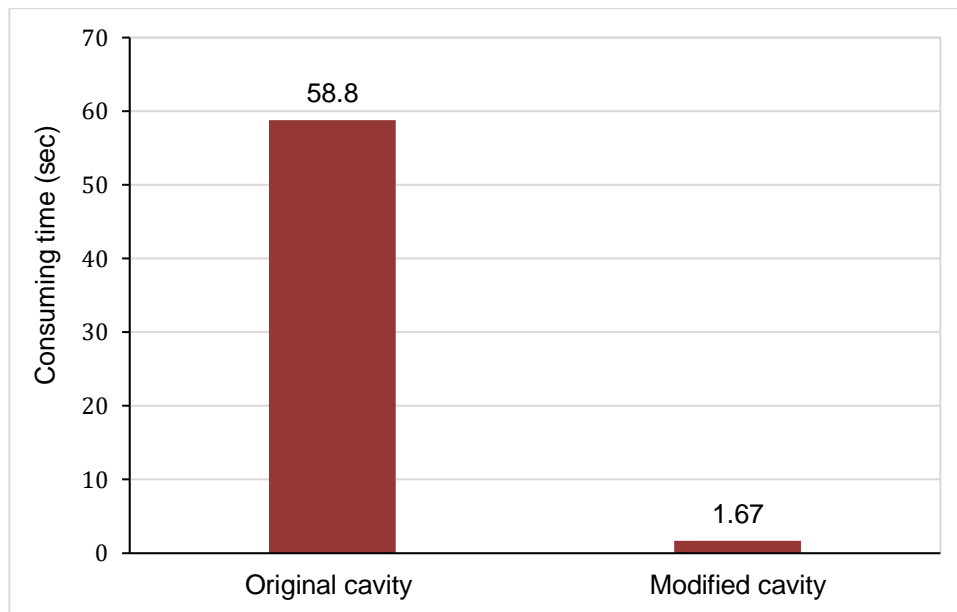


Figure 5.12: The consumption time of each wavelength tuning step with the original and new OPO designs.

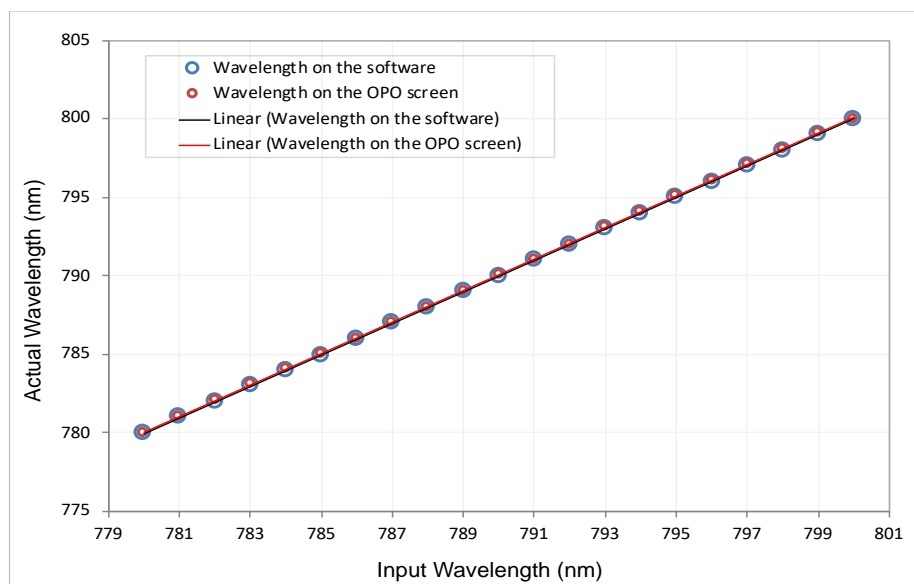


Figure 5.13: The reading of the wavelength tuning on the OPO screen (red) and on the software control panel (blue).

Development of the OPO cavity

To investigate the performance of the hyperspectral software with both OPO designs, polystyrene beads (PS) and PMMA beads were used as standard samples. The SRS hyperspectral stacks of both samples were acquired in the CH stretching vibration in the HWN region. Before doing this procedure, the accuracy of the wavelength reading on the OPO controller screen was compared with the reading on the software control panel. A perfect match in the wavelength reading was obtained, which meant that the software connected with the OPO controller in the right way (see Figure 5.13). The SRS images and spectra of the PS and PMMA in the CH stretching vibration region from 2,800 cm^{-1} to 3,100 cm^{-1} are presented in Figure 5.14.

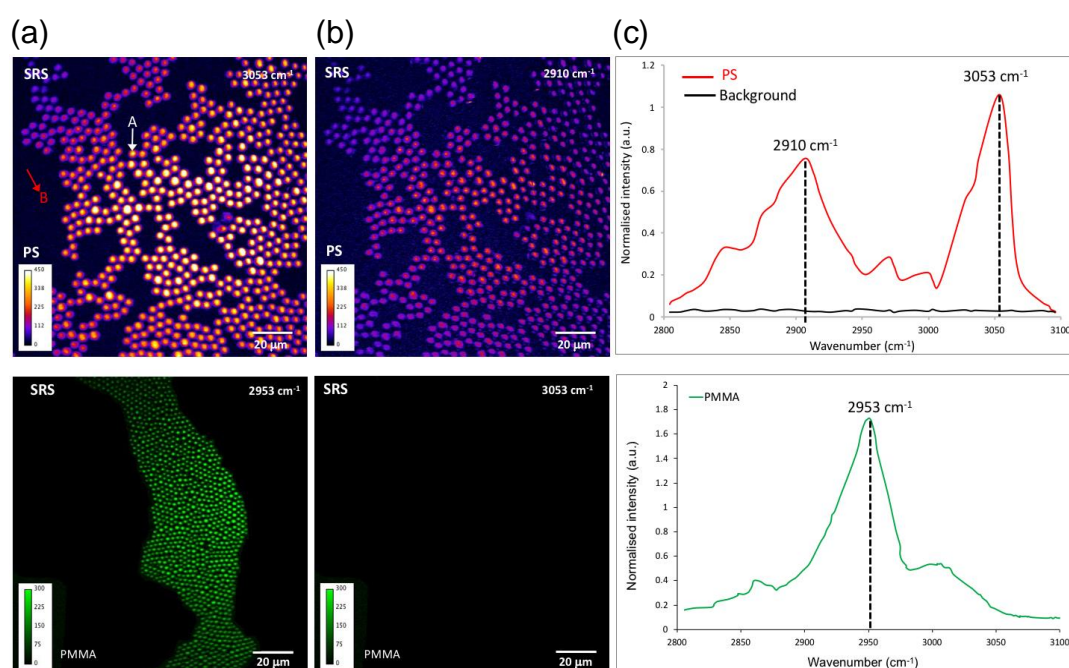


Figure 5.14: SRS images and spectra of the PS and PMMA beads. (a) shows the SRS images at the sharpest peaks of the PS at 3,053 cm^{-1} , and the PMMA at 2,953 cm^{-1} . (b) shows the SRS images for the same sample at the weaker peak of the PS at 2,910 cm^{-1} , which shows less brightness than the image in (a), and the PMMA at the same frequency, which shows nothing. (c) shows the SRS spectra of the PS (red) at Point A and the background substrate (black) at point B and spectra of the PMMA (green).

Development of the OPO cavity

The sharpest peaks were found at $3,053\text{ cm}^{-1}$ for the PS and $2,953\text{ cm}^{-1}$ for the PMMA. The software needed to acquire 44 hyperspectral SRS images to cover the whole region of interest, with a size of 50 for the piezo step, where the number of images is changeable depending on the size of the piezo step, as mentioned earlier. The SRS spectra were compared with the Raman spectra for the same samples, which fully match with the spectra available from the Raman system for the same samples (see Figure 5.15).

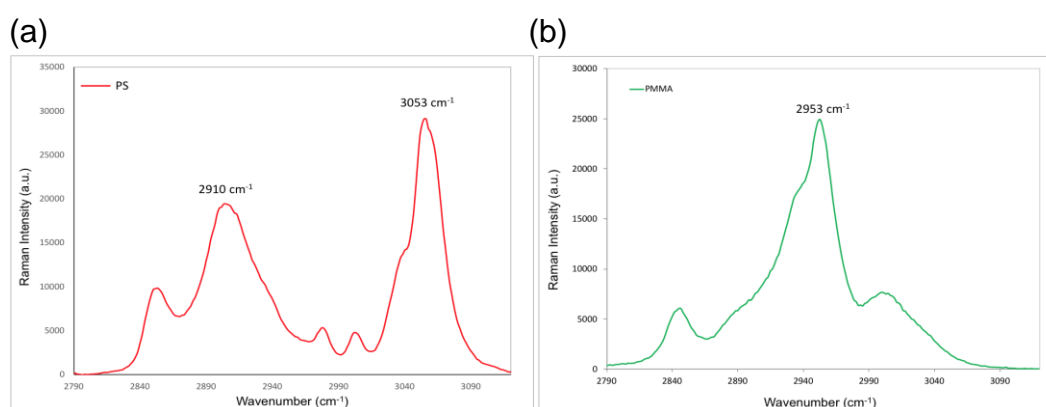


Figure 5.15: Raman spectra of the PS (a) and PMMA (b), where the sharpest peak of the PS is at $3,053\text{ cm}^{-1}$, and at $2,953\text{ cm}^{-1}$ for the PMMA.

The total consumption time that the software took to scan the whole CH stretching vibration region was more than 46 minutes with the original cavity, which meant approximately 1.05 minutes for each frame. With the modified cavity the total consuming time was significantly decreased to less than 4.5 minutes, which meant only about 5.9 seconds for each SRS image. The same parameters were used for both experiments. Figure 5.16 shows the comparison of the total consumption time recorded by the hyperspectral software between the two OPO designs.

Development of the OPO cavity

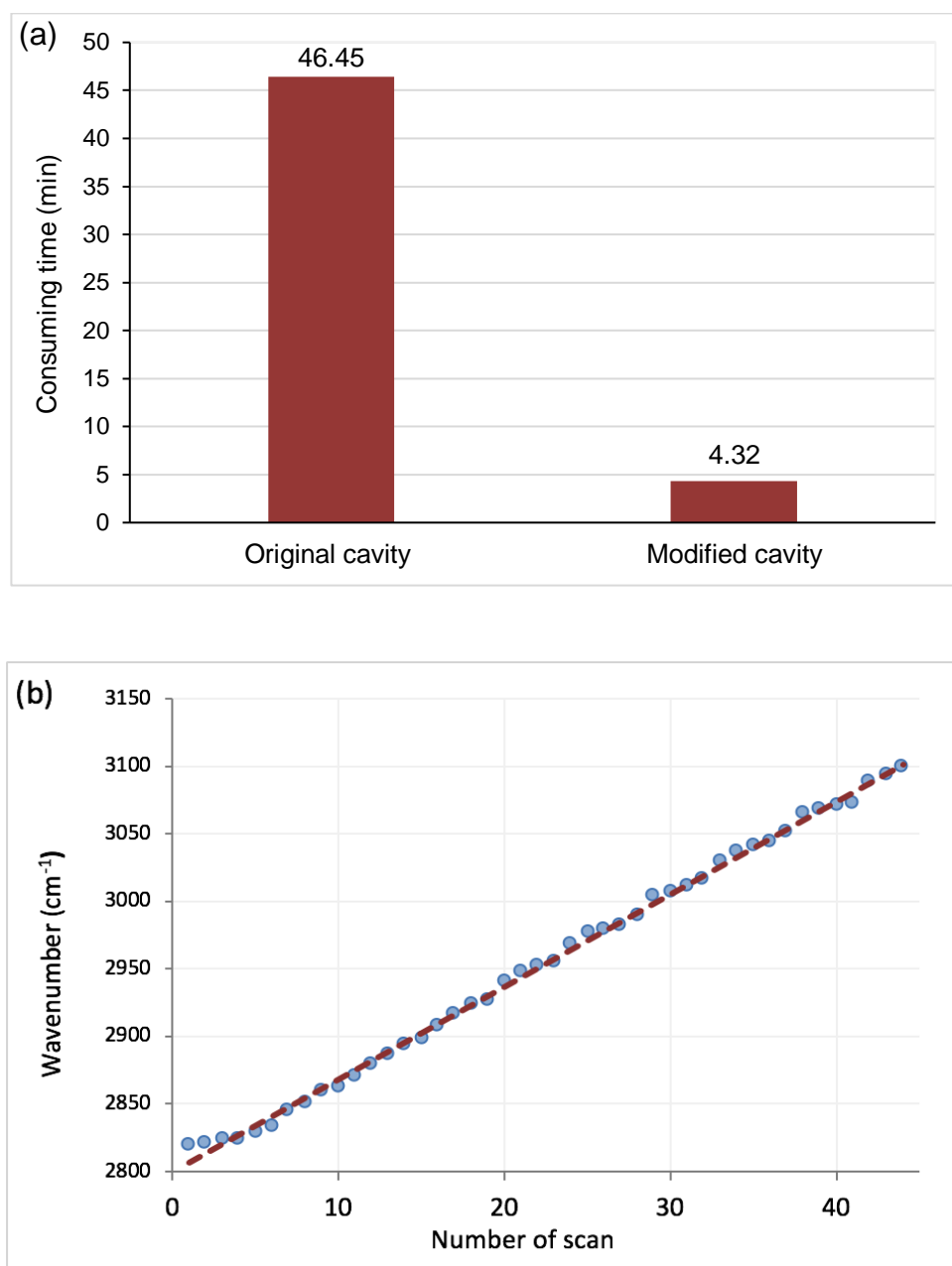


Figure 5.16: Assessing the performance of the software with the two OPO designs. (a) shows the total consumption time of the OPO tuning the high wavenumber region; and (b) shows the wavenumber produced by the OPO as a function of the scan number. The dashed line shows the ideal wavelength tuning as a function of the number of scans.

5.7 Summary

In conclusion, this chapter presents the modification that was made on the OPO cavity for rapid wavelength tuning, which is one of the main purposes of this study. The difference between the pump and the Stokes beams was necessary to produce the SRS signal. The Stokes beam was fixed at 1032 nm while the pump beam was tunable between 690 nm to 990 nm. Thus the OPO was responsible for the wavelength tuning that depends on the three mechanism steps (crystal temperature, Lyot filter, and cavity length), which caused the delay in the tuning. The phase matching of the bandwidth of the crystal was between 6nm to 10 nm. The CH stretching vibration in the HWN ($2800\text{ cm}^{-1} - 3100\text{ cm}^{-1}$) is the ROI in this study, needing about 20 nm to cover it. The OPO was modified by installing a new dispersion block to the OPO cavity. The dispersion block provided different wavelengths that had different reflective indices in the material. This modification led to an enhancement of the OPO performance by stretching the crystal bandwidth to 20 nm (300 cm^{-1}), which was enough to cover the whole CH stretching region. Also, it led to a reduction in the wavelength-tuning routine that depended on only two mechanisms, crystal temperature and cavity length.

To make this approach work more effectively, hyperspectral software was written using Matlab to automatically control the OPO cavity. This software was integrated with the Scimage software, which was used to control the scan unit in the microscope. The performance of the hyperspectral software was investigated by acquiring a hyperspectral stack using two standard samples of PS and PMMA beads. All polynomial parameters for the OPO system were provided by the APE. However, due to the variability of these parameters over time, these parameters of the LBO crystal temperature and the cavity length were successfully measured. Using these parameters with the modification made on the OPO caused a speeding up of the wavelength tuning 35 times faster than of the conventional OPO with more stability. Finally, SRS spectra of the PS and PMMA were extracted and compared with the Raman spectra and found a good agreement between these two

Development of the OPO cavity

techniques. The whole hyperspectral stack was required less than 4.5 minutes with the modified OPO cavity compared to more than 46 minutes with the conventional cavity.

Chapter 6

The Development of Coherent Raman Imaging

6.1 Introduction

Coherent Raman imaging techniques, including CARS and SRS microscopy, allow for the rapid chemical imaging of biological samples with high resolution and without requiring staining or labeling [179]. However, the CARS process suffers from a nonlinear non-resonant background, which makes it unable to provide specific chemical information. SRS has a major advantage over CARS in that it is free from the non-resonant background and it is easy to interpret the chemical contrast and extract the SRS spectra that match with the Raman [179]. The focus of this chapter is on the method used to acquire hyperspectral SRS data, which allows for the rapid extraction of the SRS spectra based on the development of the OPO and hyperspectral software as mentioned in Chapter 5. This chapter also features the development that was applied to the microscope to improve its performance in terms of providing high quality images using the SRS technique to create a large area montage. This approach will contribute to the ability to orientate the montage against the

The Development in Coherent Raman Imaging

pathology images of the gold standard method (hematoxylin and eosin, H&E) for the comparison.

A novel method was performed to solve the curvature effect on the sample when acquiring a large area montage, which was the main contribution in this chapter.

The author's contribution in this chapter:

1. All work described in this chapter was performed by the author.
2. All clinical samples used in this chapter were provided by the pathologists in the Gloucestershire Hospital.

6.2 Coherent Raman imaging

Coherent Raman scattering techniques (CRS) including CARS and SRS have opened a new window for the imaging of biological specimen without any labeling [179]. The large signal is generated as a result of the coherent addition of a CRS field from the vibrational oscillators in the focal volume, which allows for molecular imaging at high speed. Ultrashort laser pulses with ultrafast strong peak power are required for efficient signal generation in coherent Raman microscopy [180]. The CARS and SRS signals increase by increasing the laser power. However, a plasma might be generated through multiphoton processes as a result of the strong intensity at the focal centre, which might contribute to damaging the biological sample [65]. An additional reason that might cause the destruction of the biological sample is the vibration absorption that occurs in the CRS microscopy through coherent Raman processes. Therefore, equilibrium between the amount of required signal and minimising photodamage should be achieved.

6.2.1 Laser power estimation

To acquire images, the laser power should be measured before every scan to avoid photodamage as a result of the instability of the power output from the OPO. In the coherent Raman scattering setup, the suitable places where the laser power can be measured are on the bench before the scan unit, and after the scan unit before the objective lens. The power loss estimation through the bench, scan unit and objective lens is required to measure the power at the specimen. Figure 6.1 shows the comparison of the time averaged power measurements before and after the scan unit. It is clear that the relationship between these two curves is linear. The wavelength was fixed at 798 nm (2841 cm^{-1}) in the OPO, where the maximum power was achieved at this wavelength. Figure 6.2 shows the transmission through the Olympus 60X water objective lens provided by the manufacturer.

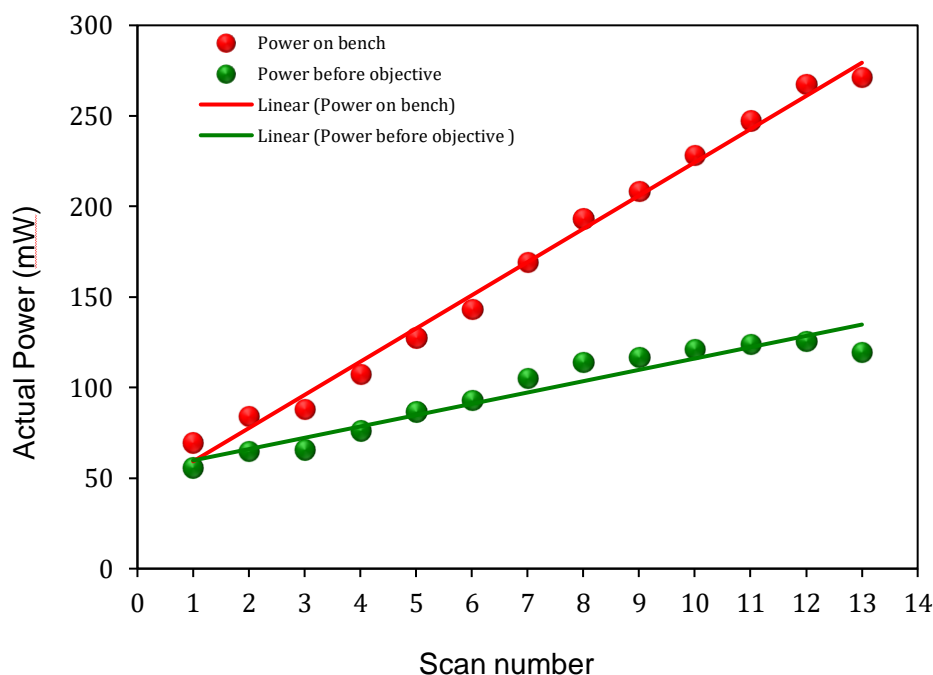


Figure 6.1: Time averaged power measurement, measured on the bench before the scan unit (red) and after the scan unit (green).

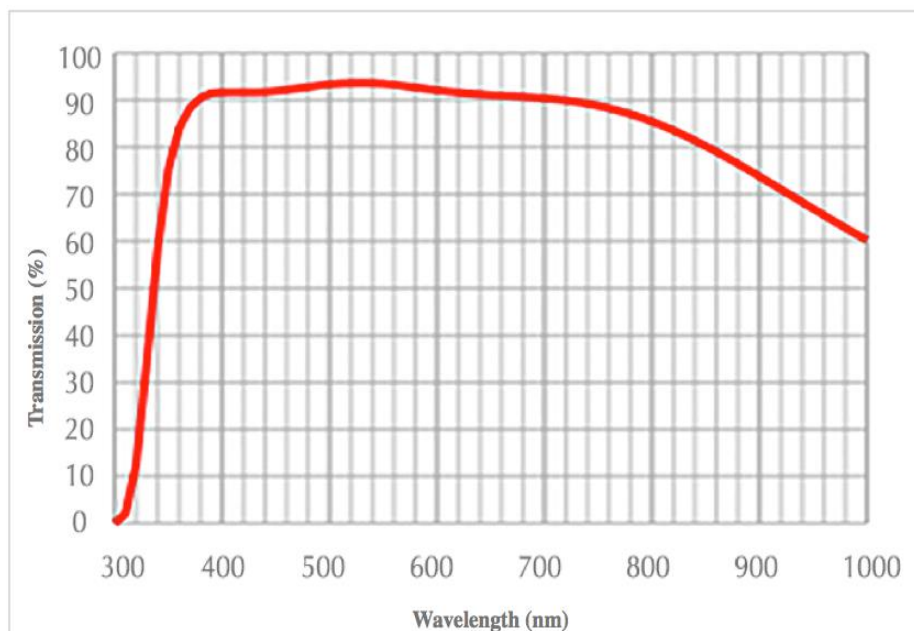


Figure 6.2: Transmission through the Olympus 60X water objective lens, data provided by manufacturer [181].

6.2.2 Laser damage threshold

The high peak power of the pulse laser is the major source of photodamage, which arises from multiphoton absorption in the biological specimens. Therefore, excitation intensity has to be maintained low enough to keep the laser power under a certain threshold. However, there is a scarcity of studies of the laser power threshold and photodamage in CRS techniques with a 2ps pulse laser and 76 MHz repetition rate. There are only two studies which have been found in the literature that present the mechanism of photodamage in CARS microscopy without any evidence for the laser power threshold [182]. Recently, another study of laser damage has been done using the same CRS setup that is used in this thesis, which found that the photodamage starts at 122 mW pump power, but without a guarantee that is the laser power threshold point [170]. Therefore, studying the laser power threshold was necessary. In this section, an experiment that was conducted to estimate the

The Development in Coherent Raman Imaging

laser power threshold from the coherent Raman setup with both pump and Stokes beams, to avoid any photodamage of biological tissues, will be highlighted.

Exposing a biological sample to a laser beam with high laser powers may cause photodamage. Reflection, scattering, absorption or transmission to the surrounding tissue can occur when the laser light hits the tissue. Scattering, reflection and transmission are highly controlled by absorption and the wavelength is the main determinant of absorption. Generally, three different main types of mechanism can be classified as laser induced damage: photochemical, photothermal and photomechanical [183].

Photochemical damage can be the result of the light inducing chemical effects and reactions within macromolecules or tissues, which allow the reactants to receive energy as photons. The light consists of photons, where the reaction starts with the absorption of these photons. When the energy is being absorbed by the reactant molecules, it leads to movement of the molecule from a relaxed state to an excited state, where the physical and chemical properties of the molecule vary from that of the original molecule. The molecule in the new excited state may convert into new structures by altering its structure or via combination with other molecules. The laser parameters (especially the wavelength) play a significant role in the radiation distribution inside the tissue, which is primarily specified by scattering. In most cases, this type of photodamage does not occur in the red and near infrared wavelengths, because of their low absorption and resulting deep penetration in the tissue. In other words, visible wavelengths and ultraviolet (UV) are responsible for this kind of damage [183, 184].

A photothermal mechanism is a form of chemical reaction, which can be the result of the transformation of absorbed light energy into heat that called “thermolysis” or a “thermal decomposition reaction”. This leads to an increase in the local temperature in the sample and most of the damage that appears on the samples used in this thesis were of this type. A thermal reaction mainly

The Development in Coherent Raman Imaging

depends on the chemical decomposition of a substance when the heat energy is applied. The decomposition temperature is the temperature at which the chemical reaction initiates. The reactants usually demand heat energy so as to break down the chemical bonds between the atoms of the molecule, which undergo the decomposition. Therefore, thermal reactions are often endothermic. Thermal damage usually spreads to tissue adjacent to the ablation crater with the long pulses [183, 184].

The key difference between the two types of damage is in a photothermal reaction the reactants obtain energy as heat, while a photochemical reaction is where the reactants obtain energy as photons. Therefore, these two reactions vary from each other based on the energy source. Furthermore, there is no direct affect by light on photothermal reactions, however, the temperature directly affects them. While, the temperature does not directly affect photochemical reactions, whereas the light directly affects them [183, 184].

Normal oesophagus tissue was used to assess the photodamage (see Figure 6.3 (a)). In this experiment, transmitted light stack images in the coherent Raman microscope were acquired at different powers. The Stokes beam was blocked and only the pump beam was used at a wavelength of 798 nm, where the highest power was generated.

The stack images were each taken at 10 mW steps in the pump power, which increased from 120 mW up to 170 mW. The tissue area was scanned 50 times to replicate the amount of laser exposure in a typical hyperspectral stack. The colour time scale feature in Fiji was used to vary the images per stack to show the stage of damage growth and the number of images before damage appeared. Assessing the laser power effect on the tissue was investigated at the beginning of scanning and after 10, 30 and 50 scans. The damage in images A to D in Figure 6.3 (a) is displayed in a different colour to the rest of the tissue. The difference between the beginning and the end

The Development in Coherent Raman Imaging

images is displayed in image E, where the white dashed circle determines the regions of tissue damage. For further clarification, a composite of the first and the last images is displayed in branch F to highlight any changes in tissue morphology. As the number of scans increases, the laser damage becomes more apparent as a hole, and significantly grows in size. Several scans were done with a different power below 120 mW (not shown here), in which no photodamage appeared. The first photodamage appeared at the pump power of 130 mW; however, the exact damage threshold is difficult to determine as it depends on the kind of sample being measured.

This experiment was repeated with the Stokes beam while the pump beam was blocked. The maximum Stokes power achievable was 116 mW, so the possibility of getting photodamage is almost non-existent (see Figure 6.3 (b)). For the SRS measurement, two laser beams were focused on the specimen, which meant that the threshold power had to be reduced to half. Figure 6.4 shows the dependence of photodamage percentage at different pump powers based on the images in Figure 6.3 (a). Laser damage did not appear at under 120 mW pump power, while about 5% of the sample was damaged at 130 mW pump power, and this increased significantly to 55% at 170 mW pump power.

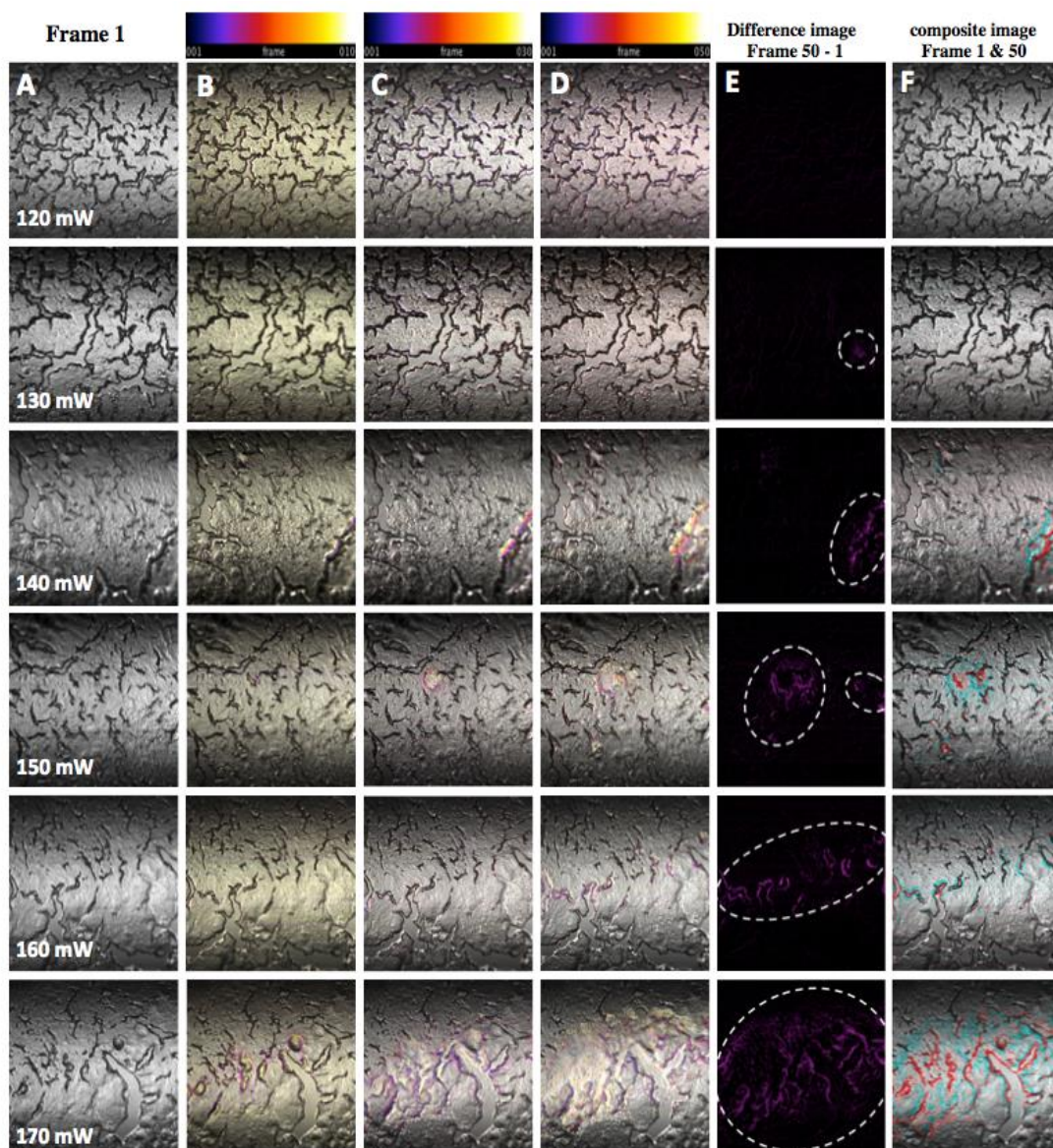


Figure 6.3 (a): Transmitted light images used to study the photodamage on a biological sample using different pump powers. (a) First scan, (b) at 10 times scan, (c) at 30 times scan, (d) at 50 times scan, (e) difference between the last and the first scan, (f) composite image of the first and the last scan. The first laser damage appears with pump power at 130 mW.

The Development in Coherent Raman Imaging

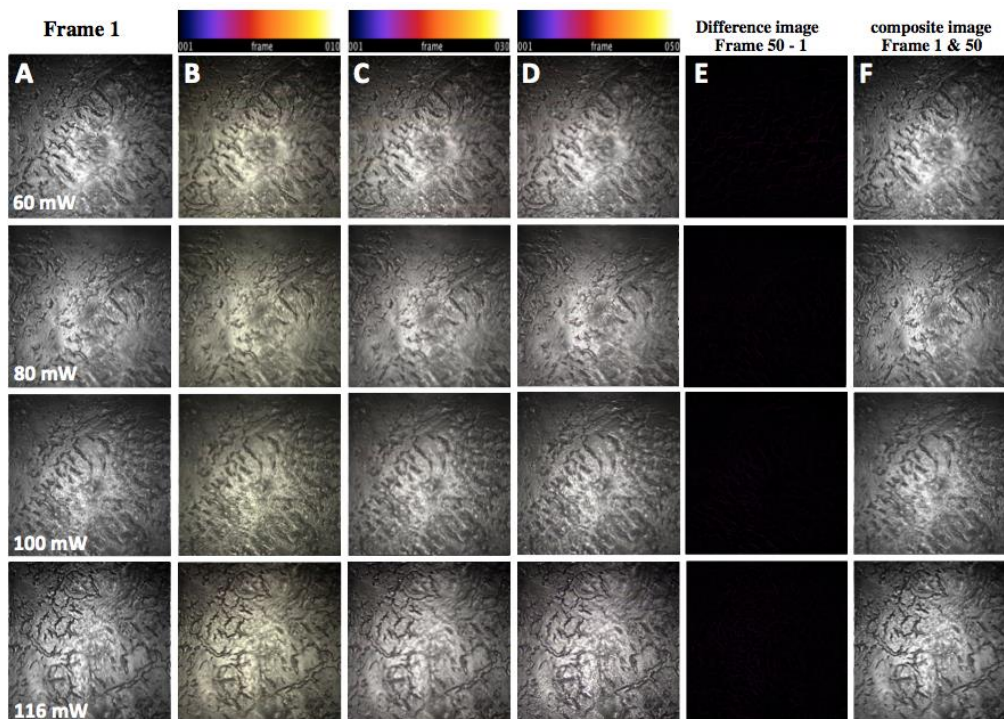


Figure 6.3 (b): Transmitted light images to study the photodamage on a biological sample using four different Stokes powers. (a) First scan, (b) at 10 times scan, (c) at 30 times scan, (d) at 50 times scan, (e) difference between the last and the first scan, (f) composite image of the first and the last scan.

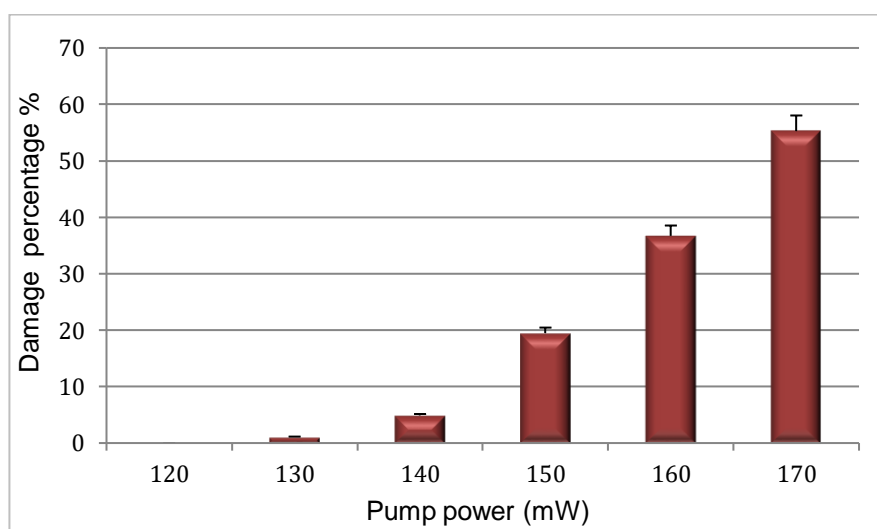


Figure 6.4: Dependence of photodamage percentage on the actual pump power from 120 mW up to 170 mW, where the power was measured before the scan unit.

6.3 Large area montage

Optical imaging techniques are considered very necessary in medical diagnostic applications designed to discover endogenous disease indicators as well as morphological tissue variations by allowing rapid, noninvasive image acquisition merged with deep tissue penetration and high-resolution. In the diagnostic routine, it is very important to image a large tissue section with sizes ranging from millimeters up to numerous centimeters for comparison, and the ability to orientate it against the pathology images of the gold standard method (H&E). However, the field of view (FOV) of a microscope is limited by the numerical aperture, required magnification and zoom factor, which do not fit larger biomedical specimens, where the zoom factor is the factor that controls how much the magnification changes by decreasing the apparent angle of view of a digital image controlled by Scanimage software. Therefore, the mosaic grid of images is adopted to overcome the FOV limitation in CRS images by obtaining a series of tiles and then rearranging them into one frame, thereby creating a large overview image with high resolution. Figure 6.5 shows the field of view using the target sample scale (THORLABS, R1L3S2P), with the different objective lenses from the forward and backward direction in the microscope.

When creating a large area montage using CRS techniques, there are two main experimental issues that usually occur. First, the space between the two coverslips is considered a major issue that affects the quality of the large area montage. The coverslips spacer thickness should fully correspond to the thickness of the tissue section to avoid the microscope curvature. The microscope curvature of the coverslips can occur from one or both sides, even with a small difference in thickness. This curvature leads to making the imaging plane within the coverslips in one place and in the biological samples in another. Thus, to obtain an image of the large area with such a curvature, the imaging plane should be deep enough into the tissue section to prevent the image plane from departing from the tissue. This normally leads to low quality images. Even if the mosaic image was obtained at a sufficient depth,

The Development in Coherent Raman Imaging

the individual images would match the different actual plane of the biological tissue as a result of the curvature. The coverslips' curvature effect of the imaging plane focusing is presented in Figure 6.6. Thus, to simplify an image interpretation, this issue should be corrected, which would improve not only the image's appearance but also its diagnostic value.

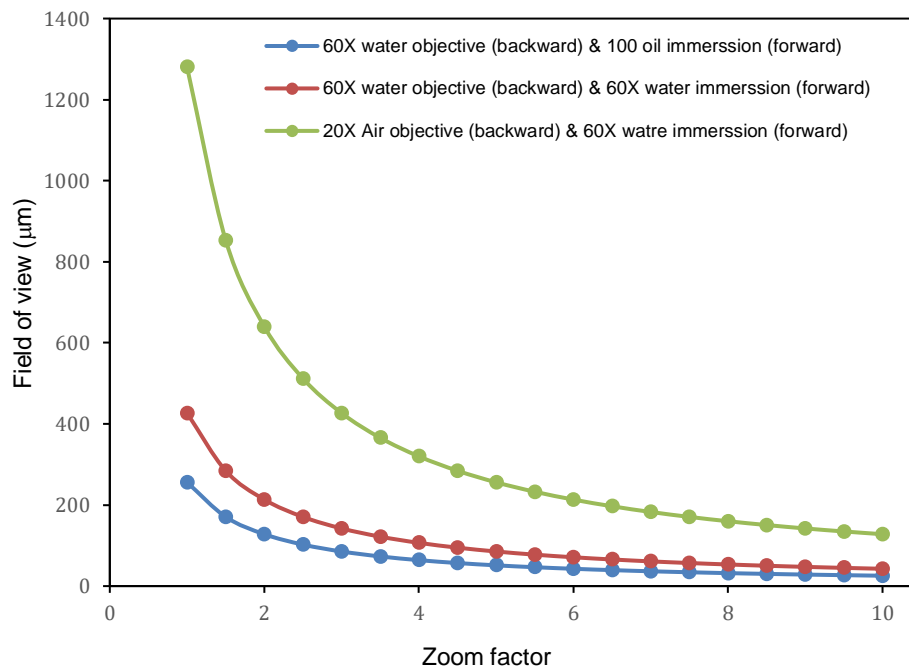


Figure 6.5: The field of view as a function of the zoom factor with two different objective lenses (20X and 60X) in the backward direction and two different objective lenses (100X and 60X) in the forward direction.

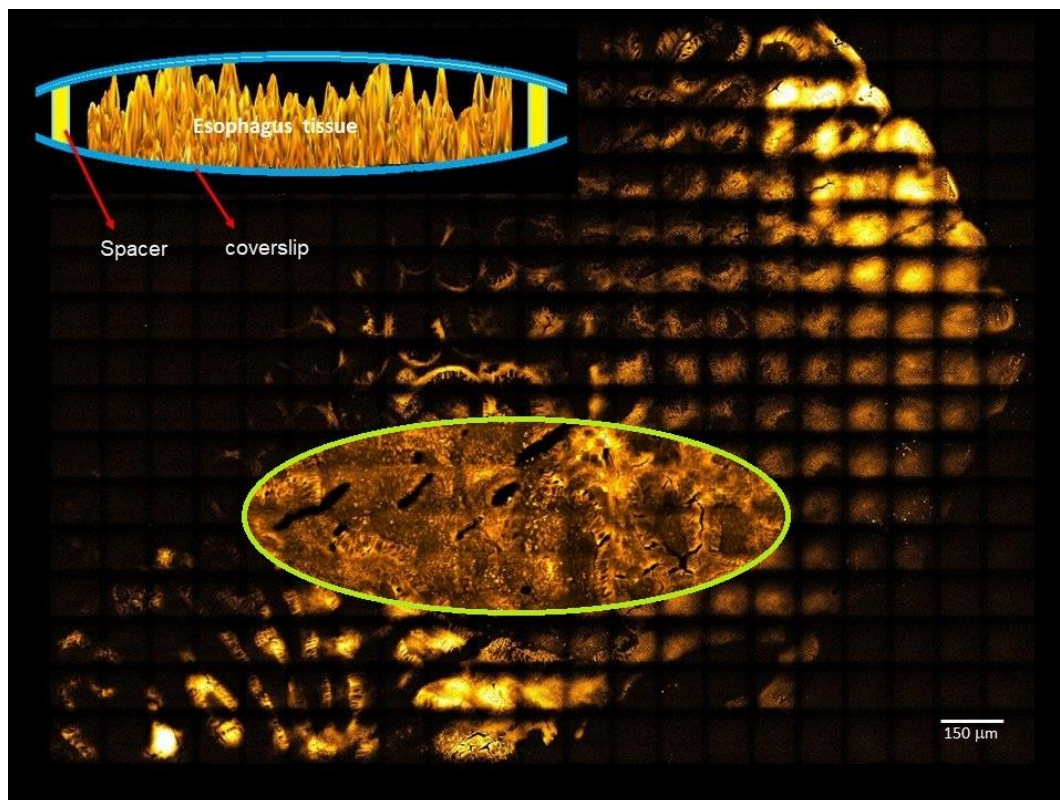


Figure 6.6: The coverslip curvature effect on SRS mosaic images. The top left sketch is a demonstration of the coverslip curvature resulting from the thinner coverslips and the uneven flat tissue surface. The green ellipse indicates the in-focus, and the rest of the image is the un-focus of the imaging plane.

One of the main aims of this part of the study was to find a method to solve the curvature effect on the sample automatically. The Scanimage software allows for the creation of a large area montage using cycle mode control. However, the user must input the coordinates of each tile individually, which is painful and time consuming. Therefore, a new Matlab script was written to readjust the image focus and acquire a large area montage at different frequencies automatically. In this approach, a 20X objective lens with a 2 zoom factor that provides a large FOV ($630 \times 630 \mu\text{m}^2$) was used first to obtain the outline tissue. The sample estimated size, the zoom factor, the objective lens and the pixel bin factor needed to be input by the user manually

The Development in Coherent Raman Imaging

before starting scanning. Figure 6.7 shows the procedure to refocus the map to acquire a large area montage with high quality.

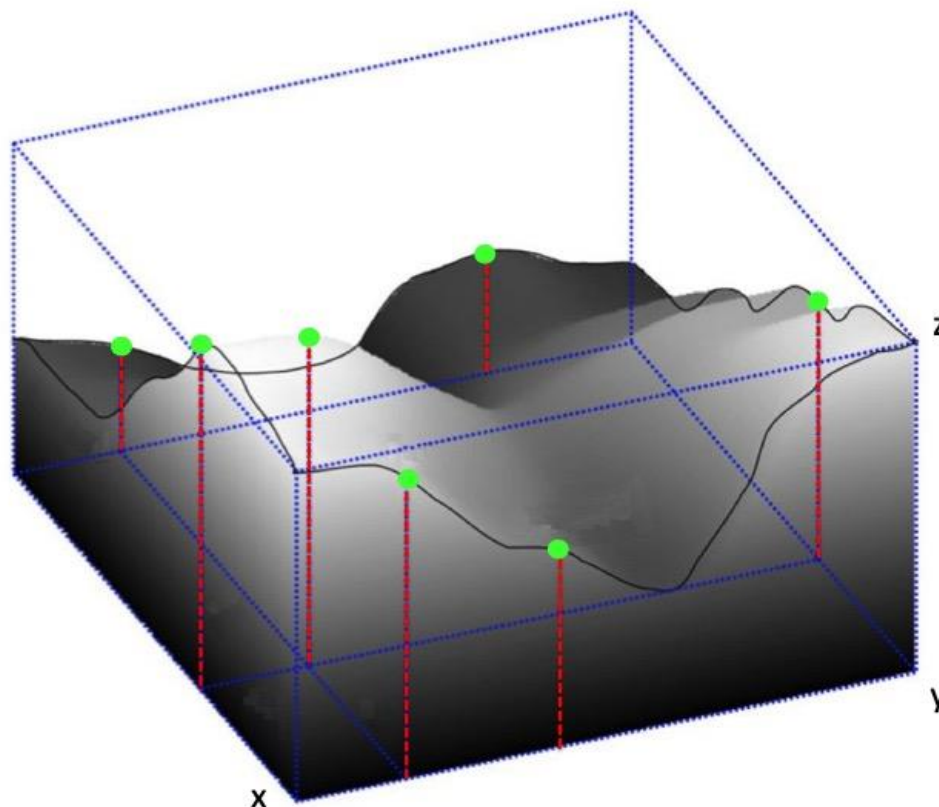


Figure 6.7: An illustration of the process of acquiring a large area montage by readjusting the brightness of tiles. The green spots indicate the focus points, and the dashed red lines indicate the difference in Z-positions.

The motorised stage is controlled by the programme and synchronised with the microscope to acquire images at different (x, y) coordinate positions. The programme will then acquire a series of tiles using the transmitted light channel and the fastest speed of scan without concentration on the resolution of the image. Then, the stitching of all of the tiles is applied in the right order to obtain a large area montage and display it in a new window. The user then should select the boundaries of the sample where the programme automatically saves it in a text file. This step can help to avoid the time wasted caused by imaging the undesirable area surrounding the sample. Also, this

The Development in Coherent Raman Imaging

method can be used to select small regions of interest in the sample without needing to image the whole sample, if that is required.

For high-resolution images, a 60X objective lens, 2.5 zoom factor with 200 x 200 μm^2 FOV (512pixel x 512 pixel), and 80-pixel bin factor (10 μs / pixel) were used in this study. It was easy to switch between the 20X and the 60X objectives by rotating the objective holder manually from the backward direction in the microscope. The FOV is automatically calculated based on the data that is presented in Figure 6.5. Due to the space between the two coverslips, the focus map is required to adjust the brightness of each tile. The user needs to click on the create focus map button in the control panel to start focusing. Based on the coordinates that were saved in the first step, the programme will move the motorised stage to the first coordinate position (X_0 , Y_0 , Z_0), and this allows for the user to readjust the brightness by changing the z-position, and then moves to the second tile position automatically, and so on. The coordinate positions of each tile (X, Y, and Z) are saved automatically once the programme moves from the current tile position to the next one. Each tile only needs a few seconds for adjustment. At the end of this step, the coordinates of all of the tiles are saved in text file form in the folder identified by the user before running the code.

The final step is to acquire the large area montage with high resolution. By loading the coordinate positions text file to the cycle mode in the Scanimage and inputting the different frequencies and clicking on the start scanning button, the programme will first tune the frequency and then start imaging the selected large area based on the saved coordinates file. The user should identify the folder where the images are saved before running the code. When the programme has finished imaging the last tile with the first frequency, the frequency is automatically changed to the second frequency, and the motorised stage goes back to the first coordinate position synchronously. When the accurate frequency and the right position are adjusted, the programme will start imaging the same large area for the second time with a different frequency, and then repeating the same steps with the other different frequencies if required.

The Development in Coherent Raman Imaging

Having acquired the high-resolution images of the large area at different frequencies, the final stitching is carried out using Fiji software and plugin (Stitching – Grid: collection stitching). The user should give the Grid/Collection Stitching a clue of what the layout of the tiles is in order to reduce the computational effort significantly and make it much more likely to succeed. There are several types of image collection that can be used, and each kind has several subtypes that the user can choose from. In this work, the row-by-row type was selected to match the same imaging order in the microscope, one line after the other, and the images were arranged in a grid, with each line always starting in the same position as the previous line. The grid size in the x and y direction should be defined by the user to find out how the input tiles are arranged. A rough estimate of the tile overlap needs to be input by the user before creating a grid stitching and the tiles that are arranged in any kind of grid should be gradually numbered. The number of the first tile in the approximate configuration is defined by the first tile index (i), where the user has to select the directory that contains the different tiles. Finally, when all of the previous parameters are set, the Fiji will present the large area montage after stitching.

Figure 6.8 shows a large area mosaic of the SRS images of a whole normal oesophagus tissue. The FOV was about 4mm by 3.2mm, which required 320 images that had a smaller FOV of 200 x 200 μm^2 . The focus map approach was applied to resolve the uneven image brightness resulting from the difference in thickness between the spacer and the tissue. Fifty focus points at different positions on the tissue were identified to automatically readjust the brightness, which only took approximately 3 minutes. Based on the minimum distance between every two focus points, the software automatically refocuses the beam on the sample by moving the motorised stage gradually in the Z-direction (increase or decrease), which makes the imaging plane deep enough in the tissue, which leads to obtaining high-quality images.

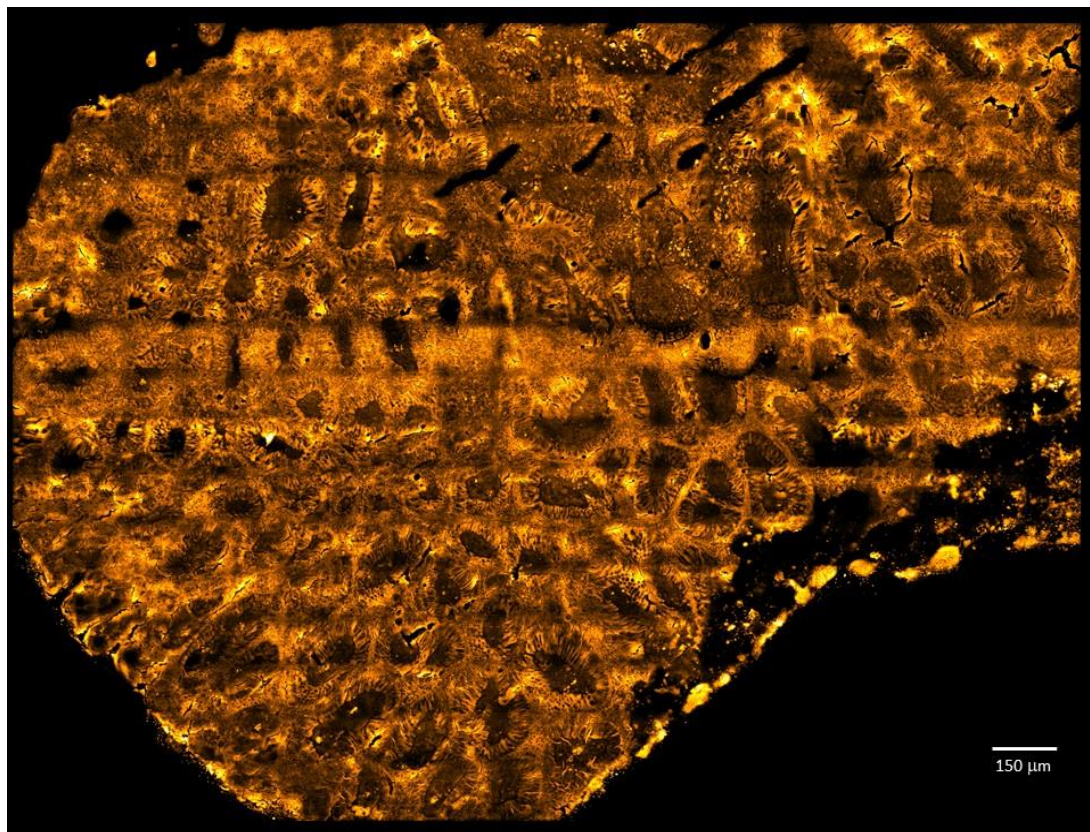


Figure 6.8: Large area montage of SRS images of an oesophagus tissue. The mosaic was acquired by stitching 320 SRS images using a 60X objective lens.

The second issue that might affect the quality of CRS images is the uneven illumination which appears in the dark area in the boundary of each tile when acquiring a large area montage. This issue might arise from the geometry of the objective lens combined with the scanning nature of multiphoton microscopy. The intensity of a CARS image, for instance, follows a phase curvature resulting in a lower signal in the image periphery. The lower signal in the image periphery is caused by the phase curvature (Gaussian Profile) that the intensity of the CRS image follows. Several studies in the literature have addressed this issue with only CARS images [185].

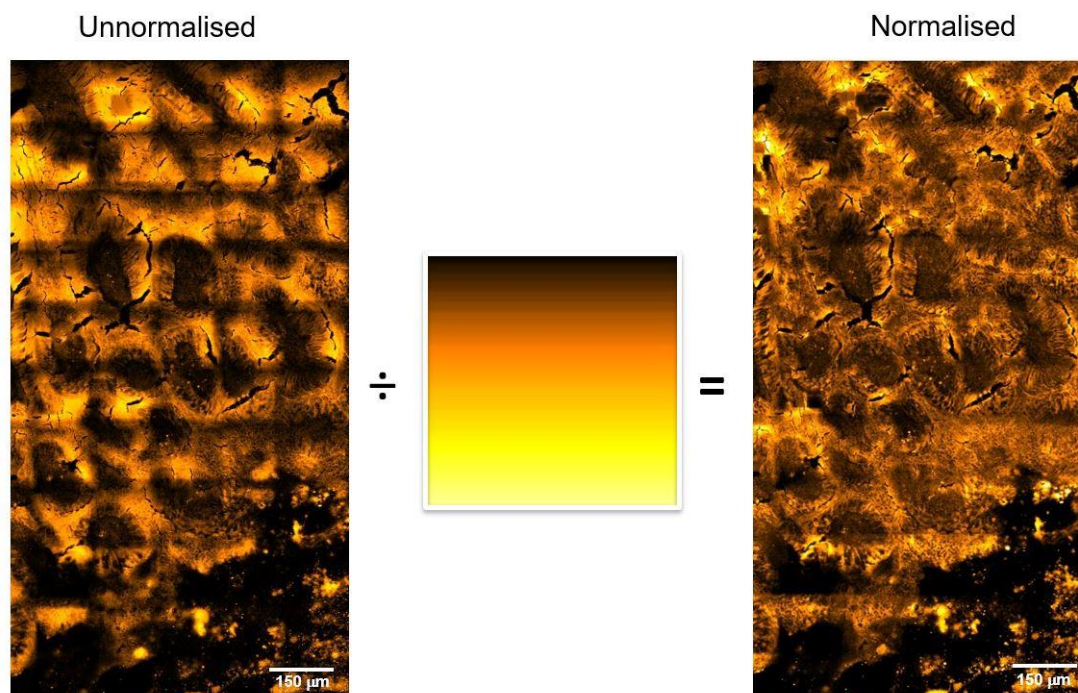


Figure 6.9: Image normalisation of an SRS mosaic of oesophagus tissue. The left image shows the uneven illumination (dark side) of the individual image. The right image is the SRS mosaic after normalisation by dividing each individual image by the bright field image of the coverslip without any sample in the centre.

The CRS signal is generated based on two pulse laser beams that are geometrically setup to satisfy the phase matching condition, as mentioned in Chapter 3. This condition can be achieved by focusing the two collinear beams with a high numerical aperture lens [163]. However, the large angle is deflected by the beam to excite points in the image periphery when scanning the beams over the field of view, while the spherical aberration degrades the phase matching. This issue was solved in two steps, during and after the experiment. During the experiment, this was achieved by optimising the imaging setup using 20X and 60X objective lenses with a 2 (630 x 630 μm^2) and 2.5 zoom factor (200 x 200 μm^2) respectively, to limit the scan to the most uniform area. After the experiment, the image intensity was normalised by dividing each image in the mosaic by a brightfield image of the coverslip

without a sample using the transmitted light images from the CRS setup. The brightfield image should have the same field of view and power as the experimental images without any sample. Figure 6.9 shows the image normalisation process of a mosaic image of normal oesophagus tissue before and after normalisation. Uneven illumination appeared at the edges of each tile in the unnormalised mosaic (left), which resulted in unwanted artefacts. This effect was almost unnoticeable after the normalisation was applied (right). The image in the middle is the brightfield image of a glass coverslip surface by which each individual tile was normalised.

6.4 Stimulated Raman scattering hyperspectral stack

There are three approaches that have been reported for SRS imaging techniques, and they are single vibration frequency, hyperspectral, and multiplex [69]. The original setup of SRS depends on the single vibration frequency method, where two narrowband picosecond pulse lasers are used to interact with the sample [154,182,183]. The signal photodiode then detects the resulting signal and is demodulated with a lock-in-amplifier (LIA). The typical experimental setup is presented in Figure 4.8. The chemical specificity is limited by this setup because of the SRS information being obtained only from a special Raman band of known types from a specimen. By sweeping one laser wavelength and fixing the other one, spectroscopic identification can be achieved. The image is created by fixing the two laser wavelengths to the specific Raman shift and scanning for an image frame, as shown in Figure 6.10.

The Development in Coherent Raman Imaging

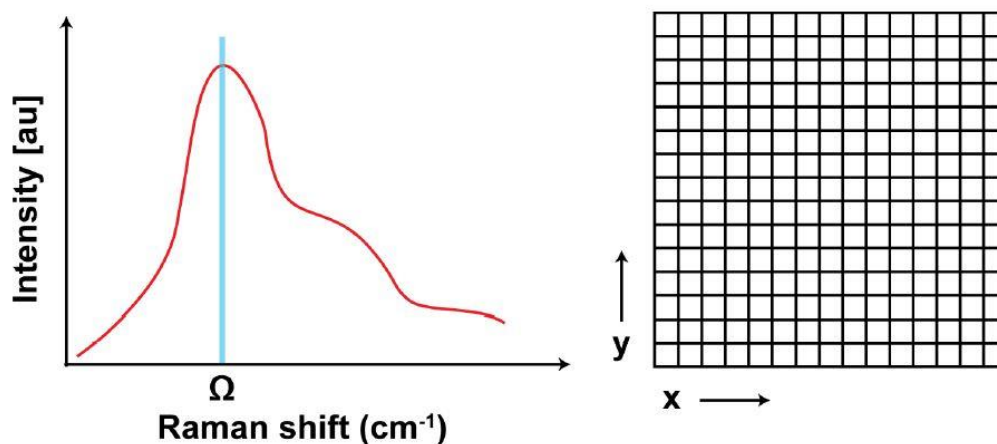


Figure 6.10: Initial fixing of the Raman shift of interest performs a single vibration frequency imaging, adapted from [169].

The wavelength tuning of one of the lasers must be applied to extract the information of another Raman band if it is requested, which leads to difficulty in obtaining the information from molecules with overlapping Raman bands. Each entire frame is imaged at one different wavelength, then the wavelength is taken for imaging the next frame, as shown in Figure 6.11. Thus, the wavelength tuning is required for imaging with this technique. The long time that is taken to complete one frame compared to the highly dynamic movement of a cell in a biological specimen is considered the main limitation of wavelength tuning, which causes spectral artifacts to occur in the image [169].

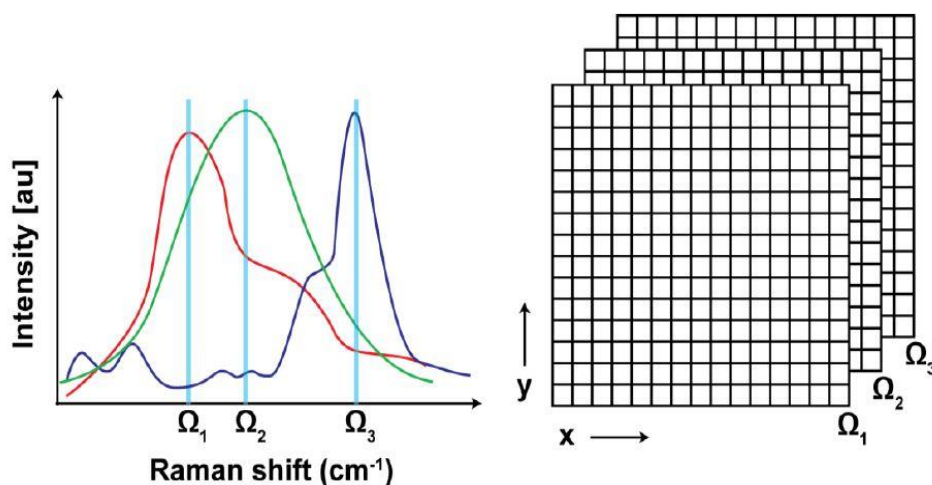


Figure 6.11: Acquired image of a multiple Raman shift using imaging techniques for wavelength tuning, adapted from [169].

The Development in Coherent Raman Imaging

Sweeping the difference of the pump and Stokes beam over a stack of frames performs the hyperspectral SRS, where each pixel in the stack has specific vibrational spectrum information, as depicted in Figure 6.12. A picosecond laser or a broadband femtosecond laser can be used for the tuning procedure to implement the Raman shift sweeping [188]. Despite the chemical species not needing to be known prior to the hyperspectral SRS compared to the single vibration frequency, the interpretation of the whole stack of images is intricate. A femtosecond laser has been used to develop the hyperspectral SRS to increase the speed of imaging, ranging from a few seconds to a few minutes to complete the imaging of the whole stack. However, the speed is still not enough to prevent spectral artifacts [189]. Furthermore, the wavelength scanning may have suffered from distortions resulting from power drift, which affect the dynamic correlation of the molecules in a biological specimen [190].

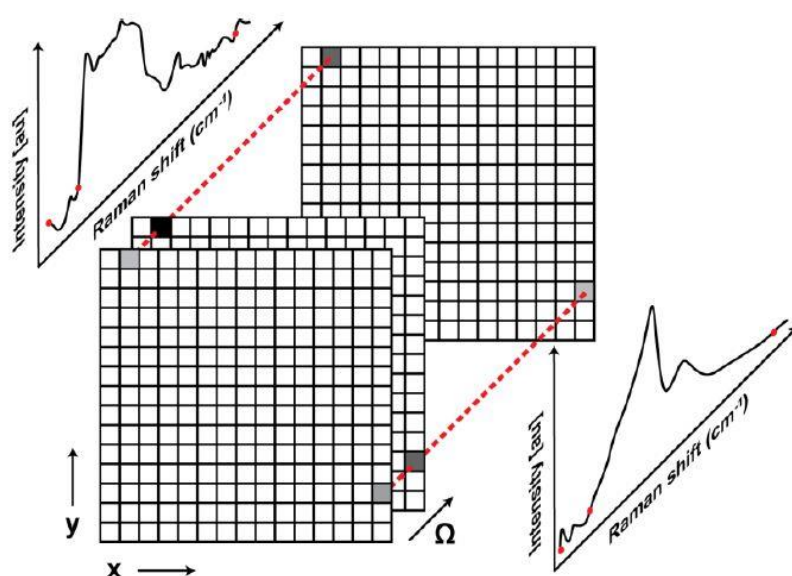


Figure 6.12: Hyperspectral SRS imaging technique, adapted from [169].

In this study, two picosecond laser beams were used to obtain hyperspectral SRS rapidly using the new development approach in the OPO, which is one of the main goals of this thesis.

6.5 Performing the SRS hyperspectral

The CARS process has no ability to provide any specific chemical information due to the serious drawback of a nonlinear non-resonant background. While the SRS is free from a non-resonant background, it can be used to extract the spectra without a non-resonant background contribution that matches with the Raman. The same field of view had to be imaged at different frequencies to perform a hyperspectral stack. Therefore, a polystyrene bead was used to acquire a hyperspectral stack at different vibration frequencies from 2796 cm^{-1} to 3097.8 cm^{-1} . Figure 6.13 shows the hyperspectral SRS stack of the polystyrene bead. This was achieved by tuning the OPO wavelength controlled by home-built hyperspectral software, which performed a gradual movement of piezo position (cavity length) for the OPO wavelength tuning. The user had to input the first and the end piezo position, which provides the first and the end frequency and the step size, depending on the number of images that are required. For the CH stretching vibration, the temperature was fixed at 152°C , which is enough to cover the whole CH vibration region between 2800 cm^{-1} and 3100 cm^{-1} .

One of the main goals of this study was to extract the SRS spectra for the region of interest (ROI). After the image is acquired, some regions are of greater importance than others, and some regions were of no interest at all. The user should input the number, size and coordinates of the ROI manually before starting scanning, with the possibility of multiple regions being acquired simultaneously. The red box is displayed on the whole channel in the software to identify the ROI. The SRS intensity of each pixel in the ROI is recorded, and then the average intensity of all of the pixels is recorded before moving to the same ROI in the next frame automatically. Figure 6.14 shows the process for extracting the SRS spectrum in the ROI. At the end of this step, the SRS spectrum is plotted and displayed in a new window promptly after the last frame is imaged. However, due to the laser power fluctuation in this technique, power normalisation must be applied to remove this effect.

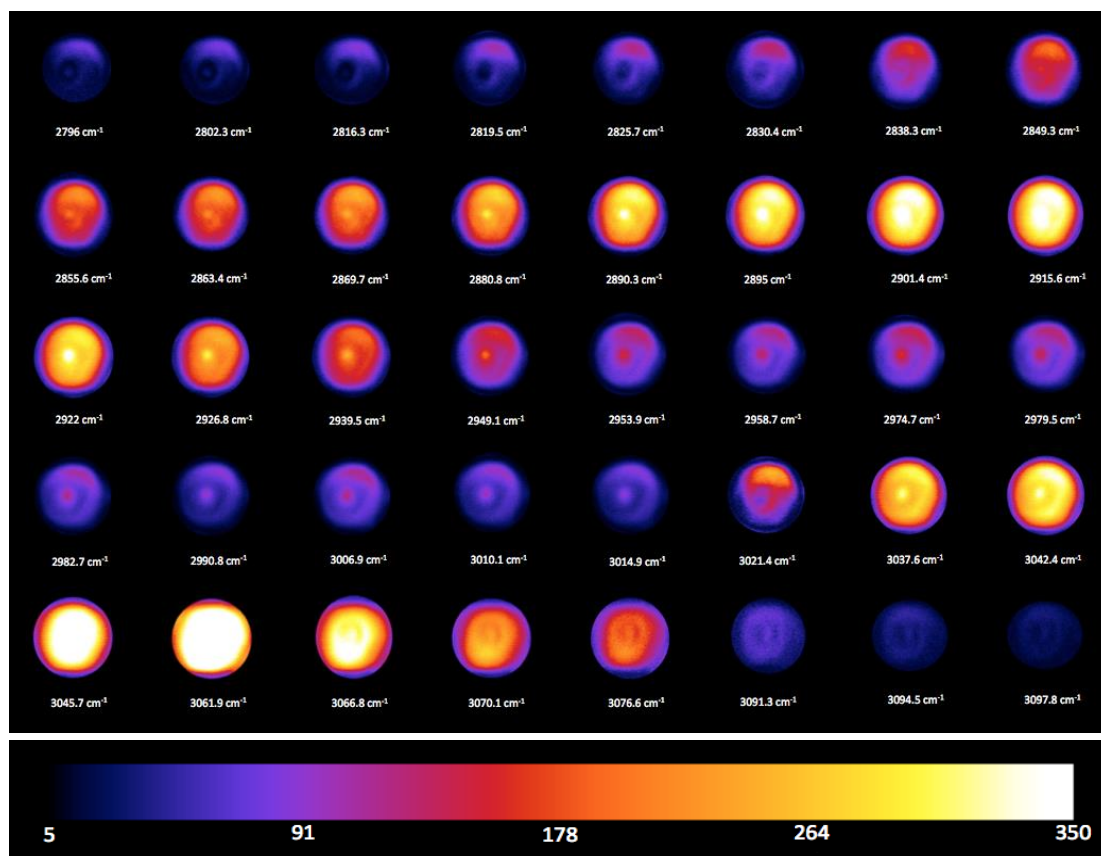


Figure 6.13: Hyperspectral SRS images of a polystyrene bead taken at different frequencies as part of a hyperspectral stack.

6.6 Laser power normalisation

As mentioned earlier, the pump beam is tunable between 690 nm and 990 nm in the OPO unit, while the Stokes beam is fixed at 1032 nm. Therefore, the OPO is responsible for generating a series of different wavelengths that have different powers. This indicates that the output power of the OPO fluctuates, while the Stokes power is constant. To generate the SRS signal, a difference between the pump and the Stokes beams is required. However, not only does the SRS signal depend on this, but also there is a linear dependence on the pump power, which means that the signal is produced as a function of the wavelength and laser power.

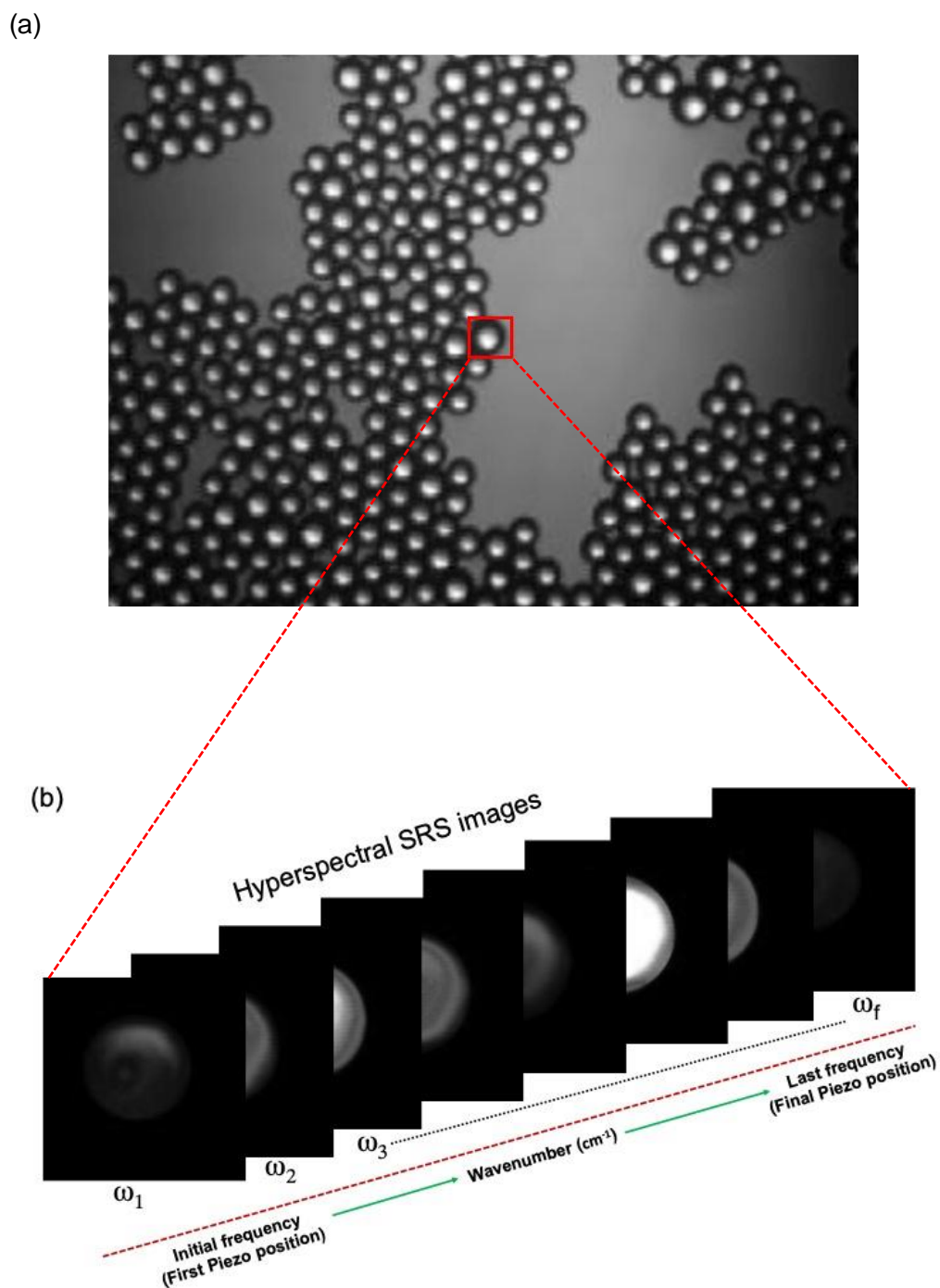


Figure 6.14: An illustration of the process for extracting the SRS spectrum of the ROI based on the piezo position. (a) the transmission image of PS and (b) is the hyperspectral SRS images of the ROI selected from image (a) by the red box.

The Development in Coherent Raman Imaging

Nevertheless, the intensity as a function of the laser power is undesirable, while only the intensity as a function of the wavelength is required. To remove the effects of laser power fluctuation, therefore, laser power normalisation has to be applied. There are two ways to record the output OPO power: direct from the OPO controller screen, or from the diode positioned after the sample using the transmitted light image. However, to use the recorded power from the OPO screen directly, it is necessary to establish that the power on the sample matches that on the screen.

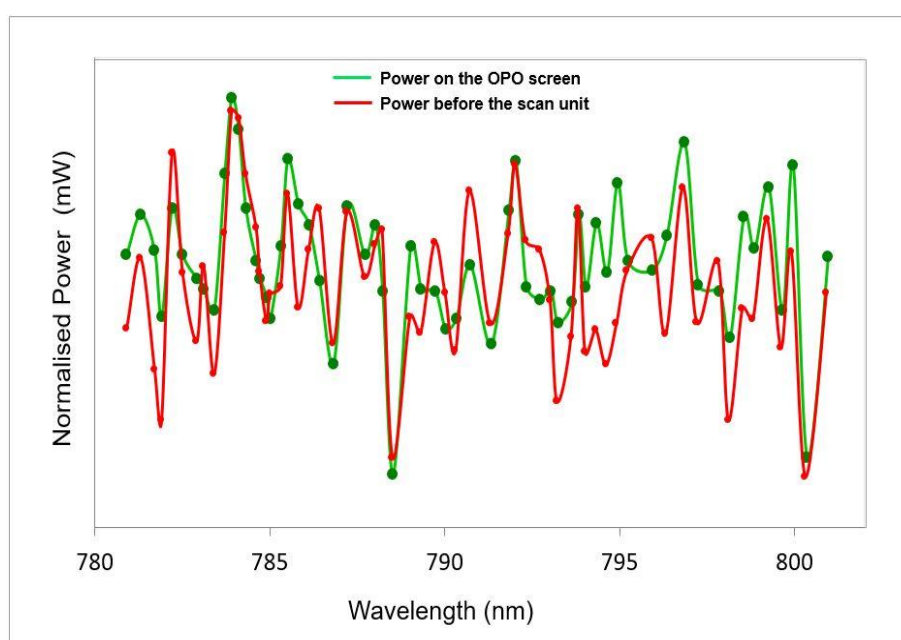


Figure 6.15: Comparison of the fluctuations in the laser power from the OPO during the tuning. The green indicates the OPO power recorded from the OPO controller screen, the red is the actual power recorded on the laser bench before the scan unit.

Figure 6.15 shows the comparison between the normalised power on the OPO screen and the actual power from the OPO, recorded before the scan unit on the laser bench during the hyperspectral stack. It is very clear that the correlation between these two curves is almost nonexistent. Therefore, it is essential to use the power that is recorded on the diode using the transmitted

The Development in Coherent Raman Imaging

light image for normalisation, to accurately reflect power fluctuation. However, for more investigation, the SRS spectra of the polystyrene bead in Figure 6.13 was extracted using the two recorded powers and compared with the Raman spectrum of the same sample, as shown in Figure 6.16. The intensity of each pixel in the ROI was recorded. The average intensity of each ROI frame was then calculated and divided by the corresponding power, which can be summarised by the following two equations:

$$SRS_{norm} = \frac{SRS \text{ (average intensity)}}{diode \text{ (average diode)}} \quad (6.1)$$

$$SRS_{norm} = \frac{SRS \text{ (average intensity)}}{OPO \text{ power}} \quad (6.2)$$

This process was applied frame by frame automatically, and then plotted and displayed on the software screen immediately after completing the scan. It is very clear that the normalised SRS intensity, by the power recorded from the diode using the transmitted light image, is similar to the Raman spectrum, while the normalised SRS intensity by the OPO power is different.

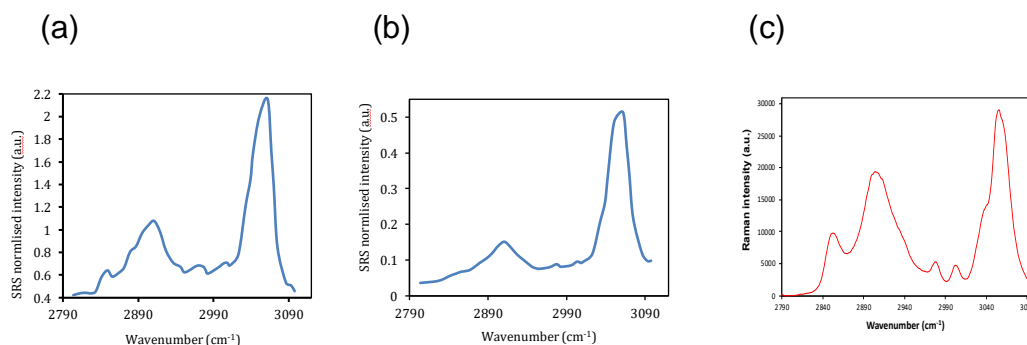


Figure 6.16: Comparison between the SRS spectra normalised by the OPO power recorded from the OPO screen (b), and the actual power recorded from the diode (a); (c) is the Raman spectrum of the PS bead.

6.7 Summary

In conclusion, SRS has proven that it has the ability to provide rapid imaging of biological samples with high resolution and without requiring staining or labelling. However, some limitations which might affect SRS imaging should be considered, such as photodamage in biological samples due to the strong intensity at the focal centre, and vibration absorption through coherent Raman processes. Therefore, the laser power threshold was studied in order to keep the excitation intensity low enough that it would keep the laser power under a certain threshold. However, determining the laser damage threshold accurately is very difficult, as the first photodamage appears at the pump power of 130 mW, without any evidence for the laser power threshold.

One of the main purposes of this research was to enhance the performance of the microscope to acquire a high-quality SRS large area montage for comparison, and the ability to orientate it against the pathology images of the gold standard method (H&E). This was achieved by writing a new Matlab script and integrating it with the Scancode to automatically create a large area montage. However, the microscope curvature due to the space between the two coverslips and the uneven elimination that appears as a dark area at the boundary of each tile are two of the main experimental issues that usually occur and affect the quality of the SRS images. Therefore, the coverslips spacer thickness should fully correspond to the thickness of the tissue section to avoid microscope curvature, which can cause the low quality of images due to the z-position being variable from one region to another. To acquire a large area montage, hundreds of images are required, sometimes reaching thousands, depending on the sample size and the FOV. This issue can be solved by readjusting the z-position. However, to adjust the Z-position manually is painful and time consuming, especially if this large area requires imaging at different frequencies. Thus, the automatic focus map method (changing the Z-position) of adjusting the brightness of each tile was applied by writing a new Matlab script and integrating it with the Scancode software and the home-built hyperspectral software. The uneven elimination that

The Development in Coherent Raman Imaging

occurs at the boundary of each SRS image is the second major issue in SRS when creating a large area montage. This issue was solved by dividing all of the tiles by the bright field image without a sample, which was taken in the same conditions in which all of the tiles were acquired. This procedure caused equilibrium in the brightness in the images and removed the uneven elimination after stitching. Normal oesophagus tissue was used in this experiment to show the SRS images before and after correction.

One of the main benefits of a large area montage is the ability to select a small ROI to extract the SRS spectrum using the hyperspectral approach. However, due to fluctuations in the output of OPO power, the normalisation power must be applied by dividing the average intensity of each frame by the corresponding power to obtain an accurate SRS spectrum. A standard sample (PS) was used in this section to show the process of extracting the SRS spectrum at the ROI. All of these steps were done automatically using the home-built software. Several methods can be used to extract the SRS spectra, and the ideal method was chosen in this work. Finally, the SRS spectra of the PS sample was compared with the Raman spectra that were obtained for the same sample using the InVia Raman system, and a good agreement was found between these two techniques.

Chapter 7

The Oesophagus

7.1 Introduction

This chapter will present the SRS and Raman measurements of oesophageal tissue. The morphological changes at the cellular level in the oesophagus wall are presented in section 1.1, which are utilised as indications of cancer progression. Histopathology is the gold standard method for cancer diagnostic, and is highly invasive, time-consuming and subjective. This chapter will mainly focus on the SRS images of oesophagus tissue, with the aim to demonstrate the ability of the SRS technique for rapidly producing images of unstained tissues over a large area similar to the H&E to identify different oesophageal structural features. This study also investigated the comparison between SRS and Raman techniques concerning the spatial and spectral information available. Finally, different regions of the tissue were determined by identifying the chemical signatures using a K-means clustering approach.

According to the author's knowledge, this is the first time that the following have been applied:

The Oesophagus

- A. A new method to rapidly acquire a large area montage and extract the SRS spectra for the ROI at different pathological areas.
- B. The SRH approach using the modified SRS system on the oesophageal tissue.

The author's contribution in this chapter:

1. All samples of oesophageal tissue used in this chapter were prepared by the pathologists at the Gloucestershire Hospital.
2. All pathological information mentioned in this chapter were provided by the pathologist Professor Neil Shepherd from Gloucestershire Hospital.
3. The author conducted all the research described in this chapter.
4. The Matlab code used to convert SRS images to be similar to the H&E images was written by the author.
5. The K-mean Matlab code was provided by Kelly Curtis and modified by Benjamin Gardner.

7.2 Measurement protocol

Acquiring an image for the whole tissue was required for comparison between different techniques with contiguous tissue sections. Figure 7.1 shows the images of the whole oesophagus tissue at different grades using three different techniques. H&E sections were presented in the first column: the middle images are the white light images from the InVia Raman system, and the right column shows the SRS large area montage at 2930 cm^{-1} . The SRS large area montage was created by stitching many tiles together. There is a slight similarity between the contiguous tissue sections but with slight differences as the sections were at different depths in the biopsy block. The large area montage is useful also to determine the region of interest and extract SRS spectra by moving the position of the motorised stage in the SRS

The Oesophagus

setup based on the development that was made in this setup as shown in Chapter 6.

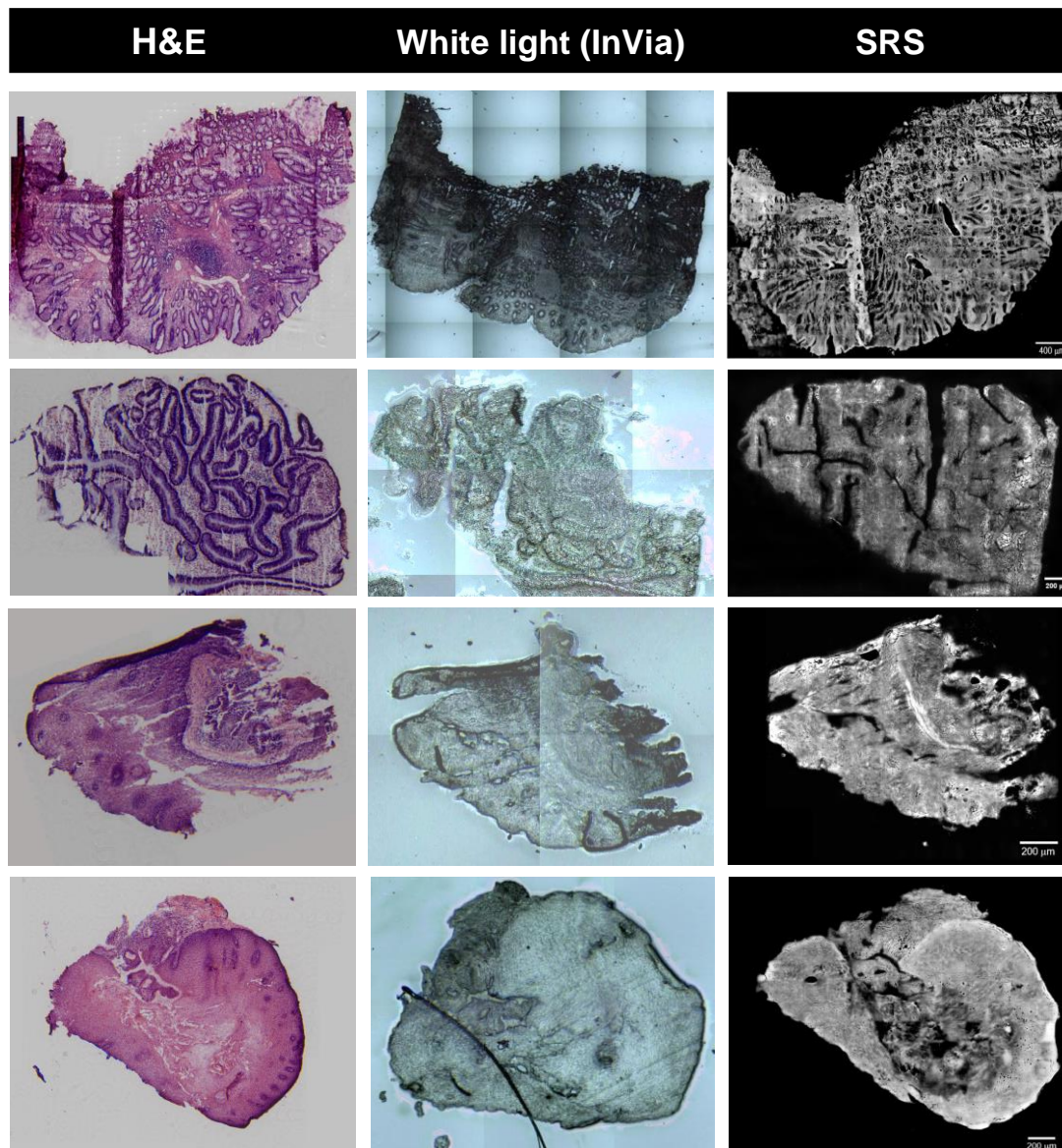


Figure 7.1: Large area images of the oesophagus tissue at different grades to show the morphological similarities between contiguous sections. H&E images are in the left column; the images in the middle column are the white light images from the InVia system, and the SRS images in the right column were taken at 2930 cm^{-1} .

7.3 SRS large area montage of oesophagus tissue

Imaging the whole appearance of tissue structures is required to determine and study the suspicious area in the biological tissue. One criterion for a histopathology cancer diagnosis is the visualisation of the cell nuclei and cell bodies. The degree and stage of the invasion for abnormal cancer cells in the tissue can be established based on the tumour grade, node, metastasis (TNM) classification, as mentioned in section 1.4. For rapid diagnosis of cancer, there is a need to speedily scan a large area of tissue without staining, which would offer a clinical benefit by providing quick and accurate images to assist in surgical and decision making. A large area montage of oesophagus tissue using the SRS technique was constructed by acquiring multiple images that had smaller FOV, which was achieved based on the development as described in section 6.3. High-resolution SRS images were acquired in this experiment using a 60X magnification water objective lens, a 2.5 zoom factor, 80-pixel Bin Factor (25 sec/frame), 200 μm by 200 μm FOV/frame, and 512 x 512 pixel per image. The pump and Stokes beams were used to generate the SRS signal, where the power of the combined two beams was 130 mW.

SRS image acquisition was performed using ScanImage software and then processed using Fiji, Photoshop, and Matlab software. All SRS images were normalised by dividing each individual image by the bright field image of the coverslip without any sample in the centre to remove the grid appearing between the 200 μm x 200 μm FOVs when stitched together as described in section 6.4. After the normalisation, the small FOV images were stitched together using Fiji software. Due to the limitation of Fiji to provide false colours similar to those used in the H&E, all montages were stained in the false colour using Photoshop software. However, the background in the SRS image was black, while in the H&E it was white. All SRS images here were a 8-bit grayscale type, which means the minimum pixel value was 0 (black) and the maximum pixel value was 255 (White). Therefore, the montage was inverted to create a reverse image like a photographic negative. This procedure makes

The Oesophagus

white 0 and black 255, so the SRS image will have a white background and the rest of the image can be stained with any chosen false colour. The white background in the SRS images can also easily change with any different colour using Photoshop. The H&E samples were imaged using a 20X air objective lens in the white light microscope. A new camera and light imaging software (Microvisioneer) were installed in the white light microscope, which allowed for fast imaging and stitching the whole tissue synchronously, which only took several seconds to a minute in this study depending on the sample size.

In this study, several oesophageal tissues, which have different pathology groups were measured. Oesophageal samples were collected from two patients using an endoscopy procedure. The first patient was diagnosed with an intra-mucosal adenocarcinoma while another patient had high-grade squamous dysplasia. Each tissue section was classified by a pathologist as belonging to one of three predetermined pathology groups: normal squamous epithelium, columnar-lined (Barrett's) oesophagus and Low-grade dysplasia. The ROI was determined by the pathologist using digital copies of the H&E stained sections, which were used later for Raman and SRS measurements. H&E sample preparation took several days to be ready for measurement, while just a few hours were needed for Raman and SRS samples.

7.3.1 Normal squamous epithelium cells in oesophagus tissue

Distinguishing the normal squamous epithelium of the esophagus from the columnar epithelium can be achieved in a gross examination of specimens and using an endoscopy. Histologically, squamous epithelium in the oesophagus consists of multiple layers of flat surface epithelial cells. The normal squamous epithelium relies on the dynamics of cell loss and replacement [191]. The cells move upward in the epithelium after they continually divide in the basal proliferative zone. These cells become

The Oesophagus

differentiated keratinocytes, which have small nuclei, which replace the cells that are continually shed at the surface [191].

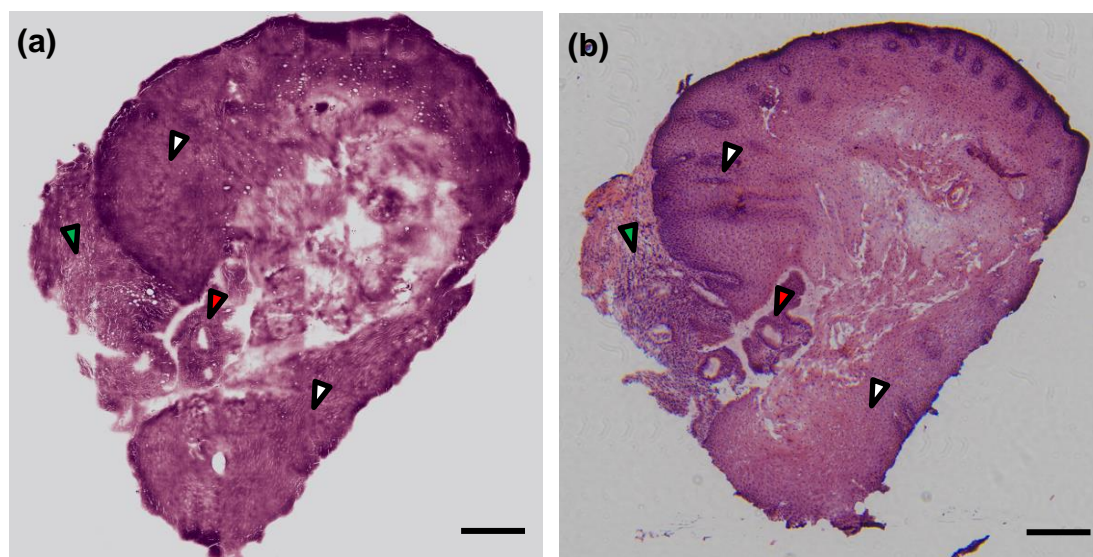


Figure 7.2: SRS large area montage for different pathological areas in the oesophageal tissue. (a) The montage constructed from several SRS images which has a smaller FOV, which presents the normal squamous epithelium, inflammation, and Barrett's type glands. (b) H&E image for comparison. The scale bar is 200 μm .

Figure 7.2 (a) and (b) shows an SRS montage and the H&E image of the different pathological areas of oesophageal tissue. It was constructed from 169 individual SRS images at $2,930\text{ cm}^{-1}$. The FOV of the montage is 2.6 mm by 2.6 mm, with the total acquisition time for the whole sample being around 70 minutes. An excellent similarity was found between the SRS montage and the H&E image in the general architecture. This tissue showed mainly normal squamous epithelium (white arrow) with inflammation appearing in the left (green arrow) and some occasional Barrett's type glands (red arrow). The uniform circles that appeared in most of the entire field of view were the normal squamous epithelium, which makes up the lining of the oesophagus. The H&E image shows the epithelial cells, basement membrane and submucosa very clearly in this sample. The epithelial metaplasia of the BO

The Oesophagus

can be identified by the glandular structure of the cells. It can be clearly distinguished between these pathological areas, which highlights the ability of the SRS technique to provide rapid images of different tissue structures similar to the H&E.

Figure 7.3 shows the large area montage of oesophageal tissue that has different morphological structures using the SRS technique at the CH_3 stretching vibration at $2,930\text{ cm}^{-1}$. The FOV of this montage was 2mm by 2mm. The total acquisition time for scanning the whole tissue was 42 minutes. Two different pathological areas can be clearly observed in this montage. First, the lower part of the tissue shows the normal squamous epithelium that goes around the sides, which are formed as a uniform circle throughout the tissue (white arrow). Second, the top part of the tissue presents a glandular epithelium that has a much more disordered structure, mostly a low-grade dysplastic (red arrow).

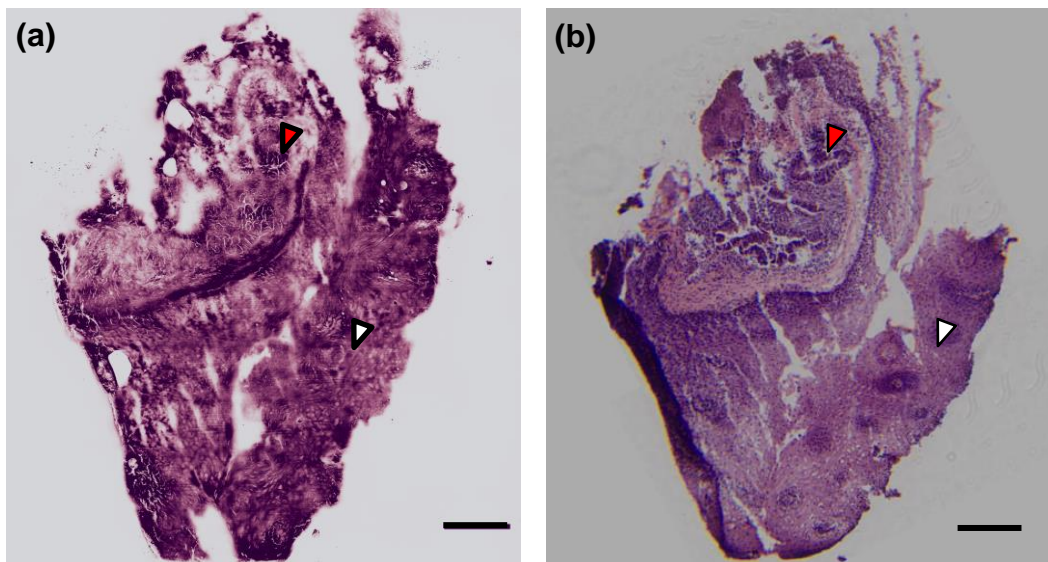


Figure 7.3: SRS and H&E images of oesophageal tissue. (a) the SRS montage shows the normal squamous epithelium (white arrow) and low-grade dysplasia in the top (red arrow). (b) H&E for comparison. The scale bar is $200\ \mu\text{m}$.

7.3.2 Columnar-lined (Barrett's) oesophagus (CLO)

Barrett's oesophagus is defined as an abnormality in the lining of the lower oesophagus, which is often due to severe, long-standing, gastroesophageal reflux disease (GERD). The columnar epithelium has a single layer of tall (rectangular cells) compared to the several layers of flat cells in the normal squamous epithelium. Barrett's oesophagus occurs as a result of the replacement of the normal squamous epithelium with the different types of columnar epithelial cells. Although BO cells are considered pathologically normal, they may be a high-risk indicator of cells' progression to cancer [192].

Figure 7.4 shows the large area montage of the columnar-lined oesophagus tissue using SRS at the CH_3 stretching vibration of $2,930\text{ cm}^{-1}$, most commonly associated with proteins. This montage was created from 960 individual images that allow for the visualisation of the whole tissue section, which is about 8 mm by 5 mm FOV. The total acquisition time for imaging the whole tissue section was more than 6.5 hours, which means about 25 seconds for each frame ($200\text{ }\mu\text{m} \times 200\text{ }\mu\text{m}$). The large area montage shows well-defined glandular epithelium throughout the tissue, which described two variants of columnar-lined (Barrett's) oesophagus (CLO). However, it also looks colonic, without convincing dysplasia. The glandular structure of the BO cells appears in this tissue as a non-uniform circle shape that is bigger than the normal squamous epithelium (yellow arrows) whereas the columnar epithelial cells appear rectangular (red arrows). This montage shows an excellent correlation with the contiguous H&E section, as shown in Figure 7.1(b) for comparison. From the H&E section, the cellular nuclei appear in dark magenta throughout the tissue and were observed surrounding the gland (nuclei line), which is not possible to be seen in the SRS montage with a single frequency. Although some important components were not visualised in the montage when using a single frequency, SRS was able to provide a fast and high-resolution montage for the large area in up to centimetre scale quicker than the H&E or the Raman.

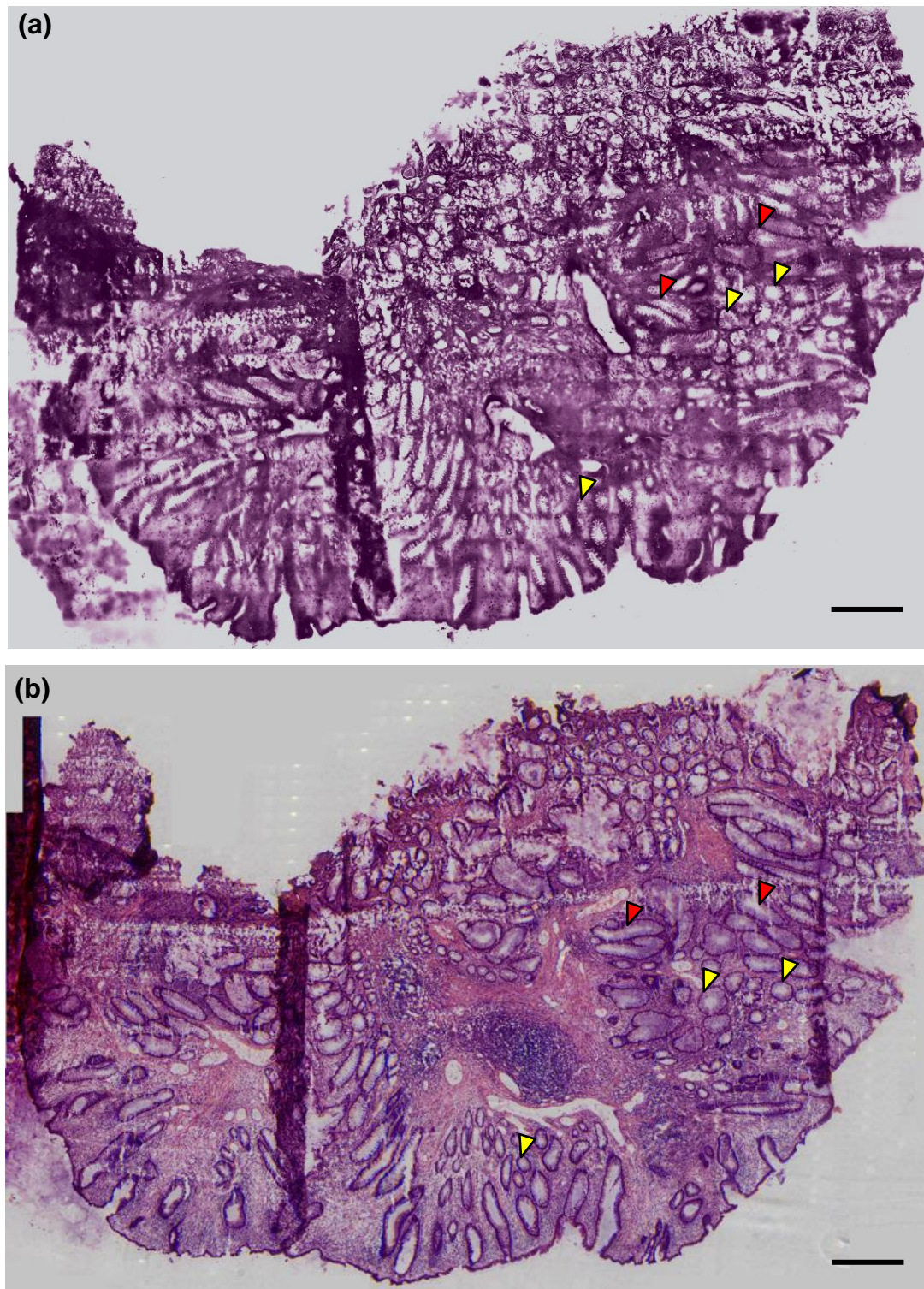


Figure 7.4: (a) Large area montage of oesophagus tissue using SRS at 2,930 cm^{-1} . The glandular epitheliums appear throughout the tissue. The montage offers a macroscopic structure similar to that of the H&E image (b). The scale bar is 400 μm .

7.3.3 Low-grade dysplasia

Dysplasia preoccupies most cellular pathologists and it can be defined as the disordered maturation of cells in the epithelium. In the normal non-dysplastic stratified squamous epithelium, the nuclei are all evenly spaced, mature and flattened off as they go up to the surface of the epithelium. As dysplasia is an alteration in the size, shape and organisation of cells, non-matured or non-flattened off cells are key signs of dysplasia and impacted cells are a sign of more severe dysplasia. There is a continuum from low grade to high-grade dysplasia. Dysplasia is premalignant in the low-grade changes, and it may regress, whereas the high-grade dysplasia has a significant opportunity of eventually developing into carcinoma [193].

Figure 7.5 shows a large area montage of low-grade dysplasia in oesophageal tissue using SRS at $2,930 \text{ cm}^{-1}$. The FOV of the SRS image was 3.5 mm by 2.2 mm, with 187 individual images used to create the montage. The total acquisition time for scanning the whole sample was approximately 77 minutes. The H&E image is presented in Figure 7.2 (b) for comparison. It is very clear that the montage offers a good similarity in size and shape with the H&E with a slight difference due to the images being taken for contiguous sections in the biopsy. This montage shows abnormal gland crypts, which became larger in size and shape than the normal squamous epithelium and CLO presented in the previous figures. This made the normal structure of the oesophagus no longer recognisable. From the H&E image, the cellular nuclei were concentrated around the gland, which was not clear in the SRS montage.

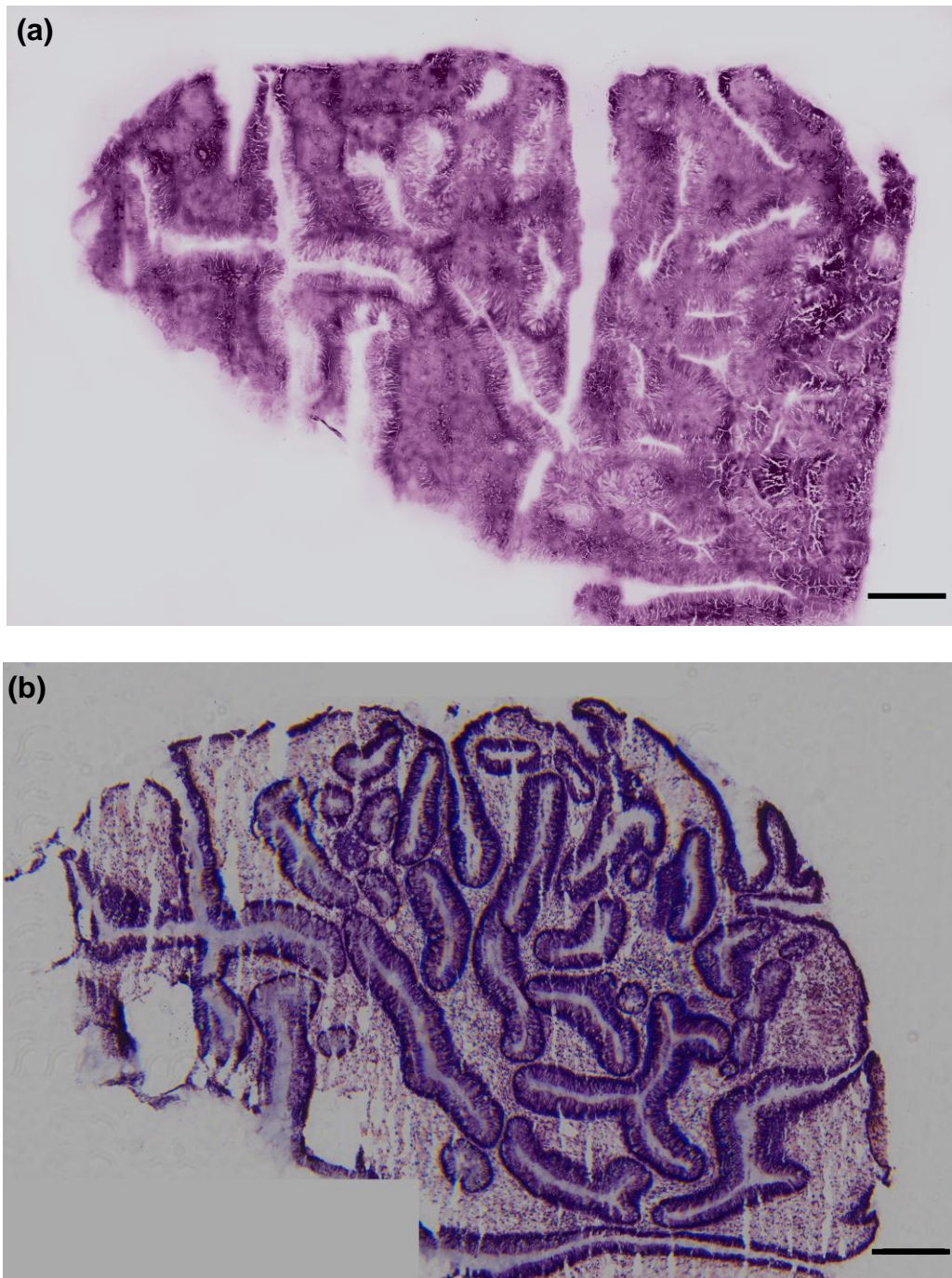


Figure 7.5: SRS images to illustrate the low-grade dysplasia in Barrett's oesophagus tissue. (a) Large area montage shows the gland throughout the tissue. (b) H&E image of the contiguous section in the same biopsy for comparison. The scale bar is 200 μm .

7.4 Stimulated Raman histology (SRH)

Stimulated Raman histology (SRH) is a new approach that has been proposed to identify cell nuclei and cell bodies by acquiring high-resolution images without staining the specimens using the SRS technique [67,191]. The tissues' macroscopic and microscopic architecture can be identified by investigating the special CH_2 (at $2,850\text{ cm}^{-1}$) and CH_3 (at $2,930\text{ cm}^{-1}$) chemical bonds that exist mainly in the cell cytoplasm and cell nuclei, which give a unique label-free molecular contrast [67,182]. Few studies in the literature review have been done with this approach to provide fast label-free microscopic images of pancreas, colon and brain tissue samples of different structures in a good agreement with gold standard histology method [67,147]. In this chapter, the SRH images will be presented for the ROI of the oesophagus tissue sections selected from the figures 7.1 and 7.2. The H&E images were acquired for each sample for comparison and assessment with SRH.

The process can be summarised as follows:

1. Acquired SRS images (two grayscale images corresponding to the $2,850\text{ cm}^{-1}$ and $2,930\text{ cm}^{-1}$ Raman spectrographs).
2. Subtracted the $2,850\text{ cm}^{-1}$ image from $2,930\text{ cm}^{-1}$ image in each FOV to create a new FOV.
3. Randomly coloured each of these with arbitrary colors close to light green for lipids and dark blue for subtracting image.
4. Blended the CH_2 image and $\text{CH}_3 - \text{CH}_2$ image together using a linear color blend (called the "SRH" image).
5. Converted the green colour to pink and the blue colour to dark violet and the black background to white.
6. Repeated from step 5 using the new starting colours until the ideal one was reached.

The Oesophagus

Figure 7.6 shows the SRH image of the small regions of interest of the CLO section selected from the SRS montage that was presented in Figure 7.3-a. The H&E image is shown in Figure 7.5-f, which was identified from Figure 7.3-b for the same ROI. The FOV of the ROI is about 1mm by 2mm, which required 50 images that had a small FOV. These images were processed using Fiji and Matlab. First, Fiji was used to normalise all individual SRS images to remove uneven illumination as applied with the large area montage in the previous section. The SRS images were then stitched together to construct the montage for the ROI. Second, the montage was transferred to a dedicated Matlab code, which was designed to convert the SRS images into "SRH" images that looked similar to H&E images (see Appendix).

The raw images presented in Figure 7.6 (a) and 7.6 (b) were directly acquired from the SRS microscope at $2,850\text{ cm}^{-1}$ (CH_2 bonds) and $2,930\text{ cm}^{-1}$ (CH_3 bonds), respectively. The image in the Figure 7.6 (c) highlights the cell nuclei, which was generated as a result of the subtraction between the $\text{SRS}_{2930\text{ cm}^{-1}}$ image and $\text{SRS}_{2850\text{ cm}^{-1}}$ image, ($\text{SRS}_{\text{nuclei}} = \text{SRS}_{2930\text{cm}^{-1}} - \text{SRS}_{2850\text{cm}^{-1}}$). The $\text{SRS}_{2850\text{cm}^{-1}}$ image and $\text{SRS}_{\text{nuclei}}$ image were merged in Figure 7.6 (d) using two different false colours green and blue, respectively. Finally, the green colour in Figure 7.6 (d) was converted to pink to be similar to the eosin staining of both the cytoplasm and the cellular body. The blue colour in the same image was replaced with a dark violet to mirror the haematoxylin staining of the cell nuclei. Meanwhile, the black background was inverted to white by replacing the intensity value of each pixel that had 0 value to 1, with 1 indicating the maximum intensity value 255 (white). The final processing was applied for smoothing and colour adjustments using Fiji on the composite image to obtain the final SRH image, see Figure 7.6 (f). Figure 7.6 (e) shows the H&E image for comparison.

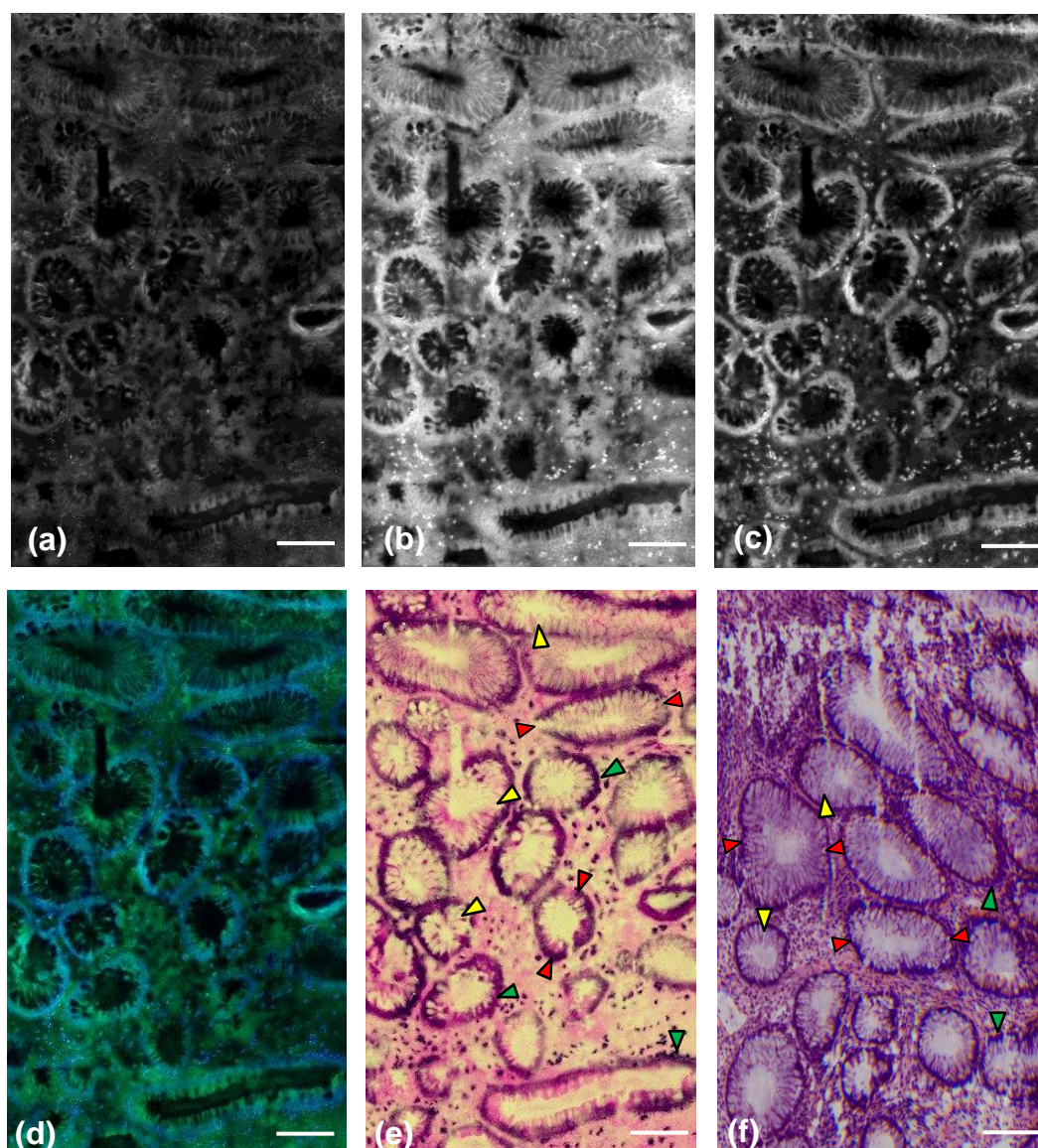


Figure 7.6: Stimulated Raman histology (SRH) for the small ROI of columnar-lined (Barrett's) oesophagus (CLO) tissue. (a) SRS_{CH_2} image at $2,850\text{ cm}^{-1}$. (b) SRS_{CH_3} image at $2,930\text{ cm}^{-1}$. (c) Subtracted $\text{CH}_3\text{-CH}_2$. (d) the composite image built from the CH_2 image assigned (green) and the $\text{CH}_3\text{-CH}_2$ image assigned (blue). (e) The SRH image is comparable to a similar section (f) after histological processing and H&E staining. The scale bar is $200\text{ }\mu\text{m}$.

The Oesophagus

In the SRH image the global architecture of the tissue is almost regular, and no dysplasia was evident. Although the glands were slightly non-uniform (longer, oval) or inhomogeneous, it did not indicate malignancy, while the morphological changes may have indicated the CLO type (red arrows). The cellular nuclei can be seen in a dark violet color distributed surrounding the glands and in the basal position (green arrows). There were vacuoles uniformly present within the crypts, which indicate that the mucus secretion was not affected (yellow arrows). All these features were in excellent accordance with the H&E image in Figure 7.6-e and revealed that SRH images of the CLO tissue can be accurately illustrated by pathologists and linked with features shown on standard H&E images.

Figure 7.7 shows the SRS images of the selected ROI of a low-grade dysplasia tissue section from Figure 7.5. The same protocol was followed as that used for acquiring and processing the SRS images in Figure 7.6. The FOV of the ROI was about 1mm by 2.2mm, which required 55 images that had small FOV. Compared to the CLO case, the general tissue architecture was altered. The shape and size of the Lieberkühn glands became larger, irregular, inhomogeneous, and occupied the most tissue, which indicates a dysplasia. By focusing carefully on the nuclei distribution, the differentiation between low- and high-grade dysplasia could be identified. SRH and H&E images in Figure 7.7 (e) and Figure 7.7 (f) show highly packed lines of nuclei surrounding the glands (yellow arrows) without being regularly spaced compared to those in the same images in Figure 7.6. The regular nuclei sizes and shapes are very noticeable in the H&E images while unclear in the SRH image. Additionally, there is an apparent reduction in the vacuoles within the crypts with loss in the mucus secretion (red arrows), which led to atrophy of the crypts lumina and also confirmed the pre-cancerous state. All these features indicate a low-grade dysplasia diagnostic.

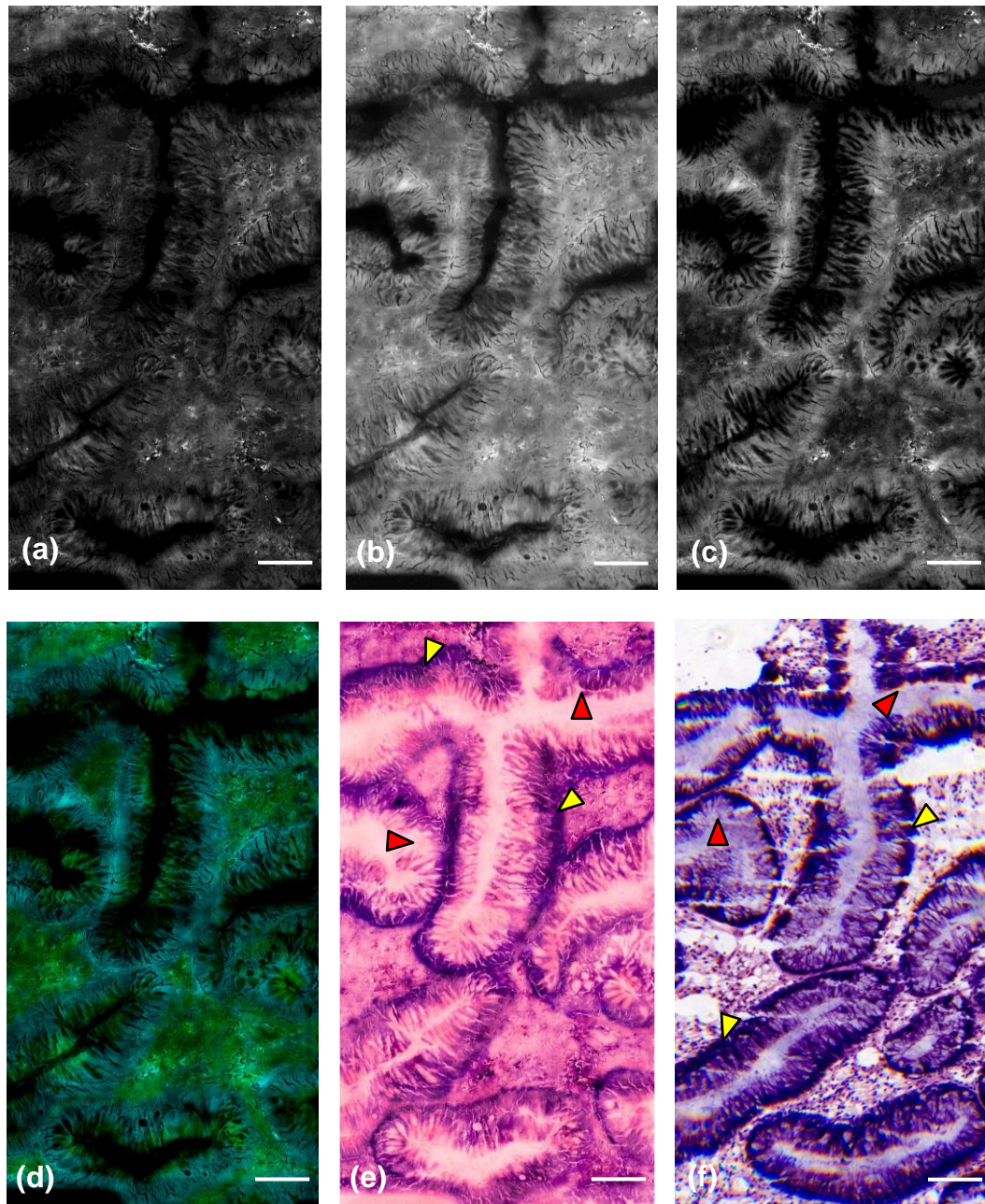


Figure 7.7: Stimulated Raman histology (SRH) for the small ROI of low-grade dysplasia in Barrett's oesophagus tissue. (a) SRS_{CH_2} image at $2,850 \text{ cm}^{-1}$. (b) SRS_{CH_3} image at $2,930 \text{ cm}^{-1}$. (c) Subtracted $\text{CH}_3\text{-CH}_2$. (d) the composite image built from the CH_2 image assigned (green) and the $\text{CH}_3\text{-CH}_2$ image assigned (blue). (e) The SRH image is comparable to a similar section (f) after histological processing and H&E staining. The scale bar is $200 \mu\text{m}$.

7.5 Comparison between Raman and SRS techniques

7.5.1 The spectra of oesophagus tissue

The Raman and SRS spectra of the oesophagus tissue for four groups (normal squamous epithelium, inflammation, CLO, and low-grade dysplasia) in the HWN will be presented in this section.

Raman of the oesophagus

The near-infrared laser illumination wavelength at 785 nm was used for all Raman measurements in this experiment. Oesophagus frozen sections were cut to a thickness of 15 μm and mounted onto CaF_2 as described in section 4.7. The ROI was identified by the pathologist based on the tissue pathology in the H&E sections. To visualise the whole tissue section the white light montage was created using an X5 objective lens, which allowed for the correct orientation of the tissue to identify the ROI. Raman spectra were extracted from multiple areas for each pathological group and then the average was applied. Before each experiment the instrument response correction was performed as described in section 4.2.2. In this study the interesting wavenumber region was the CH stretch vibration in the HWN region between 2,800 cm^{-1} and 3,100 cm^{-1} . The baseline correction was applied in all data using OriginPro 2015.

Figure 7.8 shows the mean Raman spectra in the HWN region for each of the four groups, normal squamous epithelium, inflammation, CLO, and low-grade dysplasia. Raman spectroscopy could not be used to assign specific molecular changes in the complex samples, while it was able to identify spectral changes of numerous molecules combined, which increase from disease progression. The variation in the Raman spectra between four pathological groups can be noticed. A small shift in the position of the peaks

The Oesophagus

between the four groups was observed. The main peaks can be identified at $2,850\text{ cm}^{-1}$, $2,881\text{ cm}^{-1}$, $2,930\text{ cm}^{-1}$, and $3,065\text{ cm}^{-1}$.

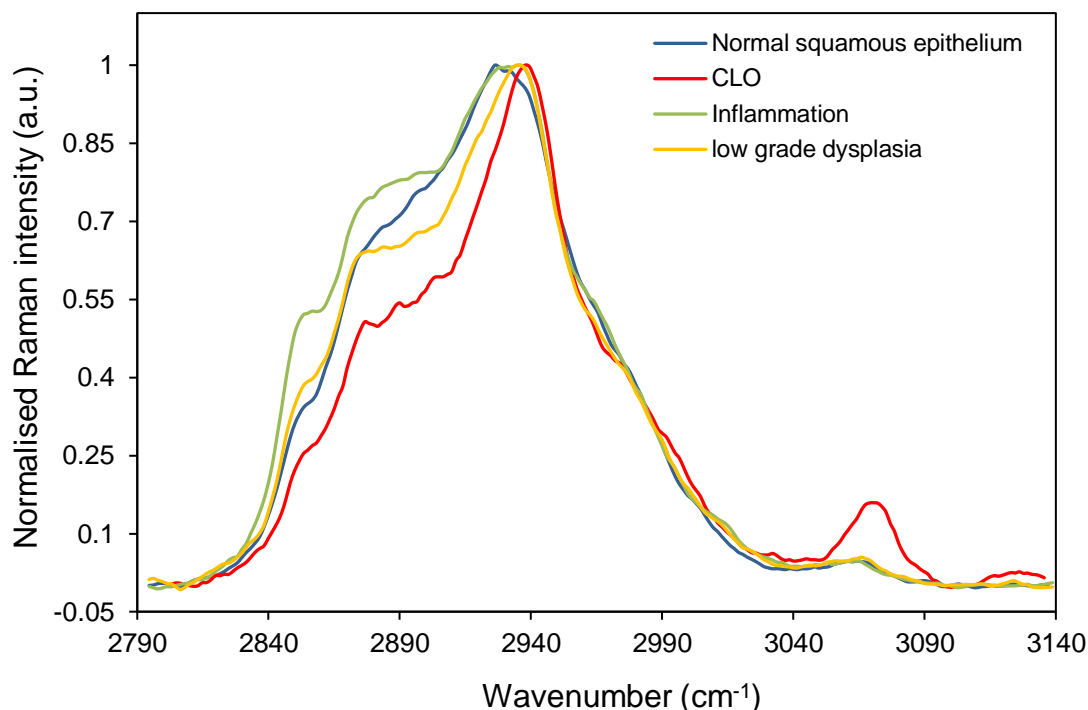


Figure 7.8: The mean Raman spectra of four pathological groups of oesophagus tissue, normal squamous epithelium, inflammation, CLO, and low-grade dysplasia at the CH chemical bond in the HWN.

In general, there was a similarity in the line shape between all groups with a difference in the normalised intensity. The most significant spectral changes can be observed in the wavenumber region between $2,830\text{ cm}^{-1}$ and $2,900\text{ cm}^{-1}$, which was mostly assigned lipids. The most prominent peaks in this region were at $2,850\text{ cm}^{-1}$ and $2,881\text{ cm}^{-1}$, where the normalised intensity in the inflammation sample was the highest and the CLO sample was the lowest at the same peak position. The normalised intensity for all groups significantly increased in the range from $2,900\text{ cm}^{-1}$ to $2,940\text{ cm}^{-1}$ (CH_3 chemical bond), which was mostly assigned protein. In this region the normal squamous epithelium had the highest normalised intensity at 2930 cm^{-1} , while the low-

The Oesophagus

grade dysplasia was the lowest at $2,932\text{ cm}^{-1}$. The Raman spectra for all groups in the region between $2,940\text{ cm}^{-1}$ and $3,050\text{ cm}^{-1}$ followed the same slope. A small peak appeared at $3,065\text{ cm}^{-1}$ in the CLO sample, which might indicate water.

SRS of the oesophagus

A hyperspectral stack was performed using SRS to extract spectral information. All samples were cut to a thickness of $15\text{ }\mu\text{m}$ and mounted on coverslips as described in section 4.7. Due to the fluctuation in the output of the OPO power, a laser power normalisation was performed on the data. All these steps were automatically done based on hyperspectral software as described in sections 6.6 and 6.7. The transmitted montage was created using the 20X objective without concentrating on the resolution of the images to identify the ROI. The objective lens was then moved to the 60X water immersion lens to provide higher resolution images where the motorised stage was automatically moved to the ROI position and then imaging was started. As far as possible, the SRS spectra were extracted from the same multiple areas that were selected in Raman measurements and then the average spectra for each group were applied. The baseline correction was applied in all data and plotted using OriginPro 2015.

Figure 7.9 shows the SRS spectra for all four pathological groups. In general, similarity was found in the shape of the lines of the SRS spectra for all pathological groups, which was also been observed in the Raman in Figure 7.8 without an identical match. However, by comparing the SRS spectra with the Raman spectra, there was no match found identically. The peaks that were located around the $2,930\text{ cm}^{-1}$ wavenumber for all pathological groups had the highest normalised intensity. The difference in the SRS spectra in the range from $2,830\text{ cm}^{-1}$ and $2,900\text{ cm}^{-1}$ appeared lower than that in the Raman spectra in the same region. The higher normalised intensity at $2,880\text{ cm}^{-1}$ appeared in the inflammation sample and the lower in the CLO sample. Although the difference between all groups was very small, it can be easily

The Oesophagus

identified. Almost the same amount appeared with all groups at 2850 cm^{-1} . The wavenumber region between $2,900\text{ cm}^{-1}$ and $2,940\text{ cm}^{-1}$ shows the similarity in the peaks position and amount in the CLO and low-grade dysplasia samples at $2,935\text{ cm}^{-1}$ whereas the highest peaks in the other two samples were found at $2,930\text{ cm}^{-1}$, which had the same position and amount of the normalised intensity. The wavenumber range from $2,940\text{ cm}^{-1}$ and $3,050\text{ cm}^{-1}$ almost followed the same pattern that appeared in the Raman spectra. The small peak appeared at 3070 cm^{-1} in the inflammation sample and CLO sample, while in the Raman spectra it only appeared in the CLO sample.

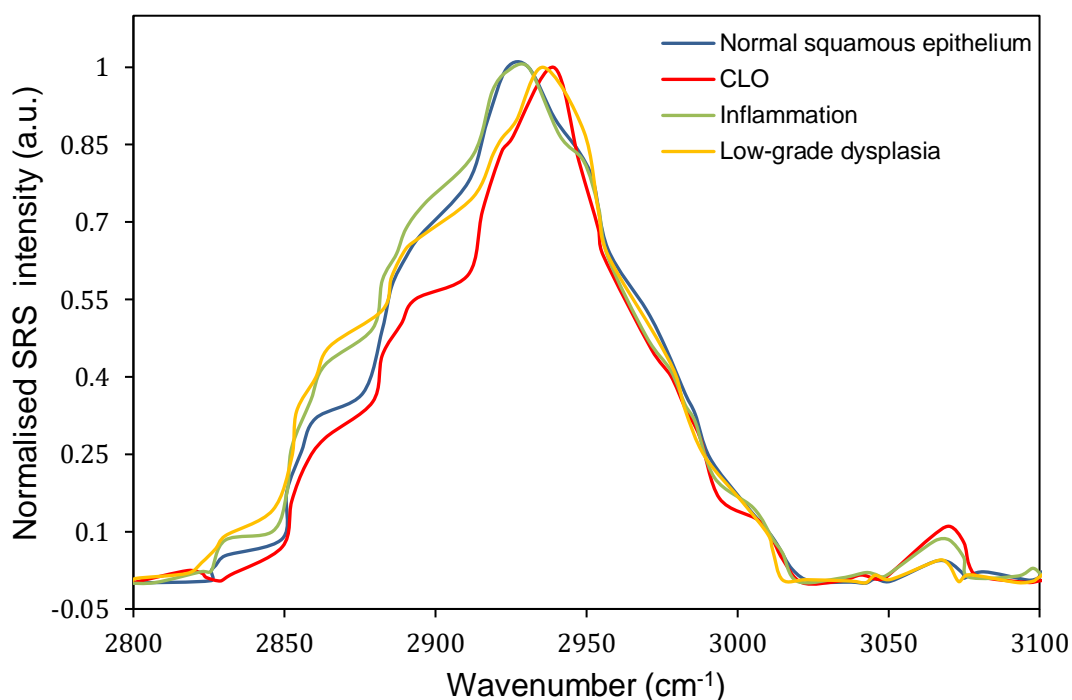


Figure 7.9: The mean SRS spectra for four pathological groups in the CH chemical bond in the HWN.

The differences between the two modalities could be due to using different factors between Raman and SRS instrumentations. In the Raman measurements, more than 200 data points were extracted to cover the region from $2,800\text{ cm}^{-1}$ to $3,100\text{ cm}^{-1}$, while there were about 44 data points in the

SRS. The big difference in the number of the data points could have affected the spectral resolution. Additionally, extracting spectral information using contiguous sections of oesophagus tissue might have led to these differences. These differences may also have been produced by the baseline in Raman and SRS. The background in the SRS is unlikely to have the origins as that in the Raman due to the method of SRS detection. Raman's background can be created from autofluorescence. However, this is unlikely to occur with a 785 nm excitation. The SRS signal detection depends on the loss of pump photons at a set modulation frequency, which would not be affected by such signals due to its being highly directional and coherent. Nevertheless, the background effect in the SRS could have been due to several factors such as cross-phase modulation, photothermal lensing and two photon absorption [196].

7.5.2 Raman and SRS images

A small region of interest of columnar-lined (Barrett's) oesophagus and low-grade dysplasia were imaged using Raman and SRS techniques. Although the cross sections were cut from two different layers in the oesophagus biopsy due to the different substrate conditions for optimal sampling on the two instruments (see section 4.7), as far as possible the same ROI was selected for both techniques. A large area montage of the whole tissue section was acquired using transmitted light images on the SRS microscope (see section 6.4) and Raman microscope to identify the coordinates for the glands of interest on the sample. The motorised stage was then moved to the selected ROI for imaging.

Figure 7.10 shows the compared images of columnar-lined (Barrett's) oesophagus tissue and low-grade dysplasia using Raman and SRS at the CH₃ chemical bond (at 2,930 cm⁻¹) most commonly assigned to proteins. For morphological comparison, H&E images were taken corresponding to each of

The Oesophagus

the crypts. A significant similarity was found in the cellular features between these two modalities that correspond to the features observed in the H&E.

For Raman measurements, streamline Raman mapping was performed using the 50X objective lens with 600 l/mm grating, 100 % laser power, and 60 s CCD exposure. The FOV of both Raman and SRS images of the CLO was 200 x 200 μm^2 , while double FOV was acquired for the low-grade dysplasia (400 x 400 μm^2). It can be seen that the Raman image in Figure (c) was smoother than that in Figure (d) due to the different pixel size, 1.4 μm and 3 μm respectively. The acquisition time required to acquire the Raman mapping in Figures (c and d) was seven and thirteen hours, respectively whereas the SRS only required 25 seconds and 50 seconds to acquire the images in Figures (e and f) at a single frequency, while the whole hyperspectral stack for the same regions was less than 20 and 40 minutes respectively. In addition to the very slow imaging in the Raman system, it had a low resolution compared to the SRS images. Therefore, numerous finer details of glandular features could be extracted using SRS.

From Raman and SRS images in figures (c and e), it could be observed that they had a very similar size with a slightly different shape due to the samples being cut in different layers. In the Raman image there was a good contribution at 2,930 cm^{-1} in the lamina propria, where a bright pixel proposed a high concentration of the line of nuclei surrounding the gland mixed with mucin (red arrow). The dark region outside the gland revealed the connective tissue (yellow arrow), while the small black holes inside the gland might indicate mucin within goblet cells (red arrow). From the SRS image in Figure (e) the higher concentration was at 2,930 cm^{-1} produced from the lamina propria and the lower amounts in the glandular epithelium, while the minimum appeared in the inner part of the gland that formed the lumen of the crypt. The connective tissue is the region that had a lower intensity outside the gland (yellow arrow), while the line of nuclei had higher intensity located around the gland (green arrow).

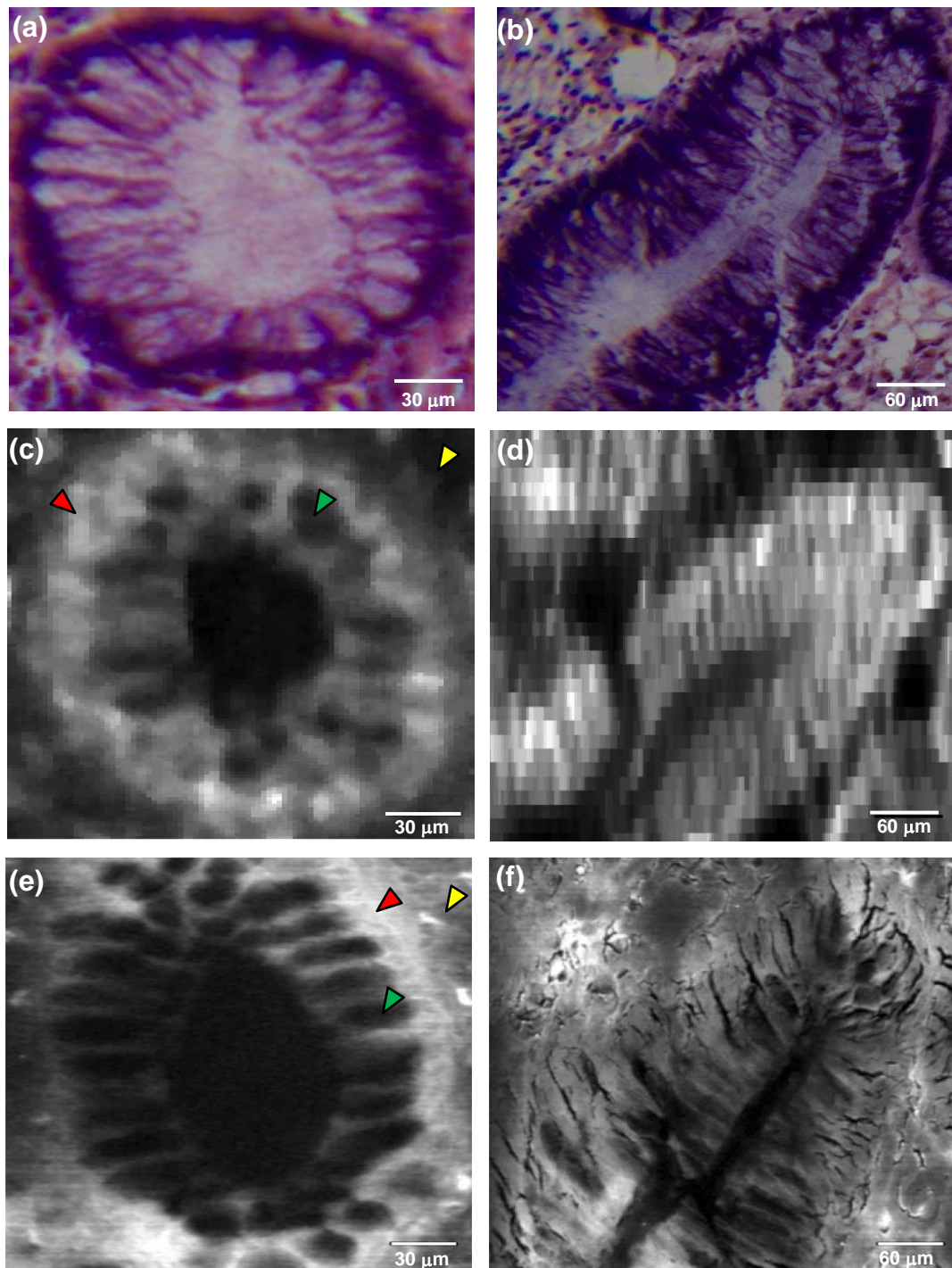


Figure 7.10: Images of oesophagus tissue at CH₃ stretch vibration at 2,930 cm⁻¹ using Raman and SRS. (a, c and e) are H&E, Raman and SRS images of columnar-lined (Barrett's) oesophagus tissue, respectively. (b, d and f) are H&E, Raman and SRS images of low-grade dysplasia, respectively.

7.6 K-means clustering

The purpose of this experiment was to compare the spatial and spectral resolution and determine the structural features of oesophagus tissue in the HWN region using Raman and SRS techniques on the normal glandular epithelium that is presented in Figure 7.10. The protocol of this experiment is described in section 7.5.2.

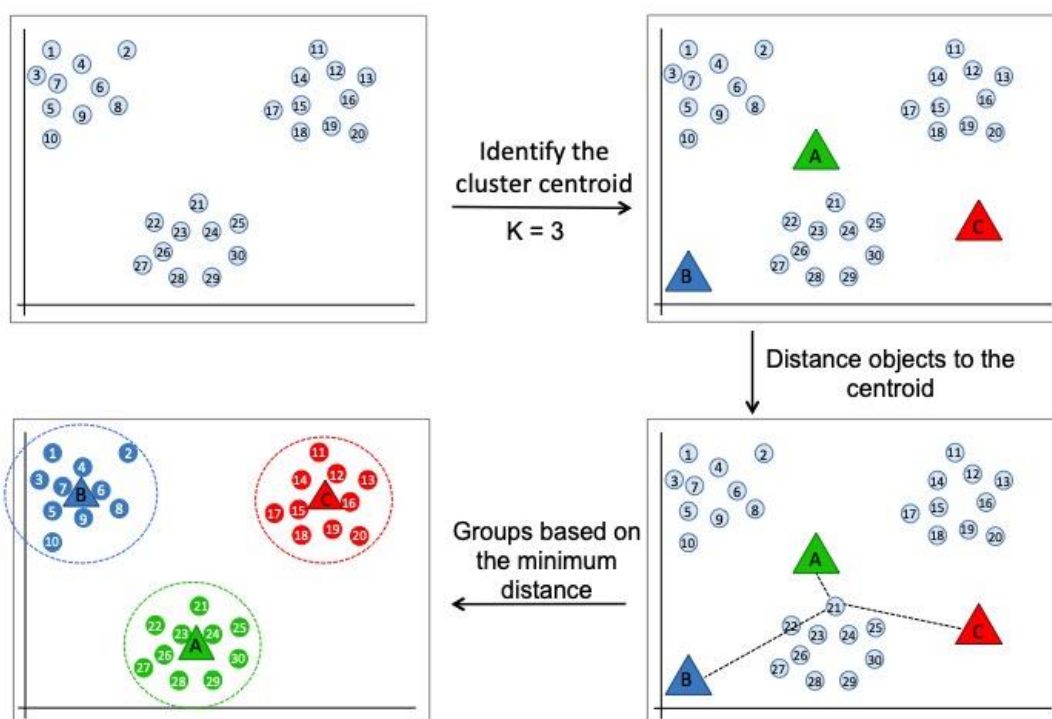


Figure 7.11: Scheme of the steps of the K-means clustering method.

K-means is a splitting method, which is commonly used for an unsupervised learning technique that solves the well-known clustering problem [174]. The data is segmented in K mutually exclusive clusters by the K-means function. A single level of clusters is produced by the K-means clustering. For a large amount of data, the K-means clustering is often more appropriate than hierarchical clustering. Each observation in the data is processed as an object

The Oesophagus

that has a specific location in space. The objects within each cluster are partitioned each together based on how close they are to each other and as far from objects in other clusters. Every cluster in the division has different features than others and it can be defined by its centroid, or centre and by its member objects.

The centroid can be identified for each cluster by minimising the distances from all objects in that cluster. To minimise the sum distances concerning the measure that it is specified, cluster centroids for each distance metric are calculated differently by K-means and then a distance matrix is the result. The object is symbolised by each column in the distance matrix. The first row is the distance of each object to the first centroid and the second row of the distance matrix corresponds to the distance of each object to the second centroid, and so on. Then this was followed by computing the distance of all objects to the new centroids. Based on the new distance matrix, each similar object was moved to one group while all the other objects remained. The last step was repeated to calculate the new centroids coordinate. Figure 7.11 shows an example on the schematic of how the K-means clustering algorithm works.

In this section the ability of hyperspectral SRS to recognise different biochemical signatures was investigated using the in-built K-means function in Matlab (version 2018a). Two standard mixed samples were used of polystyrene beads (PS) of 5 μm in diameter and polymethyl methacrylate (PMMA) of 3 μm in diameter. Both samples were stored in a water suspension by Phosphorex, US. The measurements were obtained using Raman mapping and hyperspectral SRS. Very small quantities of dissolved beads were taken by pipet and then mixed with each other very well in an Eppendorf tube. The mixture solution was dropped onto a CaF_2 slide for Raman measurement and onto a glass coverslip slide for SRS measurement, and then left to dry for 30 minutes.

The acquired Raman and SRS images were taken for the same batch but with

the different samples for each technique. The Raman spectra in the HWN region were taken separately at a single point for the PS and PMMA beads before doing Raman mapping. The SRS spectra of the PS and PMMA were obtained in two different small regions simultaneously with the hyperspectral stack. Figure 7.12(b) shows the Raman spectra of the PS and PMMA where the PS has the sharpest peak at $3,053\text{ cm}^{-1}$ and the PMMA at $2,953\text{ cm}^{-1}$, and Figure 7.12 (a and e) shows the Raman and SRS composite images of polystyrene (red) at $3,053\text{ cm}^{-1}$ and PMMA (green) at $2,953\text{ cm}^{-1}$, respectively. The SRS spectra matched well with those of the Raman with some differences in the highest peaks of the PMMA and PS as shown in Figure 7.12 (f). Figure 7.12 (c and g) show the results from the K-means cluster analysis using three clusters of the data that are shown in Figure 7.12 (a, e), respectively. The K-mean spectra of clusters are presented in Figure 7.12 (d and h). For both instruments, the red cluster indicates the PS and the green for the PMMA while the black cluster is for the substrate background of the CaF_2 in the Raman and glass coverslip in SRS. The K-means clustering identified the correct regions for the PS and PMMA beads in both techniques. However, in a Raman K-means image the pixels of the background between beads were classified as a bead, which led to losing the resolution of the actual beads whereas, the SRS K-means image improved and could be clearly distinguished due to the high-resolution SRS image.

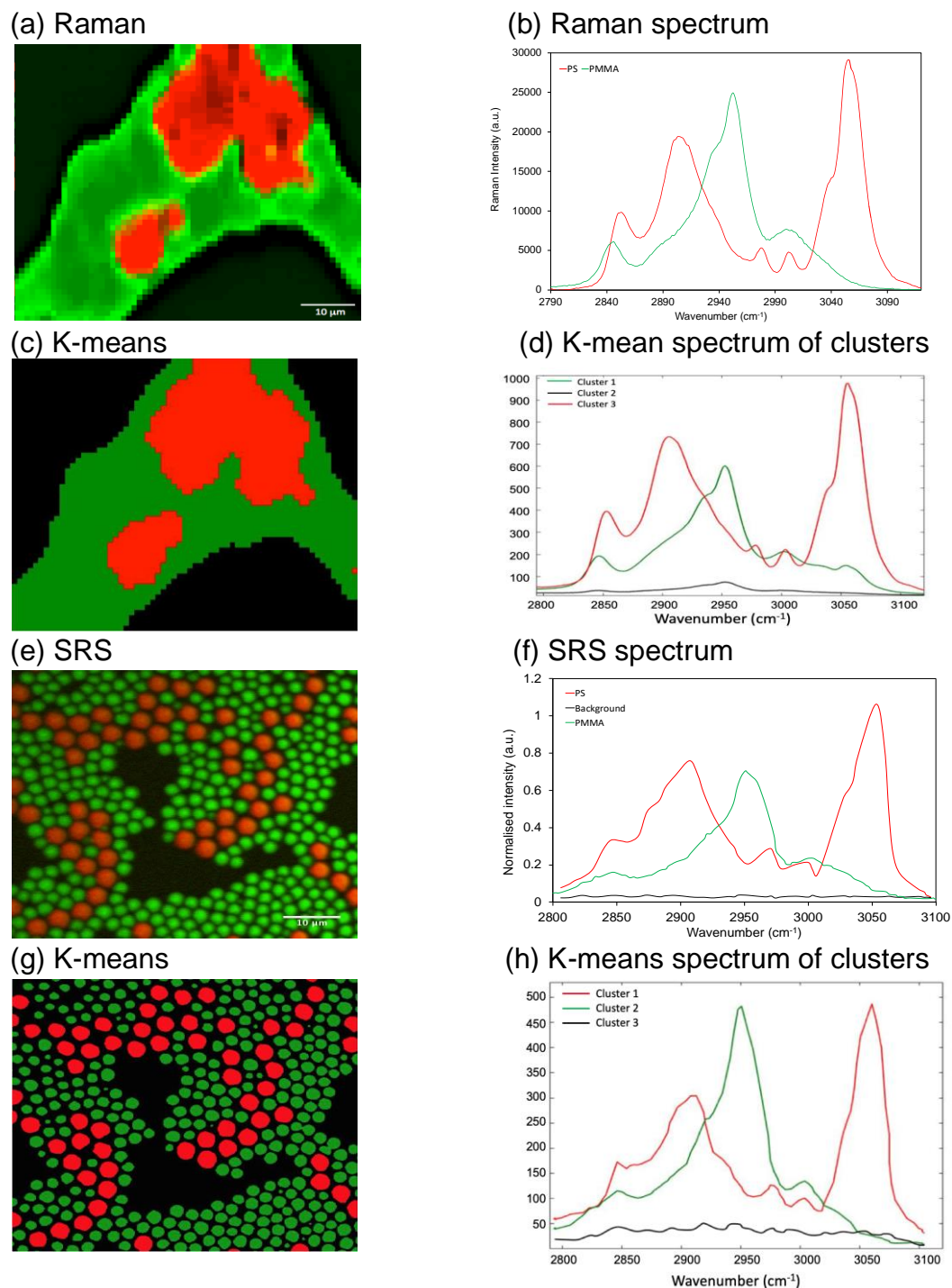


Figure 7.12: Analysis of a mixture of polystyrene and PMMA using the K-means clustering method. (a, e) Raman and SRS composite images of the mixture PS and PMMA at 3053 cm^{-1} (red) and 2953 cm^{-1} (green), while (c, g) K-means clustering with three clusters of the same images. (b, f) the Raman, SRS spectra of PS and PMMA and (d, h) K-means spectra of the clusters.

Oesophagus tissue

The differences in the biochemical information in the structures of oesophagus tissue were segmented by applying the K-means clustering to the data sets. The quality of the clustering was dependent on the number of clusters (selected by the user) to identify the number of initial centroids. The biochemical information was provided from clustering based on the pseudocolour images of clusters, a dendrogram, and the mean spectra of centroids. A Ward's algorithm provides a visual representation of the similarity of clusters to one another and calculates dendrograms using analysis of the hierarchical cluster. For each cluster, the percentage of spectra was displayed to the right of the pseudocolour image. Each pixel in Raman and SRS images has a spectrum, which is given a specific colour to determine the spatial positioning of clusters and then presented as a pseudocolour map. This map allows for a direct comparison with the histological information available from the H&E by providing the morphological information about the tissue.

To enable comparisons between Raman and SRS and extract further biochemical information, Raman mapping and SRS hyperspectral images were performed at the CH stretch vibration in the HWN region from $2,800\text{ cm}^{-1}$ to $3,100\text{ cm}^{-1}$. Figure 7.13 shows a comparison of a K-means cluster analysis for the contiguous sections measured using Raman and SRS. The same images of the glandular epithelium that presented in Figure 7.10 were analysed both in Raman and SRS. Each image was clustered using eight clusters. The clusters from 4 to 8 in Raman identified the connective tissue surrounding the gland, while clusters 2, 3, 6 and 7 in SRS. The glandular epithelium cells were determined by clusters 4 in Raman, while clusters 4 and 5 in SRS, which form the gland. Clusters 5 and 6 in Raman highlight the inside of the gland in Raman and clusters 1 and 8 in SRS.

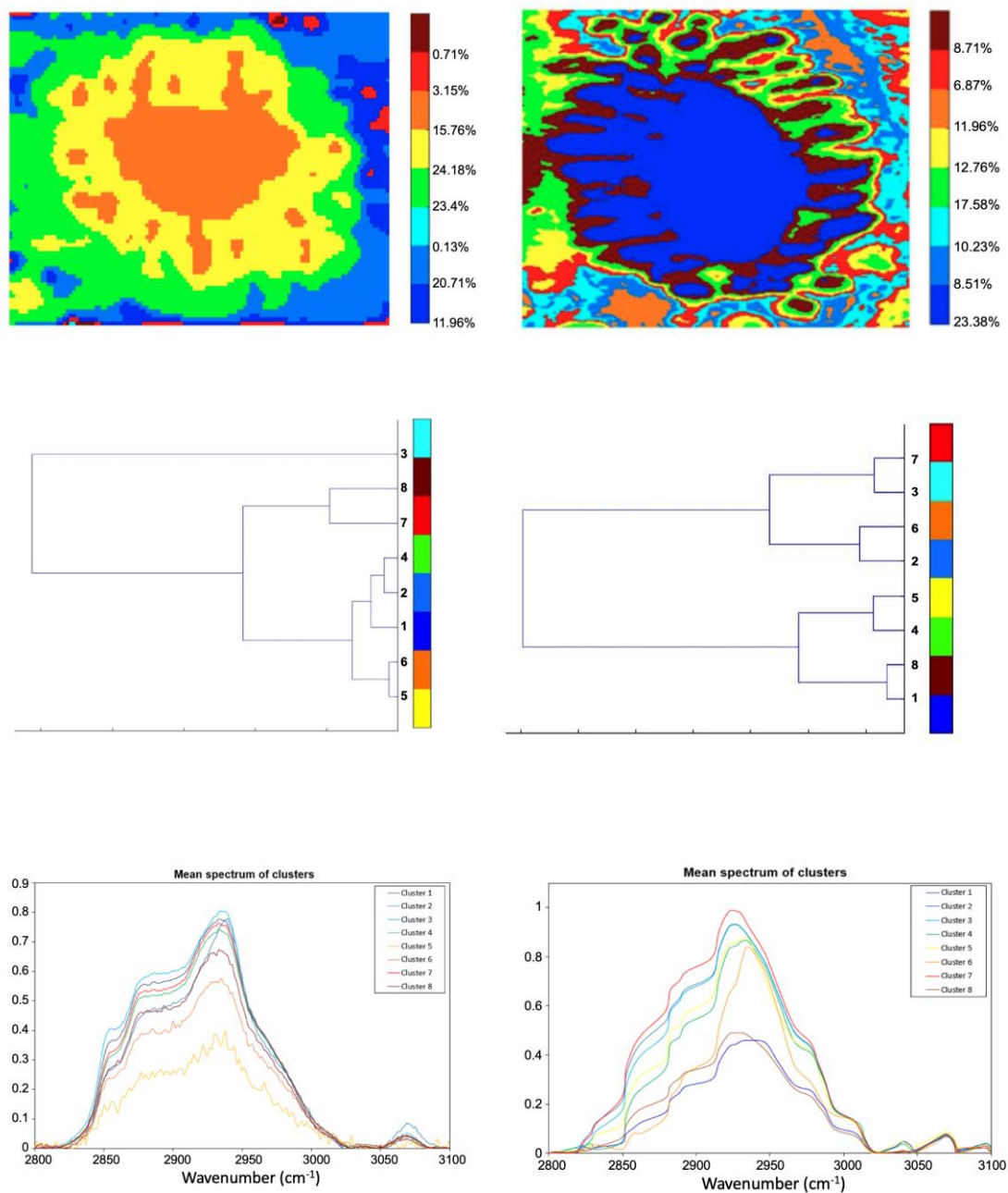


Figure 7.13: Comparison of the result of K-means cluster analysis for contiguous sections of CLO in oesophagus tissue in the HWN region using Raman and SRS.

The Oesophagus

The dendrograms figures show the similarity between the clusters. In the SRS, it can be observed that the greatest similarity is seen between clusters 1 and 8 that make up the inner gland. The spectral similarity of these two clusters is shown by looking at the mean spectra of the centroids. Clusters 4 and 5 are the other two similar clusters that form the gland, which is very similar in the spectra. The other four clusters are shown as being similar, which highlights the different biological structure in the connective tissue. The K-mean result from Raman shows a good agreement with that available from the SRS.

Table 7.1 shows the most important measurement parameters for comparison between Raman and SRS techniques. SRS provides rapid and high resolution imaging, which rapidly identifying morphological changes in the tissue quicker than Raman. However, Raman is effective to extract considerably more spectral information than SRS by providing higher quality spectra over a wide range of the wavenumber over the fingerprint and HWN regions. Using SRS in the HWN region proved the ability to visualise the complex structure of oesophagus tissue and found the result matched well to the structures observed in contiguous histological samples. To measure a region 200 x 200 μm requires 7 hours and 20 minutes of measurement time for Raman and SRS, respectively.

	Raman	SRS
Pixel size	1.4 μm	0.39 μm
Image size	200 x 200 μm	200 x 200 μm
Number of pixels per image	150 x 150	512 x 512
Spectral range	1500 cm^{-1} to 3300 cm^{-1}	2800 cm^{-1} to 3100 cm^{-1}
Wavenumber step size	1.8 cm^{-1}	6 cm^{-1}
Wavenumber sampled	1015	50
pixel dwell time	1.2 sec	10 μs
Total imaging time	7 hours	20 minutes

Table 7.1: The most important measurement parameters used for comparison between Raman and SRS techniques.

7.7 Summary

In conclusion, the application of Raman and SRS techniques of oesophagus tissue have been discussed in this chapter. The SRS technique has proven that it can provide a fast and high-quality montage for the whole sample using a single frequency at $2,930\text{ cm}^{-1}$. The montage successfully distinguished the differences between the pathological areas in the tissue without the need for staining, which identically matched with the shape of the histopathological image. However, a histopathological diagnostic depends on the visualisation of some specific components in the tissue section such as cell nuclei and cell bodies, which the SRS cannot provide with a single frequency.

Stimulated Raman histology is a new approach that was applied to the ROI of the CLO and low-grade dysplasia sections to highlight these components using the SRS technique. Two different frequencies at $2,850\text{ cm}^{-1}$ and $2,930\text{ cm}^{-1}$ were used to acquire the grayscale SRS images and then were analysed using the Matlab script to convert the images to be comparable with the corresponding H&E images. This approach was able to provide histological images by assigning virtual colours to mimic H&E staining. These images showed the changes in the general architecture and morphology at the subcellular level, which were generally similar to the standard H&E images.

A comparison between Raman and SRS was performed at the level of imaging and spectral information. Both techniques provided similar morphological features at the $2,930\text{ cm}^{-1}$ peak corresponding to the CH_3 symmetric stretch vibration. A significant similarity in the spectra was observed between these two modalities with a slightly difference that might have been due to using different factors and detection method between the Raman and SRS instrumentations. In addition, using contiguous tissue sections might be another reason. With regard to imaging, the glandular epithelium was imaged using Raman and SRS techniques. SRS provided a faster and higher spatial resolution image than Raman, which enabled the identification of more numerous finer details of glandular features. Finally, K-

The Oesophagus

mean clustering was performed in the HWN using the same Raman and SRS images of glandular epithelium. The pseudocolour images of clusters identify morphological features of glandular epithelium from the surrounding connective tissues. The SRS technique is a promising technique for the identification of structural regions of oesophageal tissue compared to Raman and the images correlate well with morphological features that can be visualised in the standard H&E sections.

Chapter 8

Conclusion and Future perspective

The work presented in this thesis considers the result of experiments implemented to develop the stimulated Raman scattering technique for rapid histopathological imaging. Three experimental chapters presented the results that show a novel modification and automation of the OPO cavity, the new method used to acquire hyperspectral SRS data, and the measurements of oesophageal tissue using SRS and Raman techniques.

The first experimental chapter described to the best of the author's knowledge for the first time the modification of the OPO cavity controlled by hyperspectral software to provide rapid wavelength tuning and to perform hyperspectral images to extract the SRS spectra. The difference between the pump and the Stokes beams is required to generate the SRS signal. The Stokes beam was fixed at 1032 nm while the pump beam was tunable between 690 nm and 990 nm in the OPO. Therefore, the OPO was responsible for the wavelength tuning in the CRS techniques based on three main mechanism steps (crystal temperature, Lyot filter, and Piezo position), which caused a delay in the wavelength tuning. These steps were reduced to two steps by replacing the Lyot filter in the OPO cavity with a dispersive block. This procedure also led to stretching the phase-matched bandwidth up to 300 cm^{-1} . In this study, the CH

Conclusion and Future perspective

stretching vibration in the HWN region between 2800 cm^{-1} and 3100 cm^{-1} was the region of interest. The LBO crystal temperature was fixed at $152\text{ }^{\circ}\text{C}$ to cover this region, and the wavelength was tuned by changing the piezo position only. The performance of the OPO was investigated with both OPO designs for a comparison. It was found that the modification in the OPO cavity led to an enhancement of the OPO performance with the wavelength tuning becoming more stable and 35 times faster (1,67 second) than the conventional OPO (58 seconds). The performance of the piezo was also investigated and it was found that the piezo offered only one wavelength at each position with the modified cavity, while the same wavelength was shown at the different piezo positions with the original cavity.

The OPO was calibrated and the polynomial parameters were provided by the APE Company. However, these parameters are variable over time. Therefore, the OPO was recalibrated and the new polynomial parameters were extracted. The OPO cavity was controlled by new hyperspectral software, which was written using Matlab (2018a). This software was then integrated with the Scanimage software for running the whole setup automatically. The performance of the hyperspectral software was investigated using two standard samples PS and PMMA beads. Hyperspectral SRS images at the CH stretching vibration in the HWN between 2800 cm^{-1} and 3100 cm^{-1} were acquired and the normalisation SRS spectra were extracted. A significant similarity was found between the SRS spectra with the spectra available from the Raman technique for the same samples. This is a major contribution to field of Raman cancer diagnostics.

The second experimental chapter presented a novel method to enhance the quality of SRS images when acquiring large area montage and extracting the SRS spectra. SRS provided fast and high-resolution images in the biological sample. However, some limitations (i.e., photodamage, the microscope curvature, and the uneven elimination) occurred in this work, which affected the quality of images, mainly when acquiring hyperspectral images and a large area montage. These drawbacks were resolved in several stages. The

Conclusion and Future perspective

photodamage in biological samples occurred due to the strong intensity at the focal centre, and vibration absorption through coherent Raman processes. Therefore, the laser power was maintained under a certain threshold to keep the excitation intensity low enough. In this study, the laser damage threshold was investigated using the transmitted images of oesophagus tissue at different pump powers from 120 mW up to 170 mW. The same region was exposed to the laser 50 times and the first photodamage appeared at the pump beam of 130 mW without guarantee of the laser power threshold. The same experiment was repeated with the Stokes power, but the maximum achievable power was 116 mW, so there was no possibility of photodamage.

Acquiring an SRS large area montage was necessary to visualise the whole sample and to orientate it against the pathology images of the gold standard method (H&E). However, the FOV of the microscope was limited to 200 μm by 200 μm , and thus did not fully capture larger biomedical specimens. Thus, a series of tiles to create a large overview image for the whole sample was required. The microscope curvature is one of the main limitations when creating a montage for a large size sample, which is due to the space between the two coverslips. This issue was solved by having the spacer thickness correspond as far as possible with the thickness of the tissue section. However, the Z-position in the microscope was still variable from one region to another due to the uneven tissue surface. To solve this issue, a new Matlab script was written and integrated with the Scanimage to control the Z-position automatically, which contributed to acquiring high-resolution images. The last experimental issue was the uneven illumination, which appeared as a dark area at the boundary of each tile that had a small FOV. This issue was solved by acquiring a bright field image using the transmitted channel in the CRS setup without a sample on the coverslips and then each SRS image was divided by this image. The bright field image was taken in exactly the same conditions as for the SRS images. By applying this procedure and stitching all SRS images, this issue almost disappeared.

Conclusion and Future perspective

One of the primary purposes of this study was to extract the SRS spectra that match the Raman spectra. This was achieved by writing a new Matlab script that allows for the selection of the ROI in a large area montage followed by the acquisition of hyperspectral images and then the rapid and automatic extraction of the SRS spectra. However, the output power of the OPO fluctuated. Therefore, the normalisation power was applied by dividing the average intensity of each frame by the corresponding power. Different methods for extracting an accurate SRS spectrum similar to that available from the Raman technique were investigated, and the best method was chosen. The main contribution to the field in this chapter is to enhance the SRS imaging to make it a valuable tool for clinical diagnostics.

The third experimental chapter aims for the first time to verify the efficiency of this development, done by applying this method to the clinical samples using four different oesophagus tissues that had different morphological structures: normal squamous epithelium, inflammation, CLO, and low-grade dysplasia. Large area montage SRS, at 2930 cm^{-1} , were acquired for all samples for fast and high-resolution images. The different pathological areas in the oesophagus tissue were clearly distinguished using the label-free SRS montage similar to the H&E. Although the montage had the capability to identify these different areas in the tissue at a single frequency, there was still a need to highlight other specific components such as cell nuclei and cell bodies, which play a significant role for the histopathological diagnosis. This was achieved by applying the SRH approach on the selected ROI in the CLO and low-grade dysplasia samples. The ROI was imaged using the SRS technique at two different frequencies at 2850 cm^{-1} (CH_2 bond) and 2930 cm^{-1} (CH_3 bond). The subtraction image $\text{CH}_3\text{-CH}_2$ was calculated to highlight the cell nuclei in the tissue. The Matlab script was then written to analyse these images and then it converted them to be comparable with the corresponding H&E images. Excellent images were achieved that looked very similar to the H&E images, which making them compatible with current histological reporting. The ability to produce images that mimic the contrast of conventional histopathology (i.e. H&E) is a good strength because, if

Conclusion and Future perspective

translated into clinical diagnostic pathway allows existing expertise in histopathological diagnosis to be retained.

Finally, a comparison was made between the SRS technique and the Raman technique at the imaging and spectra level. Both techniques presented the same morphological features of the glandular epithelium in the oesophagus tissue. However, SRS provided faster and higher resolution images than Raman, which showed more precise details for the glandular features. In addition, the SRS spectra at the CH stretching vibration in the HWN region for all four different pathological groups were extracted, which were in near-perfect concordance with the spectra available from the Raman system. This was then followed by applying the K-mean clustering method to the glandular epithelium by acquiring SRS hyperspectral images and Raman mapping to identify morphological features of glandular epithelium from the surrounding connective tissues. The major contributions in this chapter are to apply a novel method to enhance the SRS imaging, to acquire a rapid large area montage, to extract SRS spectra rapidly and to apply, for the first time, the SRH approach on oesophagus tissues for cancer diagnostic.

Future perspective

This thesis has provided the ability of the SRS technique for rapid and high-resolution hyperspectral images of the clinical samples compared to the Raman system. It has also offered rapid extraction the SRS spectra in the HWN region. However, there are many factors in the SRS technique limit the existence of large-scale studies with large clinical sample numbers, such as the high initial costs of equipment and a complex optical bench several metres long that requires highly trained users. Moreover, the SRS spectral resolution still needs further optimisation due to the large wavenumber steps (depends on the piezo step size) and also the acquisition time increases whenever the wavenumber step is reduced. Therefore, more development is needed to be applied to make the SRS more reliable and suitable as a new clinical technique. Recently, we started to build a new facility using a Spectral

Conclusion and Future perspective

Focusing Timing and Recombination Unit (SF-TRU) module for dual-output and dual-wavelength lasers [194, 195]. This method is based on chirping the excitation femtosecond pulses in order to their entire broad bandwidth into a narrow spectral region, which allows achieving high spectral resolution in nonlinear spectroscopy and microscopy. The SF-TRU offers a very simple procedure for the wavelength tuning by controlling the time delay between the chirped pump and Stokes pulses, which provide faster hyperspectral imaging with a high spectral resolution up to 5 cm^{-1} . Compared to the current SRS with synchronised picosecond beams, the SF-TRU has a compact and flexible design, easily controlled and integrated with a laser scanning microscope for SRS experiments and it provides convenient and rapid Raman tuning for hyperspectral imaging purposes. For extracting SRS spectra, the current technique requires approximately 4.5 minutes with between 6 cm^{-1} to 8 cm^{-1} spectral resolution to cover the HWN region, while the SF-TRU requires less than one minute to acquire, with up to 5 cm^{-1} spectral resolution. In addition, the SF-TRU is designed to allow easily switching from dual- to single-beam modes and from chirped picosecond to femtosecond regimes and vice versa without affecting the functionality and alignment inside the microscope. In the next study, the same clinical samples used in this thesis will be used with the SF-TRU setup for comparison. The data acquired from this experiment could also be used in later experiments for comparison with both Raman and IR techniques and see whether the technique is able to identify the morphological structure and extract the biochemical information of oesophagus tissue.

References

- [1] “Cancer Research UK “Cancer in general“.” [Online]. Available: <https://www.cancerresearchuk.org/about-cancer/cancer-in-general>. [Accessed: 06-Jan-2019].
- [2] F. Bray, J. Ferlay, I. Soerjomataram, R. L. Siegel, L. A. Torre, and A. Jemal, “Global Cancer Statistics 2018: GLOBOCAN Estimates of Incidence and Mortality Worldwide for 36 Cancers in 185 Countries,” *CA. Cancer J. Clin.*, vol. 68, no. 6, pp. 394–424, 2018.
- [3] “Cancer Research UK, ‘Oesophageal cancer statistics.’” [Online]. Available: <https://www.cancerresearchuk.org/health-professional/cancer-statistics/statistics-by-cancer-type/oesophageal-cancer#heading-zero>. [Accessed: 06-Jan-2019].
- [4] “Cancer Research UK, ‘Cancer incidence for common cancers.’” [Online]. Available: <https://www.cancerresearchuk.org/health-professional/cancerstatistics>. [Accessed: 06-Jan-2019].
- [5] R. . Ruddon, “Cancer biology,” *Oxford Univ. Press*, 2007.
- [6] D. A. Corley and P. A. Buffler, “Oesophageal and gastric cardia adenocarcinomas: Analysis of regional variation using the Cancer Incidence in Five Continents database,” *Int. J. Epidemiol.*, vol. 30, no. 6, pp. 1415–1425, 2001.
- [7] “Macmillan Cancer Support “The oesophagus - Understanding.”” [Online]. Available: <https://www.macmillan.org.uk/information-and-support/oesophageal-gullet-cancer/understanding-cancer/the->

References

- oesophagus.html. [Accessed: 06-Jan-2019].
- [8] “SlidePlayer ’ ‘Histology of digestive system oesophagus, stomach-fundus & pylorus - ppt video online.” [Online]. Available: <https://slideplayer.com/slide/5258423/>. [Accessed: 06-Jan-2019].
- [9] M.C. Wong, D.C. Hamilton, J.Y. Jiang, Y. Qiao, F.D. Fung, H.H. Wang, P.W. Chiu, E.K. Ng, J.C. Wu, and J. Yu, “Global Incidence and mortality of oesophageal cancer and their correlation with socioeconomic indicators temporal patterns and trends in 41 countries,” *Sci. Rep.*, vol. 8, no. 1, pp. 1–13, 2018.
- [10] “Cancer Research UK, “Oesophageal cancer survival statistics by age.”” [Online]. Available: <https://www.cancerresearchuk.org/health-professional/cancer-statistics/statistics-by-cancer-type/oesophageal-cancer/survival#heading-Zero>. [Accessed: 06-Jan-2019].
- [11] D. Romero, “Genetics: Oesophageal cancer-not all alike,” *Nat. Rev. Clin. Oncol.*, vol. 14, no. 3, p. 138, 2017.
- [12] J.M. Daly, W.A. Fry, A.G. Little, D.P. Winchester, R.F. McKee, A.K. Stewart, and A.M. Fremgen, “Esophageal cancer: results of an American College of Surgeons patient care evaluation study11No competing interests declared.” *J. Am. Coll. Surg.*, vol. 190, no. 5, pp. 562–572, 2000.
- [13] R. Pötter and E. Van Limbergen, “Oesophageal Cancer,” *Surg. (United Kingdom)*, vol. 32, no. 11, pp. 588–593, 2014.
- [14] E. E. van der Wall, “Increasing recognition of NHJ: A first-time impact factor of 1.4!,” *Netherlands Hear. J.*, vol. 18, no. 9, p. 399, 2010.
- [15] E. L. Bird-Lieberman and R. C. Fitzgerald, “Early diagnosis of oesophageal cancer,” *Br. J. Cancer*, vol. 101, no. 1, pp. 1–6, 2009.
- [16] R. Maric and K. K. Cheng, . “Classification of adenocarcinoma of the oesophagogastric junction,” *Br. J. Surg.*, vol. 86, no. 8, pp. 1098–1098, 1999.
- [17] J. Lagergren, R. Bergstrom, A. Lindgren, and O. Nyren, “Symptomatic Gastroesophageal Reflux As A Risk Factor for Esophageal Adenocarcinoma,” *N. Engl. J. Med.*, vol. 340, no. 11, pp. 825–831, 1999.

References

- [18] W. Chow, J. F. Fraumeni, W. D. Finkle, J. K. Mclaughlin, H. Frankl, and H. K. Ziel, "The Relation of Gastroesophageal Reflux Disease and Its Treatment to Adenocarcinomas of the Esophagus and Gastric Cardia," *JAMA J. Am. Med. Assoc.*, vol. 274, no. 6, pp. 474–477, 1995.
- [19] J. Lagergren, "Influence of Obesity on the Risk for Esophageal Disorders: Obesity and GERD," *Nature review Gastroenterology & hepatology*, vol. 8, no. 6, pp. 1–12, 2011.
- [20] D.C. Whiteman, S. Sadeghi, N. Pandeya, B.M. Smithers, D.C. Gotley, C.J. Bain, P.M. Webb, and A.C. Green, "Combined effects of obesity, acid reflux and smoking on the risk of adenocarcinomas of the oesophagus," *Gut*, vol. 57, no. 2, pp. 173–180, 2008.
- [21] J. Powell, C. C. McConkey, E. Walford Gillison, and R. T. Spychal, "Continuing rising trend in oesophageal adenocarcinoma," *Int. J. Cancer*, vol. 102, no. 4, pp. 422–427, 2002.
- [22] E. Bollschweiler, E. Wolfgarten, C. Gutschow, and A. H. Hölscher, "Demographic variations in the rising incidence of esophageal adenocarcinoma in white males," *Cancer*, vol. 92, no. 3, pp. 549–555, 2001.
- [23] L.A. Anderson, M.M. Cantwell, R.P. Watson, B.T. Johnston, S.J. Murphy, H.R. Ferguson, J. McGuigan, H. Comber, J.V. Reynolds, and L.J. Murray, "The Association Between Alcohol and Reflux Esophagitis, Barrett's Esophagus, and Esophageal Adenocarcinoma," *Gastroenterology*, vol. 136, no. 3, pp. 799–805, 2009.
- [24] P. Terry, J. B. Terry, and A. Wolk, "Fruit and vegetable consumption in the prevention of cancer: an update.," *J. Intern. Med.*, vol. 250, no. 4, pp. 280–90, 2001.
- [25] J. F. Fléjou, "Barrett's oesophagus: From metaplasia to dysplasia and cancer," *Gut*, vol. 54, no. SUPPL. 1, pp. 6–12, 2005.
- [26] J.A. Jankowski, N.A. Wright, S.J. Meltzer, G. Triadafilopoulos, K. Geboes, A.G. Casson, D. Kerr, and L.S. Young, "Molecular evolution of the metaplasia-dysplasia-adenocarcinoma sequence in the esophagus," *Am. J. Pathol.*, vol. 154, no. 4, pp. 965–973, 1999.

References

- [27] J. a Jankowski, R. F. Harrison, I. Perry, F. Balkwill, and C. Tselepis, "Barrett ' s metaplasia," *Lancet*, vol. 356, pp. 2079–2085, 2000.
- [28] R. C. Fitzgerald, "Molecular basis of Barrett's oesophagus and oesophageal adenocarcinoma," *Gut*, vol. 55, no. 12, pp. 1810–1820, 2006.
- [29] S. S.J., F. R.C., P. G.A., and W. K.K., "History, Molecular Mechanisms, and Endoscopic Treatment of Barrett's Esophagus," *Gastroenterology*, vol. 138, no. 3, pp. 854–869, 2010.
- [30] M.B. Cook, C.P. Wild, S.M. Everett, L.J. Hardie, K.E. Bani-Hani, I.G. Martin, and D. Forman, "Risk of mortality and cancer incidence in Barrett's esophagus," *Cancer Epidemiol. Biomarkers Prev.*, vol. 16, no. 10, pp. 2090–2096, 2007.
- [31] M. A. Eloubeidi and D. Provenzale, "Clinical and demographic predictors of Barrett's esophagus among patients with gastroesophageal reflux disease: A multivariable analysis in veterans," *J. Clin. Gastroenterol.*, vol. 33, no. 4, pp. 306–309, 2001.
- [32] S. Rajendra and P. Sharma, "Management of Barrett's oesophagus and intramucosal oesophageal cancer: A review of recent development," *Therap. Adv. Gastroenterol.*, vol. 5, no. 5, pp. 285–299, 2012.
- [33] E. W. Gilbert, R. A. Luna, V. L. Harrison, and J. G. Hunter, "Barrett's Esophagus: A Review of the Literature," *J. Gastrointest. Surg.*, vol. 15, no. 5, pp. 708–718, 2011.
- [34] F. Yousef, C. Cardwell, M. M. Cantwell, K. Galway, B. T. Johnston, and L. Murray, "The incidence of esophageal cancer and high-grade dysplasia in Barrett's esophagus: A systematic review and meta-analysis," *Am. J. Epidemiol.*, vol. 168, no. 3, pp. 237–249, 2008.
- [35] M. Sikkema, PJ. De Jonge, EW. Steyerberg, EJ. Kuipers, "Risk of Esophageal Adenocarcinoma and Mortality in Patients With Barrett's Esophagus: A Systematic Review and Meta-analysis," *Clin. Gastroenterol. Hepatol.*, vol. 8, no. 3, pp. 235–244, 2010.
- [36] M. Rugge, M. Fassan, F. Cavallini, and G. Zaninotto, "Re: Risk of Malignant Progression in Barrett's Esophagus Patients: Results from a Large Population-Based Study," *JNCI J. Natl. Cancer Inst.*, vol. 104, no.

References

- 22, pp. 1771–1772, 2012.
- [37] L.A. Anderson, L.J. Murray, S.J. Murphy, D.A. Fitzpatrick, B.T. Johnston, R.G.P. Watson, P. McCarron, and A.T. Gavin, “Mortality in Barrett’s oesophagus: Results from a population based study,” *Gut*, vol. 52, no. 8, pp. 1081–1084, 2003.
- [38] A. Chonan *et al.*, “Endoscopic resection of early gastric cancer,” *Gastroenterol. Endosc.*, vol. 36, no. 9, pp. 1692–1701, 2007.
- [39] R. S. Gill and R. Singh, “Endoscopic imaging in Barrett’s esophagus: Current practice and future applications,” *Ann. Gastroenterol.*, vol. 25, no. 2, pp. 89–95, 2012.
- [40] “Oncology Practice ‘ ’ Barrett’s Esophagus: cancer risk id highest in first year after diagnosis”.” [Online]. Available: <https://www.mdedge.com/oncologypractice/article/132833>. [Accessed: 06-Jan-2019].
- [41] E. Montgomery, M.P. Bronner, J.R. Goldblum, J.K. Greenson, M.M. Haber, J. Hart, L.W. Lamps, G.Y. Lauwers, A.J. Lazenby, D.N. Lewin, and M.E. Robert, “Reproducibility of the diagnosis of dysplasia in Barrett esophagus: A reaffirmation,” *Hum. Pathol.*, vol. 32, no. 4, pp. 368–378, 2001.
- [42] S. Jain and S. Dhingra, “Pathology of esophageal cancer and Barrett’s esophagus,” *Ann. Cardiothorac. Surg.*, vol. 6, no. 2, pp. 99–109, 2017.
- [43] R. Nakadate *et al.*, “Endoscopy,” *Int. J. Comput. Assist. Radiol. Surg.*, vol. 9, no. S1, pp. 181–186, 2014.
- [44] T. Fukuhara, S. J. Vorster, and M. G. Luciano, “Risk factors for failure of endoscopic third ventriculostomy for obstructive hydrocephalus,” *Neurosurgery*, vol. 46, no. 5, pp. 1100–1111, 2000.
- [45] “Medical Encyclopedia , ‘Esophageal tissue culture.’” [Online]. Available: <https://medlineplus.gov/ency/imagepages/9303.htm>. [Accessed: 06-Jan-2019].
- [46] R. Soetikno, T. Kaltenbach, R. Yeh, and T. Gotoda, “Endoscopic mucosal resection for early cancers of the upper gastrointestinal tract,” *J. Clin. Oncol.*, vol. 23, no. 20, pp. 4490–4498, 2005.
- [47] A. Mescher, *Jungueira’s Basic histology: Text and atlas, 12th edition*.

References

- The McGraw-Hill companies, 2010.* .
- [48] T. W. Rice and T. W. Rice, "Martinez Pastur 1999-Regeneracion lenga y guanaco.pdf," vol. 6516, pp. 157–163, 2015.
- [49] T. Schrader, A. Sieg, F. Koller, W. Schreier, Q. An, W. Zinth, and P. Gilch, "Vibrational relaxation following ultrafast internal conversion: Comparing IR and Raman probing," *Chem. Phys. Lett.*, vol. 392, no. 4–6, pp. 358–364, 2004.
- [50] M.J. Baker, H.J. Byrne, J. Chalmers, P. Gardner, R. Goodacre, A. Henderson, S.G. Kazarian, F.L. Martin, J. Moger, N. Stone, and J. Sulé-Suso, "Clinical applications of infrared and Raman spectroscopy: State of play and future challenges," *Analyst*, vol. 143, no. 8, pp. 1735–1757, 2018.
- [51] H.J. Byrne, M. Baranska, G.J. Puppels, N. Stone, B. Wood, K.M. Gough, P. Lasch, P. Heraud, J. Sulé-Suso, and G.D. Sockalingum, "Spectropathology for the next generation: Quo vadis?," *Analyst*, vol. 140, no. 7, pp. 2066–2073, 2015.
- [52] M. B. Fenn, P. Xanthopoulos, G. Pyrgiotakis, S. R. Grobmyer, P. M. Pardalos, and L. L. Hench, "Raman spectroscopy for clinical oncology," *Adv. Opt. Technol.*, 2011.
- [53] R. Petry, M. Schmitt, and J. Popp, "Raman Spectroscopy---A Prospective Tool in the Life Sciences - Petry - 2002 - ChemPhysChem - Wiley Online Library," *ChemPhysChem*, vol. 4, pp. 14–30, 2003.
- [54] K. H. Rieder, S. Nie, and S. R. Emory, "Probing Single Molecules and Single Nanoparticles by Surface-Enhanced Raman Scattering Downloaded from," *Angew. Chem. Int. Ed. Engl*, vol. 50, no. 1, p. 1828, 1994.
- [55] M.S. Bergholt, W. Zheng, K. Lin, K.Y. Ho, M. Teh, K.G. Yeoh, J.B.Y. So, and Z. Huang, "Raman endoscopy for in vivo differentiation between benign and malignant ulcers in the stomach," *Analyst*, vol. 135, no. 12, pp. 3162–3168, 2010.
- [56] L. Gao, H. Zhou, M.J. Thrall, F. Li, Y. Yang, Z. Wang, P. Luo, K.K. Wong, G.S. Palapattu, and S.T. Wong, "Label-free high-resolution imaging of prostate glands and cavernous nerves using coherent anti-

References

- Stokes Raman scattering microscopy,” *Biomed. Opt. Express*, vol. 2, no. 4, p. 915, 2011.
- [57] C. Krafft, A.A. Ramoji, C. Bielecki, N. Vogler, T. Meyer, D. Akimov, P. Rösch, M. Schmitt, B. Dietzek, I. Petersen, and A. Stallmach, “A comparative Raman and CARS imaging study of colon tissue,” *J. Biophotonics*, vol. 2, no. 5, pp. 303–312, 2009.
- [58] C.Y. Lin, E.O. Potma, J.L. Suhalim, C.L. Nien, J.V. Jester, M.D. Miljkovic, and M. Diem, “Picosecond spectral coherent anti-Stokes Raman scattering imaging with principal component analysis of meibomian glands,” *J. Biomed. Opt.*, vol. 16, no. 2, p. 021104, 2011.
- [59] C. J. Strachan, M. Windbergs, and H. L. Offerhaus, “Pharmaceutical applications of non-linear imaging,” *Int. J. Pharm.*, vol. 417, no. 1–2, pp. 163–172, 2011.
- [60] C. Aku-Leh, J. Zhao, R. Merlin, J. Menéndez, and M. Cardona, “Long-lived optical phonons in ZnO studied with impulsive stimulated Raman scattering,” *Phys. Rev. B - Condens. Matter Mater. Phys.*, vol. 71, no. 20, pp. 1–4, 2005.
- [61] B.G. Saar, Y. Zeng, C.W. Freudiger, Y.S. Liu, M.E. Himmel, X.S. Xie, and S.Y. Ding, “Label-free, real-time monitoring of biomass processing with stimulated raman scattering microscopy,” *Angew. Chemie - Int. Ed.*, vol. 49, no. 32, pp. 5476–5479, 2010.
- [62] S. Shim, C. M. Stuart, and R. A. Mathies, “Resonance Raman cross-sections and vibronic analysis of rhodamine 6G from broadband stimulated raman spectroscopy,” *ChemPhysChem*, vol. 9, no. 5, pp. 697–699, 2008.
- [63] C.C. Wang, S. Moorhouse, C. Stain, M. Seymour, E. Green, S. Penfield, and J. Moger, “In situ chemically specific mapping of agrochemical seed coatings using stimulated Raman scattering microscopy,” *J. Biophotonics*, vol. 11, no. 11, pp. 1–7, 2018.
- [64] C. Krafft, I. W. Schie, T. Meyer, M. Schmitt, and J. Popp, “Developments in spontaneous and coherent Raman scattering microscopic imaging for biomedical applications,” *Chem. Soc. Rev.*, vol. 45, no. 7, pp. 1819–1849, 2016.

References

- [65] C.H. Camp Jr, Y.J. Lee, J.M. Heddleston, C.M. Hartshorn, A.R.H. Walker, J.N. Rich, J.D. Lathia, and M.T. Cicerone, “High-speed coherent Raman fingerprint imaging of biological tissues,” *Nat. Photonics*, vol. 8, no. 8, pp. 627–634, 2014.
- [66] D.A. Orringer, B. Pandian, Y.S. Niknafs, T.C. Hollon, J. Boyle, S. Lewis, M. Garrard, S.L. Hervey-Jumper, H.J. Garton, C.O. Maher, and J.A. Heth, “Rapid intraoperative histology of unprocessed surgical specimens via fibre-laser-based stimulated Raman scattering microscopy,” *Nat. Biomed. Eng.*, vol. 1, no. 2, pp. 1–10, 2017.
- [67] B. Sarri, R. Canonge, X. Audier, E. Simon, J. Wojak, F. Caillol, C. Cador, D. Marguet, F. Poizat, M. Giovannini, and H. Rigneault, “Fast stimulated Raman imaging for intraoperative gastro- intestinal cancer detection,” *arXiv Prepr. arXiv*, vol. 1902.08859, 2019.
- [68] H.J. Butler, L. Ashton, B. Bird, G. Cinque, K. Curtis, J. Dorney, K. Esmonde-White, N.J. Fullwood, B. Gardner, P.L. Martin-Hirsch, and M.J. Walsh, “Using Raman spectroscopy to characterise biological materials,” *Nat. Protoc.*, vol. 11, no. 4, pp. 664–687, 2016.
- [69] C. V. Raman and K. S. Krishnan, “A New Type of Secondary Radiation. Nature, vol. 121, pp. 501–502, 1928.
- [70] K. Kong, C. Kendall, N. Stone, and I. Notingher, “Raman spectroscopy for medical diagnostics — From in-vitro biofluid assays to in-vivo cancer detection,” *Advanced drug delivery reviews*, vol. 89, pp.121-134, 2015.
- [71] A. Sakudo, “Near-infrared spectroscopy for medical applications: Current status and future perspectives,” *Clin. Chim. Acta*, vol. 455, pp. 181–188, 2016.
- [72] K. Kong, C. Kendall, N. Stone, and I. Notingher, “Raman spectroscopy for medical diagnostics - From in-vitro biofluid assays to in-vivo cancer detection,” *Adv. Drug Deliv. Rev.*, vol. 89, pp. 121–134, 2015.
- [73] R. M. Santos, Luís F. Wolthuis, Rolf. Koljenović, S. Almeida and G. J. Puppels, “Fiber-optic probes for in vivo Raman spectroscopy in the high-wavenumber region,” *Anal. Chem.*, vol. 77, no. 20, pp. 6747–6752, 2005.
- [74] J. M. Koljenović, S. Schut, T. C.Bakker. Wolthuis, R. Vincent, A. J.P.E.

References

- Hendriks. Hagevi, G. Santos, L. Kros and G. J. Puppels, "Raman spectroscopic characterization of porcine brain tissue using a single fiber-optic probe," *Analytical Chemistry*, vol. 79, no. 2, pp. 557–564, 2007.
- [75] S. Koljenovic, T.C.B. Schut, R. Wolthuis, B. De Jong, L. Santos, P.J. Caspers, J.M. Kros, and G.J. Puppels, "Tissue characterization using high wave number Raman spectroscopy," *J. Biomed. Opt.*, vol. 10, no. 3, p. 031116, 2005.
- [76] R. Kirsch, Matthias. Schackert, Gabriele. Salzer and C. Krafft, "Raman spectroscopic imaging for in vivo detection of cerebral brain metastases," *Anal. Bioanal. Chem.*, vol. 398, no. 4, pp. 1707–1713, 2010.
- [77] R. Krafft, Christoph. Belay, Birhanu. Bergner, Norbert. Romeike, Bernd F.M. Reichart, Rupert. Kalff and J. Popp, "Advances in optical biopsy-correlation of malignancy and cell density of primary brain tumors using Raman microspectroscopic imaging," *Analyst*, vol. 137, no. 23, pp. 5533–5537, 2012.
- [78] C. Bergner, N. Medyukhina, A. Geiger, K. Kirsch, M. Schackert, G. Krafft and J. Popp, "Hyperspectral unmixing of Raman micro-images for assessment of morphological and chemical parameters in non-dried brain tumor specimens," *Anal. Bioanal. Chem.*, vol. 405, no. 27, pp. 8719–8728, 2013.
- [79] F. X. Liu, Y. Xiao, and Y. S. Li, "Near-infrared raman spectroscopy of human lung tissues: Possibility of molecular-level cancer diagnosis," *J. Raman Spectrosc.*, vol. 32, no. 2, pp. 139–141, 2001.
- [80] Z. Huang, A. McWilliams, H. Lui, D. I. McLean, S. Lam, and H. Zeng, "Near-infrared Raman spectroscopy for optical diagnosis of lung cancer," *Int. J. Cancer*, vol. 107, no. 6, pp. 1047–1052, 2003.
- [81] G. Shetty, C. Kendall, N. Shepherd, N. Stone, and H. Barr, "Raman spectroscopy: Elucidation of biochemical changes in carcinogenesis of oesophagus," *Br. J. Cancer*, vol. 94, no. 10, pp. 1460–1464, 2006.
- [82] J. Hutchings, C. Kendall, B. Smith, N. Shepherd, H. Ban, and N. Stone, "The potential for histological screening using a combination of rapid

References

- Raman mapping and principal component analysis,” *J. Biophotonics*, vol. 2, no. 1–2, pp. 91–103, 2009.
- [83] C. Kendall, N. Stone, N. Shepherd, K. Geboes, B. Warren, R. Bennett, and H. Barr, “Raman spectroscopy, a potential tool for the objective identification and classification of neoplasia in Barrett’s oesophagus,” *J. Pathol.*, vol. 200, no. 5, pp. 602–609, 2003.
- [84] N. Stone, C. Kendall, N. Shepherd, P. Crow, and H. Barr, “Near-infrared Raman spectroscopy for the classification of epithelial pre-cancers and cancers,” *J. Raman Spectrosc.*, vol. 33, no. 7, pp. 564–573, 2002.
- [85] T. C. B. Schut, N. Stone, C. A. Kendall, H. Barr, H. A. Bruining, and G. J. Puppels, “Progress in the detection of neoplastic progress and cancer by Raman spectroscopy,” *BiOS 2000 Int. Symp. Biomed. Opt.*, pp. 106–113, 2000.
- [86] G. R. Lloyd, J. Hutchings, L. M. Almond, H. Barr, C. Kendall, and N. Stone, “Assessing the performance of spectroscopic models for cancer diagnostics using cross-validation and permutation testing,” *SPIE BiOS*, pp. 82190C--82190C, 2012.
- [87] J. Wang, K. Lin, W. Zheng, K.Y. Ho, M. Teh, K.G. Yeoh, and Z. Huang, “Simultaneous fingerprint and high-wavenumber fiber-optic Raman spectroscopy improves in vivo diagnosis of esophageal squamous cell carcinoma at endoscopy,” *Sci. Rep.*, vol. 5, pp. 1–10, 2015.
- [88] Z. Huang, M.S. Bergholt, W. Zheng, K. Lin, K.Y. Ho, and K.G. Yeoh, “In vivo early diagnosis of gastric dysplasia using narrow-band image-guided Raman endoscopy,” *J. Biomed. Opt.*, vol. 15, no. 3, p. 037017, 2010.
- [89] Z. Huang, S.K. Teh, W. Zheng, K. Lin, K.Y. Ho, M. Teh, and K.G. Yeoh, “In vivo detection of epithelial neoplasia in the stomach using image-guided Raman endoscopy,” *Biosens. Bioelectron.*, vol. 26, no. 2, pp. 383–389, 2010.
- [90] M.S. Bergholt, W. Zheng, K. Lin, K.Y. Ho, M. Teh, K.G. Yeoh, J.B.Y. So, and Z. Huang, “Raman endoscopy for in vivo differentiation between benign and malignant ulcers in the stomach.,” *Analyst*, vol. 135, pp. 3162–3168, 2010.

References

- [91] L. F. Santos, R. Wolthuis, S. Koljenović, R. M. Almeida, and G. J. Puppels, "Fiber-optic probes for in vivo Raman spectroscopy in the high-wavenumber region," *Anal. Chem.*, vol. 77, no. 20, pp. 6747–6752, 2005.
- [92] M.S. Bergholt, W. Zheng, K. Lin, K.Y. Ho, M. Teh, K.G. Yeoh, J.B.Y. So, A. Shabbir, and Z. Huang, "Fiber-optic Raman spectroscopy probes gastric carcinogenesis in vivo at endoscopy," *J. Biophotonics*, vol. 6, no. 1, pp. 49–59, 2013.
- [93] C. L. Evans and X. S. Xie, "Coherent Anti-Stokes Raman Scattering Microscopy: Chemical Imaging for Biology and Medicine," *Annu. Rev. Anal. Chem.*, vol. 1, no. 1, pp. 883–909, 2008.
- [94] Z. Huang, S.K. Teh, W. Zheng, K. Lin, K.Y. Ho, M. Teh, and K.G. Yeoh, "In vivo detection of epithelial neoplasia in the stomach using image-guided Raman endoscopy," *Biosens. Bioelectron.*, vol. 26, no. 2, pp. 383–389, 2010.
- [95] M.S. Bergholt, W. Zheng, K. Lin, K.Y. Ho, M. Teh, K.G. Yeoh, J.B.Y. So, and Z. Huang, "Raman endoscopy for in vivo differentiation between benign and malignant ulcers in the stomach," *Analyst*, vol. 135, no. 12, p. 3162, 2010.
- [96] M.S. Bergholt, W. Zheng, K. Lin, K.Y. Ho, M. Teh, K.G. Yeoh, J.B. So, and Z. Huang, "In vivo diagnosis of gastric cancer using Raman endoscopy and ant colony optimization techniques," *Int. J. Cancer*, vol. 128, no. 11, pp. 2673–2680, 2011.
- [97] C. Kendall, J. Day, J. Hutchings, B. Smith, N. Shepherd, H. Barr, and N. Stone, "Evaluation of Raman probe for oesophageal cancer diagnostics," *Analyst*, vol. 135, no. 12, p. 3038, 2010.
- [98] L.M. Almond, J. Hutchings, G. Lloyd, H. Barr, N. Shepherd, J. Day, O. Stevens, S. Sanders, M. Wadley, N. Stone, and C. Kendall, "Endoscopic Raman spectroscopy enables objective diagnosis of dysplasia in Barrett's esophagus," *Gastrointest. Endosc.*, vol. 79, no. 1, pp. 37–45, 2014.
- [99] M.S. Bergholt, W. Zheng, K. Lin, Z. Huang, K.Y. Ho, K.G. Yeoh, and J.B. So, "Characterizing variability in in vivo Raman spectra of different

References

- anatomical locations in the upper gastrointestinal tract toward cancer detection,” *J. Biomed. Opt.*, vol. 16, no. 3, p. 037003, 2011.
- [100] M.S. Bergholt, W. Zheng, K. Lin, K.Y. Ho, M. Teh, K.G. Yeoh, J.B. So, and Z. Huang, “Combining near-infrared-excited autofluorescence and Raman spectroscopy improves in vivo diagnosis of gastric cancer,” *Biosens. Bioelectron.*, vol. 26, no. 10, pp. 4104–4110, 2011.
- [101] M.S. Bergholt, W. Zheng, K. Lin, K.Y. Ho, M. Teh, K.G. Yeoh, J.B. So, and Z. Huang, “*In Vivo* Diagnosis of Esophageal Cancer Using Image-Guided Raman Endoscopy and Biomolecular Modeling,” *Technol. Cancer Res. Treat.*, vol. 10, no. 2, pp. 103–112, 2011.
- [102] S. Duraipandian, M.S. Bergholt, W. Zheng, K.Y. Ho, M. Teh, K.G. Yeoh, J.B.Y. So, A. Shabbir, and Z. Huang, “Real-time Raman spectroscopy for in vivo, online gastric cancer diagnosis during clinical endoscopic examination,” *J. Biomed. Opt.*, vol. 17, no. 10, 2012.
- [103] C.W. Freudiger, W. Min, B.G. Saar, S. Lu, G.R. Holtom, C. He, J.C. Tsai, J.X. Kang, and X.S. Xie, “Label-Free Biomedical Imaging with High Sensitivity by Stimulated Raman Scattering Microscopy,” *Science* (80-.), vol. 322(5909), pp. 1857-1861., 2008.
- [104] Y. Ozeki, F. Dake, S. Kajiyama, K. Fukui, and K. Itoh, “Analysis and experimental assessment of the sensitivity of stimulated Raman scattering microscopy,” *Opt. Express*, vol. 17, no. 5, p. 3651, 2009.
- [105] P. Nandakumar, A. Kovalev, and A. Volkmer, “Vibrational imaging Based on stimulated Raman scattering microscopy,” *New J. Phys.*, vol. 11, no. 3, p. 33026, 2009.
- [106] D. Zhang, P. Wang, M. N. Slipchenko, D. Ben-Amotz, A. M. Weiner, and J. X. Cheng, “Quantitative vibrational imaging by hyperspectral stimulated raman scattering microscopy and multivariate curve resolution analysis,” *Anal. Chem.*, vol. 85, no. 1, pp. 98–106, 2013.
- [107] R.W. Terhune, P.D. Maker, and C.M. Savage, “Measurements of nonlinear light scattering,” *Physical Review Letters*, vol.14, no.17, p.681, 1965.
- [108] M.D. Duncan, J. Reintjes, and T. J. Manuccia, “Scanning coherent anti-Stokes Raman microscope,” *Opt. Lett.*, vol. 7, no. 8, p. 350, 1982.

References

- [109] A. Zumbusch, G. R. Holtom, and X. S. Xie, "Three-Dimensional Vibrational Imaging by Coherent Anti-Stokes Raman Scattering," *Phys. Rev. Lett.*, vol. 82(20), p. 4142, 1999.
- [110] J. X. Cheng, L. D. Book, and X. S. Xie, "Polarization coherent anti-Stokes Raman scattering microscopy," *Opt. Lett.*, vol. 26, no. 17, pp. 1341–1343, 2001.
- [111] X. S. Xie, J.-X. Cheng, Y. K. Jia, and G. Zheng, "Laser-scanning coherent anti-Stokes Raman scattering microscopy and applications to cell biology," *Biophys. J.*, vol. 83, no. 1, pp. 502–9, 2002.
- [112] A. Volkmer, J. X. Cheng, and X. S. Xie, "Vibrational imaging with high sensitivity via epideTECTED coherent anti-stokes raman scattering microscopy," *Phys. Rev. Lett.*, vol. 87, no. 2, pp. 2–5, 2001.
- [113] C. L. Evans, E. O. Potma, M. Puoris'haag, D. Cote, C. P. Lin, and X. S. Xie, "Chemical imaging of tissue in vivo with video-rate coherent anti-Stokes Raman scattering microscopy," *Proc. Natl. Acad. Sci.*, vol. 102, no. 46, pp. 16807–16812, 2005.
- [114] J.-X. Cheng, A. Volkmer, and X. S. Xie, "Theoretical and experimental characterization of coherent anti-Stokes Raman scattering microscopy," *J. Opt. Soc. Am. B*, vol. 19, no. 6, p. 1363, 2002.
- [115] M. Müller and J. M. Schins, "Imaging the thermodynamic state of lipid membranes with multiplex CARS microscopy," *J. Phys. Chem. B*, vol. 106, no. 14, pp. 3715–3723, 2002.
- [116] J. X. Cheng, A. Volkmer, L. D. Book, and X. S. Xie, "Multiplex coherent anti-stokes Raman scattering microspectroscopy and study of lipid vesicles," *J. Phys. Chem. B*, vol. 106, no. 34, pp. 8493–8498, 2002.
- [117] H. A. Rinia, M. Bonn, and M. Müller, "Quantitative multiplex CARS spectroscopy in congested spectral regions," *J. Phys. Chem. B*, vol. 110, no. 9, pp. 4472–4479, 2006.
- [118] T. W. Kee, H. Zhao, and M. T. Cicerone, "One-laser interferometric broadband coherent anti-Stokes Raman scattering," *Opt. Express*, vol. 14, no. 8, p. 3631, 2006.
- [119] D. L. Marks and S. A. Boppart, "Nonlinear interferometric vibrational imaging," *Phys. Rev. Lett.*, vol. 92, no. 12, pp. 1–5, 2004.

References

- [120] F. Lehmann-Horn, R. Rüdél, and K. Ricker, "Label-Free Delineation of Brain Tumors by Coherent Anti-Stokes Raman Scattering Microscopy in an Orthotopic Mouse Model and Human Glioblastoma," *PLoS One*, vol. 9(9), p. 107115, 2014.
- [121] M. Lee, A. Downes, Y.Y. Chau, B. Serrels, N. Hastie, A. Elfick, V. Brunton, M. Frame, and A. Serrels, "In vivo imaging of the tumor and its associated microenvironment using combined CARS / 2-photon microscopy," *IntraVital*, vol. 4, no. 1, pp. 1–8, 2015.
- [122] B. Dietzek, T. Meyer, A. Medyukhina, N. Bergner, C. Krafft, B.F. Romeike, R. Reichart, R. Kalff, M. Schmitt, and J. Popp, "Interpreting CARS images of tissue within the C-H-stretching region," *J. Biophotonics*, vol. 5, no. 10, pp. 729–733, 2012.
- [123] L. Gao, Z. Wang, F. Li, A.A. Hammoudi, M.J. Thrall, P.T. Cagle, and S.T. Wong, "Differential diagnosis of lung carcinoma with coherent anti-stokes raman scattering imaging," *Arch. Pathol. Lab. Med.*, vol. 136, no. 12, pp. 1502–1510, 2012.
- [124] L.S. Gao, F. Li, Y. Yang, J. Xing, A.A. Hammoudi, H. Zhao, Y. Fan, K.K. Wong, Z. Wang, S.T. Wong, and M.J. Thrall, "On-the-spot lung cancer differential diagnosis by label-free, molecular vibrational imaging and knowledge-based classification," *J. Biomed. Opt.*, vol. 16, no. 9, p. 096004, 2011.
- [125] T. T. Le, T. B. Huff, and J. X. Cheng, "Coherent anti-Stokes Raman scattering imaging of lipids in cancer metastasis," *BMC Cancer*, vol. 9, pp. 1–14, 2009.
- [126] C. L. Evans, X. Xu, S. Kesari, X. S. Xie, S. T. C. Wong, and G. S. Young, "Chemically-selective imaging of brain structures with CARS microscopy," *Opt. Express*, vol. 15, no. 19, p. 12076, 2007.
- [127] R. Mitra, O. Chao, Y. Urasaki, O. B. Goodman, and T. T. Le, "Detection of Lipid-Rich Prostate Circulating Tumour Cells with Coherent Anti-Stokes Raman Scattering Microscopy," *BMC Cancer*, vol. 12, 2012.
- [128] P. D. Chowdary, Z. Jiang, E.J. Chaney, W.A. Benalcazar, D.L. Marks, M. Gruebele, and S.A. Boppart, "Molecular histopathology by spectrally reconstructed nonlinear interferometric vibrational imaging," *Cancer*

References

- Res., vol. 70, no. 23, pp. 9562–9569, 2010.
- [129] T. Meyer, N. Bergner, C. Krafft, D. Akimov, B. Dietzek, J. Popp, C. Bielecki, B.F. Romeike, R. Reichart, and R. Kalff, “Nonlinear microscopy, infrared, and Raman microspectroscopy for brain tumor analysis,” *J. Biomed. Opt.*, vol. 16, no. 2, p. 021113, 2011.
- [130] S. Yue, J. M. Cárdenas-Mora, L. S. Chaboub, S. A. Lelivre, and J. X. Cheng, “Label-free analysis of breast tissue polarity by Raman imaging of lipid phase,” *Biophys. J.*, vol. 102, no. 5, pp. 1215–1223, 2012.
- [131] T. Meyer, M. Chemnitz, M. Baumgartl, T. Gottschall, T. Pascher, C. Matthäus, B.F. Romeike, B.R. Brehm, J. Limpert, A. Tünnermann, and M. Schmitt, “Expanding multimodal microscopy by high spectral resolution coherent anti-stokes Raman scattering imaging for clinical disease diagnostics,” *Anal. Chem.*, vol. 85, no. 14, pp. 6703–6715, 2013.
- [132] J.W. Chan, D.S. Taylor, S.M. Lane, T. Zwerdling, J. Tuscano, and T. Huser, “Nondestructive identification of individual leukemia cells by laser trapping Raman spectroscopy Nondestructive Identification of Individual Leukemia Cells by Laser Trapping Raman Spectroscopy,” *Anal. Chem.*, vol. 80, no. 6, pp. 2180–2187, 2015.
- [133] A. Rajwade, S. Member, and A. Rangarajan, “Image Denoising Using the Higher Order Singular Value DecompositionXplore Full-Text PDF:,” vol. 35, no. 4, 2013.
- [134] J. G. Porquez, R. A. Cole, and A. D. Slepko, “Comparison of two photonic crystal fibers for supercontinuum-Stokes spectral-focusing-CARS hyperspectroscopy,” *OSA Contin.*, vol. 1, no. 4, p. 1385, 2018.
- [135] A. F. Pegoraro, A. Ridsdale, D.J. Moffatt, J.P. Pezacki, B.K. Thomas, L. Fu, L. Dong, M.E. Fermann, and A. Stolow, “All-fiber CARS microscopy of live cells,” *Opt. Express*, vol. 17, no. 23, p. 20700, 2009.
- [136] H. Kano and H. Hamaguchi, “Near-infrared coherent anti-Stokes Raman scattering microscopy using supercontinuum generated from a photonic crystal fiber,” *Appl. Phys. B Lasers Opt.*, vol. 80, no. 2, pp. 243–246, 2005.
- [137] S. H. Parekh, Y. J. Lee, K. A. Amer, and M. T. Cicerone, “Label-free

References

- cellular imaging by Broadband coherent anti-stokes raman scattering microscopy," *Biophys. J.*, vol. 99, no. 8, pp. 2695–2704, 2010.
- [138] C. Pohling, T. Buckup, A. Pagenstecher, and M. Motzkus, "Chemoselective imaging of mouse brain tissue via multiplex CARS microscopy," *Biomed. Opt. Express*, vol. 2, no. 8, p. 2110, 2011.
- [139] C. H. Camp, Y. J. Lee, and M. T. Cicerone, "Quantitative, comparable coherent anti-Stokes Raman scattering (CARS) spectroscopy: Correcting errors in phase retrieval," *J. Raman Spectrosc.*, vol. 47, no. 4, pp. 408–415, 2016.
- [140] D. J. G. and P.R.Graves, "Practical Raman spectroscopy," *Springer-Verlag*, 1989.
- [141] C. Ram, S. Sivamani, T. Micha Premkumar, and V. Hariram, "Computational study of leading edge jet impingement cooling with a conical converging hole for blade cooling," *ARPJ. Eng. Appl. Sci.*, vol. 12, no. 22, pp. 6397–6406, 2017.
- [142] D. Fu, G. Holtom, C. Freudiger, X. Zhang, and X. S. Xie, "Hyperspectral imaging with stimulated raman scattering by chirped femtosecond lasers," *J. Phys. Chem. B*, vol. 117, no. 16, pp. 4634–4640, 2013.
- [143] M. S. Alshaykh, C.S. Liao, O.E. Sandoval, G. Gitzinger, N. Forget, D.E. Leaird, J.X. Cheng, and A.M. Weiner, "High-speed stimulated hyperspectral Raman imaging using rapid acousto-optic delay lines," *Opt. Lett.*, vol. 42, no. 8, p. 1548, 2017.
- [144] Y. Ozeki, W. Umemura, Y. Otsuka, S. Satoh, H. Hashimoto, K. Sumimura, N. Nishizawa, K. Fukui, and K. Itoh, "High-speed molecular spectral imaging of tissue with stimulated Raman scattering," *Nat. Photonics*, vol. 6, no. 12, pp. 845–851, 2012.
- [145] C. S. Liao, M.N. Slipchenko, P. Wang, J. Li, S.Y. Lee, R.A. Oglesbee, and J.X. Cheng, "Microsecond scale vibrational spectroscopic imaging by multiplex stimulated Raman scattering microscopy," *Light Sci. Appl.*, vol. 4, no. 3, pp. 1–9, 2015.
- [146] F. K. Lu, D. Calligaris, O.I. Olubiyi, I. Norton, W. Yang, S. Santagata, X.S. Xie, A.J. Golby, and N.Y. Agar, "Label-free neurosurgical pathology with stimulated Raman imaging," *Cancer Res.*, vol. 76, no. 12, pp.

References

- 3451–3462, 2016.
- [147] M. Ji, S. Lewis, S. Camelo-Piragua, S.H. Ramkissoon, M. Snuderl, S. Venneti, A. Fisher-Hubbard, M. Garrard, D. Fu, A.C. Wang, and J.A. Heth, “Detection of human brain tumor infiltration with quantitative stimulated Raman scattering microscopy,” *Sci. Transl. Med.*, vol. 7, no. 309, 2015.
- [148] S. Cui, P. Wang, and S. Yue, “Hyperspectral stimulated Raman scattering imaging facilitates accurate diagnosis of human prostate cancer,” vol. 10069, p. 100690M, 2017.
- [149] Y. Otsuka, S. Satoh, M. Kyogaku, H. Hashimoto, K. Itoh, and Y. Ozeki, “High-speed stimulated Raman spectral imaging for digital staining of mouse cancer tissues,” vol. 8947, p. 89470C, 2014.
- [150] M. Egawa, K. Tokunaga, J. Hosoi, S. Iwanaga, and Y. Ozeki, “*In situ* visualization of intracellular morphology of epidermal cells using stimulated Raman scattering microscopy,” *J. Biomed. Opt.*, vol. 21, no. 8, p. 086017, 2016.
- [151] C. W. Freudiger, R. Pfannl, D.A. Orringer, B.G. Saar, M. Ji, Q. Zeng, L. Ottoboni, W. Ying, C. Waeber, J.R. Sims, and P.L. De Jager, “Multicolored stain-free histopathology with coherent Raman imaging,” *Lab. Investig.*, vol. 92, no. 10, pp. 1492–1502, 2012.
- [152] R. Galli, O. Uckermann, A. Temme, E. Leipnitz, M. Meinhardt, E. Koch, G. Schackert, G. Steiner, and M. Kirsch, “Assessing the efficacy of coherent anti-Stokes Raman scattering microscopy for the detection of infiltrating glioblastoma in fresh brain samples,” *J. Biophotonics*, vol. 10, no. 3, pp. 404–414, 2017.
- [153] S. Yue, J. Li, S.Y. Lee, H.J. Lee, T. Shao, B. Song, L. Cheng, T.A. Masterson, X. Liu, T.L. Ratliff, and J.X. Cheng, “Cholesteryl ester accumulation induced by PTEN loss and PI3K/AKT activation underlies human prostate cancer aggressiveness,” *Cell Metab.*, vol. 19, no. 3, pp. 393–406, 2014.
- [154] P. Berto, E. R. Andresen, and H. Rigneault, “Background-free stimulated raman spectroscopy and microscopy,” *Phys. Rev. Lett.*, vol. 112, no. 5, pp. 1–5, 2014.

References

- [155] X. Zhang, M.B. Roeffaers, S. Basu, J.R. Daniele, D. Fu, C.W. Freudiger, G.R. Holtom, and X.S. Xie, "Label-free live-cell imaging of nucleic acids using stimulated raman scattering microscopy," *ChemPhysChem*, vol. 13, no. 4, pp. 1054–1059, 2012.
- [156] D. Fu, W. Yang, and X. S. Xie, "Label-free imaging of neurotransmitter acetylcholine at neuromuscular junctions with stimulated Raman scattering," *J. Am. Chem. Soc.*, vol. 139, no. 2, pp. 583–586, 2017.
- [157] Z. Wang, W. Zheng, J. Lin, and Z. Huang, "Hyperspectral stimulated Raman scattering and multiphoton imaging for digital pathology of colonic disease," *SPIE*, vol. 9712, p. 97120G, 2016.
- [158] G. Turrell, T. George, and C. Jacques, "The Raman Effect, in Raman Microscopy," *Acad. Press London*, pp. 1–25, 1996.
- [159] J. . Laserna, "Modern techniques in Raman spectroscopy," *John Wiley and Sons Ltd*, 1996. [Online]. Available: <https://www.olympus-lifescience.com/en/objectives/>. [Accessed: 31-Jan-2019].
- [160] M. J. Baker, S. R. Hussain, L. Lovergne, V. Untereiner, C. Hughes, R. A. Lukaszewski, "Developing and Understanding Biofluid Vibrational Spectroscopy: A Critical Review Journal:," *Chem. Soc. Rev.*, vol. 45, pp. 1803–1818, 2016.
- [161] J. Cheng and X. S. Xie, "Coherent anti-Stokes Raman scattering microscopy: instrumentation, theory, and applications," *J. Phys. Chem. B*, vol. 108, pp. 827–840, 2004.
- [162] C. L. Evans and X. S. Xie, "Coherent Anti-Stokes Raman Scattering Microscopy: Chemical Imaging for Biology and Medicine," *Annu. Rev. Anal. Chem.*, vol. 1, no. 1, pp. 883–909, 2008.
- [163] A. Zumbusch, G. R. Holtom, and X. S. Xie, "Three-Dimensional Vibrational Imaging by Coherent Anti-Stokes Raman Scattering," *Phys. Rev. Lett.*, vol. 82(20), p. 4142., 1999.
- [164] and X. S. X. Ji-xin Cheng, Andreas Volkmer, Lewis D Book, "An epidetected coherent anti-stokes raman scattering (e-cars) microscope with high spectral resolution and high sensitivity," *J. Phys. Chem. B*, vol. 105(7), pp. 1277–1280, 2001.
- [165] J.-X. Cheng, A. Volkmer, and X. S. Xie, "Theoretical and experimental

References

- characterization of coherent anti-Stokes Raman scattering microscopy,” *J. Opt. Soc. Am. B*, vol. 19, no. 6, p. 1363, 2002.
- [166] M.D. Levenson and S.S. Kano, “Introduction to Nonlinear Laser Spectroscopy,” *Acad. Press. San Diego*, 1988.
- [167] J.-X. C. and X. S. Xie, “Coherent Raman Scattering Microscopy,” *CRC Press. USA*, 2016.
- [168] M. B. J. Roeffaers, X. Zhang, C.W. Freudiger, B.G. Saar, X.S. Xie, M. van Ruijven, G. van Dalen, and C. Xiao, “Label-free imaging of biomolecules in food products using stimulated Raman microscopy,” *J. Biomed. Opt.*, vol. 16(2), no. 021118, pp. 1–6, 2011.
- [169] L. I. O. E. De Xing, “A Study on CMOS Image Sensors for Stimulated Raman Scattering Using High-Speed Lateral Electric Field Charge Modulators,” *Dr. Diss. 静岡大学*, 2016.
- [170] K. M. Curtis and P. January, “Comparing coherent and spontaneous Raman modalities for the investigation of gastrointestinal cancers,” PhD thesis, Exeter University, 2017.
- [171] “Renishaw apply innovation, StreamLine: generate chemical images rapidly.” [Online]. Available: <https://www.renishaw.com/en/streamline-generate-chemical-images-rapidly--9449>. [Accessed: 31-Jan-2019].
- [172] V. Deckert and W. KIEFER, “Scanning Multichannel Technique for Improved Spectrochemical Measurements with a CCD Camera and its Application to Raman Spectroscopy,” *John Wiley Sons Ltd*, vol. 46, no. 2, pp. 322–328, 1992.
- [173] C. Zhang, D. Zhang, and J. Cheng, *Coherent Raman Scattering Microscopy in Biology and Medicine. Annual review of biomedical engineering*, vol. 17, pp.415-445, 2015.
- [174] H. Martens and M. Martens, “Multivariate analysis of quality. An introduction,” *John Wiley Sons*, 2001.
- [175] F. Z. Ingo Rimke, Volker Siffrin, Raluca Niesner, Tina Leuenberger, “A new light source for multimodal multiphoton microscopy including CARS Ingo,” *Multiphot. Microsc. Biomed. Sci. IX, SPIED*, vol. 7183, p. 718314, 2009.
- [176] T. Neicke, “Levante Emerald ps, APE.” [Online]. Available:

References

- <https://www.ape-berlin.de/en/opo-optical-parametric-oscillator/levante-ir-pps/>. [Accessed: 08-Feb-2018].
- [177] O. Aharon and I. Abdulhalim, "Liquid crystal Lyot tunable filter with extended free spectral range," *Opt. Express*, vol. 17, no. 14, p. 11426, 2009.
- [178] S. Suresh, A. Ramanand, D. Jayaraman, and P. Mani, "Review on theoretical aspect of nonlinear optics," *Rev. Adv. Mater. Sci.*, vol. 30, no. 2, pp. 175–183, 2012.
- [179] M. T. Cicerone and C. H. Camp, "Histological coherent Raman imaging: A prognostic review," *Analyst*, vol. 143, no. 1, pp. 33–59, 2018.
- [180] R. W. Maker, P.D. and Terhune, "Study of optical effects due to an induced polarization third order in the electric field strength," *Phys. Rev.*, vol. 137(3A), p, 1965.
- [181] "No cover, Specific Objectives | Olympus Life Science." [Online]. Available: [https://www.olympus-lifescience.com/en/objectives/no-cover/#!cms\[tab\]=%2Fobjectives%2Fno-cover%2F60x](https://www.olympus-lifescience.com/en/objectives/no-cover/#!cms[tab]=%2Fobjectives%2Fno-cover%2F60x). [Accessed: 30-Apr-2019].
- [182] Y. Fu, H. Wang, R. Shi, and J. Cheng, "Characterization of photodamage in coherent anti-Stokes Raman scattering microscopy," vol. 14, no. 9, pp. 3942–3951, 2006.
- [183] T. Vo-Dinh, *Laser and optical radiation safety in biophotonics*. CRC press, second ed.,. 2014.
- [184] K. Hatanaka, M. Kawao, Y. Tsuboi, H. Fukumura, and H. Masuhara, "Switching from photochemical to photothermal mechanism in laser ablation of benzene solutions," *J. Appl. Phys.*, vol. 82, no. 11, pp. 5799–5806, 1997.
- [185] R. Legesse, F.B., Chernavskaia, O., Heuke, S., Bocklitz, T., Meyer, T., Popp, J. and Heintzmann, "Seamless stitching of tile scan microscope images," *Journal of Microscopy*, vol. 258, no. 3, pp. 223–232, 2015.
- [186] Y. Ozeki, F. Dake, S. Kajiyama, K. Fukui, and K. Itoh, "Analysis and experimental assessment of the sensitivity of stimulated Raman scattering microscopy," vol. 17, no. 5, pp. 3651–3658, 2009.
- [187] B. G. Saar, C. W. Freudiger, J. Reichman, C. M. Stanley, G. R. Holtom,

References

- and X. S. Xie, "Video-Rate Molecular Imaging in Vivo with Stimulated Raman Scattering," *science*, vol. 330, no. 6009, pp. 1368–1371, 2010.
- [188] H. T. Beier, G. D. Noojin, and B. A. Rockwell, "Stimulated Raman scattering using a single femtosecond oscillator with flexibility for imaging and spectral applications," *Optical express*, vol. 19, no. 20, pp. 18885–18892, 2011.
- [189] R. Summary, "Vibrational spectroscopic imaging of living systems: An emerging platform for biology and medicine," *science*, vol. 8870, 2015.
- [190] D. Zhang, P. Wang, M. N. Slipchenko, and J. Cheng, "Fast Vibrational Imaging of Single Cells and Tissues by Stimulated Raman Scattering Microscopy," 2014.
- [191] P. T. Chandrasoma, "Histologic Definition and Diagnosis of Epithelia in the Esophagus and Proximal Stomach," *Current opinion gastroenterology*, vol. 29, no. 4, pp. 460–467, 2013.
- [192] A. J. Cameron, D. J. Ballard, A. R. Zinsmeister, and J. A. Carney, "Prevalence of Columnar-Lined (Barrett's) Esophagus," *Gastroenterology*, vol. 99, no. 1, pp. 919–922, 1990.
- [193] W. Hameeteman, "Barrett's Esophagus: Development of Dysplasia and Adenocarcinoma," *Gastroenterology*, vol. 96, no. 5, pp. 1249–1256, 1989.
- [194] A. Zeytunyan, T. Baldacchini, and R. Zadoyan, "Module for multiphoton high-resolution hyperspectral imaging and spectroscopy," *Multiphoton Microscopy in the Biomedical Sciences*, vol. 1, no. 2, 2018.
- [195] T. Hellerer, A. M. K. Enejder, and A. Zumbusch, "Spectral focusing: High spectral resolution spectroscopy with broad-bandwidth laser pulses," *Appl. Phys. Lett.*, vol. 85, no. 1, pp. 25–27, 2004.
- [196] D. Zhang, M. N. Slipchenko, D. E. Leaird, A. M. Weiner, and J.-X. Cheng, "Spectrally modulated stimulated Raman scattering imaging with an angle-to-wavelength pulse shaper," *Opt. Express*, vol. 21, no. 11, p. 13864, 2013.

Appendices

1. Hyperspectral scanning software

Serial Port Settings

The OPO controller was connected via an external serial port to the PC. When the programme is running, the serial port (interface) and baud rate (38,400) must be selected by the user manually from the control panel of the programme. The correct serial port and baud rate must be matched with the same port and baud rate value in the OPO controller.

Programme running controls

Several buttons in the programme running controls are used, such as:

Check Comms button: when the user clicks the Check Comms button, all the OPO parameters of the last measurements are displayed on the screen in the Signal Status section, such as the crystal temperature, OPO power, piezo position, wavelength, and wavenumber. It is also used to ensure that the programme is correctly connected with the OPO controller before running the experiment.

Appendices

Start Scanning button: used to start imaging and recording the hyperspectral stack and all parameters during the experiment.

PAUSE button: used to pause the programme at any time during the imaging to make the user able to readjust the settings before continuing.

STOP button: used to stop scanning completely.

Scanimage button: used to start running the Scanimage software synchronously with the main programme.

Indicators

The indicators are designed on the right-hand side of the control panel of the programme. This includes the programme status and the signal status. In the programme status, there are four Booleans used by the programme to decide which state the programme is in and what to do. The programme runs the Scanimage software to record an image when the imaging wavelength is highlighted (TRUE). The imaging light is turned on when the Scanimage starts recording an image. After the programme finishes scanning, the Serial Port Open light should be off. Each time the wavelength, the Raman wavenumber, OPO power, OPO temperature, time for running, and piezo position are recorded from the OPO controller, they are displayed in the Signal Status section.

Scanimage control

The Scanimage software is used for controlling the laser-scanning microscope and adjusting the experiment parameters as mentioned earlier. However, there are vast numbers of parameters in this software, and most of them were not used in this study. The most commonly used parameters have been redesigned and linked with the programme for quick and smooth access, e.g. channels, image control (to change the brightness of images), cycle data (for the large area montage), data logging (to save data), pixel bin factor (to adjust the speed of the scan), and acquisition modes (FOCUS, GRAB, and LOOP).

Main settings

This section consists of the most critical input options for controlling the experiment, such as:

2. Hyperspectral scanning software, Matlab code

```
classdef RamanToolbox < matlab.apps.AppBase
```

```
properties (Access = private)
```

```
    serialport ;% Serial port object for communication with OPO
    portProps = struct('portname','COM3','baudrate',384000); % serial
    port properties
    piezo =
    struct('current',2000,'next',2000,'set',2000,'tuningdata',[],'start
    ',1,'end',4000,'step',10,'list',[]); % piezo position
    temperature =
    struct('current',152,'next',152,'set',152,'tuning',[],'file',[]); %
    temperature
    power = struct('current',200,'min',100); % power output
    wavelength = struct('current',780,'next',780,'set',780,'list',[]);
    % wavelength
    cycleProps = struct('xspan',95,'yspan',95,'boxsize',95);
    hROIManager =
    struct('roi',struct('xstart',1,'ystart',1,'xlength',1,...
    'ylength',1,'rect',gobjects(1),'enable',0,'pixelsPerLine',128),'cin
    d',1,...
    'numroi',0,'enable',0,'shuttertime',0);
    tissueProps =
    struct('length',3,'width',3,'fov',230.4,'Nfocuspoints',10,'objectiv
    e','60x');
    channels ; %% variable for storing images of each channel
    zoom2fov; % data for converting zoom factor to fov in um
    tuning_file;
    imaging_time; % Time for imaging
    n_images; % number of images at the wavelength
    maxattempts; % maximum attempts to check comms
    checking_time; % time to check for each value
    stop_program; % variable to stop the execution of the loop
    pause_program; % variable to pause the execution
    at_wl_number; % store loop numbe when program is paused to start
    from there when released
    hSI; % hSI is a scanimage.SI object that gives access to the
    operation and configuration of the microscope.
    hSICtl; % hSI is a scanimage.SI object that gives access to the
    operation and configuration of the microscope.
```

Appendices

```
    infopath; % Filepath for recording wavelength information
    scanmode = 'wlscan';
    fullImage; % stores a large area image in cycle mode
    prevMotorPos = [0,0,0]; % stores the previous motor position
end

methods (Access = private)

function checkcomms(app)
    for i = 1:app.maxattempts
        [app.power.current, ~] = getOPOPower(app.RamanImagingUIFigure,...
            app.serialport,app.PowerDispField);
        [app.temperature.current, ~] =
            getOPOTemperature(app.RamanImagingUIFigure,...
            app.serialport,app.OPOTemperatureDispField);
        [app.wavelength.current, ~] = getOPOWavelength(app.serialport,...
            app.WavelengthnmDispField, app.RamanWavenumberDispField);
        [app.piezo.current, err] =
            getPiezoVoltage(app.RamanImagingUIFigure,...
            app.serialport,app.PiezoPositionDispField);
        if err == -1
            uialert(fig,['Could not communicatw with serial port.',...
                'Check Settings and press check comms button'],'Communication
                Error');
            instrreset;
            break
        end
    end
end

function disablecontrols(app)
    app.BaudrateSpinner.Enable = 'Off';
    app.VISAresourceNameDropDown.Enable = 'Off';
    app.AddwavenumberButton.Enable = 'Off';
    app.MaxattemptsSpinner.Enable = 'Off';
    app.TunePeizoButton.Enable = 'Off';
end

function enablecontrols(app)
    app.BaudrateSpinner.Enable = 'On';
    app.VISAresourceNameDropDown.Enable = 'On';
    app.AddwavenumberButton.Enable = 'On';
    app.MaxattemptsSpinner.Enable = 'On';
    app.TunePeizoButton.Enable = 'On';
end

function tuneauto(app)
    checkcomms(app);
    if app.stop_program
        return;
    end
    %     if app.power.current < 50
    %     piezopower(app, 500);
end
```

Appendices

```
%     end
%     templambda(app);
piezolambda(app);
checkcomms(app);

app.AtimagingwavelengthLamp.Color = 'green';
end

function tunepiezo(app, step, s)
range = app.piezo.current:s*step:app.piezo.next;
for i = range(2:end)
    app.piezo.set = i;
    [app.piezo.current, ~] = setPiezoPos(app.piezo.set,
    app.RamanImagingUIFigure,...
    app.serialport,app.PiezoPositionDispField);
    pause(0.1);
    [app.wavelength.current, ~] =
    getOPOWavelength(app.serialport,...
    pp.WavelengthnmDispField, app.RamanWavenumberDispField);
    if stopOrpause(app)
        return;
    end
end
end

function piezolambda(app)
s = sign(app.wavelength.next - app.wavelength.current);
while sign(app.wavelength.next - app.wavelength.current) == s
    step = 100;
    app.piezo.next = app.piezo.current + s*step;
    tunepiezo(app, step, s);
    if stopOrpause(app)
        return;
    end
    pause(0.01);
end
if abs(app.wavelength.next - app.wavelength.current) <=0.1
    return
end
s = sign(app.wavelength.next - app.wavelength.current);
while sign(app.wavelength.next - app.wavelength.current) == s
    step = 10;
    app.piezo.next = app.piezo.current + s*step;
    tunepiezo(app, step, s);
    if stopOrpause(app)
        return;
    end
    pause(0.01);
end
if abs(app.wavelength.next - app.wavelength.current) <=0.1
    return
end
s = sign(app.wavelength.next - app.wavelength.current);
```

Appendices

```
    while (sign(app.wavelength.next - app.wavelength.current) == s)
        && abs(app.wavelength.next - app.wavelength.current) > 0.1
            step = 1;
            app.piezo.next = app.piezo.current + s*step;
            tunePiezo(app, step, s);
            if stopOrPause(app)
                return;
            end
            pause(0.01);
        end
    end

function templambda(app)
    n = sign(app.temperature.current*10-app.temperature.set);
    for i = app.temperature.current*10:n:app.temperature.set
        fprintf(app.serialport, ['STS', num2str(i, '%04d'), ', ']);
        if app.stop_program
            return;
        end
        pause(1);
        [app.temperature.current, ~] =
            getOPOTemperature(app.RamanImagingUIFigure, ...
                app.serialport, app.OPOTemperatureDispField);
    end
end

function break_flag = stopOrPause(app)
    if app.stop_program
        if strcmpi(app.serialport.Status, 'open')
            fclose(app.serialport);
            if scannimagerunning(app)
                app.hSI.hCycleManager.abort();
            end
        end
        break_flag = 1;
        return;
    end
    if app.pause_program
        break_flag = 1;
        return ;
    end
    break_flag = 0;
end

function updatechannels(app)
    lastStripe =
        app.hSI.hDisplay.stripeDataBuffer{app.hSI.hDisplay.stripeDataBuffer
            rPointer};
    channels = lastStripe.roiData{1}.channels;
    app.channels = cell(length(channels),1);
    for idx = 1:length(channels)
        app.channels{idx} = lastStripe.roiData{1}.imageData{idx}{1}; %
            extract all channels
    end
end
```

Appendices

```
for i = 1:app.hROIManager.numroi
    if ~isempty(app.hROIManager.roi(i).rect)
        subfig =
            app.channels{idx}(app.hROIManager.roi(i).xstart:...
                app.hROIManager.roi(i).xstart+app.hROIManager.roi(i).xl
                    ength,...
                app.hROIManager.roi(i).ystart:app.hROIManager.roi(i).y
                    tart +...
                app.hROIManager.roi(i).ylength);
        app.hROIManager.roi(i).intensity(idx) =
            mean(mean(subfig));
    end
end

imshow(mat2gray(app.channels{idx}),'Parent',
    app.(['Channel',num2str(idx),'Axes']));
axis(app.(['Channel',num2str(idx),'Axes']),'image');
end
end

function setroi(app,
    if ~isgraphics(app.hROIManager.roi(i).rect)
        for j =1:3
            app.hROIManager.roi(i).rect = rectangle(app.(['Channel',
                num2str(j), 'Axes']),'Position',[app.hROIManager.roi(i)
                    .xstart ...
                app.hROIManager.roi(i).ystart app.hROIManager.roi(i).
                    xlength app.hROIManager.roi(i).ylength],...
                'EdgeColor','r','LineWidth',2);
        end
    else
        app.hROIManager.roi(i).rect.Position = [app.hROIManager.roi(i).
            xstart app.hROIManager.roi(i).ystart ....
            app.hROIManager.roi(i).xlength app.hROIManager.roi(i).ylength];
    end
end

function cyclemode(app, tstart, filename)
    if scannimagerunning(app)
        assert(strcmpi(app.hSI.acqState,'idle')); % make sure scanimage
            is in an idle state
        app.hSI.hScan2D.logFileStem = filename; % set the base file name
            for the Tiff file
        app.infopath = [app.hSI.hScan2D.logFilePath,'\Info.txt'];
        app.hSI.hScan2D.logFileCounter = 1; % set the current Tiff file
            number
        app.hSI.hChannels.loggingEnable = true; % enable logging
        startMotorPos = app.hSI.hMotors.motorPosition;
        if app.hSI.hCycleManager.enabled
            app.hSI.startCycle(); % start the cycle
        else
            uialert(app.RamanImagingUIFigure,'Cycle mode not enable. Set
                cycle data.','Cycle data error');
```

Appendices

```
        return;
    end
    pause(0.01);
    while ~strcmpi(app.hSI.acqState, 'idle')
        pause(1);
    end
    app.hSI.hCycleManager.resetCounters();
    app.hSI.hMotors.moveStartRelative(startMotorPos);
    while app.hSI.hMotors.nonblockingMoveInProgress
        pause(0.01);
    end
    imagefilenames = dir([app.hSI.hScan2D.logFilePath, '*.tif']);
    imagefilenames = string({imagefilenames.name});
    l = length(imagefilenames);
    for i = 1:length(app.hSI.hChannels.channelsActive)

        images = struct('IM', []);
        for j = 1:length(imagefilenames)
            images(j).IM = imread(strjoin([app.hSI.hScan2D.
                logFilePath, imagefilenames(j)], '\\'), i);
        end
        ximages = ceil(app.cycleProps.xspan/app.cycleProps.boxsize)
            + 1;
        yimages = ceil(app.cycleProps.yspan/app.cycleProps.boxsize)
            + 1;
        overlap = 1 - app.cycleProps.xspan/(ximages-1)/app.
            tissueProps.fov;
        app.fullImage{app.hSI.hChannels.channelsActive(i)} =
            stitchimage(images, ximages, yimages, overlap);
    % blockproc(reshape(1:l, sqrt(l), sqrt(l)), [1,1], @(x) images(:,:,
    x.data));
    end
    idx = str2num(app.ChannelDropDown.Value);
    try
        imshow(mat2gray(app.fullImage{idx}'), 'Parent', app.
            FullImageAxes);
        axis(app.FullImageAxes, 'image');
    catch ME
        uialert(app.RamanImagingUIFigure, ME.message, ME.identifier);
    end

    else
        pause(10);
    end
    telapsed= toc(tstart);
    app.TimeforRunDisp.Value = telapsed;
    try
        dlmwrite(app.infopath, ...

[app.wavelength.current, app.RamanWavenumberDispField.Value, app.power
.current, ...
    app.temperature.current, telapsed], 'delimiter', '\t', 'newline',
    'pc', '-append');
```

Appendices

```
    catch
        uialert(app.RamanImagingUIFigure, 'Could not create text file to
        write information array', ...
        'File creation error');
    end
end

function updatedisplayinscanmode(app, i)
    app.AtimagingwavelengthLamp.Color = [0.26 0.47 0.26];
    app.NextwavelengthDispField.Value = app.wavelength.list(i);
    app.NumberofscansremaningDispField.Value = length
    (app.wavelength.list)-i;

end

function setupscan(app)
    app.pause_program = 0;
    app.stop_program = 0;
    disablecontrols(app);
    if strcmpi(app.serialport.Status, 'closed')
        try
            fopen(app.serialport);
        catch
            uialert(app.RamanImagingUIFigure, 'Could not open serial port.
            Check if port available', 'Serial port error');
            enablecontrols(app);
            return;
        end
        app.at_wl_number = 1;
    end
    [app.temperature.tuning_data, app.piezo.tuning_data] =
    loadTuningParams(app.RamanImagingUIFigure, ...
    app.tuning_file);
    app.wavelength.list = 1./((app.WavelengthTable.Data/10000000) +
    1/1032);
    if isempty(app.wavelength.list) && isempty(app.piezo.list)
        uialert(app.RamanImagingUIFigure, 'No wavelengths or piezo
        position added to image. Please add wavelengths', 'Empty array');
        enablecontrols(app);
        return
    end
    if scannimagerunning(app)
        if isempty(app.hSI.hCycleManager.cycleDataGroup.cycleIters)
            uialert(app.RamanImagingUIFigure, 'Cycle Data not set. Please
            set Cycle Data', 'Empty array');
            enablecontrols(app);
            return
        end
    end
    if isempty(app.hSI)
        [fname, pname] = uiputfile('InfoTest.txt', 'File Open Dialog');
        app.infopath = fullfile(pname, fname);
    else
```

Appendices

```
    app.infopath = [app.hSI.hScan2D.logFilePath, '\Info.txt'];
end
fid = fopen(app.infopath, 'wt');
if fid == -1
    uialert(app.RamanImagingUIFigure, 'Could not create text file to
    write information array', 'File creation error');
    enablecontrols(app);
    return
end
fprintf(fid, '%s\t%s\t%s\t%s\t%s\t%s', 'Wavelength', 'Raman
Wavenumber', 'Power', 'Temperature', 'Exec. time', 'SRS Intensity');
fclose(fid);
end

function updatemotorpos(app)
    app.XEditField.Value = app.hSI.hMotors.motorPosition(1);
    app.YEditField.Value = app.hSI.hMotors.motorPosition(2);
    app.ZEditField.Value = app.hSI.hMotors.motorPosition(3);
    app.REditField.Value = sqrt(app.hSI.hMotors.motorPosition(1)^2+app.
    hSI.hMotors.motorPosition(2)^2+app.hSI.hMotors.motorPosition(3)^2);
end

function updaterrates(app)
    app.LineperiodusEditField.Value = app.hSI.hRoiManager.linePeriod;
    app.FrameRateHzEditField.Value = app.hSI.hRoiManager.scanFrameRate;
    app.ScanLineRateEditField.Value = app.hSI.hScan2D.scanPixelTimeMean;
    app.ScanLineRateSlider.Value = app.hSI.hScan2D.scanPixelTimeMean;
end

function err = scannimagerunning(app)
    if isempty(app.hSI)
        err = 0;
        uialert(app.RamanImagingUIFigure, 'Scan image not running. Please
        start scanimage.', 'Scanimage error');
    else
        err = 1;
    end
end

end

% Callbacks that handle component events
methods (Access = private)
% Code that executes after component creation
function startupFcn(app)
    instrreset;
    lCOM_Port = getAvailableComPort();
    app.VISAresourcenameditField.Items = lCOM_Port;
    app.portProps.baudrate = app.BaudrateSpinner.Value;
    app.tuning_file = app.OPOTuningFilePath.Value{1};
    app.piezo.file = app.PiezotuningfilepathText.Value{1};
    app.stop_program = 0;
```


Appendices

```
app.pause_program = 0;
app.at_wl_number = 1;
app.cycleProps.xspan = app.XspanSpinner.Value;
app.cycleProps.yspan = app.YspanSpinner.Value;
app.cycleProps.boxsize = app.BoxsizeSpinner.Value;
app.maxattempts = 1;
app.temperature.set = app.TemperatureEditField.Value*10;
app.piezo.set = app.PiezoPositionEditField.Value;
app.piezo.list = [];
tmpfile = app.Zoom2FOVTextPath.Value;
m = importdata(tmpfile{1});
app.zoom2fov = m.data;
app.ABORTButton.Visible = 'off';
end
% Button pushed function: AddwavenumberButton
function AddwavenumberButtonPushed(app, event)
    app.WavelengthTable.Data = [app.WavelengthTable.Data; app.
        Wavenumber1cmEditField.Value];
end
% Callback function
function ImagingtimesSpinnerValueChanged(app, event)
    app.imaging_time = app.ImagingtimesSpinner.Value;
end
% Callback function
function NumberofimagesSpinnerValueChanged(app, event)
    app.n_images = app.NumberofimagesSpinner.Value;
end
% Callback function
function MinimumPowerallowedSpinnerValueChanged(app, event)
    app.min_power = app.MinimumPowerallowedSpinner.Value;
end
% Callback function
function SizeofLyotFilterIncrementsSpinnerValueChanged(app, event)
    app.lyot_filter_inc = app.SizeofLyotFilterIncrementsSpinner.Value;
end
% Value changed function: BaudrateSpinner
function BaudrateSpinnerValueChanged(app, event)
    app.portProps.baudrate = app.BaudrateSpinner.Value;
end
% Button pushed function: STARTSCANNINGButton
function STARTSCANNINGButtonPushed(app, event)
    rtstart = tic;
    selection = 'Continue';
    if ~scannimagerunning(app)
        selection = uiconfirm(app.RamanImagingUIFigure, 'Scan image no
            running. Do you wish to continue?', ...
            'Scan options', 'Options', {'Continue', 'Cancel'}, ...
            'DefaultOption', 2);
    end
    if strcmpi(selection, 'cancel')
        return
    else
        setupscan(app);
    end
end
```

```
switch app.scanmode
case 'wlscan'
    if ~isempty(app.wavelength.list)
        for i = app.at_wl_number:length(app.wavelength.list)
            %tstart = tic;
            app.wavelength.next = app.wavelength.list(i);
            updatedisplayinscanmode(app, i)
            tuneauto(app);
            if stopOrpause(app)
                app.at_wl_number = i;
                break;
            end
            LOOPCYCLEButtonPushed(app, event);
        end
    end
case 'piezoscanscan'
    if ~isempty(app.piezo.list)
        app.piezo.next = app.piezo.start;
        steplist = [100,10,1];
        for j = steplist
            step =j;
            s = sign(app.piezo.start - app.piezo.current);
            tunepiezo(app, step, s);
        end
        for i = app.at_wl_number:length(app.piezo.list)
            %tstart = tic;
            app.AtimagingwavelengthLamp.Color = [0.26 0.47 0.26];
            app.NextwavelengthDispField.Value = app.piezo.list(i);
            app.NumberofscansremaningDispField.Value = length(app.piezo.list)-i;
            app.piezo.next = app.piezo.list(i);
            s= sign(app.piezo.next - app.piezo.current);
            step = app.piezo.step;
            tunepiezo(app, step, s);
            [app.power.current, ~] = getOPOPower
            (app.RamanImagingUIFigure,...
            app.serialport,app.PowerDispField);
            if stopOrpause(app)
                app.at_wl_number = i;
                break;
            end
            LOOPCYCLEButtonPushed(app, event);
        end
    end
case 'roiscanscan'
    if and(~isempty(app.piezo.list),app.hROIManager.enable == 1)
        app.piezo.next = app.piezo.start;
        steplist = [100,10,1];
        for j = steplist
            step =j;
            s = sign(app.piezo.start - app.piezo.current);
            tunepiezo(app, step, s);
```

```

end
for i = app.at_wl_number:length(app.piezo.list)
    tstart = tic;
    % updatedisplayinscanmode(app, i)
    app.AtimagingwavelengthLamp.Color = [0.26 0.47 0.26];
    app.NextwavelengthDispField.Value = app.piezo.list(i);
    app.NumberofscansremaningDispField.Value = length
        (app.piezo.list)-i;
    app.piezo.next = app.piezo.list(i);
    s = sign(app.piezo.next - app.piezo.current);
    step = app.piezo.step;
    tunepiezo(app, step, s);
    [app.power.current, ~] = getOPOPower
        (app.RamanImagingUIFigure,...
        app.serialport,app.PowerDispField);

    if stopOrpause(app)
        app.at_wl_number = i;
        break;
    end
    pause(app.hROIManager.shuttertime);
    GRABButtonPushed(app, []);
    for j = 1:app.hROIManager.numroi
        if ~isempty(app.hROIManager.roi(j).rect)
            app.hROIManager.cars(i,j) = app.hROIManager.
                roi(j).intensity(1)/app.hROIManager.roi(j).
                intensity(3); %app.power.current;
            app.hROIManager.srs(i,j) = app.hROIManager.
                roi(j).intensity(2)/app.hROIManager.roi(j).
                intensity(3); %app.power.current;
        end
    end
    app.wavelength.wavenumber(i) =
        app.RamanWavenumberDispField.Value;
    telapsed = toc(tstart);
    try
        dlmwrite(app.infopath,...
            [app.wavelength.current,app.
            RamanWavenumberDispField.Value,app.power.
            current,...
            app.temperature.current, telapsed,app.
            hROIManager.srs(i,:)],...
            'delimiter','\t','newline','pc','-append');
    catch
        uialert(app.RamanImagingUIFigure,'Could not
            create text file to write information array',...
            'File creation error');
    end
end
hold(app.srsint,'on');
for j = 1:app.hROIManager.numroi

```

Appendices

```
        plot(app.srsint,app.wavelength.wavenumber,app.hROIManager.srs(:,j), 'o', 'MarkerSize',3);
        end
        hold(app.srsint, 'off');
        GRABButtonPushed(app, []);
    end
    otherwise
        uialert(app.RamanImagingUIFigure, 'Unrecognized scan mode', 'Scan error');
    end
    if scannimagerunning(app)
        app.hSI.hCycleManager.reset();
    end
    enablecontrols(app);
end
rtelapsed = toc(rtstart);
app.RunningTimeEditField.Value = rtelapsed;
end
% Button pushed function: CheckCommsButton
function CheckCommsButtonPushed(app, event)
    fprintf(app.serialport, 'SHC');
    checkcomms(app);
end

% Close request function: RamanImagingUIFigure
function RamanImagingUIFigureCloseRequest(app, event)
    if ~isempty(app.serialport)
        if strcmpi(app.serialport.Status, 'open')
            fclose(app.serialport);
        end
    end
    if ~isempty(app.hSI)
        app.hSI.exit();
    end
    delete(app)
end

% Value changed function: VISAResourcenamDropDown
function VISAResourcenamDropDownValueChanged(app, event)
    app.portProps.portname = app.VISAResourcenamDropDown.Value;
    instrreset;
    app.serialport = configurecomport(app.RamanImagingUIFigure, ...
    app.portProps.portname, app.portProps.baudrate);
    if ~isempty(app.serialport)
        app.SerialportopenLamp.Color = 'green';
    end
end

% Callback function
function ChoosefileTempPushed(app, event)
    [app.filename, app.pathname] = uigetfile('*.txt', 'File Open Dialog');
```

Appendices

```
        app.opo_temp_tuning_file = fullfile(app.pathname, app.filename);
    end
    % Button pushed function: ClearTableButton
    function ClearTableButtonPushed(app, event)
        app.WavelengthTable.Data = [];
    end
    % Button pushed function: STOPButton
    function STOPButtonPushed(app, event)
        app.stop_program = 1;
    end
    % Button pushed function: PAUSEButton
    function PAUSEButtonPushed(app, event)
        app.pause_program = 1;
    end
    % Value changed function: XspanSpinner
    function XspanSpinnerValueChanged(app, event)
        app.cycleProps.xspan = app.XspanSpinner.Value;
    end
    % Value changed function: YspanSpinner
    function YspanSpinnerValueChanged(app, event)
        app.cycleProps.yspan = app.YspanSpinner.Value;
    end
    % Value changed function: BoxsizeSpinner
    function BoxsizeSpinnerValueChanged(app, event)
        app.cycleProps.boxsize = app.BoxsizeSpinner.Value;
    end
    % Button pushed function: SetCycleDataButton
    function SetCycleDataButtonPushed(app, event)
        if scannimagerunning(app)
            fov = app.tissueProps.fov; %app.zoom2fov(app.zoom2fov(:,1) ==
            app.hSI.hRoiManager.scanZoomFactor,2);
            fullimagelength = round(app.cycleProps.xspan/fov*app.hSI.
            hRoiManager.pixelsPerLine);
            app.fullImage = cell(length(app.hSI.hChannels.
            channelsActive),1);
            for i = length(app.hSI.hChannels.channelsActive)
                app.fullImage{app.hSI.hChannels.channelsActive(i)} = zeros
                (fullimagelength,fullimagelength,1);
            end
            app.hSI = setCycleData(app.cycleProps, app.hSI, app.
            RamanImagingUIFigure);
            app.SetCycleDataButton.Text = 'Reset Cycle Data';
            idx = str2num(app.ChannelDropDown.Value);
            imshow(app.fullImage{idx}', 'Parent', app.FullImageAxes);
            axis(app.FullImageAxes, 'image');
        end
    end
    % Button pushed function: StartScanImageButton
    function StartScanImageButtonPushed(app, event)
        try
            if ~ismember('hSI',evalin('base','who')) || ~ismember
            ('hSI',evalin('base','who'))
                scanimage;
            end
        end
    end
end
```

Appendices

```
    end
    app.hSI = evalin('base','hSI');
    app.hSICtl = evalin('base','hSICtl');
catch ME
    uialert(app.RamanImagingUIFigure,ME.message, ME.
        identifier(8:end));
end
    updatemotorpos(app);
    m = importdata(app.Zoom2FOVTextPath.Value{1});
    app.zoom2fov = m.data;
end
% Button pushed function: LoopmodeButton
function LoopmodeButtonPushed(app, event)
    app.hSI.hCycleManager.enabled = false;
end
% Button pushed function: LOOPCYCLEButton
function LOOPCYCLEButtonPushed(app, event)
    tstart = tic;
    filename = ['Wavelength_',num2str(round
        (app.wavelength.current*10)),'_'];
    fprintf(app.serialport,'SH0');
    cyclemode(app, tstart, filename);
    fprintf(app.serialport,'SHC');
end
% Value changed function: MaxattemptsSpinner
function MaxattemptsSpinnerValueChanged(app, event)
    app.maxattempts = app.MaxattemptsSpinner.Value;
end
% Callback function
function CheckingtimesSpinnerValueChanged(app, event)
    app.checking_time = app.CheckingtimesSpinner.Value;
end

% Button pushed function: TunePeizoButton
function TunePeizoButtonPushed(app, event)
    disablecontrols(app);
    piezopower(app);
    enablecontrols(app);
end
% Callback function
function DistanceofpiezotravelSpinnerValueChanged(app, event)
    app.dist = app.DistanceofpiezotravelSpinner.Value;
end

% Callback function
function PowerdifferenceSpinnerValueChanged(app, event)
    app.power_diff = app.PowerdifferenceSpinner.Value;
end
% Value changed function: TemperatureEditField
function TemperatureEditFieldValueChanged(app, event)
    app.set_temp = app.TemperatureEditField.Value*10;
end
% Button pushed function: SetTempButton
```

Appendices

```
function SetTempButtonPushed(app, event)
    disablecontrols(app);
    if ~isempty(app.current_temp) && ~isempty(app.set_temp)
        templambda(app);
    else
        uialert(app.RamanImagingUIFigure, 'Opo temeprature not set. Press
        check comms', 'Comms error');
    end
    enablecontrols(app);
end
% Value changed function: PiezoPositionEditField
function PiezoPositionEditFieldValueChanged(app, event)
    app.piezo.set = app.PiezoPositionEditField.Value;
end
% Button pushed function: SetPiezoPosButton
function SetPiezoPosButtonPushed(app, event)
    disablecontrols(app);
    [app.piezo.current, ~] = setPiezoPos(app.piezo.set,
    app.RamanImagingUIFigure, ...
    app.serialport, app.PiezoPositionDispField);
    enablecontrols(app);
end
% Callback function
function StartscanButtonPushed(app, event)
    checkcomms(app);
    fname = app.ParamFilePath.Value{1};
    fid = fopen(fname, 'wt');
    if fid == -1
        uialert(app.RamanImagingUIFigure, 'Could not create text file to
        write information array', ...
        'File creation error');
        return
    end
    formatspec = '%s\t%s\t%s\t%s\n';
    fprintf(fid, formatspec, 'Temperature', 'Piezo Position', 'Power',
    'Wavelength');
    fclose(fid);

    % writetofile(app, fname, formatspec, text);
    stemp = app.StarttempEditField.Value;
    etemp = app.EndtempEditField.Value;
    temp_step = app.stepsizeEditField.Value;
    piezo_step = app.PiezostepsizeEditField.Value;
    for i = stemp:temp_step:etemp
        if app.stop_program
            return;
        end
        app.set_temp = i*10;
        getOPOTemperature(app);
        templambda(app);
        getOPOTemperature(app);
        app.set_piezo_pos = 0;
        [app.piezo.current, ~] = setPiezoPos(app.piezo.set, app.
```

Appendices

```
RamanImagingUIFigure,...
app.serialport,app.PiezoPositionDispField);
app.set_piezo_pos = 4095;
[P, S, W] = setpiezopos(app,piezo_step);
try
    dlmwrite(fname, [ones(length(P),1)*app.current_temp,S,P,W],...
            'delimiter','\t','newline','pc','-append');
catch
    uialert(app.RamanImagingUIFigure,'Could not create text file
    to write information array',...
            'File creation error');
    break;
end
end
end

% Callback function
function ChooseParamFileButtonPushed(app, event)
    [fname,pname] = uiputfile('PiezoLamda.txt','File Open Dialog');
    app.ParamFilePath.Value = fullfile(pname,fname);
end

% Callback function
function ChoosefilePiezoButtonPushed(app, event)
    [fname, pname] = uigetfile('*.txt','File Open Dialog');
    app.opo_piezo_tuning_file = fullfile(pname, fname);
    app.PiezotuningfilepathText.Value = app.opo_piezo_tuning_file;
end

% Button pushed function: ImportwavenumbersButton
function ImportwavenumbersButtonPushed(app, event)
    [fname, pname] = uigetfile({'*.xlsx','*.txt'},'File Open Dialog');
    [~,~,ext] = fileparts(fullfile(pname,fname));
    if strcmpi(ext,'.xlsx')
        w1 = xlsread(fullfile(pname,fname));
    elseif strcmpi(ext,'.txt')
        w1 = importdata(fullfile(pname,fname));
    else
        uialert(app.RamanImagingUIFigure,'Wrong file format','File
        error');
    end
    app.WavelengthTable.Data = [app.WavelengthTable.Data; w1];
end

% Button pushed function: ChoosefileTemp
function ChoosefileTempButtonPushed(app, event)
    [fname, pname] = uigetfile({'*.txt'},'File Open Dialog');
    app.OPOTuningFilePath.Value = fullfile(pname,fname);
    app.tuning_file = fullfile(pname,fname);
end

% Value changed function: SetTemperatureSpinner
function SetTemperatureSpinnerValueChanged(app, event)
```


Appendices

```
    app.temperature.set = app.SetTemperatureSpinner.Value;
end
% Button pushed function: ChangeTemperatureButton
function ChangeTemperatureButtonPushed(app, event)
    templambda(app);
end
% Value changed function: PiezoEndSpinner
function PiezoEndSpinnerValueChanged(app, event)
    app.piezo.end = app.PiezoEndSpinner.Value;
end
% Value changed function: PiezoStepSpinner
function PiezoStepSpinnerValueChanged(app, event)
    app.piezo.step = app.PiezoStepSpinner.Value;
end
% Value changed function: PiezoStartSpinner
function PiezoStartSpinnerValueChanged(app, event)
    app.piezo.start = app.PiezoStartSpinner.Value;
end
% Button pushed function: SetpiezoscanButton
function SetpiezoscanButtonPushed(app, event)
    app.piezo.list = app.piezo.start:app.piezo.step:app.piezo.end;
end
% Button pushed function: GRABButton
function GRABButtonPushed(app, event)
    fprintf(app.serialport, 'SH0');
    if scannimagerunning(app)
        app.hSI.startGrab();
        while ~strcmpi(app.hSI.acqState, 'idle')
            pause(0.01);
        end
        updatechannels(app);
        app.AcquisitionDispField.Value = app.hSI.hScan2D.logFileCounter;
    end
    if app.hROIManager.enable
        for i = 1:app.hROIManager.numroi
            setroi(app,i);
        end
    end
    fprintf(app.serialport, 'SHC');
end
% Button pushed function: DIRButton_2
function DIRButton_2Pushed(app, event)
    if scannimagerunning(app)
        app.hSI.hScan2D.logFilePath = uigetdir
            ('C:\Users\LV13109\Desktop\Test');
        app.BaseNameEditField_2.Value = app.hSI.hScan2D.logFilePath;
    end
end
% Value changed function: SaveCheckBox_2
function SaveCheckBox_2ValueChanged(app, event)
    app.hSI.hChannels.loggingEnable = app.SaveCheckBox_2.Value;
end
% Value changed function: XStartPixelSpinner
```

Appendices

```
function XStartPixelSpinnerValueChanged(app, event)
    app.hROIManager.roi(app.hROIManager.cind).xstart =
        app.XStartPixelSpinner.Value;
end
% Value changed function: YStartPixelSpinner
function YStartPixelSpinnerValueChanged(app, event)
    app.hROIManager.roi(app.hROIManager.cind).ystart =
        app.YStartPixelSpinner.Value;
end
% Value changed function: XlengthSpinner
function XlengthSpinnerValueChanged(app, event)
    app.hROIManager.roi(app.hROIManager.cind).xlength =
        app.XlengthSpinner.Value;
end
% Value changed function: YlengthSpinner
function YlengthSpinnerValueChanged(app, event)
    app.hROIManager.roi(app.hROIManager.cind).ylength =
        app.YlengthSpinner.Value;
end
% Button pushed function: SetROIButton
function SetROIButtonPushed(app, event)
    app.hROIManager.enable = 1;
    setroi(app, app.hROIManager.cind);
end
% Value changed function: ZoomSpinner
function ZoomSpinnerValueChanged(app, event)
    if scannimagerunning(app)
        if strcmpi(app.ABORTButton.Visible, 'on')
            app.ABORTButton.Visible = 'off';
            pause(1);
            app.hSI.hRoiManager.scanZoomFactor = app.ZoomSpinner.Value;
            pause(1);
            FOCUSButtonPushed(app, event);
        else
            app.hSI.hRoiManager.scanZoomFactor = app.ZoomSpinner.Value;
        end
    end
end
end

% Button pushed function: ChoosefileZoom2FovTextPath
function ChoosefileZoom2FovTextPathButtonPushed(app, event)
    [fname, pname] = uigetfile({'*.txt'}, 'File Open Dialog');
    app.Zoom2FOVTextPath.Value = fullfile(pname, fname);
    m = importdata(fullfile(pname, fname));
    app.zoom2fov = m.data;
end
% Value changed function: XEditField
function XEditFieldValueChanged(app, event)
    app.hSI.hMotors.motorPosition(1) = app.prevMotorPos(1) +
        app.XEditField.Value;
end
% Value changed function: YEditField
```

Appendices

```
function YEditFieldValueChanged(app, event)
    app.hSI.hMotors.motorPosition(2) = app.prevMotorPos(2) +
    app.YEditField.Value;
end
% Value changed function: ZEditField
function ZEditFieldValueChanged(app, event)
    app.hSI.hMotors.motorPosition(3) = app.prevMotorPos(3) +
    app.ZEditField.Value;
end
% Button pushed function: FOCUSButton
function FOCUSButtonPushed(app, event)
    app.ABORTButton.Visible = 'on';
    while strcmpi(app.ABORTButton.Visible, 'on')
        if scannimagerunning(app)
            app.hSI.startGrab();
            while ~strcmpi(app.hSI.acqState, 'idle')
                pause(0.01);
            end
            updatechannels(app);
        end
    end
end
% Button pushed function: ABORTButton
function ABORTButtonPushed(app, event)
    app.ABORTButton.Visible = 'off';
end

% Value changed function: SCANMODEDropDown
function SCANMODEDropDownValueChanged(app, event)
    app.scanmode = app.SCANMODEDropDown.Value;
end
% Callback function
function RoiPixelsLineValueChanged(app, event)
    app.roi.pixelsPerLine = app.RoiPixelsLine.Value;
end
% Callback function
function RoiZoomSpinnerValueChanged(app, event)
    app.roi.zoom(2) = app.RoiZoomSpinner.Value;
end
% Button pushed function: NEWROIButton
function NEWROIButtonPushed(app, event)
    app.hROIManager.numroi = app.hROIManager.numroi + 1;
    app.hROIManager.cind = app.hROIManager.numroi;
    app.ROINumberSpinner.Value = app.hROIManager.numroi;
    app.hROIManager.roi(app.hROIManager.cind).xstart =
    app.XStartPixelSpinner.Value;
    app.hROIManager.roi(app.hROIManager.cind).ystart =
    app.YStartPixelSpinner.Value;
    app.hROIManager.roi(app.hROIManager.cind).xlength =
    app.XlengthSpinner.Value;
    app.hROIManager.roi(app.hROIManager.cind).ylength =
    app.YlengthSpinner.Value;
```

Appendices

```
end
% Value changed function: OPOShutterSwitch
function OPOShutterSwitchValueChanged(app, event)
    if strcmpi(app.OPOShutterSwitch.Value, 'on')
        fprintf(app.serialport, 'SH0');
    else
        fprintf(app.serialport, 'SHC');
    end
end
% Value changed function: ShutterTimeSpinner
function ShutterTimeSpinnerValueChanged(app, event)
    app.hROIManager.shuttertime = app.ShutterTimeSpinner.Value;
end
% Value changed function: ChannelDropDown
function ChannelDropDownValueChanged(app, event)
    idx = str2num(app.ChannelDropDown.Value);
    try
        imshow(mat2gray(app.fullImage{idx}), 'Parent',
            app.FullImageAxes);
        axis(app.FullImageAxes, 'image');
    catch ME
        uialert(app.RamanImagingUIFigure, ME.message, ME.identifier);
    end
end
% Value changed function: ActiveImagingsystemDropDown
function ActiveImagingsystemDropDownValueChanged(app, event)
    app.hSI.imagingSystem = app.ActiveImagingsystemDropDown.Value;
end
% Value changed function: ScanTypeDropDown
function ScanTypeDropDownValueChanged(app, event)
    app.hSI.hScan2D.scannerType = app.ScanTypeDropDown.Value;
end
% Value changed function: PixelsLineDropDown
function PixelsLineDropDownValueChanged(app, event)
    app.hSI.hRoiManager.pixelsPerLine = app.PixelsLineDropDown.Value;
end
% Value changed function: LinesFrameEditField
function LinesFrameEditFieldValueChanged(app, event)
    app.hSI.hRoiManager.linesPerFrame = app.LinesFrameEditField.Value;
end
% Value changed function: PixLinCheckBox
function PixLinCheckBoxValueChanged(app, event)
    app.hSI.hRoiManager.forceSquarePixelation = app.PixLinCheckBox.Value;
    if app.PixLinCheckBox.Value
        app.LinesFrameEditField.Enable = 'on';
    else
        app.LinesFrameEditField.Enable = 'off';
    end
end
% Value changed function: SquarePixCheckBox
function SquarePixCheckBoxValueChanged(app, event)
    app.hSI.hRoiManager.forceSquarePixels = app.SquarePixCheckBox.Value;
```

Appendices

```
end
% Value changed function: FrameRateHzEditField
function FrameRateHzEditFieldValueChanged(app, event)
    app.hSI.hRoiManager.scanFrameRate = app.FrameRateHzEditField.Value;
end
% Value changed function: BidirectionalScanCheckBox
function BidirectionalScanCheckBoxValueChanged(app, event)
    app.hSI.hScan2D.bidirectional = app.BidirectionalScanCheckBox.Value;
end
% Value changed function: ScanPhaseEditField
function ScanPhaseEditFieldValueChanged(app, event)
    app.hSI.hScan2D.linePhase = app.ScanPhaseEditField.Value*1e-6;
end
% Value changed function: ScanPhaseSlider
function ScanPhaseSliderValueChanged(app, event)
    app.hSI.hScan2D.linePhase = app.ScanPhaseSlider.Value*1e-6;
end
% Value changed function: ScanLineRateDropDown
function ScanLineRateDropDownValueChanged(app, event)
    value = app.ScanLineRateDropDown.Value;
end
% Value changed function: RotateSpinner
function RotateSpinnerValueChanged(app, event)
    app.hSI.hRoiManager.scanRotation = app.RotateSpinner.Value;
end
% Button pushed function: SetRotationton0Button
function SetRotationton0ButtonPushed(app, event)
    app.hSI.hRoiManager.scanRotation = 0;
    app.RotateSpinner.Value = 0;
end
% Button pushed function: SetZoomFullButton
function SetZoomFullButtonPushed(app, event)
    app.hSI.hRoiManager.scanZoomFactor = 1;
    app.ZoomSpinner = 1;
end
% Callback function
function ShiftEditFieldValueChanged(app, event)
    app.hSI.hRoiManager.scanAngleShiftFast = app.ShiftEditField.Value;
end
% Callback function
function ShiftSlowEditFieldValueChanged(app, event)

    app.hSI.hRoiManager.scanAngleMultiplierFasthSI.hRoiManager.scanAngle
    ShiftSlow = app.ShiftSlowEditField.Value;
end
% Value changed function: FastEditField
function FastEditFieldValueChanged(app, event)
    app.hSI.hRoiManager.scanAngleMultiplierFast =
    app.FastEditField.Value;
end
% Value changed function: SlowEditField
function SlowEditFieldValueChanged(app, event)
```

Appendices

```
    app.hSI.hRoiManager.scanAngleMultiplierSlowhSI.hRoiManager.scanAngle
    MultiplierSlow = app.SlowEditField.Value;
end
% Value changed function: ScanLineRateEditField
function ScanLineRateEditFieldValueChanged(app, event)
    app.hSI.hScan2D.scanPixelTimeMean =app.ScanLineRateEditField.Value;
    app.ScanLineRateSlider.Value = app.ScanLineRateEditField.Value;
end
% Value changed function: SpatialEditField
function SpatialEditFieldValueChanged(app, event)
    if strcmpi(app.hSI.imagingSystem, 'LinScanner')
        app.hSI.hScan2D.fillFractionTemporal =
            app.SpatialEditField.Value;
        app.hSI.hScan2D.fillFractionSpatial =
            app.SpatialEditField.Value;
        app.TemporalEditField.Value = app.SpatialEditField.Value;
    else
        app.hSI.hScan2D.fillFractionSpatial =app.SpatialEditField.Value;
    end
    updaterrates(app);
end
% Value changed function: TemporalEditField
function TemporalEditFieldValueChanged(app, event)
    if strcmpi(app.hSI.imagingSystem, 'LinScanner')
        app.hSI.hScan2D.fillFractionTemporal =
            app.SpatialEditField.Value;
        app.hSI.hScan2D.fillFractionSpatial =
            app.SpatialEditField.Value;
        app.SpatialEditField.Value = app.SpatialEditField.Value;
    else
        app.hSI.hScan2D.fillFractionSpatial =app.SpatialEditField.Value;
    end
    updaterrates(app);
end
% Value changed function: PixelBinFactorEditField
function PixelBinFactorEditFieldValueChanged(app, event)
    app.hSI.hScan2D.pixelBinFactor = app.PixelBinFactorEditField.Value;
    app.hSI.hScan2D.scanPixelTimeMean =
        app.PixelBinFactorEditField.Value/app.hSI.hScan2D.sampleRate;
    updaterrates(app);
end
% Value changed function: sampleRateMHzEditField
function sampleRateMHzEditFieldValueChanged(app, event)
    app.hSI.hScan2D.sampleRate = app.sampleRateMHzEditField.Value*1e6;
    app.hSI.hScan2D.scanPixelTimeMean =
        app.PixelBinFactorEditField.Value/app.hSI.hScan2D.sampleRate;
    updaterrates(app);
end
% Value changed function: PixelTimemaxminEditField
function PixelTimemaxminEditFieldValueChanged(app, event)
    app.hSI.hScan2D.scanPixelTimeMaxMinRatio =
        app.PixelTimemaxminEditField.Value;
```

Appendices

```
end
% Value changed function: FrameflybackmsEditField
function FrameflybackmsEditFieldValueChanged(app, event)
    app.hSI.hScan2D.flybackTimePerFrame =
        app.FrameflybackmsEditField.Value;
end
% Button pushed function: ReadPosButton_2
function ReadPosButton_2Pushed(app, event)
    updatemotorpos(app);
end
% Button pushed function: ZeroXYButton_2
function ZeroXYButton_2Pushed(app, event)
    app.prevMotorPos(1) = app.hSI.hMotors.motorPosition(1);
    app.prevMotorPos(2) = app.hSI.hMotors.motorPosition(2);
    app.XEditField.Value = 0;
    app.YEditField.Value = 0;
end
% Button pushed function: ZeroXYZButton_2
function ZeroXYZButton_2Pushed(app, event)
    app.prevMotorPos(1) = app.hSI.hMotors.motorPosition(1);
    app.prevMotorPos(2) = app.hSI.hMotors.motorPosition(2);
    app.prevMotorPos(3) = app.hSI.hMotors.motorPosition(3);
    app.XEditField.Value = 0;
    app.YEditField.Value = 0;
    app.ZEditField.Value = 0;
end
% Button pushed function: ZeroZButton_2
function ZeroZButton_2Pushed(app, event)
    app.prevMotorPos(3) = app.hSI.hMotors.motorPosition(3);
    app.ZEditField.Value = 0;
end
% Button pushed function: CleargraphButton
function CleargraphButtonPushed(app, event)
    cla(app.srsint);
end
% Value changed function: TissueLengthmmSpinner
function TissueLengthmmSpinnerValueChanged(app, event)
    app.tissueProps.length = app.TissueLengthmmSpinner.Value;
end
% Value changed function: TissueWidthmmSpinner
function TissueWidthmmSpinnerValueChanged(app, event)
    app.tissueProps.width = app.TissueWidthmmSpinner.Value;
end
% Button pushed function: GettissueoutlineButton
function GettissueoutlineButtonPushed(app, event)
    uialert(app.RamanImagingUIFigure,['Tissue size is set at',...

        num2str(app.tissueProps.length),'x',num2str(app.tissueProps.len
        gth),...
        'mm. Make sure this is correct. Make sure 20x objective is
        installed and focussed on bottom right of the tissue'],...
        'Tissue Outline');
    app.cycleProps.xspan = app.tissueProps.length*1000;
```

Appendices

```
app.cycleProps.yspan = app.tissueProps.width*1000;
ObjectiveDropDownValueChanged(app, event);
startMotorPos = app.hSI.hMotors.motorPosition;
app.cycleProps.boxsize = floor(app.tissueProps.fov);
SetCycleDataButtonPushed(app, event);
LOOPCYCLEButtonPushed(app, event);
imagefilenames = dir([app.hSI.hScan2D.logFilePath, '\*.tif']);
for i = 1:length(imagefilenames)

    delete([app.hSI.hScan2D.logFilePath, '\', imagefilenames(i).name]);
end
fig = figure('Name', 'Select tissue outline');
idx = str2num(app.ChannelDropDown.Value);
imagesc(app.fullImage{idx}');
[~, app.tissueProps.Xoutline, app.tissueProps.Youtline] = roipoly;
close(fig);
for idx = 1:3
    app.tissueProps.image{idx} =
        app.fullImage{idx}(ceil(min(app.tissueProps.Xoutline)):...

            ceil(max(app.tissueProps.Xoutline)), ceil(min(app.tissueProps.
                Youtline)):ceil(max(app.tissueProps.Youtline)));
end
s = size(app.fullImage{idx});
umPerPixel = app.tissueProps.length./s*1000;
app.tissueProps.motor.start = [startMotorPos(1) +
    min(app.tissueProps.Xoutline)*umPerPixel(1), ...
    startMotorPos(2) + min(app.tissueProps.Youtline)*umPerPixel(2)];
app.cycleProps.xspan = (max(app.tissueProps.Xoutline)
    min(app.tissueProps.Xoutline))*umPerPixel(1);
app.cycleProps.yspan = (max(app.tissueProps.Youtline)
    min(app.tissueProps.Youtline))*umPerPixel(2);
end
% Value changed function: FOVumSpinner
function FOVumSpinnerValueChanged(app, event)
    app.tissueProps.fov = app.FOVumSpinner.Value;
end
% Value changed function: ObjectiveDropDown
function ObjectiveDropDownValueChanged(app, event)
    app.tissueProps.objective = app.ObjectiveDropDown.Value;
    if strcmpi(app.tissueProps.objective, '20x')
        app.tissueProps.fov = app.zoom2fov(app.zoom2fov(:,1) ==
            app.hSI.hRoiManager.scanZoomFactor, 3);
    elseif strcmpi(app.tissueProps.objective, '60x')
        app.tissueProps.fov = app.zoom2fov(app.zoom2fov(:,1) ==
            app.hSI.hRoiManager.scanZoomFactor, 2);
    end
end
% Button pushed function: CreatefocusmapButton
function CreatefocusmapButtonPushed(app, event)
    fov = floor(app.tissueProps.fov);
    if scannimagerunning(app)
```


Appendices

```
        setMotorPos =
        [app.tissueProps.motor.start,app.hSI.hMotors.motorPosition(3)];
        app.hSI.hMotors.moveStartRelative(setMotorPos);
    while app.hSI.hMotors.nonblockingMoveInProgress
        pause(0.01);
    end
else
    return
end

app.cycleProps.boxsize = fov;
SetCycleDataButtonPushed(app, event);
Nx = ceil(app.cycleProps.xspan/fov) + 1;
Ny = ceil(app.cycleProps.yspan/fov)+ 1;
app.tissueProps.focus = nan(1,Nx*Ny);
app.tissueProps.Nfocuspoints = Nx*Ny;
    for i = 1:app.tissueProps.Nfocuspoints
        setPos=str2num(app.hSI.hCycleManager.cycleDataGroup.
            cycleIters(i).motorStep);
        if scannimagerunning(app)
            app.hSI.hMotors.moveStartRelative(setPos);
            while app.hSI.hMotors.nonblockingMoveInProgress
                pause(0.01);
            end
        else
            return
        end
        app.FInumberEditField.Value = i;
        app.hSI.startFocus();
        while ~strcmpi(app.hSI.acqState,'idle')
            pause(0.01);
        end
        app.tissueProps.focus(i) = app.hSI.hMotors.motorPosition(3);
        updatechannels(app);
    end
    app.tissueProps.focus = round(fillmissing(app.tissueProps.
        focus,'linear',2));
    if any(isnan(app.tissueProps.focus))
        uialert(app.RamanImagingUIFigure,'Extrpolation of focus
        points failed. Select more focus points.','Focusing error');
        app.tissueProps.okayToStart = 0;
        return
    else
        app.tissueProps.okayToStart = 1;
    end
    cycleDatapath =[app.hSI.hScan2D.logFilePath,
        '\CycleData.txt'];
    fid = fopen(cycleDatapath,'w');
    for i = 1:Nx*Ny
        XYPos =str2num(app.hSI.hCycleManager.cycleDataGroup.
            cycleIters(i).motorStep);
        app.hSI.hCycleManager.cycleDataGroup.cycleIters(i).
        motorStep = num2str([XYPos(1:2),app.tissueProps.focus(i)],15);
```

Appendices

```
        fprintf(fid, '%s\n', app.hSI.hCycleManager.  
        cycleDataGroup.cycleIters(i).motorStep);  
    end  
    fclose(fid);  
end  
% Value changed function: NumberoffocuspointsSpinner  
function NumberoffocuspointsSpinnerValueChanged(app, event)  
    app.tissueProps.Nfocuspoints = app.NumberoffocuspointsSpinner.Value;  
end  
% Button pushed function: StartImagingTissueButton  
function StartImagingTissueButtonPushed(app, event)  
    if app.tissueProps.okayToStart  
        app.scanmode = 'w\lscan'  
        STARTSCANNINGButtonPushed(app, event);  
        %LOOPCYCLEButtonPushed(app, event);  
    end  
end  
% Button pushed function: LoadCycleDataButton  
function LoadCycleDataButtonPushed(app, event)  
    [fname, pname] = uigetfile({'*.txt'}, 'File Open Dialog');  
    fFilename = fullfile(pname, fname);  
    CycleData = importdata(fFilename);  
% perform relative move  
    if isempty(app.hSI)  
        uialert(app.RamanImagingUIFigure, 'Scanimage is notrunning. Please  
        start scan image', ...  
        'Scanimage error');  
    return;  
end
```

3. Matlab code for the SRH images

```
clear;close all

% Load images
img1 = imread('CH2.tif'); % assume that they are both 2D arrays.
img2 = imread('CH3.tif');

% Make the lowest intensity in each img 0
img1 = img1 - min(img1(:));
img2 = img2 - min(img2(:));

% Distribute intensities from 0 to 1;
img1 = double(img1);
img1 = img1/max(img1(:));
img2 = double(img2);
img2 = img2/max(img2(:));

% Subtract image, so img3 is the CH3-CH2 image.
img3 = img2-img1;

% Set up the Green-Blue image.
sz = size(img1); %assume same size for all images
img_RB = cat(3,zeros(sz),img1,img3);
subplot(2,2,1);imshow(img_RB);


% Convert to HE-ish colors.
% For pink: Map low intensities to [1 1 1] (white), and high
intensities to
% [1 0 1] (pink). Scale the green channel in between.
img_HE_pink = cat(3,ones(sz),(1-img1),ones(sz));
subplot(2,2,2);imshow(img_HE_pink);

% For deep violet: Map low intensities to [1 1 1] (white), and high
% intensities to
violet = [0 0 1];

img_HE_violet = cat(3,1-img3*(1-violet(1)), 1-img3*(1-violet(2)), 1-
img3*(1-violet(3))); % Scales all channels with img3
subplot(2,2,3);imshow(img_HE_violet);

img_comb = (img_HE_pink + img_HE_violet);
sc = .4; %scales intensities in final image
subplot(1,1,1);imshow(img_comb*sc);
```

4. Ethical approval


Avon, Gloucestershire and Wiltshire 
Health Authority

Gloucestershire LREC
Gloucestershire Royal Hospital
Great Western Road
Gloucester
GL1 3NN
Tel: 01452 395726
Fax: 01452 395720
Email: Hazel.Gage@gloucr-tr.swest.nhs.uk

Our Ref: 02_112G(28_4)

28 April 2003

Professor Hugh Barr
Consultant Surgeon
Ward 9
Gloucestershire Royal Hospital
Great Western Road
Gloucester GL1 3NN

Dear Professor Barr 

Study No 02/112G : Investigation of cancerous and pre-cancerous changes in Barrett's oesophagus using techniques to advance the early diagnosis of malignancy

Thank you for your letter dated 11 April 2003 enclosing the amendments for the above study. I have now reviewed the amendments and will be advising the committee that in my view there is now no objection on ethical grounds to the proposed study. Therefore, I am happy to give you approval on the understanding that you will follow the conditions of the approval set out below. The following documents were reviewed by the committee: -

- LREC application form
 - Protocol (Version 2, April 2003)
 - Consent Form (Version 1, January 2003)
 - Patient Information Sheet (Version 1, January 2003)
 - Curriculum Vitae
- a) It is the responsibility of the investigator to notify the LREC immediately of any information received by him/her, or of which he/she becomes aware which would cast doubt upon, or alter, any information contained in the original application, a later amendment application or verbal resume submitted to the LREC. The committee should be informed immediately if this information would raise questions about the safety and/or continued conduct of the research.
- b) The need to comply with the Data Protection Act 1998.
- c) You will need to comply with the Research Governance Framework for Health and Social Care (Department of Health 2001). This includes the requirement to

Appendices

make available records for the monitoring of the study by the research sponsor. Further information regarding this document can be obtained from Gloucestershire Research & Development Support Unit on 01452 395726.

- d) The need to refer proposed amendments to the protocol to the LREC for further review and to obtain LREC approval thereto prior to implementation (except only in cases of emergency where the welfare of the subject is paramount).
- e) The requirement to furnish the LREC with details of the progress of the research project periodically (usually annually) and **failure to do this could result in approval to continue with the study being withdrawn**. Please also inform us of the conclusion and outcome of the research project and inform the LREC should the research be discontinued or any subject withdrawn altogether.
- f) It is the responsibility of the person conducting any Trial to ensure that all professional staff and management of NHS Trusts involved are notified that it is taking place.

Gloucestershire LREC is fully compliant with the International Conference on Harmonisation/ Good Clinical Practice (ICH GCP) Guidelines for the Conduct of Trials Involving the Participation of Human Subjects.

Please indicate your agreement to comply with the requirements outlined in this letter by signing both copies of this letter and returning one to Hazel Gage. Full approval does not commence until the signed copy is returned.

Yours sincerely



Dr M J Richards
Chairman, Gloucestershire LREC

cc: Dr Sally Pearson, Director of Clinical Strategy, Glos Hospitals NHS Trust
Catherine Kendall, Cranfield Postgraduate Medical School

I agree to comply with the requirements outlined in this letter.

Signed

Date

Appendices

- **Extension approval**

From: WALKER, Mark (GLOUCESTERSHIRE HOSPITALS NHS FOUNDATION TRUST)
Sent: 03 January 2018 12:41
To: KENDALL, Catherine (GLOUCESTERSHIRE HOSPITALS NHS FOUNDATION TRUST)
Cc: BATES, Allison (GLOUCESTERSHIRE HOSPITALS NHS FOUNDATION TRUST);
JOHNSON, Nigel (GLOUCESTERSHIRE HOSPITALS NHS FOUNDATION TRUST)
Subject: RE: 02/112G and 03/142G amendments

Dear Catherine

Re: Raman Spectroscopy for cancer and pre-cancer detection
REC/R&D Ref: 02/112G

Extension Amendment #1 – 1st June 2017

This email is to confirm approval for Extension Amendment #1, dated 1st June 2017 for the above study in line with the email below. Due to the age of the study and two subsequent REC Committees being changed, there are no active records of this study at the HRA and it has been agreed that we can provide our own approval for this amendment in lieu of any HRA review.

I have updated the relevant information on the EDGE record and will inform the NIHR of the changes.

If you have any questions, please let me know.

Kind regards

Mark

Senior Research Manager - Governance
Gloucestershire Research Support Service
Leadon House
Gloucestershire Royal Hospital
Great Western Road
Gloucester
GL1 3NN

Tel: 0300 422 5463

Fax: 0300 422 5469

Please note my NHS email is now mark.walker9@nhs.net please update your records

Appendices



From: carmen.pinder@nihr.ac.uk [<mailto:carmen.pinder@nihr.ac.uk>] **On Behalf Of**
Portfolio Team
Sent: 04 September 2018 11:37
To: KENDALL, Catherine (GLOUCESTERSHIRE HOSPITALS NHS FOUNDATION TRUST)
Cc: HALL, Julia (GLOUCESTERSHIRE HOSPITALS NHS FOUNDATION TRUST); Thomas Llewellyn; LLEWELLYN, Thomas (GLOUCESTERSHIRE HOSPITALS NHS FOUNDATION TRUST); BATES, Allison (GLOUCESTERSHIRE HOSPITALS NHS FOUNDATION TRUST); David Rea; JOHNSON, Nigel (GLOUCESTERSHIRE HOSPITALS NHS FOUNDATION TRUST); Stone, Nick (N.Stone@exeter.ac.uk)
Subject: Re: RECaD (Division 1, ID 1203) - extension request

Dear Catherine/Study Team

Re: CPMS ID: 1203, IRAS ID: 0
RECaD - Raman spectroscopy for cancer and pre-cancer detection in the oesophagus

Thank you for providing us with the information needed to amend the planned recruitment end date for the above study in CPMS.

We have updated the planned end of recruitment date for your study from 01/08/2017 to 30/06/2020.

Many thanks and kind regards,

Carmen

Portfolio Team



e. crncc.portfoliob@nihr.ac.uk

a. 21 Queen Street, Leeds, LS1 2TW

We would really appreciate you taking 5-10 minutes to tell us about your experience of working with us. Providing this feedback will help us to understand how we can improve our service to you. Please click here to complete our survey:

<https://www.surveymonkey.co.uk/r/studysupportservice>

Portfolio Facilitators Chris Walsh: 0151 282 4717 (07717714453) / Jennifer Green: 0191 229 9524 / Samantha Sutulic: 0113 343 4440 / Deana Irvine: 0113 343 0412 / Ed Park: 0113 343 8940 /

Appendices

Suzan Yalcin: 0203 328 6721 Senior Portfolio Research Officer Amy Rebane: 0113 343 9364
Portfolio Research Officers Amber Hayes: 0191 229 9514 / Angela Early: 0113 343 0345 /
Alex Broadie: 0113 343 3493 Support Assistants Heather Harper: 0113 343 0026 / Jessica
Kjenstad: 0113 343 2988 / Tom Hustler: 0113 343 9366